Multiscale Modeling of Planetary Boundary Layers on Earth and Mars

Dissertation presented to obtain the degree of
Doctor in Engineering Sciences & Technology
by **Cem Berk Senel**

2023

Committee

Promoter:	
Prof. Alessandro Parente	Université Libre de Bruxelles
Co-Promoter:	
Prof. Jeroen van Beeck	von Karman Institute for Fluid Dynamics
Doctoral committee:	
Dr. Ozgur Karatekin	Royal Observatory of Belgium
Dr. Orkun Temel	KU Leuven & Royal Observatory of Belgium
Prof. M. Isabelle Calmet	École Centrale de Nantes
Prof. Clara García-Sánchez	Delft University of Technology
Dr. Domingo Muñoz-Esparza	National Center of Atmospheric Research
Secrétaire:	
Prof. Patrick Hendrick	Université Libre de Bruxelles
Président:	
Prof. Axel Coussement	Université Libre de Bruxelles

Acknowledgements

A voyage through turbulence on Earth and Mars... I am grateful to everyone who made this dream come true.

First of all, my beloved wife Asli Irem, and my parents have my eternal thanks who have been by my side and always helped me with endless support. I am greatly thankful to my scientific advisors, Dr. Ozgur Karatekin, Dr. Orkun Temel, and Dr. Domingo Munoz-Esparza that I would not have succeeded without their guidance. I want to thank my promoters, Prof. Alessandro Parente and Prof. Jeroen van Beeck, for their continuous support during my doctoral journey. I want to express my gratitude to all my jury members for their constructive feedback and helpful suggestions. My special thanks go to Dr. Ozgur Karatekin, for his eye-opening planetary science vision, which helped me a lot once my thesis travels from Earth to the Red Planet. I want to thank Dr. Orkun Temel, for his brilliant ideas on atmospheric physics that have been helpful while modeling turbulence on challenging occasions. I am thankful to Prof. Jeroen van Beeck, for his unique teaching on turbulence theory and modeling and support at von Karman Institute for Fluid Dynamics. I want to thank Prof. Veronique Dehant, for her tremendous inspiration on Mars science and habitability. I am truly thankful to Dr. Ozgur Karatekin, Prof. Veronique Dehant, and Dr. Ronald Van der Linden who provided me with the great opportunity to study on Mars science & exploration at Royal Observatory of Belgium. I want to thank all my great colleagues and friends (Adriana Enache, David Henneaux, Domenico Fiorini, Dr. Bart Van Hove, Dr. Bayindir Saracoglu, Dr. Birgit Ritter, Dr. Elodie Gloesener, Dr. Matthias Noeker, Dr. Fabian Roosbeek, Dr. Sara Porchetta, Dr. Sebastien Le Maistre, Elisa Tasev, Elisabeta Petrescu, Emmanuel Gamby, Ertan Umit, Fleur Seuren, Gregoire Henry, Guillaume Noiset, Hakan Sert, Sarah Willems, Valerio Filice, -sorted alphabetically) to share such memorable moments all together, especially during our beer meetings. While I didn't touch upon it in my thesis, this four-year journey involved a fascinating Chicxulub asteroid impact story crafted with the AMGC team at VUB (in review at Nature Geoscience, by the time this was written), for which I want to thank Prof. Philippe Claeys, Pim Kaskes, Prof. Johan Vellekoop, Prof. Steven Goderis. Finally, I would also like to thank Dr. Cristopher Lee (University of Toronto), Dr. Claire Newman (Aeolis Research), Dr. Aymeric Spiga (LMD Paris), and Dr. Michael Mischna (NASA Jet Propulsion Laboratory), for their tremendous support of Mars atmosphere modeling.

Turbulence - "*Big whorls have little whorls which feed on their velocity, and little whorls have lesser whorls and so on to viscosity*". Lewis Fry Richardson, 1922.

For Asli Irem.
For my parents.

Abstract

The planetary boundary layer (PBL) is the turbulently most active part of the Earth's and Martian lower atmospheres. Over the last few decades, high-resolution satellite and in-situ measurements, plus the rapid growth in the massive computing have provided a growing interest in this phenomenon, ranging from weather and climate studies to planetary science applications. Thanks to the ongoing lander and rover missions, in-situ observations of Martian surface processes, such as dust, water and methane transport, have been attracting more attention, especially in to search for the signatures of the planet's habitability. This highlights the significance of PBL dynamics, which is the primary governor of surface-atmosphere exchange processes on Mars. The PBL, on the other hand, has various physical phenomena associated with a large range of length scales, from planetary scales to microscales. Therefore, the present thesis proposes a series of novel turbulence models in a multiscale framework to advance the current knowledge on the nature of PBL turbulence forming in the atmospheres of Earth and Mars. This study, for the first time, presents a novel scale-aware gray-zone turbulence, fully representing the three-dimensional turbulence fluxes in the so-called "Terra Incognita" range of scales, in which traditional turbulence models become invalid as they were initially designed for their own either mesoscale or microscale limits. Here, the new gray-zone turbulence model offers an advanced framework for bridging the mesoscale and microscale limits that is suitable for the development of next-generation three-dimensional multiscale turbulence models for Earth and Mars. The generic formulation of new turbulence models developed here is extensively applicable to a wide range of terrestrial planetary atmospheres, ranging from Saturn's moon Titan towards terrestrial exoplanets.

Contents

Doctoral committee i

Acknowledgements iii

Abstract vii

List of Figures xi

List of Tables xvii

1 General introduction 1
- 1.1 Introduction . . . 1
- 1.2 Atmospheric instability . . . 4
- 1.3 Earth vs. Mars . . . 7
- 1.4 Monin-Obukhov similarity theory . . . 8
- 1.5 PBL scaling parameters . . . 10
- 1.6 Large-eddy simulation (LES) modeling . . . 11
- 1.7 Subgrid-scale (SGS) models . . . 14
  - 1.7.1 Smagorinsky SGS model . . . 14
  - 1.7.2 One-Equation-Eddy-Viscosity SGS model . . . 15
  - 1.7.3 Lagrangian-Averaged Scale-Invariant Dynamic SGS model . . . 15
  - 1.7.4 Nonlinear-Backscatter-Anisotropy (NBA) SGS model . . . 18
- 1.8 Motivation and thesis outline . . . 18

2 From large-eddy simulations to a new 1D PBL model for Earth 21
- 2.1 Introduction . . . 21
- 2.2 Theory & Modeling . . . 24
  - 2.2.1 Description of the new planetary boundary layer scheme . . . 24
  - 2.2.2 Large-eddy simulation (LES) setup . . . 30
  - 2.2.3 Idealized PBL Simulations . . . 43
  - 2.2.4 Application to the XPIA field campaign . . . 45
- 2.3 Discussion and conclusions . . . 54

3 From large-eddy simulations to a new 1D PBL model for Mars 57
- 3.1 Introduction . . . 57
- 3.2 Theory & Modeling . . . 62

3.2.1 MarsWRF and large-eddy simulation methodology 62
3.2.2 Martian LES configuration 65
3.2.3 Description of the new Mars-specific PBL scheme 75
3.2.4 Determination of the closure coefficients 76
3.2.5 Turbulent mixing length scale formulation 77
3.2.6 Mesoscale simulations in comparison with in-situ observations of NASA's InSight Mars Lander 81
3.3 Discussion & Conclusions 86

4 General circulation modeling of Martian convective PBL with a new semi-interactive dust transport model **89**
4.1 Introduction 89
4.2 Theory & Modeling 94
4.2.1 Description of the MarsWRF general circulation model . . . 94
4.2.2 Development of a new semi-interactive dust transport scheme 94
4.2.3 Verification of the new dust transport model 98
4.2.4 Martian GCM results: Seasonal and inter-annual variations . 102
4.2.5 Martian GCM results: Regional variations 112
4.2.6 Comparison with Mars Express (MEX) radio occultations . . 118
4.3 Discussion and Conclusions 122

5 Towards next-generation PBL models: Bridging meso-microscale limits with a new 3D scale-adaptive gray-zone turbulence model **125**
5.1 Introduction 125
5.2 Theory & Modeling 129
5.2.1 Details of the high-resolution LES setup 129
5.2.2 Coarse-graining the LES to gray-zone scales 131
5.2.3 Determination of the order of the Butterworth filter 132
5.2.4 Functional form for the gray-zone partitioning functions . . 134
5.2.5 Development of scale-aware three-dimensional gray-zone (Senel-Temel 3DPBL) turbulence model 139
5.3 Discussion & Conclusions 150

6 General conclusions **153**
6.1 Summary and main results 153
6.2 Areas for future research and improvements 155

Appendices **159**
Appendix A: Derivation of the turbulence kinetic energy budget equation . 159
Appendix B1: Sensitivity of the SGS model coefficients 163
Appendix B2: Sensitivity of the mixing length scale on the GCM 164
Appendix C: GCM vs. MEX radio occultations in terms of CBL depth . . . 165

Bibliography **195**

List of publications **197**

List of Figures

1.1 Layers of the Earth's atmosphere and location of the planetary boundary layer lying within the ~ 12-km depth troposphere. (Stull, 2016). 2

1.2 Atmospheric models depending on model resolution spectrum from global to microscales. Top panels: (left) Latest Cretaceous paleogeoraphic map for paleoEarth GCM that we develop to reconstruct the climatic conditions in the aftermath of Chicxulub asteroid impact (Senel et al., 2021a), (center) nested mesoscale domains centered in Colorado with the terrain elevation (Senel et al., 2019), (right) microscale convective cells within the Earth's PBL from high-resolution LES (Senel et al., 2020b). Bottom panels: (left) Martian global topography for MarsGCM (Senel et al., 2021b), obtained from Mars Orbiter Laser Altimeter (MOLA) (Smith et al., 2001). (center) Martian mesoscale domain centered at NASA's InSight landing site, in Elysium Planitia (Senel et al., 2020a). (right) Microscale convective rolls forming within the Martian convective PBL (Senel et al., 2020a). 3

1.3 Diurnal variation of the planetary boundary layer from deep convective to shallow stable regimes (Stull, 2016). 5

1.4 Vertical potential temperature gradient, $\partial\theta/\partial z$, profiles for statically unstable and stable conditions (Stull, 2016). 6

1.5 Comparison of the Earth's and Martian atmosphere in terms of the atmospheric composition by volume. Credit: The European Space Agency - ESA. 7

1.6 Flux Richardson number map regarding the turbulence kinetic energy generation by shear and buoyancy forcing. Dashed lines divide different atmospheric instability regions (Stull, 2016). R_f and SST denote the flux Richardson number and stably-stratified turbulence, respectively. 11

1.7 Schematic view of the LES filtering process which decomposes the space-time variable as resolved and subgrid scales by a sharp cutoff filtering in Fourier space (Sagaut, 2006). 12

1.8 Turbulent energy spectrum along with the eddy wavenumbers, related to the test and grid filters in dynamic SGS model (Davidson, 2011). 17

2.1 Horizontally-averaged wind speed profiles normalized by the reference friction velocity depending on the atmospheric stability. Solid lines refer to the LES results and open markers refer to the Høvsøre experiment (Gryning et al., 2007). (Subscripts, vu: Very unstable, mu: Moderate unstable, nu: Near-neutral unstable, n: Near-neutral, ns: Near-neutral stable, ms: Moderate stable, vs: Very stable) 34

2.2 Vertical profiles of the time- and horizontal averaged wind speed (a), potential temperature (b), total TKE (c) and SGS TKE (d) for different atmospheric stabilities. Horizontal gray dashed lines show the PBL height. (Subscripts, vu: Very unstable, mu: Moderate unstable, nu: Near-neutral unstable, n: Near-neutral, ns: Near-neutral stable, ms: Moderate stable, vs: Very stable) 36

2.3 Time- and streamwise averaged energy spectra vs. spanwise wavenumber, κ_2, for very unstable (top), near neutral (middle) and very stable (bottom) conditions at two different altitudes, i.e. $z/z_i = 0.05$ and $z/z_i = 0.80$. Black, blue and red solid lines denote the averaged energy spectra of resolved $\widetilde{u_1}\widetilde{u_1}$, $\widetilde{u_2}\widetilde{u_2}$, $\widetilde{u_3}\widetilde{u_3}$ fluctuations respectively. Gray dashed line denote the theoretical Kolmogorov -5/3 slope. 39

2.4 TKE budgets of very unstable (a), near neutral (b) and very stable (c) PBLs. Positive & negative signs of the budget denote TKE production & destruction. Horizontal gray dashed lines show the PBL height. Vertical profile of the dissipation (d) is given for unstable (red), near neutral (black) and stable (blue) conditions respectively. 40

2.5 Vertical profiles of the proposed mixing length scale compared to LES results. Solid lines refer to the proposed model and circular markers refer to LES results. The gray dashed lines refer to the PBL height. 42

2.6 Horizontally-averaged potential temperature predictions. Gray line with circle markers denotes Høvsøre LES results. Red, blue and green lines show the MYNN, BouLac and VKI01 (VKIPBL) schemes. Panels refer to very unstable (a), moderately unstable (b), near-neutral unstable (c) near-neutral stable (d), moderately stable (e), very stable (f) and near-neutral (g) conditions from left to right. 46

2.7 Horizontally-averaged wind speed predictions. Gray line with circle markers denotes Høvsøre LES results. Red, blue and green lines show the MYNN, BouLac and VKI01 (VKIPBL) schemes respectively. Panels refer to very unstable (a), moderately unstable (b), near-neutral unstable (c) near-neutral stable (d), moderately stable (e), very stable (f) and near-neutral (g) conditions from left to right. 47

2.8 WRF domain for the mesoscale simulation with the terrain elevation [m] where it is located at the Boulder Atmospheric Observatory (BAO) in Colorado (40.05°N, 105°W). The outer black line encircles the outer zone with the resolution 27 km where the inner region demonstrates the inner zone with 9 km resolution. 48

2.9 Time evolution of the turbulence kinetic energy, k, (top-left), dissipation rate, ϵ, (top-right), wind speed (bottom-left) and temperature (bottom-right) profiles at $z = 50\ m$ obtained from the VKI01 (VKIPBL) (blue line), MYNN (red line), BouLac (green line) schemes. Gray solid line denotes the mast measurements during March 7^{th}-9^{th} in 2015 at the XPIA field campaign from Muñoz-Esparza et al. (2018). 51

2.10 Time evolution of wind direction (top-left, top-right, bottom-left) and vertical speed (bottom-right) profiles at $z = 50\ m$ obtained from the VKI01 (VKIPBL) (blue line), MYNN (red line), BouLac (green line) schemes. Gray solid line denotes the mast measurements during March 7^{th}-9^{th} in 2015 at the XPIA field campaign from Muñoz-Esparza et al. (2018). 52

2.11 Time evolution of the friction velocity (top-left), PBL height (top-right), temperature at 2m (bottom-left) and mixing length scale at 300m (bottom-right) profiles obtained from the VKI01 (VKIPBL) (blue line), MYNN (red line), BouLac (green line) schemes. 53

3.1 Vertical profiles of time- and horizontally averaged wind speed (a), potential temperature (b), turbulence kinetic energy (c) and dissipation rate (d). Black dashed line denotes the normalized PBL height. All the LES computations are scaled by its own PBL height listed in Tab. 3.1 as z_i. 70

3.2 Time- and streamwise-averaged energy spectra vs. spanwise wavenumber, κ_2, for $q_s = 10\ W/m^2$ (top), $q_s = 20\ W/m^2$ (middle) and $q_s = 30\ W/m^2$ (bottom) conditions at two different altitudes, $z = 230\ m$ (left) and $z = 7.7\ km$ (right). Black, blue and red solid lines denote the averaged spectra of resolved $\widetilde{u_1'u_1'}$, $\widetilde{u_2'u_2'}$, $\widetilde{u_3'u_3'}$ fluctuations, respectively. Gray dashed line denotes the theoretical Kolmogorov -5/3 slope. 72

3.3 Vertical profiles of time- and horizontally averaged non-dimensional eddy heat flux (a), eddy momentum fluxes of streamwise (b), spanwise (c) and vertical (d) velocities. Black dashed line denotes the PBL height. All the LES computations are scaled by its own PBL height listed in Tab. 3.1 as z_i. 74

3.4 Instantaneous fields of the vertical velocity at $z/z_i \sim 0.05$ and $z/z_i \sim 0.40$ when $t = 2h$ for value of q_s between $q_s = 10$ (top) and $30\ W/m^2$ (bottom). . 75

3.5 Vertical profiles of time- and horizontally averaged mixing length scale profiles for different amount of convective instability. Dashed lines display the results of LES computations and solid lines refer to the proposed model. The gray highlight marks the region where the minimum and maximum values of the proposed l appears. Black dotted line denotes the convective PBL height. Note that all the LES computations are scaled by its own PBL height listed in Tab. 3.1 as z_i. 79

3.6 Vertical profiles of the potential temperature at $27.5°\ N, 107°\ W$ (left) and $21.8°\ N, 205°\ E$ (right), the reported locations of two radio occultations of MEX (Hinson et al., 2008). Blue and red solid lines with markers denote the θ predictions from our new scheme and the MRF scheme, respectively. Blue and red dashed lines show the PBL height estimations of our new scheme and the MRF scheme. Black dashed lines show the altitude above the surface, where the PBL height is diagnosed based on the MEX observations from Hinson et al. (2008). Note that the local time is 17.0h. 82

3.7 Global and mesoscale domains with terrain altitude (in km): d1 (Resolution: 298 km), d2 (Resolution: 99 km), d3 (Resolution: 33 km). The purple star at the center of innermost domain, d3, stands for the location of NASA's InSight lander, which is displayed at bottom-left (Credit: NASA Jet Propulsion Laboratory). 84

3.8 Observed and computed diurnal variations of air temperature (a) and wind speed (b). InSight observations, which are obtained each second, are smoothed by averaging for 15 min. MarsWRF output is for each 15 min. T_{air} and wind speed corresponds to the temperature and wind speed at the rover height (1.2 m). 85

4.1 Vertical profiles of dust mixing ratio $[kg/kg]$ at Oxia Planum ($335.45°E, 24.55°N$) in the northern late winter for Mars years **(a)** 31 and **(b)** 32. Colored solid lines indicate results from GCM simulations at local afternoon, from 12:30h to 15:30h. Gray markers refer to the whole available vertical MCS observations falling into local time between 12:00h-16:00h as reported in Forget and Montabone (2017), while the gray solid lines correspond to the mean of given vertical profiles having relative uncertainties in the dust opacity lower than 1 (see the details in Forget and Montabone (2017)). Vertical profiles of daytime dust opacity $[km^{-1}]$ from GCM (blue dashed lines) and MCS observations (Heavens et al., 2011b) (green solid lines) at following locations and seasons: **(c)** West of Huygens Crater (MY29, L_s ~166°), **(d)** Southwest of Amazonis Planitia (MY29, L_s ~165°), **(e)** North of Valles Marineris (MY29, L_s ~163°), **(f)** Southwest of Gusev Crater (MY30, L_s ~90°). The horizontal dashed line in each panel displayed is the reference scale-height of Mars, i.e., 11 km. 99

4.2 Seasonal variation of density-scaled dust opacity, $log_{10}\ dz\tau_d/\rho\ [m^2/kg]$ in MY 29 at $t = 15h$ (LMST). Latitudinal and vertical cross-sections are plotted at two longitudinal locations over $25°W$ (left panels) and $137°E$ (right panels). Black dashed lines represent the dust-top height, calculated at the altitude where the $\overline{\tau}_d = -3.3$, following Wu et al. (2020). 100

4.3 Seasonal evolution of dust particle effective radius through MY 32 **(a)** and MY 31 **(b)** above Gale crater. Blue (MY 32) and green (MY 31) solid lines show our GCM simulations with semi-interactive dust transport model. Light-blue solid lines with error bars refer to the rover measurements using the UV sensor (UVS) of the Rover Environmental Monitoring Station (REMS) and the Mastcam instrument, from Vicente-Retortillo et al. (2017). **(c)** Seasonal variation of column dust optical depth (CDOD) referenced to 700 Pa based on the dust climatology observations of Montabone et al. (2015) in MY 31 and MY 32. 101

4.4 Annual variation of the zonally averaged **(a)** CBL depth, **(b)** column dust optical depth referenced to 7 mb, **(c)** surface kinematic heat flux, **(d)** surface temperature, **(e)** Deardorff's convective velocity, **(f)** friction velocity. Here, the simulated case is Mars Year 33 in the local afternoon, $t = 15h$ (LMST). Note that the colorbar limits are set to same range as in Fig. 4.5. 105

4.5 As in Figure 4 but now showing results for Mars Year 34 106

4.6 Inter-annual variation of simulated globally averaged **(a)** surface kinematic heat flux, **(b)** surface temperature; and equatorial **(c)** Deardorff's convective velocity, **(d)** friction velocity, **(e)** column dust optical depth (CDOD) referenced to 7 mb, **(f)** daytime CBL depth, **(g)** daytime dust top height, shown for MY 24 through 34 in the local afternoon, $t = 15h$ (LMST). Note that the Deardoff's convective velocity, by definition $w_* = [(g/T_s)q_s z_i)]^{1/3}$, physically sounds when convection occurs. Here, we computed the Deardroff's convective velocity at local afternoon, therefore, even global dust storms block the sunlight, very weak conditions can occur between L_s ~185-250°. 110

4.7 The decade-long evolution of zonally averaged CBL depth from MY 24 to MY 34, in the local afternoon, $t = 15h$ (LMST). GDS-25, GDS-28 and GDS-34 are the global dust storm events occurring in MY 25, MY 28 and MY 34, respectively. 113

4.8 The regional variability in MY 33, in terms of the CBL depth in the northern early-summer (L_s=120°) **(a)** and southern early-summer (L_s=300°) **(b)**, in the local afternoon, $t = 15h$ (LMST) at all locations. Deardorff's convection velocity, w_*, **(c)**, the friction velocity, u_*, **(d)** and surface sensible heat flux, $\mathcal{H}_s$, **(e)** are depicted in the northern early-summer season. Locations of some particular regions addressed in the present study, marked on the topographic map of Mars **(f)** based on Mars Orbiter Laser Altimeter (MOLA) data (Smith et al., 2001). 115

4.9 The annual evolution of the zonally averaged daytime CBL depth in the northern (left panels) and southern (right panels) hemispheres. The cyan and blue solid lines denote the simulated cases MY 33 and MY 34, respectively. The shaded areas refer to the GDS in MY 34 (GDS-34) and RDS in MY 34 (RDS-34). 116

4.10 Regional distribution of CBL depth retrieved from MEX RO measurements (Hinson et al., 2008, 2019) at (a) t=14-15h (LTST), (c) t=15-17h (LTST) and MarsWRF GCM simulations at (b) t=14-15h (LTST), (d) t=15-17h (LTST) for given RO profiles as listed in Tab. C1-C2. The locations of RO experiments are marked with purple circles. The black dashed lines display the contour lines of topographic map of Mars retrieved by the datasets of Mars Orbiter Laser Altimeter (MOLA) (Smith et al., 2001). (e) The RO locations are also depicted together with the MOLA map. Here the green and magenta circles mark the RO profiles collected at MY 27 and MY 28 respectively. (f) The temporal variation of CBL depth is displayed at all available RO locations during northern early and late spring of MY 27 and MY 28. The dark and light blue markers show the GCM and RO results respectively, while the solid lines display their smoothed behaviour via Gaussian smoothing. 119

5.1 Time- and spanwise averaged $E_{ii}(\kappa_1)$ where $i = u, v, w, \theta$ along with the streamwise wavenumber, i.e. κ_1, normalized by the reference wavenumber, i.e. $\kappa_f = 2\pi/(7\Delta)$. The energy spectra is averaged in time between $t = 6 - 7h$ and computed at $z/z_i \approx 0.04$. Black solid line shows the reference-LES with $\Delta_{LES} = 50\ m$ grid spacing, while the colored solid lines refer to the filtered LES. Cyan, blue and purple solid lines are the filtered LES, inferred from the Butterworth filter at the gray-zone grid spacing of $\widehat{\Delta} = 250\ m$ (i.e. $\widehat{\Delta}_f = 1750\ m$) where $n = 2, 3, 4$ respectively. Red solid line presents the filtered LES by the top-hat filter at $\widehat{\Delta} = 250\ m$. Herein, gray dashed line displays the theoretical Kolmogorov $-5/3$ slope. 133

5.2 Instantaneous horizontal cross-sections of the potential temperature, θ, for the CBL5 case. Presented contour plots are calculated at $z/z_i \approx 0.04$ when t=6h. Top-left panel displays the reference-LES field having $\Delta^{LES} = 50\ m$ grid spacing. Top-right and bottom-right panels show the filtered LES fields at the gray-zone grid spacing of $\widehat{\Delta} = 250\ m$ by means of the top-hat and 2nd-order Butterworth (BW2) filters, respectively. Besides the bottom-left panel demonstrates the effective grid spacing of $\widehat{\Delta} = 250\ m$, resulting in $\widehat{\Delta}_f = 7\widehat{\Delta} = 1750\ m$ in order to mimic the model response of the WRF. The color bar ranges between 304.5 K (blue) and 306.5 K (red). 136

5.3 Instantaneous horizontal cross-sections of the vertical wind speed, w, at t=6h. From left to right panels, different convective instabilities are demonstrated respectively: purely buoyant (CBL1, 1st column), forced buoyant (CBL5, 2nd column), weakly sheared (CBL7, 3rd column) and strongly sheared (CBL8, 4th column) cases. Top panels display the coherent structures inferred from the reference-LES ($\Delta^{LES} = 50\ m$), while the below panels show the coarse-grained results at the gray-zone grid spacings of $\widehat{\Delta} = 75\ m, 150\ m, 250\ m, 500\ m, 1000\ m$ respectively. The color bar ranges between $-0.8\ m/s$ (blue) and $0.8\ m/s$ (red). 138

5.4 Gray-zone partitioning functions of resolved and SGS turbulence kinetic energy $\mathcal{P}_k$. Results are horizontally averaged in x, y, then averaged in time between $t = 6 - 7h$, for different levels of the convective instability scale, i.e. $\zeta_i = -z_i/L_o$. Plus and circular markers refer to the resolved and SGS TKE partitioning respectively, at each altitude within the given CBL region. Solid lines represent the proposed model in terms of the sigmoidal Gompertz functions. 141

5.5 Gray-zone partitioning functions of the SGS turbulence kinetic energy, i.e. $\mathcal{P}_k^{sgs}$, along with the normalized gray-zone grid spacing, i.e. Δ/z_i. Markers display the SGS TKE partitioning at each altitude within the given CBL region. Circular and asterisk markers denote the partitioning ratios within the lower and upper mixed layers respectively. Blue dashed and solid lines refer to the proposed model derived via the Butterworth filter. Red dashed and solid lines are the mean of partitioning at each altitude display by the red circular and asterisk markers, respectively. Black solid line refers to the model of Honnert et al. (2011) proposed for $0.05 \leq z/z_i \leq 0.85$, where the black dashed lines denote the first as well as last vigintiles of the corresponding model. Solid line colored by cyan is the model of Shin and Hong (2013) described for $0.10 \leq z/z_i \leq 0.80$. 146

5.6 Time- and horizontally averaged gray-zone partitioning functions of momentum/heat eddy fluxes along with the normalized gray-zone grid spacing. Partitioning results are obtained for the CBL4 case ($Q_s = 0.20\ Km/s, U_g = 10\ m/s$) at 3 different CBL regions: $0.10 \leq z/z_i \leq 0.50$, $0.50 \leq z/z_i \leq 0.85$ and $0.85 \leq z/z_i \leq 1.10$. Plus and circular markers refer to the resolved and SGS partitioning respectively, at each altitude within the given CBL region. Solid lines represent the proposed model in terms of the sigmoidal Gompertz functions. Bottom panels show the time- and horizontally averaged vertical profiles of the total eddy momentum (left) and eddy heat (right) fluxes. 148

B1 Sensitivity of LES computations to model coefficients: Vertical profiles of potential temperature (a), turbulent heat flux (b), turbulence kinetic energy (c), dissipation rate of turbulence kinetic energy (d) - blue: the present set of coefficients, red: the updated coefficients of (Muñoz-Esparza et al., 2014a). . . 163

B2 Regarding the mixing length scale sensitivity on potential temperature profiles, vertical profiles of potential temperature are plotted at $27.5°\ N, 107°\ W$ for $L_s = 44.5°$. The local time is 17.0h. 1.0L denotes the present value of length scale (black solid line). 0.8L and 1.2L are the scaled length scales with 80% (red solid line) and 120% (blue solid line) of the baseline length scale. 164

List of Tables

2.1 Reference PBL parameters based on the measurements of Høvsøre test site at 10 m (Gryning et al., 2007). (Subscripts, vu: very unstable, mu: moderate unstable, nu: near-neutral unstable, n: near-neutral, ns: near-neutral stable, ms: moderate stable, vs: very stable). 32

2.2 The details of the computational domain and the grid resolution depending on the atmospheric stability. 34

2.3 Main PBL parameters based on LES results. 35

2.4 Mean absolute errors of three PBL schemes compared to the Høvsøre LES results in terms of horizontally-averaged potential temperature and wind speed where $z \leq z_{i,LES}$. Bold values denote the best performance as the lowest MAE among the three PBL schemes. 44

2.5 Mean absolute errors of TKE, its dissipation rate, temperature wind speed and wind direction obtained by three PBL schemes in comparison to XPIA measurements at $z = 50m$ from Muñoz-Esparza et al. (2018). Bold values denote the best performance as the lowest error among the three PBL schemes. 50

3.1 Main PBL parameters acquired from the LES simulations for different surface sensible heat flux, q_s. Here, L_o is the Obukhov length, u_* is the friction velocity, w_* is the Deardorff convective velocity, z_i is the PBL height, and θ_0 is the potential temperature near the ground. e_{max} and ϵ_{max} are the maximum values of horizontally averaged turbulence kinetic energy and its dissipation rate along the vertical direction. The angle bracket, $\langle\rangle$, denotes horizontally averaged values. These values are averaged over 500 seconds following a 2-hours simulation period. 66

3.2 Vertical grid configuration of MarsWRF: altitude of the center of the vertical layers above the ground level. 83

5.1 Forcing parameters for the selected large-eddy simulation cases. Here, L_o is the Obukhov length, Q_s is the surface kinematic heat flux and U_g is the geostrophic wind speed. Time and horizontally averaged CBL characteristics are calculated for $t = 6 - 7\ h$ in terms of the friction velocity, u_*, Deardorff's convective velocity, w_*, planetary boundary layer height, z_i, and convective instability scale, $\zeta_i = -z_i/L_o$. 130

5.2 Mean Percentage Error (ϵ) for the energy spectra of $E_{uu}, E_{vv}, E_{ww}, E_{\theta\theta}$ along with the κ_r. Errors are calculated when $1.0 \leq \kappa_r \leq 3.5$, with respect to the reference-LES ($\Delta_{LES} = 50\ m$). 132

5.3 Best order for the Butterworth filter, i.e. $\widetilde{n}_{u,v,w,\theta}$, giving the lowest mean percentage error for the energy spectra of $E_{uu}, E_{vv}, E_{ww}, E_{\theta\theta}$, with respect to the reference-LES. 135
5.4 Model parameters of the proposed partitioning functions, $\mathcal{P}^{sgs}$, in the turbulence gray-zone for 3 different CBL regions: $0.10 \leq z/z_i \leq 0.50$, $0.50 \leq z/z_i \leq 0.85$ and $0.85 \leq z/z_i \leq 1.10$. 149

C1 Comparison between GCM vs. MEX RO measurements for profiles 1-59. . . 166
C2 Comparison between GCM vs. MEX RO measurements for profiles 60-118. . 167

Chapter 1

General introduction

1.1 Introduction

The planetary boundary layer (PBL) is the part of troposphere that forms where the troposphere contacts the planet (Fig.1.1) at depths ranging from hundreds of meters to a few kilometers on Earth (Stull, 1988). It can even reach beyond 10 kilometers on Mars as a consequence of extreme radiative heating, thus strong turbulent convection activity (Petrosyan et al., 2011; Hinson et al., 2019; Senel et al., 2021b). The PBL is of great significance, as it has prominent impact on land-ocean-atmosphere interactions as well as the near-surface exchange of aerosols and volatiles. Therefore, it has gained much attention in various scientific fields ranging from planetary applications (Martinez et al., 2013; Spiga, 2019) through weather forecasting and climate research (Flaounas et al., 2011), wind energy (Storm et al., 2009; Parente et al., 2011) and optical turbulence (Basu and He, 2014) studies.

Moreover, the planetary boundary layer consists of various physical phenomena associated with large range of length scales, thus model resolutions. To illustrate, general circulation models (GCM) are used to model planetary scale atmospheric events, such as planetary waves and atmospheric tides, by using coarse horizontal grid resolutions, i.e., $\Delta^{GCM} > 100$ km (Randall, 2000; Forget et al., 1999). Mesoscale models (Muñoz-Esparza et al., 2018; Newman et al., 2017), on the other hand, are applied for regional weather and climate predictions with mesoscale model resolutions, i.e., mesoscale limit, Δ^{meso}, from 100 km down to either 1 km or 10 km for Earth or Mars, respectively. For higher grid resolutions, large-eddy simulations (Schmidt and

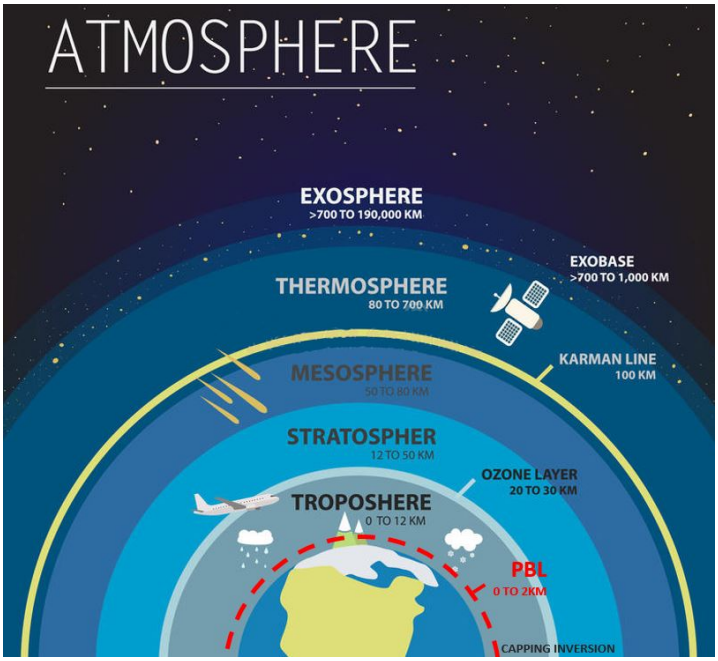

Figure 1.1: Layers of the Earth's atmosphere and location of the planetary boundary layer lying within the ~ 12-km depth troposphere. (Stull, 2016).

Schumann, 1989; Spiga and Lewis, 2010) are used to model microscale events like flow over complex terrains (Balogh et al., 2012) (Δ^{LES} < either 100 m (LES limit for Earth) or 1 km (LES limit for Mars). Hence, different types of atmospheric models, as listed below, are used to simulate various atmospheric events (Temel, 2018). Fig. 1.2 shows three fundamental types of atmospheric models over model resolution spectrum for Earth and Mars.

- **General circulation models - GCM** are based upon the Euler equations, by neglecting the molecular diffusion term, whereas considering solely the vertical momentum/heat turbulent fluxes, on relatively coarse model resolutions. The results of GCM are used as boundary and initial conditions for regional, i.e., mesoscale, models. Lateral periodic and polar boundary conditions are applied in GCM simulations in which the surface boundary conditions are evaluated by using theoretical models. The atmospheric turbulence within the planetary boundary layer is treated by one-dimensional turbulence closures, namely the PBL schemes.

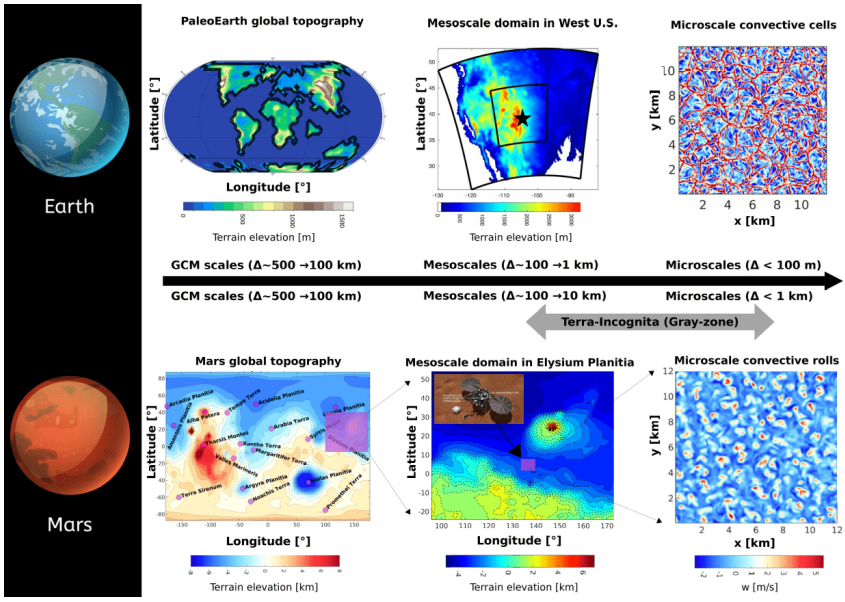

Figure 1.2: Atmospheric models depending on model resolution spectrum from global to microscales. Top panels: (left) Latest Cretaceous paleogeographic map for paleoEarth GCM that we develop to reconstruct the climatic conditions in the aftermath of Chicxulub asteroid impact (Senel et al., 2021a), (center) nested mesoscale domains centered in Colorado with the terrain elevation (Senel et al., 2019), (right) microscale convective cells within the Earth's PBL from high-resolution LES (Senel et al., 2020b). Bottom panels: (left) Martian global topography for MarsGCM (Senel et al., 2021b), obtained from Mars Orbiter Laser Altimeter (MOLA) (Smith et al., 2001). (center) Martian mesoscale domain centered at NASA's InSight landing site, in Elysium Planitia (Senel et al., 2020a). (right) Microscale convective rolls forming within the Martian convective PBL (Senel et al., 2020a).

- **Mesoscale models** are based upon the identical transport equations as the GCMs, yet the model resolution herein is relatively fine. The initial as well as boundary conditions are retrieved from the precursor GCMs. According to the horizontal homogeneity assumption, solely the vertical momentum/heat turbulent fluxes are considered similar to GCMs. The vertical turbulent fluxes are modelled by either algebraic or a turbulence kinetic energy closures, in which the turbulence dissipation rate is modeled through theoretical length scale formulation. Similar to GCM approach, the atmospheric turbulence is treated by the one-dimensional PBL schemes.

- **Microscale models** are classified into three distinct branches, consisting of large-eddy simulation (LES) models, Reynolds-Averaged Navier-Stokes (RANS) models and Direct Numerical Simulation (DNS) models. Here, the latter is the most computationally-expensive approach as it resolves the full spectrum of eddy scales appeared in atmospheric turbulence, which makes it limited with idealized cases. On the other hand, three-dimensional LES (Muñoz-Esparza et al., 2014a) or RANS (Temel et al., 2018a) models, either constrained by theoretical or observational data or nested with mesoscale simulations, are used to represent microscale type atmospheric events. However, three-dimensional LES models are more extensively used to improve the low-fidelity PBL models, such as those used in GCM and mesoscale models. This is because of the fact that the RANS approach models only the mean-state of atmospheric turbulence. Whereas the LES resolves the energy-containing large eddies explicitly, yet models the small and dissipative eddies, as a more realistic approach. For the details of LES modeling see Sec. 1.6.

1.2 Atmospheric instability

Diurnal variation of the planetary boundary layer (Fig.1.3) is mainly controlled by solar fluxes and the atmospheric instability, which is subdivided into three instability classes which are unstable, neutral and stable, these are classified based on the surface heat flux.

The unstable PBL, also called the convective PBL, exists when the ground is warmer than the surrounding air, often occurring during daytime. The air parcel is then positively buoyant, $\overline{w'\theta'} > 0$, and tends to rise (Fig.1.3). The unstable PBL is characterized by light winds but strong turbulence intensity since the warm air rises from the ground to heights of 200 m to 4 km, this by mixing the whole flow field with the convectively intense driven turbulence (Moeng, C. -H., 2016). A typical unstable PBL can be divided into three main layers including a surface layer, a convective or mixed layer and an entrainment zone. The surface layer is the closest sublayer to the ground, in which the surface-atmosphere exchanges are dominant. Here, the eddy fluxes are relatively uniform or varying linearly along the vertical direction. However, wind speed, temperature, and humidity profiles vary considerably

due to the existence of frictional drag, heat conduction, and evaporation from the surface (Stull, 2016). The height of the surface layer reaches around 10% percent of the PBL height. The convective or mixed layer is the main sublayer where strong large-eddies mix the air during the daytime. Above the convective layer, a preventing zone against the rising thermals appears and restricts the formation of turbulence that behaves statically stable. It is referred to as the entrainment zone, this is because the air from the free atmosphere entrains into this layer. The general characteristics of the entrainment zone can be expressed by temperature inversion, intermittent turbulence and internal gravity waves (Moeng, C. -H., 2016).

In cases where the ground is cooler than its surrounding air, stable boundary layer occurs, taking place during nighttime which followed the sunset. The air parcel is negatively buoyant, $\overline{w'\theta'} < 0$, and tends to suppress its vertical motion so that the turbulence is mostly caused by the shear fluxes instead of the buoyancy fluxes (Fig.1.4). Similar to the unstable PBL, stable PBL is characterized by light winds but weak turbulence and can be separated into four main layers including a surface layer, a stable or nocturnal layer, a residual layer and a capping inversion. The turbulent production can reach such low levels that non-local atmospheric disturbances lead to intermittent

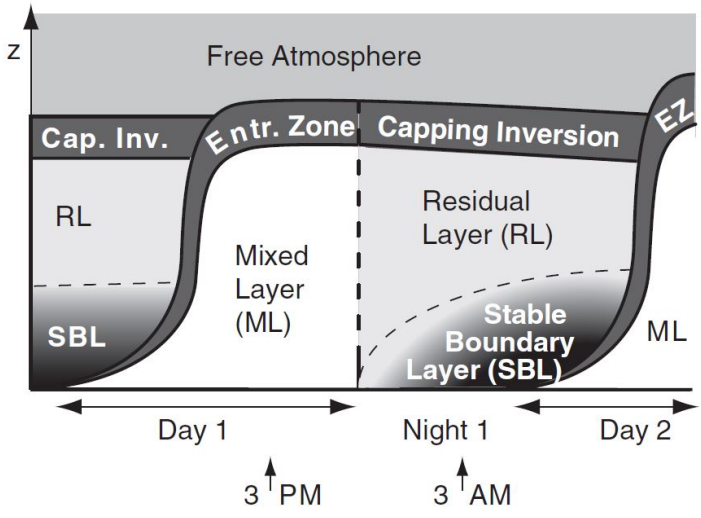

Figure 1.3: Diurnal variation of the planetary boundary layer from deep convective to shallow stable regimes (Stull, 2016).

turbulence (Sun et al., 2004). The surface layer behaves as in the unstable conditions. The stable layer generally is really shallow with heights at nighttime, i.e. 20 - 500 m, considerably lower than the unstable PBL (Stull, 2016) since the convective motion is weakened by downward buoyancy. Above the stable layer, a residual layer appears that covers pollutants and moisture as residual of the former convective layer. It is bounded by a capping inversion that restricts the entrainment of air, unlike the unstable PBL but behaves still statically stable.

The last instability condition, i.e. neutral PBL, is something between these two conditions in which the intensity of winds reach high levels and the buoyancy flux, $\overline{w'\theta'} \approx 0$ (Gryning et al., 2007) still exists but is negligible. Neutral PBL is actually an idealized state of the atmospheric boundary layer. Therefore, only near-neutral conditions have only been reported by full-scale experiments.

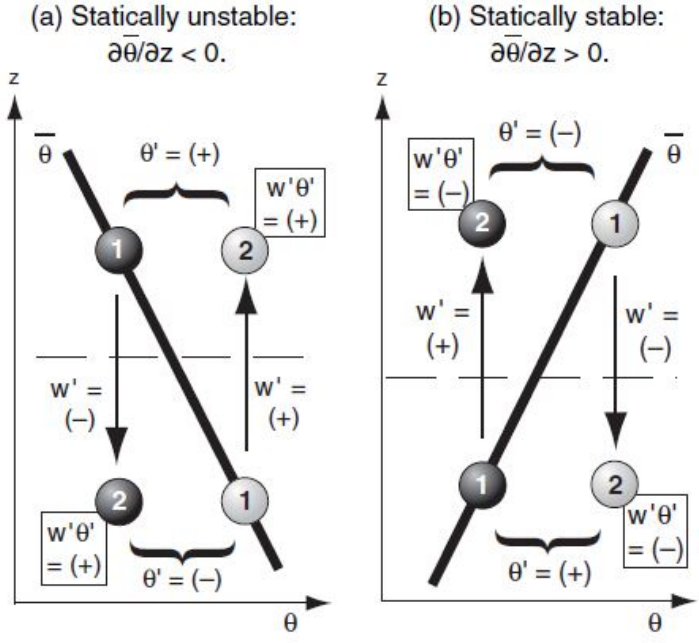

Figure 1.4: Vertical potential temperature gradient, $\partial\theta/\partial z$, profiles for statically unstable and stable conditions (Stull, 2016).

1.3 Earth vs. Mars

Earth and Mars share several similarities in common, possessing stark contrasts though. Both are terrestrial planets having an atmosphere but in distinct mass, size and compositions. Although it is almost half the diameter of Earth, Mars has a very thin atmosphere, which is 100 times less dense than the atmosphere of Earth. Concerning the compositions, Earth's atmosphere is rich in nitrogen (78.1%), oxygen (20.9%) and argon (0.93%), plus trace gases, i.e., carbon dioxide, water vapor and methane. While, Martian atmosphere consists primarily of carbon dioxide (95.3%), argon (2.7%) and nitrogen (1.6%), including trace amounts of water vapor and methane.

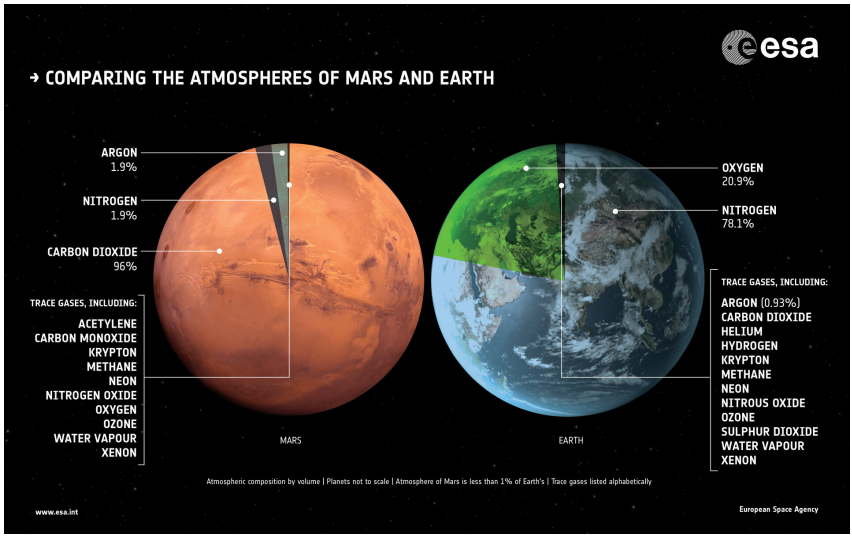

Figure 1.5: Comparison of the Earth's and Martian atmosphere in terms of the atmospheric composition by volume. Credit: The European Space Agency - ESA.

Because of a thinner atmosphere, which ceases the retained solar energy at the surface, and the farther distance from the Sun, Mars is an extremely cold world, compared to our home planet, Earth. The surface temperatures on Mars is around -60°C on average, far colder than surface temperatures on Earth averaged at 15°C. Mars, due to its high orbital eccentricity (0.093) and axial tilt (25.2°) (Petrosyan et al., 2011), experiences large diurnal and seasonal temperature swings on the surface, varying from as low as -140°C at poles in winter, up to 30°C at local afternoon in summer through the tropical

regions. Mars has four seasons like those on Earth, yet lasting almost twice as long. Besides, one day on Mars (called, "Sol"), which is almost same as on Earth, is nearly 40 minutes longer. Both planets show further similarities, such as, the active dust and water cycles despite particular features. The surface of Earth, to illustrate, is vastly covered by liquid water (71%). Besides the water cycle is prone to active evaporation, condensation and precipitation events on Earth. Mars, despite the lack of precipitation, shows similarities to Earth, among which the water vapor/ice cycle through evaporation and condensation, the frost formation on polar regions, and water ice clouds. Moreover, Mars is an arid and dusty planet with local and planet-encircling global dust storms. Given the similarities and differences between the Earth and Mars, governed primarily by the solar radiative transfer, affects differently the turbulent exchange of surface and atmosphere, therefore the planetary boundary layer phenomenon.

1.4 Monin-Obukhov similarity theory

Within the surface layer, wind profiles behave self-similarly with proper length and velocity parameters leading to a universally known similarity theory for stratified atmospheric surface layer of Monin-Obukhov (Monin and Obukhov, 1954). This theory is based on the logarithmic law of the wall incorporating thermal stratification influences (Moeng, C. -H., 2016). When the thermal stratification is negligible, wind profile of the neutral stratified PBL is ideally adapted for log wind profile,

$$\frac{\partial U(z)}{\partial z} = \frac{1}{\kappa}\frac{u_*}{z} \tag{1.1}$$

where $U(z) = \left(\overline{u}^2 + \overline{v}^2\right)^{1/2}$ denotes the horizontal wind speed at height z and κ denotes von Karman constant being typically $\kappa \approx 0.40$ and $u_* = \sqrt{\tau_w/\rho}$ denotes friction velocity which depends on wall shear stress, τ_w, and fluid density, ρ. u_* can also be expressed in terms of surface eddy stresses.

$$u_* = \left(\overline{u'w'}_0^2 + \overline{v'w'}_0^2\right)^{1/4} \tag{1.2}$$

After vertically integrating Eq.1.1

$$U(z) = \frac{u_*}{\kappa} ln \frac{z}{z_0} \tag{1.3}$$

where z_0 denotes roughness height corresponding to the height in which the mean wind becomes zero. However, for the non-neutral atmospheric conditions, it needs to be accounted for thermal stratification effect. To do this, Monin-Obukhov similarity theory includes buoyancy effect with the buoyancy parameter, g/θ_0, and the surface eddy heat flux, $q_s = \overline{w'\theta'}_0$ in addition to u_* and z_0 parameters. Then, this theory offers a combined non-dimensional parameter referring to the measure of atmospheric instability, $\zeta = z/L_{MO}$, where L_{MO} is called Monin-Obukhov length scale,

$$L_{MO} = -\frac{u_*^3}{\kappa \frac{g}{\theta_0} \overline{w'\theta'}_0} \tag{1.4}$$

where L_{MO} indicates the height where shear and buoyancy production become equal. In case of $L_{MO} > 0$ and $L_{MO} < 0$, then PBL is called stable and unstable respectively. If the PBL is neutrally stratified, then L tends to reach infinity.

According to Monin-Obukhov similarity theory, non-dimensional vertical gradient of the mean wind and potential temperature can be expressed in terms of the instability parameter, $\zeta = z/L_{MO}$,

$$\frac{\kappa z}{u_*} \frac{\partial U(z)}{\partial z} = \phi_m(\zeta) \tag{1.5}$$

$$\frac{\kappa z}{\theta_*} \frac{\partial \theta(z)}{\partial z} = \phi_h(\zeta) \tag{1.6}$$

where $\theta_* = \overline{w'\theta'}_0/u_*$ is the potential temperature scale, ϕ_m and ϕ_h denote non-dimensional stability functions of momentum and heat which enable to obtain the velocity and potential temperature profiles inside the surface layer. These equations are also known as flux-gradient relations. An empirical relation by Dyer and Hicks (Dyer and Hicks, 1970) for the stability functions regarding the field experiments,

$$\phi_m = \begin{cases} (1 - 16\zeta)^{-1/4} & \zeta < 0 \\ 1 + 5\zeta & \zeta > 0 \end{cases} \tag{1.7}$$

$$\phi_h = \begin{cases} (1 - 16\zeta)^{-1/2} & \zeta < 0 \\ 1 + 5\zeta & \zeta > 0 \end{cases} \tag{1.8}$$

1.5 PBL scaling parameters

Shear-dominated boundary layers distinct from buoyancy effects, i.e. neutrally stratified PBL, can be characterized by friction velocity, u_*, and roughness height, z_0. However in case of non-neutral conditions, convective velocity scale,

$$w_* = \left(\frac{g}{\theta_0} \overline{w'\theta'}_0 z_i \right)^{1/3} \tag{1.9}$$

proposed by Deardorff (Deardorff, 1972) being more proper preference for the scaling parameter instead of u_*.

One of the most important PBL parameters is the flux Richardson number, $\mathcal{R}i_f$, which represents the measure of atmospheric instability similarly to Monin-Obukhov length scale, L_{MO}. Under assuming horizontal homogeneity, it is defined as,

$$\mathcal{R}i_f = \frac{\frac{g}{\theta_0}\overline{w'\theta'}}{\overline{u'w'}\frac{\partial \bar{u}}{\partial z} + \overline{v'w'}\frac{\partial \bar{v}}{\partial z}} \tag{1.10}$$

where $\mathcal{R}i_f$ stands for the relative magnitude between buoyancy fluxes to shear fluxes. Once $\mathcal{R}i_f < 0$, PBL is called statically unstable and if $\mathcal{R}i_f > 0$ then PBL is called statically stable (Fig.1.6). If $\mathcal{R}i_f \approx 0$, PBL being statically neutral. Richardson number can also be defined in terms of flux gradients,

$$\mathcal{R}i_g = \frac{\frac{g}{\theta_0}\frac{\partial \bar{\theta}}{\partial z}}{\left(\frac{\partial \bar{u}}{\partial z}\right)^2 + \left(\frac{\partial \bar{v}}{\partial z}\right)^2} \tag{1.11}$$

As mentioned in Sec. 1.2, during the daytime, a preventing zone appears above the convective layer which is called entrainment zone and while during the nighttime, stable PBL is bounded by capping inversion. The altitude of this zone is another commonly-used scaling parameter, namely inversion height, z_i, and shows the height of the PBL.

Finally, the lapse rate of the inversion or briefly inversion strength, Γ_i, is also of great importance for the PBL physics. $\Gamma_i = \Delta\theta_i/\Delta h_i$ corresponds to the potential temperature gradient, $\Delta\theta_i$, along the inversion width, Δh_i. Above the PBL, the atmospheric lapse rate can be obtained to be $\Gamma_a \sim 3.4$ K/m in the free atmosphere of Earth, where the dry adiabatic lapse rate is $\Gamma_a \sim 9.8$ K/m (Stull, 2016). While for Mars, the observed atmospheric lapse rate is $\Gamma_a \sim 2.5$ K/m

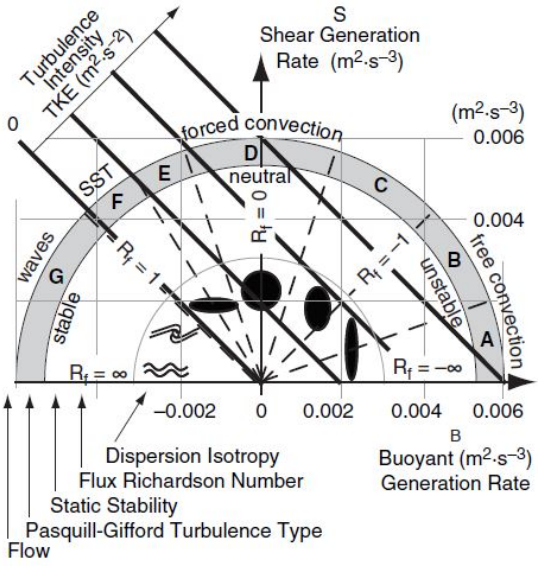

Figure 1.6: Flux Richardson number map regarding the turbulence kinetic energy generation by shear and buoyancy forcing. Dashed lines divide different atmospheric instability regions (Stull, 2016). R_f and SST denote the flux Richardson number and stably-stratified turbulence, respectively.

from the entry of Viking and Pathfinder landers, in which the dry adiabatic lapse rate is $\Gamma_a \sim 4.3$ K/m (Haberle, 2015).

1.6 Large-eddy simulation (LES) modeling

LES technique consists in the filtering process in which large scales are directly resolved but small or subgrid scales are modeled (Fig.1.7). This filtering is determined mathematically in the physical space by,

$$\widetilde{\phi}(x,t) = \int_{-\infty}^{+\infty} \int_{-\infty}^{+\infty} \phi(\xi,\tau)\mathcal{G}(x-\xi,t-\tau)d\tau d^3\xi \qquad (1.12)$$

where $\widetilde{\phi}(x,t)$ denotes the resolved part of a state variable $\phi(x,t)$ in space, x, and time, t. ξ and τ are the change variable in space and time. $\mathcal{G}$ is the space-time convolution kernel which is the key parameter of the filtering related to the cutoff scales in space and time, $\widetilde{\Delta}$ and $\widetilde{\tau_c}$, respectively (Sagaut, 2006).

Filtered continuity and Navier-Stokes equation can be expressed as,

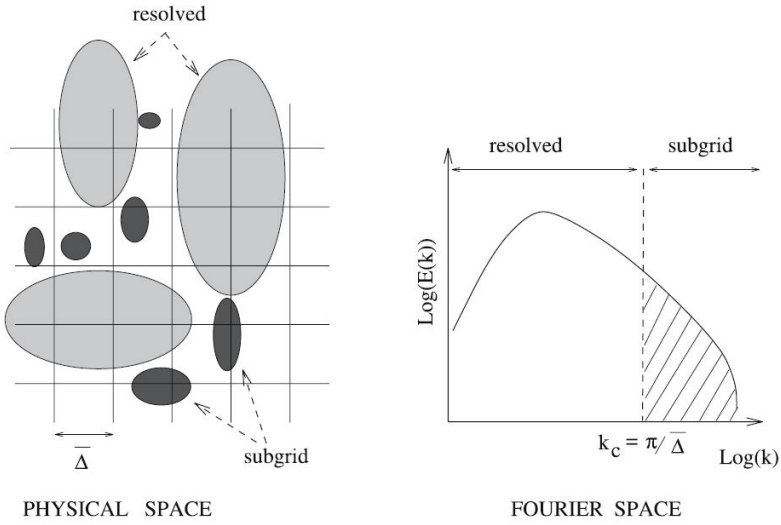

Figure 1.7: Schematic view of the LES filtering process which decomposes the space-time variable as resolved and subgrid scales by a sharp cutoff filtering in Fourier space (Sagaut, 2006).

$$\frac{\partial \widetilde{u}_i}{\partial x_i} = 0 \tag{1.13}$$

$$\frac{\partial \widetilde{u}_i}{\partial t} + \frac{\partial}{\partial x_j}\left(\widetilde{u}_j \widetilde{u}_i\right) = -\frac{1}{\rho_0}\frac{\partial \widetilde{p}}{\partial x_i} + \frac{g_i}{\theta_0}(\widetilde{\theta} - \theta_0)\delta_{i3} - 2\epsilon_{ijk}\Omega_j \widetilde{u}_k + \frac{\partial \tau_{ij}^v}{\partial x_j} - \frac{\partial \tau_{ij}^D}{\partial x_j} \tag{1.14}$$

where $\widetilde{u}_i$ is resolved velocity field and subscript i corresponds to x, y, z coordinates denoting by 1, 2, 3. The first and second terms on LHS refer to the change in velocity and the advection of flow, respectively. The first term on RHS denotes the gradient of resolved pressure which can be expanded as,

$$\frac{\widetilde{p}}{\rho_0} = \widetilde{p}^* + \frac{\rho_k}{\rho_0} g_j x_j \delta_{j3} + \frac{\langle \widetilde{p}_0^* \rangle}{\rho_0} \tag{1.15}$$

where the terms on RHS are respectively modified resolved pressure, buoyant pressure and driving pressure gradient to fulfill geostrophic wind at a desired height. Herein, angle brackets denote horizontal averaging. The second term on RHS in Eq.1.14 represents buoyancy force where $\widetilde{\theta}$ is the resolved potential temperature, g_i is the gravity, $\widetilde{\theta_0}$ is the reference potential temperature and δ_{i3} denotes the Kronecker delta. The third term on RHS is the Coriolis force due

to the Earth rotation where ϵ_{ijk} is alternating tensor and Ω_j is the planetary rotation rate vector,

$$\Omega_j = \omega \begin{pmatrix} 0 \\ cos\phi \\ sin\phi \end{pmatrix} \tag{1.16}$$

where $\omega = 7.2722 \times 10^{-5}$rad/s is the planetary rotation rate and $\phi = 56.43°$ stands for the latitude of Høvsøre, Denmark. The fourth term on RHS, τ_{ij}^{v} in Eq.1.14 presents viscous stress which can be neglected since the contribution of the viscous diffusion is negligible due to the large Reynolds number of atmospheric flows. And the last term is the deviatoric part of the SGS stress,

$$\tau_{ij}^{D} = \tau_{ij} - \tau_{kk}\delta_{ij}/3 \tag{1.17}$$

where $\tau_{kk}\delta_{ij}/3$ denotes the isotropic component in the SGS stress. SGS stress which originates from the effects of subgrid (or small) scales on filtered (or large) scales can be expressed as,

$$\tau_{ij} = \widetilde{\widetilde{u_i}\widetilde{u_j}} - \widetilde{u}_i\widetilde{u}_j \tag{1.18}$$

Buoyancy term in Eq.1.14 can be replaced by,

$$+\frac{g_i}{\theta_0}(\widetilde{\theta} - \theta_0)\delta_{i3} = -\frac{g_i}{\rho_0}(\rho_b - \rho_0)\delta_{i3} = +g_i\frac{\rho_k}{\rho_0}\delta_{i3} \tag{1.19}$$

where ρ_b is the buoyant density, ρ_0 is the reference density, and ρ_k is the effective buoyant density. After differentiating the pressure terms in Eq.1.15,

$$\frac{1}{\rho_0}\frac{\partial\widetilde{p}}{\partial x_i} = \frac{\partial\widetilde{p}^*}{\partial x_i} + \frac{1}{\rho_0}\frac{\partial}{\partial x_i}\left(\rho_k g_j x_j \delta_{j3}\right) + \frac{1}{\rho_0}\frac{\partial\left\langle\widetilde{p}_0^*\right\rangle}{\partial x_i} \tag{1.20}$$

The second term on RHS can be expanded as,

$$\frac{1}{\rho_0}\frac{\partial\widetilde{p}}{\partial x_i} = \frac{\partial\widetilde{p}^*}{\partial x_i} + g_j x_j \delta_{j3}\frac{\partial}{\partial x_i}\left(\frac{\rho_k}{\rho_0}\right) + g_j\frac{\rho_k}{\rho_0}\delta_{j3}\frac{\partial x_j}{\partial x_i} + \frac{1}{\rho_0}\frac{\partial\left\langle\widetilde{p}_0^*\right\rangle}{\partial x_i} \tag{1.21}$$

When the third term on RHS is replaced,

$$g_j\frac{\rho_k}{\rho_0}\delta_{j3}\frac{\partial x_j}{\partial x_i} = g_i\frac{\rho_k}{\rho_0}\delta_{i3} \tag{1.22}$$

Thereafter, substituting Eq.1.21 and Eq.1.22 into Eq.1.14,

$$\frac{\partial \widetilde{u}_i}{\partial t} + \frac{\partial}{\partial x_j}\left(\widetilde{u}_j \widetilde{u}_i\right) = -\left(\frac{\partial \widetilde{p}^*}{\partial x_i} + g_j x_j \delta_{j3} \frac{\partial}{\partial x_i}\left(\frac{\rho_k}{\rho_0}\right) + g_i \frac{\rho_k}{\rho_0}\delta_{i3} + \frac{1}{\rho_0}\frac{\partial \left\langle \widetilde{p}_0^* \right\rangle}{\partial x_i}\right) + g_i \frac{\rho_k}{\rho_0}\delta_{i3} - 2\epsilon_{ijk}\Omega_j \widetilde{u}_k - \frac{\partial \tau_{ij}^D}{\partial x_j} \tag{1.23}$$

Eventually, the last status of the filtered Navier-Stokes equation reads,

$$\frac{\partial \widetilde{u}_i}{\partial t} + \frac{\partial}{\partial x_j}\left(\widetilde{u}_j \widetilde{u}_i\right) = -\frac{\partial \widetilde{p}^*}{\partial x_i} + g_j x_j \delta_{j3} \frac{\partial}{\partial x_i}\left(\frac{\rho_k}{\rho_0}\right) + \frac{1}{\rho_0}\frac{\partial \left\langle \widetilde{p}_0^* \right\rangle}{\partial x_i} - 2\epsilon_{ijk}\Omega_j \widetilde{u}_k - \frac{\partial \tau_{ij}^D}{\partial x_j} \tag{1.24}$$

And the following equation gives the filtered potential temperature equation,

$$\frac{\partial \widetilde{\theta}}{\partial t} + \frac{\partial}{\partial x_j}\left(\widetilde{u}_j \widetilde{\theta}\right) = -\frac{\partial q_j}{\partial x_j} \tag{1.25}$$

where, q_j denotes the SGS flux and defined as,

$$q_j = \widetilde{\widetilde{\theta}\widetilde{u}_j} - \widetilde{\theta}\widetilde{u}_j \tag{1.26}$$

1.7 Subgrid-scale (SGS) models

LES resolves the large scales of motion, whereas the small scales are parametrized by means of SGS models. The main idea is that SGS stress, τ_{ij}^D, in Eq.1.18 and SGS flux, q_j, in Eq.1.26 terms can be modeled using resolved scales by LES. The descriptions of typical SGS models are given below.

1.7.1 Smagorinsky SGS model

Smagorinsky model (Smagorinsky, 1963) is the earliest SGS model proposed in 1963 and still commonly used in most of the LES applications. The idea is pretty similar to the Boussinesq eddy viscosity hypothesis,

$$\tau_{ij}^D = -2\nu^{sgs}\widetilde{S}_{ij} \tag{1.27}$$

$$q_j = -\frac{\nu^{sgs}}{Pr_t}\frac{\partial \widetilde{\theta}}{\partial x_j} \tag{1.28}$$

Here, $\widetilde{S}_{ij}$ is the resolved strain-rate tensor,

$$\widetilde{S}_{ij} = \frac{1}{2}\left(\frac{\partial \widetilde{u}_i}{\partial x_j} + \frac{\partial \widetilde{u}_j}{\partial x_i}\right) \tag{1.29}$$

Pr_t in Eq.1.28 is the turbulent Prandtl number. If the conditions are unstable or neutral, it can be adjusted to be 1/3, otherwise taken to be 1 for the stable conditions (Churchfield et al., 2012).

As already mentioned above, the main thought in this model to parameterize the ν^{sgs} as in eddy-viscosity models,

$$\nu_{sgs} = (C_s\Delta)^2 \left(2\widetilde{S}_{ij}\widetilde{S}_{ij}\right)^{1/2} \tag{1.30}$$

where C_s is the Smagorinsky coefficient and set to 0.13 and $\Delta = (\Delta_x\Delta_y\Delta_z)^{1/3}$ is the grid filter scale and $\Delta_x, \Delta_y, \Delta_z$ are local cell heights of the grid.

1.7.2 One-Equation-Eddy-Viscosity SGS model

Despite the universal usage of Smagorinsky model, it assumes balance between shear production and dissipation terms so that it is no longer entirely valid for the buoyancy-driven and transitional PBL flows (Moeng, 1984). According to One-Equation-Eddy-Viscosity SGS model by Moeng (Moeng, 1984), a prognostic equation for the SGS kinetic energy is solved in addition to the filtered governing equations,

$$\frac{\partial k^{sgs}}{\partial t} + \widetilde{u}_j\frac{\partial k^{sgs}}{\partial x_j} = \frac{\partial}{\partial x_j}\left(2\nu^{sgs}\frac{\partial k^{sgs}}{\partial x_j}\right) + 2\nu^{sgs}\widetilde{S}_{ij}\widetilde{S}_{ij} + \frac{g}{\theta_0}\left(-\frac{\nu^{sgs}}{Pr_t}\frac{\partial\widetilde{\theta}}{\partial z}\right) - \underbrace{0.7\frac{(k^{sgs})^{3/2}}{\Delta}}_{\epsilon^{sgs}} \tag{1.31}$$

where ϵ^{sgs} denotes SGS dissipation and ν^{sgs} can be determined by (Churchfield et al., 2012),

$$\nu^{sgs} = 0.143\Delta\,(k^{sgs})^{1/2} \tag{1.32}$$

1.7.3 Lagrangian-Averaged Scale-Invariant Dynamic SGS model

For the Smagorinsky based SGS models, Smagorinsky coefficient, C_s, is a constant that behaves non-locally. On the contrary, dynamic SGS models make the C_s dynamically-changing in space and time without the need for an earlier selection (Han et al., 2016). Lagrangian-Averaged Scale-Invariant (LASI) dynamic SGS model by Meneveau (Meneveau et al., 1996) is created

where the Germano identity (Germano et al., 1991) is averaged in a certain while throughout the fluid pathlines in a Lagrangian sense instead of over directions of statistical homogeneity. Another important feature is that an additional filter which is called test filter scale, $\widehat{\Delta} = 2\widetilde{\Delta}$, is imposed in addition to grid filter scale, $\widetilde{\Delta}$. The Germano identity stands for,

$$L_{ij} = T_{ij} - \tau_{ij} = \widehat{\widetilde{u}_i \widetilde{u}_j} - \widehat{\widetilde{u}}_i \widehat{\widetilde{u}}_j \tag{1.33}$$

where T_{ij} and τ_{ij} denote SGS stresses at the test, $\widehat{\Delta}$, and the grid, $\widetilde{\Delta}$, scales as,

$$T_{ij} = \widehat{\widetilde{u_i u_j}} - \widehat{\widetilde{u}}_i \widehat{\widetilde{u}}_j \tag{1.34}$$

and

$$\tau_{ij} = \widehat{\widetilde{u_i u_j}} - \widehat{\widetilde{u_i}\widetilde{u_j}} \tag{1.35}$$

So that, as shown in Fig.1.8, L_{ij} can be considered as the contribution of resolved turbulent stresses by the scales between the grid and test scales, $\widehat{\Delta} - \widetilde{\Delta}$, (Germano et al., 1991). T_{ij} and τ_{ij} can be modeled by means of Smagorinsky model,

$$T_{ij} = -2\left(C_s\left(\widehat{\Delta}\right)\widehat{\Delta}\right)^2 \left|\widehat{\widetilde{S}}\right| \widehat{\widetilde{S}}_{ij} \tag{1.36}$$

$$\tau_{ij} = -2\left(C_s\left(\widetilde{\Delta}\right)\widetilde{\Delta}\right)^2 \left|\widetilde{S}\right| \widetilde{S}_{ij} \tag{1.37}$$

where $\widehat{\widetilde{S}}_{ij}$ and $\widetilde{S}_{ij}$ resolved strain-rate tensors at scale $\widehat{\Delta}$ and $\widetilde{\Delta}$ respectively. Here,

$$\left|\widehat{\widetilde{S}}\right| = \sqrt{2\widehat{\widetilde{S}}_{ij}\widehat{\widetilde{S}}_{ij}} \tag{1.38}$$

and,

$$\left|\widetilde{S}\right| = \sqrt{2\widetilde{S}_{ij}\widetilde{S}_{ij}} \tag{1.39}$$

Since substituting all these into Eq.1.33 cause over-determined system, an error definition take places to be (Meneveau et al., 1996),

$$e_{ij} = L_{ij} - \left(T_{ij} - \tau_{ij}\right) \tag{1.40}$$

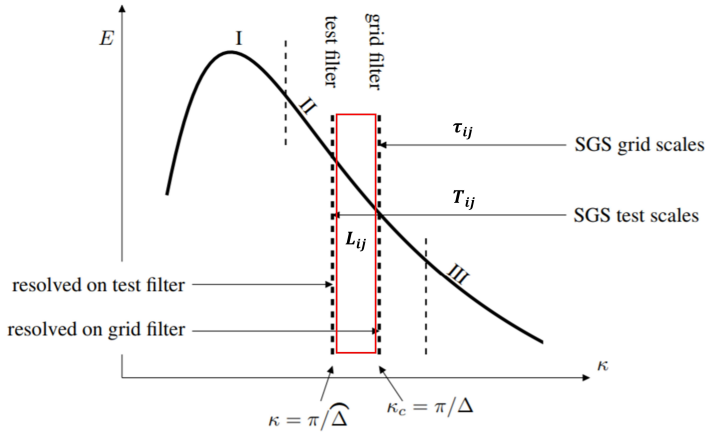

Figure 1.8: Turbulent energy spectrum along with the eddy wavenumbers, related to the test and grid filters in dynamic SGS model (Davidson, 2011).

$$e_{ij} = L_{ij} - 2\left(\left(C_s\left(\widetilde{\Delta}\right)\widetilde{\Delta}\right)^2\left|\widetilde{S}\right|\widetilde{S}_{ij} - \left(C_s\left(\widehat{\Delta}\right)\widehat{\Delta}\right)^2\left|\widehat{\widetilde{S}}\right|\widehat{\widetilde{S}}_{ij}\right) \tag{1.41}$$

that needs to be minimized. Supposing C_s is scale-invariant,

$$C_s\left(\widetilde{\Delta}\right) = C_s\left(\widehat{\Delta}\right) \tag{1.42}$$

mean-square error can be minimized by least-squares method as,

$$C_s^2 = \frac{\mathfrak{F}_{LM}}{\mathfrak{F}_{MM}} = \frac{\langle M_{ij}L_{ij}\rangle}{\langle M_{kl}M_{kl}\rangle} \tag{1.43}$$

where angle brackets indicate backward averaging through a streamline solving following equations,

$$\frac{\partial\mathfrak{F}_{LM}}{\partial t} + \widetilde{u}_j\frac{\partial\mathfrak{F}_{LM}}{\partial x_j} = \frac{1}{\theta\widetilde{\Delta}\left(\mathfrak{F}_{LM}\mathfrak{F}_{MM}\right)^{-1/8}}\left(L_{ij}M_{ij} - \mathfrak{F}_{LM}\right) \tag{1.44}$$

$$\frac{\partial\mathfrak{F}_{MM}}{\partial t} + \widetilde{u}_j\frac{\partial\mathfrak{F}_{MM}}{\partial x_j} = \frac{1}{\theta\widetilde{\Delta}\left(\mathfrak{F}_{LM}\mathfrak{F}_{MM}\right)^{-1/8}}\left(M_{ij}M_{ij} - \mathfrak{F}_{MM}\right) \tag{1.45}$$

where θ being a constant which is set to 1.5 (Han et al., 2016).

1.7.4 Nonlinear-Backscatter-Anisotropy (NBA) SGS model

Although linear SGS schemes have been widespread in LES modeling, they possess significant limitations (see Sec. 3.2.1). To overcome the deficiencies of linear SGS models, the nonlinear backscatter and anisotropy (NBA) SGS model of Kosović (1997) is a promising model available in WRF and planetWRF. It is an updated version of the linear Smagorinsky model, yet in a nonlinear framework. It builds the nonlinear SGS stress tensor as,

$$\begin{aligned}\tau_{ij} = &-(C_s l)^2 \left[2\left(2\widetilde{S}_{mn}\widetilde{S}_{mn}\right)^{1/2}\widetilde{S}_{ij}\right] \\ &-(C_s l)^2 \left[C_1\left(\widetilde{S}_{ik}\widetilde{S}_{kj} - \frac{1}{3}\widetilde{S}_{mn}\widetilde{S}_{mn}\delta_{ij}\right) + C_2\left(\widetilde{S}_{ik}\widetilde{R}_{kj} - \widetilde{R}_{ik}\widetilde{S}_{kj}\right)\right],\end{aligned} \tag{1.46}$$

where $\widetilde{R}_{ij} = \frac{1}{2}(\partial\widetilde{u}_i/\partial x_j - \partial\widetilde{u}_j/\partial x_i)$ denotes the resolved rotation rate tensor, $\widetilde{S}_{ij} = \frac{1}{2}(\partial\widetilde{u}_i/\partial x_j + \partial\widetilde{u}_j/\partial x_i)$ is the resolved shear strain rate tensor, δ_{ij} is the Kronecker delta. Note that Eq. 3.8 contains model coefficients as follows: $C_s = \left[8(1+C_b)/27\pi^2\right]^{1/2}$, $C_1 = C_2 = 960^{1/2}C_b/7(1+C_b)S_k$, with $S_k = 0.5$, and the backscatter coefficient, $C_b = 0.36$.

1.8 Motivation and thesis outline

The planetary boundary layer is the turbulently most active part of the Earth's and Martian lower atmospheres. Over the past decades, thanks to the high-resolution satellite and in-situ measurements as well as the rapid growth in the massive computing power, there has been a growing interest dealing with this phenomena, i.e. PBL turbulence, in both scientific and engineering applications. Such examples are the aviation turbulence (Muñoz-Esparza et al., 2018), i.e., crucial for aircraft operation and coordination, onshore/offshore wind energy assessments, i.e., considering the impact of local meteorology on power output (Lu and Porté-Agel, 2015), as well as weather & climate (Cohen et al., 2015) and pollutant dispersion (Moreira and Moret, 2018) studies.

Moreover, thanks to the ongoing lander and rover missions, in-situ observations of Martian surface processes (dust, water and methane transport) have been attracting more attention, especially to search for the signatures of the planet's habitability (Changela et al., 2021). From this emerges the significance of planetary boundary layer dynamics, which is the key governor

of surface exchange processes in the lowermost portion of Martian atmosphere. Enhanced understanding of the PBL turbulence, for instance, would extend our knowledge on the landing phase of the Entry, Descent and Landing (EDL) of spacecrafts. It therefore would improve EDL risk assessments due to atmospheric hazards (Tyler et al., 2008), such as strong turbulent winds, convective vortices and local dust-devils (Spiga and Lewis, 2010). It is of great importance for better lift/drag predictions to ensure a safe landing and a better reconstruction for the lander trajectory (Vasavada et al., 2012). Further examples address surface operations to examine the local meteorology (Newman et al., 2017), exchange of aerosols and trace gases. In addition, following the successful touchdowns of NASA's InSight lander (Golombek et al., 2017) and Perseverance rover (Pla-García et al., 2020) on Mars, it would help the selection process of possible landing sites in next exploration missions. It would also be vital in experimental flight tests on Mars, for example in current operations of NASA's Mars helicopter Ingenuity (Veismann et al., 2021), and in the upcoming Dragonfly's journey to Saturn's moon, Titan (Lavely et al., 2021).

The ultimate goal of this PhD research is to advance the current knowledge on the nature of PBL turbulence in the atmosphere of Earth, and beyond, Mars. This is on the grounds that the turbulence governs the surface-atmosphere exchanges of momentum, heat, aerosols and tracers, hence advanced approaches are essential to accurately represent the turbulence in planetary atmosphere models at all scales, from the global and meso to micro scales. Large-eddy simulations (LES) on a global scale are one explicit option, yet extremely heavy and not feasible given the limitations of current computing power. LES, on the other hand, has been extensively used to improve the PBL schemes in global and mesoscale models. Therefore, the present doctoral research commences with the construction of novel planetary boundary layer schemes for global and mesoscales, derived from a theoretical analysis based on large eddy simulations on Earth **(Chapter 2)**, then on Mars **(Chapter 3)**. When exploring the nature of Martian PBL, understanding the turbulence-dust interactions is vital, especially during major dust storms. Hence, the Mars-specific PBL scheme is followed by the development of a state-of-the-art Martian dust transport model **(Chapter 4)**. Eventually, the present thesis enlightens one of the enigmas of the PBL phenomenon, emerging in the so-called Terra Incognita, the gray zone of atmospheric

turbulence. For the first time, a novel three-dimensional gray-zone model is derived, providing a framework that bridges the mesoscale and microscale limits **(Chapter 5)**. More specifically,

- In **Chapter** 2, we develop a novel 1D PBL turbulence model based on a new theoretical mixing length scale formulation. Here, I led the research conceptualization, model development and validation, formal analysis, simulations and visualization of results, and the writing of the manuscript (published in Journal of Advances in Modeling Earth Systems).
- In **Chapter** 3, we develop the first Mars-specific 1D PBL turbulence model. This is handled by making use of Martian large-eddy simulations and projecting the new mixing length scale formulation (Chapter 2) into extreme Martian conditions. Here, I, as the second co-author of the paper, contributed to the research conceptualization, performing MarsWRF large-eddy simulations, energy spectra analysis, development of the turbulent mixing length scale formulation and the Mars-specific PBL scheme, post-processing the GCM and mesoscale simulation results, and the writing of the manuscript (published in Icarus).
- In **Chapter** 4, we develop a new semi-interactive dust transport model coupled with our Mars-specific turbulence model (Chapter 3), in order to examine the Martian dust-turbulence interaction, especially during major dust storms. This chapter was published in Journal of Advances in Modeling Earth Systems. Here, I led the research conceptualization, model development and validation, formal analysis, simulations and visualization of results, and the writing of the manuscript. Here, I led the research conceptualization, model development and validation, formal analysis, simulations and visualization of results, and the writing of the manuscript (published in Journal of Geophysical Research: Planets).
- In **Chapter** 5, we develop a state-of-the-art gray-zone turbulent model in the so-called Terra-Incognita range of scales, as the first time. This model provides a framework that bridges the mesoscale and microscale limits, which is suitable for the development of next generation planetary boundary layer schemes. Here, I led the research conceptualization, model development and validation, formal analysis, simulations and visualization of results, and the writing of the manuscript (published in Journal of Geophysical Research: Atmospheres).

Chapter 2

From large-eddy simulations to a new 1D PBL model for Earth[1]

2.1 Introduction

The planetary boundary layer (PBL), which is the lowest part of the troposphere, gained much attention in many scientific fields ranging from space applications (Martinez et al., 2013), over wind energy studies (Storm et al., 2009), optical turbulence (Basu and He, 2014), to weather forecasting and climate research (Flaounas et al., 2011). The parameterization of the vertical turbulent fluxes is essential for the correct modeling of the diurnal evolution of winds, temperature and water vapor within the boundary layer (Shin and Hong, 2011; Zhang and Zheng, 2004) as well as for the large-scale atmospheric processes such as mesoscale convective rainfall systems (Jankov et al., 2005), hurricanes (Braun and Tao, 2000) and even for the radiation budgets for example in the case of boundary layer clouds in polar regions (Tjernström et al., 2005).

Except for the cases, where the spatial resolution is sufficiently high to use large-eddy simulation techniques, turbulent fluxes are parameterized using planetary boundary layer (PBL) schemes, which are based on the eddy diffusivity concept. This approach basically assumes a relation between turbulent fluxes and mean velocity gradients where this proportionality is

[1]This chapter is written based on the published article: Senel, C. B., Temel, O., Porchetta, S., Muñoz-Esparza, D., & van Beeck, J. (2019). A new planetary boundary layer scheme based on LES: Application to the XPIA campaign. Journal of Advances in Modeling Earth Systems, 11(8), 2655-2679. Here, Cem Berk Senel led the research conceptualization, model development and validation, formal analysis, simulations and visualization of results, and the writing of the manuscript.

called the eddy diffusivity. To calculate the vertical turbulent fluxes, eddy diffusivity is either determined by algebraic closures, e.g. Yonsei University (YSU) scheme (Hong et al., 2006), or by turbulence kinetic energy (TKE) closures, which solve a transport equation for the TKE and empirically models its sink term, the dissipation rate of TKE (Janjić, 1994). Several different TKE closures were proposed in the literature, e.g. Bougeault-Lacarrere (BouLac) scheme (Bougeault and Lacarrere, 1989b), Mellor-Yamada-Janjic (MYJ) scheme (Janjić, 1994), Mellor-Yamada-Nakanishi-Niino (MYNN) scheme (Nakanishi and Niino, 2009). The main difference between these TKE closures depends mainly on the formulation of the length scale and closure coefficients for the calculation of the eddy momentum/heat diffusuvities. These TKE closures are used as the one-dimensional turbulence closures by neglecting streamwise and spanwise turbulent fluxes as well as all the horizontal derivatives. Although these schemes are suitable for mesoscale simulations, however, in case of high horizontal grid resolutions, the microscale atmospheric turbulence must be regarded as a three dimensional process (Muñoz-Esparza et al., 2016). For such circumstances, large-eddy simulation (LES) technique has been widely used, e.g. Chow et al. (2006); Rotunno et al. (2009); Kosović et al. (2017). Furthermore, LES studies can be used to improve the existing TKE closures like the derivation of the MYNN scheme (Nakanishi, 2001) and the improved Tim-Marht (TM) scheme (Noh et al., 2003). Another approach is to implement 3D PBL schemes to model flows over complex terrain by using high-resolution models (Kosović et al., 2017). In either case, attention should be paid to PBL schemes with varying stability parameters for high spatial resolution models, where the span- and streamwise turbulence can not be neglected. This can lead to realizability issues meaning that the predicted turbulence kinetic energy would become negative (Shih et al., 1995a). In numerical weather prediction (NWP) models, turbulent fluxes are parameterized using a turbulent transport coefficients, i.e. eddy diffusivity. This is calculated as a function of a velocity scale, a length scale and a model coefficient, the eddy diffusivity coefficient. It has been shown that in case of using high eddy diffusivity coefficients for the flows with high velocity gradients, such as flow over complex terrain, the turbulence model can become unrealizable. In terms of the threshold value for the eddy diffusivity coefficient, various suggestions have been proposed for industrial flows (Shih et al., 1995b). However, a similar investigation, regarding the realizability

issues in modeling the horizontal turbulent fluxes, is missing. Therefore, a turbulence model with constant closure coefficients would stand as a more promising starting point to develop future 3D PBL schemes. Based on this idea, Temel et al. (2018b) have revised the BouLac scheme conducting a theoretical investigation under realizability constraints. A new formulation was in turn proposed for the turbulent Prandtl number. However, for this latest version of the revised BouLac scheme (hereafter VKI00), the classical Blackadar length scale formulation (Blackadar, 1962a) is used.

In this present study, we present a new PBL scheme (hereafter VKI01), using a mixing length scale parameterization derived from a set of LES results. It incorporates the turbulent Prandtl number definition proposed by Temel et al. (2018b). Our LES simulations (hereafter, referred to as reference-LES) are first compared with the available wind mast measurements by Risø National Laboratory at the Test Centre for Large Wind Turbines at Høvsøre, Denmark (Gryning et al., 2007). These mast measurements were made through cup anemometers from 2 to 160 meter altitude, wheres the momentum and heat turbulence fluxes were carried out by the METEK scientific 3D sonic anemometers. Afterwards, the new PBL scheme is implemented into the Weather Research and Forecasting (WRF) model. The performance of the proposed PBL scheme is evaluated by performing idealized (imposed surface heat fluxes) mesoscale simulations. The WRF results obtained by the new PBL scheme are compared with the reference-LES and two state-of-the-art PBL schemes (BouLac and MYNN). This can be regarded as the baseline of the proposed model for various aspects. Finally, the new PBL scheme is assessed in real-case mesoscale simulations (i.e., referring to the regional climate simulations on real-topography guided by National Centre of Environmental Prediction (NCEP) North American Regional Reanalysis - NARR datasets) in Colorado. (Lundquist et al., 2017). Our simulation results are then compared with the available mast measurements from the eXperimental Planetary boundary layer Instrumentation Assessment (XPIA) campaign (40.05°N, 105°W) conducted at the Boulder Atmospheric Observatory (BAO) from March 2^{nd} to May 31^{st} in 2015 (Lundquist et al., 2017). The measurements led by Pacific Northwest National Laboratory were conducted through multiple Doppler lidars and temperature/relative humidity sensors, consist of the high-resolution time evolution of the wind speed, temperature, turbulence kinetic energy and dissipation rate.

2.2 Theory & Modeling

2.2.1 Description of the new planetary boundary layer scheme

The new planetary boundary scheme proposed in this study is a non-local turbulence kinetic energy (TKE) closure. So that the one-dimensional transport equation for the TKE can be defined as,

$$\frac{\partial k}{\partial t} = \frac{\partial}{\partial z}\left[lk^{0.5}S_k\frac{\partial k}{\partial z}\right] + P_s + P_b - \epsilon \tag{2.1}$$

The source and sink terms on the right hand side of Eq. 2.1 stand for the shear production of turbulence, P_s, the buoyancy production/destruction of turbulence, P_b, and the dissipation rate of turbulence, ϵ, which can be calculated as follows,

$$P_s = K_m\left[\left(\frac{\partial u}{\partial z}\right)^2 + \left(\frac{\partial v}{\partial z}\right)^2\right] \tag{2.2}$$

$$P_b = -\beta g K_h\frac{\partial \theta_v}{\partial z} \tag{2.3}$$

$$\epsilon = \frac{k^{1.5}}{B_1 l} \tag{2.4}$$

In Eq. 2.1, l is the mixing length scale and S_k is the turbulence kinetic energy diffusion coefficient. K_m is the eddy diffusivity of momentum in Eq. 2.2. K_h is the eddy diffusivity of heat, $\beta = 1/300K$ is the thermal expansion coefficient and g is the gravitational acceleration in Eq. 2.3. B_1 is the dissipation coefficient in Eq. 2.4. The K_m and K_h are calculated as follows,

$$K_m = S_m k^{0.5} l \tag{2.5}$$

$$K_h = S_h k^{0.5} l \tag{2.6}$$

where S_m and S_h denote the stability functions of momentum and heat. One of the main difference between mesoscale PBL schemes is based on the mixing length scale formulation, which in turn is used to compute eddy diffusivities and the dissipation as can be seen in Eq. 2.4, 2.5 and 2.6. By making use of the Høvsøre LES results presented in Sec. 2.2.2, we propose a new mixing length parameterization. This modeling starts with the classical Blackadar (1962a)

formulation that is basically the harmonic average of two length scales,

$$\frac{1}{l_{Blackadar}} = \frac{1}{l_0} + \frac{1}{l_s} \tag{2.7}$$

where l_0 and l_s denote the asymptotic and surface layer length scales. By this way, Blackadar's mixing length scale switches from the surface layer throughout the well-mixed boundary layer limit. This approach constitutes the basis of different PBL schemes as well, for instance, the UW PBL scheme of Bretherton and Park (2009), the scale-adaptive turbulence kinetic energy closure of Kurowski and Teixeira (2018) and MYJ scheme (Janjić, 1994). For the latter, Janjić (1994) set the asymptotic component of Blackadar's mixing length scale, l_0, to

$$l_0 = \alpha \frac{\int_{p_t}^{p_s} q\, z\, dp}{\int_{p_t}^{p_s} q\, dp} \tag{2.8}$$

where p_s and p_t are the pressures at the bottom and top of the model atmosphere, α is an empirical constant to be 0.30 and $q = \sqrt{k}$ is the square root of turbulence kinetic energy. Later on, this length scale (Eq. 2.8) is used in the MYNN scheme by setting $\alpha = 0.23$ where they named the l_0 "the length scale dependent on the PBL depth".

According to our proposed model, above the surface layer, asymptotic component of Blackadar's mixing length scale is expanded to two components, i.e. $l_0 = (1/l_k + 1/l_\lambda)^{-1}$. These are turbulence kinetic energy length scale, l_k, related to turbulence kinetic energy of the PBL and asymptotic length scale, which is used to fit the mixing length scale to our reference LES data along the mixed layer. Furthermore, the mixing length scale becomes constant above the surface layer and it asymptotically converges to a constant value since the grid resolution of mesoscale simulations falls in the mesoscale limit, $\Delta_{meso} > L$, where L denotes the size of energy containing eddies (Wyngaard, 2004). This is consistent with the observations of Ito et al. (2015) where they find the dissipation length scale converges to a unique value at the mesoscale limit. Considering the study of Ito et al. (2015), the mixing length scale becomes constant above the surface layer, i.e. $\partial l/\partial z \rightarrow 0 \quad if\ z > z_s$. Ito et al. (2015) also showed that the vertical profiles of dissipation length scale, $l_\epsilon = B_1 l$, reach to a nearly asymptotic shape if the horizontal grid resolution approaches to the mesoscale limit. In other words, as the grid resolution increases from LES limit

towards the mesoscale limit, i.e.

$$\lim_{\Delta \to \Delta_{meso}} \langle B_1\ l \rangle = \langle B_1\ l \rangle\ (\infty) \tag{2.9}$$

where the infinity symbol denotes this asymptote. Note that, the angular bracket denotes the horizontal-averaging operator applied in the horizontal directions, i.e. streamwise (x) and spanwise (y), similar to Catalano and Moeng (2010). In this context, the total contribution of our l_k and l_λ tends to be constant in the mixed layer as the altitude increases similar to Ito et al. (2015). In addition to this, the sum of l_k and l_λ reach to an asymptotic value independent from the grid resolution. As discussed above, this is because the length scale profiles coincide at the mesoscale limit in accordance with the self-similarity. Since the l_λ brings the l_k towards the mixed-layer asymptote at the mesoscale limit, we call the l_λ "asymptotic" length scale. Another essential point is to adjust the value of the B_1 coefficient. In this manner, we directly compute the dissipation, i.e. $\epsilon = \left\langle \tau_{ij}^{D'} S'_{ij} \right\rangle$, as well as the turbulence kinetic energy by making use of the LES. Since $B_1\ l$ is equal to $k^{1.5}/\epsilon$ and considering the value of $B_1\ l$ converges to a constant value (from the Eq. 2.9). The problem itself becomes independent from the selection of B_1 at the mesoscale limit, Δ_{meso}. From this aspect, we simply set B_1 to 24 following the MYNN model. Consequently, we define the length scale based on MYNN's harmonic mean of three length scales, i.e.

$$\frac{1}{l} = \frac{1}{l_k} + \frac{1}{l_\lambda} + \frac{1}{l_s} \tag{2.10}$$

$$l_k = \kappa\ \frac{\int_0^\infty k\ z\ dz}{\int_0^\infty k\ dz} \tag{2.11}$$

$$l_\lambda = \lambda e^{\zeta_1} z_i \begin{cases} \lambda = 0.150, & -1000m \leq L_O < 0 \quad (unstable) \\ \lambda = 0.100, & |L_O| > 1000m \quad (neutral) \\ \lambda = 0.032, & 0 < L_O \leq 1000m \quad (stable) \end{cases} \tag{2.12}$$

$$l_s = \begin{cases} \kappa z\,(1 - 80\ \zeta)^{1/4}, & -1000m \leq L_O < 0 \quad (unstable) \\ 2.5\kappa z, & |L_O| > 1000m \quad (neutral) \\ \kappa z\left(1 + \kappa^{-1}\ \zeta\right), & 0 < L_O \leq 1000m \quad (stable) \end{cases} \tag{2.13}$$

where l_k is the turbulence kinetic energy length scale, l_λ is the asymptotic length scale and l_s is the surface layer length scale. If we further introduce

this parameterization, the functional form of the proposed turbulence kinetic energy length scale in Eq. 2.11 is based on Mellor and Yamada (1974),

$$l_k = \alpha \frac{\int_0^\infty q\, z\, dz}{\int_0^\infty q\, dz} \tag{2.14}$$

as the ratio of the first to the zeroth moment of the turbulence kinetic energy velocity scale, $q = \sqrt{2k}$. This definition can be interpreted as the turbulence kinetic energy tendency of the length scale related to changes in the atmospheric stability and the altitude. Accordingly, the turbulence kinetic energy tends to decay with the stability and the altitude as can be seen from the vertical profiles of turbulence kinetic energy in Fig. 2.2-c. Both k and q are able to represent this description, however, we prefer the turbulence kinetic energy itself for its direct implementation rather than its velocity scale. Note that, the closure constant, α, has been selected to be 0.10 in Mellor and Yamada (1974), 0.30 in MYJ scheme (Janjić, 1994) and 0.23 in MYNN scheme (Nakanishi and Niino, 2009). In this study, we choose $\alpha = \kappa$ where $\kappa = 0.40$ denotes the von Karman constant. The reason can be explained by the physical representation of l_k, such that it corresponds to the center of turbulence kinetic energy analogous to the center of gravity of a particular object. If α is 1, this gives the absolute center of turbulence kinetic energy where $z \to \infty$. To make the l_k more dominant along the middle boundary layer, the center of turbulence kinetic energy can be moved to $z = 0.40 z_i$. This location can be determined as the center of $z = 0.80 z_i$ where the middle boundary layer is still effective, before the top boundary layer starts.

According to our asymptotic length scale parameterization, it enables the mixing length scale to fit our reference LES results above the surface layer, i.e.

$$l_0 = (1/l_k + 1/l_\lambda)^{-1} \to l_{LES} \quad if\ z > z_s \tag{2.15}$$

We introduce this parameterization by postulating that the asymptotic length scale be the function of the PBL height, z_i, and the non-dimensional stability parameter, i.e. $\zeta_1 = z_1/L_O$, at the first wall adjacent cell center, z_1, where L_O is the Obukhov length scale,

$$L_O = \frac{-u_*^3}{\kappa \frac{g}{\theta_0} \overline{w'\theta'}_s} \tag{2.16}$$

where u_* is the surface friction velocity, g/θ_0 is the buoyancy parameter and

$\overline{w'\theta'}_s$ is the kinematic heat flux at the surface. Then,

$$l_\lambda = f(z_i, \zeta_1) \tag{2.17}$$

similar to the University of Washington (UW) scheme (Bretherton and Park, 2009), which is

$$l_{\lambda,UW} = z_i \eta \tag{2.18}$$

where they adjust $\eta = 0.085\left(2 - e^{[min(Ri^{CL},0)]}\right)$ by using LES results. Note that, Ri^{CL} is the bulk Richardson number for the convective turbulent layer. Recalling our postulate given in Eq. 2.17, a curve fitting is made by the linear regression considering the quasi-linear behaviour of mixing length scale above the surface layer. Supposing that the PBL height is proportional to the asymptotic length scale with the power of 1, i.e.

$$l_\lambda \propto z_i^{p=1} \tag{2.19}$$

This enables l_λ to satisfy the unit of meter. Then, $l_\lambda \propto z_i$ can be linked to the LES results through the atmospheric stability in different functional forms (logarithmic, exponential, hyperbolic tangent, etc.), i.e. $l_\lambda = \mathcal{F}(\lambda, \zeta_1) z_i$. Note that, here λ is the fitting parameter. Following the UW scheme (Bretherton and Park, 2009), the exponential function provided the best agreement for our l_λ model in our regression analysis. Beside this, since the exponential function tended to be more aware of the stability, we choose the exponential form as,

$$l_\lambda = e^{(ln\lambda + \zeta_1)} z_i = \lambda e^{\zeta_1} z_i \tag{2.20}$$

Then, the asymptotic length scale is defined as a piecewise function in three different stability regimes based on the classification of Gryning et al. (2007), in Eq. 2.12. By this way, the model itself tends to be adaptive to the atmospheric stability.

If the functional form of the surface layer length scale is addressed, it can be assumed to be proportional with the altitude based on Businger et al. (1971), Dyer and Hicks (1970) and Gryning et al. (2007), $l_{s,neutral} = 2.5\kappa z$ where $\kappa = 0.4$ is the von Karman constant. This selected value matches well with our LES results for the near-neutral condition (LES-n case). On the other hand, for non-neutral conditions, we begin with the functional form of l_s from MYNN scheme as $l_{s,unstable} = \kappa z(1 - a_1\zeta)^{p_1}$ and $l_{s,stable} = (1 + a_2\zeta)^{p_2}$. Then, by means

of curve fitting to the predicted LES results, we end up with the final functional form for the non-neutral conditions given in Eq. 2.13.

As mentioned earlier, a new length scale formulation is proposed to build a new PBL scheme which later can be used as a baseline for further extension, for instance towards a 3D PBL scheme. After applying the closure assumption for dissipation rate (Eq. 2.4) into Eq. 2.5, then the turbulent viscosity can be redefined independent from the mixing length scale,

$$K_m = \frac{S_m}{B_1}\frac{k^2}{\epsilon} \tag{2.21}$$

where S_m/B_1 is the equivalent closure coefficient of C_μ appearing in computational fluid dynamics (CFD) simulations of turbulent flows by using three-dimensional turbulence closures. Based on the realizability constraints (Shih et al., 1995a), C_μ is set to 0.09 (Rodi, 2017) for industrial flow applications and to 0.033 for wind engineering applications (Alinot and Masson, 2005). In this present study, B_1 and S_m are taken to be 24.0 and 0.144, which is equivalent to a smaller value of $C_\mu = 0.006$, ensuring the realizability of the turbulence closure for further extensions as a 3D PBL scheme. Finally, the eddy heat diffusivity coefficient is computed by utilizing the formulation of turbulent Prandtl number, i.e. $Pr_t = S_m/S_h$, proposed by Temel et al. (2018b) as,

$$Pr_t = \begin{cases} 1.25 & Ri < Ri_{cr} \\ \dfrac{Ri}{1-\left(\frac{\phi_e}{\phi_m}\right)_{|\zeta|=1.0}} & Ri > Ri_{cr} \end{cases} \tag{2.22}$$

where ϕ_m is the stability function of Monin-Obukhov theory for velocity gradient and ϕ_e is the stability function for potential temperature gradient (Businger et al., 1971). Ri stands for the gradient Richardson number,

$$Ri = \frac{g\beta\frac{\partial\theta_v}{\partial z}}{\left(\frac{\partial u}{\partial z}\right)^2} \tag{2.23}$$

In Eq. 2.22, Ri_{cr} refers to the critical Richardson number, which assumed to be 0.23 (Temel et al., 2018b). Moreover, similar to the MYJ scheme, the minimum value for the turbulence kinetic energy is set to 0.01 m^2/s^2. For determination of the boundary layer height, the way of BouLac scheme, which is similar to the 1.5-theta-increase method (Nielsen-Gammon et al., 2008), is applied. In the original BouLac scheme (Bougeault and Lacarrere, 1989b), the boundary layer height is determined at the first height where the

potential temperature is increased by 0.5K for all stability levels. We keep this value for the convective atmosphere, however it is set to 1.0K to avoid the possible instantaneous temperature rise at the near surface for non-convective conditions. As noted before, the present PBL scheme is a non-local scheme, So that the non-local term is computed in the following equation as suggested by Therry and Lacarrère (1983) (see Sec. 4.2, Eq.40).

$$\overline{w'\theta'} = -K_h \left(\frac{\partial \theta}{\partial z} - \gamma_{cg} \right) \tag{2.24}$$

2.2.2 Large-eddy simulation (LES) setup

Since the proposed scheme is derived based on large-eddy simulations, its details will be presented in this section. For the LES experiments, OpenFOAM based Simulator for Offshore Wind Farm Applications (SOWFA) ABLSolver, an open source LES code written in C++, is utilized in the present study. This code solves the resolved continuity, Navier-Stokes and energy equations based on the finite volume method. The details of governing equations are described in Churchfield et al. (2012).

ABLSolver, the spatial and time discretizations are based on the second order centered-difference (i.e., Gaussian linear in terms of OpenFoam) and Crank-Nicolson methods respectively. The Courant-Friedrichs-Lewy (CFL) number is kept lower than a critical value, i.e. $Co < 0.375$. The pressure-velocity coupling is preformed by successively-solved implicit equations using pressure-implicit with splitting of operators (PISO) algorithm (Issa, 1986). Velocity and pressure fields are handled implicitly to increase the stability of the numerical scheme. However, the buoyancy, SGS viscosity and Coriolis terms are explicitly treated (Churchfield et al., 2010).

For the subgrid scale (SGS) parameterization, despite the universal usage of Smagorinsky model which assumes a balance between shear production and dissipation terms, it is inadequate for the buoyancy-driven and transitional PBL flows (Moeng, 1984). Therefore, a prognostic equation for the SGS kinetic energy is solved besides the filtered governing equations. This model, namely Deardorff's SGS model (Deardorff, 1980), is used for the convective simulations. On the other hand, the effects of SGS modeling become more important for the non-convective conditions. This arises particularly for the stable PBL due to the excess in unresolved small eddies

(Kosović and Curry, 2000). We therefore use the Lagrangian-Averaged Scale-Invariant (LASI) dynamic SGS model (Meneveau et al., 1996) for the neutral and stable conditions, which is available in the ABLSolver. As SGS schemes is of particular significance, more advanced approaches can extend our understanding on the PBL phenomenon. Advanced approaches have been emerged in this context, such as the nonlinear-backscatter-ansisotropy model (Kosović and Curry, 2000) and scale-dependent dynamic SGS model (Porté-Agel et al., 2000). Although those models have not been available in ABLSolver, attempts will be made in the future.

To derive a new PBL scheme, seven cases are investigated based on different stability classes. Atmospheric stability conditions are as reported by Gryning et al. (2007) and listed in Tab.2.1 where U_{ref}, $u_{*,ref}$ and $q_{s,ref}$ denote reference mean velocity, friction velocity and kinematic heat flux at 10m. While $z_{i,ref}$ and $z_{0,ref}$ stand for the reference PBL height and the roughness height. The initial velocity field is set to a constant value, i.e., the initial wind speed, U_0, at a certain height, h_0, based on the atmospheric conditions at Høvsøre test site (Tab.2.1). Then, to drive the LES, ABLSolver forces the simulation by keeping this given velocity at this desired altitude. On the other hand, the initial potential temperature field is determined relying on the LES experiments by Pedersen et al. (2012) performed at the same test site in Høvsøre, Denmark. Reference potential temperature is kept constant as $\theta_{ref} = 280K$ up to the PBL height, z_i and then increasing with the atmospheric lapse rate $\Gamma_a = 0.0034\, Km^{-1}$ within the free atmosphere. To restrict the growing of the PBL, a three-layer potential temperature profile is described inserting a capping inversion similar to the study of Muñoz-Esparza et al. (2014a),

$$\theta_0 = \begin{cases} \theta_{ref}, & 0 < z < z_i - \Delta h_i/2 \\ \theta_{ref} + \Gamma_i \left(z - (z_i - \Delta h_i/2)\right), & z_i - \Delta h_i/2 < z < z_i + \Delta h_i/2 \\ \theta_{ref} + \Gamma_i \Delta h_i + \Gamma_a \left(z - (z_i + \Delta h_i/2)\right), & z > z_i + \Delta h_i/2 \end{cases} \tag{2.25}$$

where Γ_i and Δh_i are set to different values related to the different atmospheric stabilities, i.e., $\Gamma_i/\Delta h_i$ is $2.5K/100m$, $1K/50m$, $0K/0m$ for unstable, neutral and stable PBL respectively.

The dimensions and grid resolutions of the computational domain are determined depending on the atmospheric stability and in accordance with the earlier studies. So that the domain size and the grid resolution are $5\times5\times2\ km^3$

Case	L_O $[m]$	$u_{*,ref}$ $[m/s]$	$q_{s,ref}$ $[Km/s]$	U_{ref} $[m/s]$	(U_0, h_0) $[m/s]$	$z_{i,ref}$ $[m]$	$z_{0,ref}$ $[m]$
LES-vu	−71	0.340	0.051	4.91	(5.90, 80)	612	0.0180
LES-mu	−142	0.367	0.032	5.71	(7.08, 80)	459	0.0130
LES-nu	−275	0.405	0.023	6.63	(8.23, 80)	614	0.0120
LES-n	3910	0.388	−0.001	6.39	(7.85, 40)	316	0.0140
LES-ns	323	0.358	−0.013	6.15	(8.27, 60)	279	0.0130
LES-ms	108	0.249	−0.013	4.69	(6.89, 60)	207	0.0080
LES-vs	28	0.152	−0.012	3.85	(7.28, 60)	231	0.0013

Table 2.1: Reference PBL parameters based on the measurements of Høvsøre test site at 10 m (Gryning et al., 2007). (Subscripts, vu: very unstable, mu: moderate unstable, nu: near-neutral unstable, n: near-neutral, ns: near-neutral stable, ms: moderate stable, vs: very stable).

and $40 \times 40 \times 16$ m^3 for the unstable PBL (Brooks and Fowler, 2012; Cancelli et al., 2014; Degrazia et al., 2009), 3×3×1 km^3 and 24×24×10 m^3 for the neutral PBL (Khani and Porté-Agel, 2017), $0.4 \times 0.4 \times 0.4$ km^3 and $6.25 \times 6.25 \times 6.25$ m^3 for the stable PBL (Basu and Porté-Agel, 2006) respectively. The details of the domain size, L, grid resolution, Δ, and the number of grid points, N, are given in Tab.2.2. The lower boundary is ideally flat but rough with different roughness heights given in Tab.2.1.

Periodic boundary conditions are applied at the lateral boundaries. At the top surface, a slip wall boundary condition is imposed for the velocity while the Schumann-Grötzbach wall model (Schumann, 1975) is applied for the surface shear stress and the kinematic heat flux at the lower surface. For the potential temperature, a Neumann boundary condition and a fixed gradient equal to the capping inversion gradient are imposed at the top and lower surfaces respectively. For the unstable and neutral simulations the kinematic heat flux is specified on the ground whereas the surface cooling rate is imposed for the stable simulations following the model developed by (Basu et al., 2008). The cooling rate is determined based on the surface kinematic heat flux ($q_{s,ref}$) values of Høvsøre test site (Tab.2.1) through the trial and error approach. The corresponding cooling rates are set to 0.5 K/h, 0.42 K/h and 0.36 K/h for the very stable, moderate stable and near-neutral stable conditions. Besides these, in order to create the turbulence rapidly within the large-eddy simulations, divergence-free perturbations similar to De Villiers (2007) are included only close to the ground.

Large-eddy simulations in dry-air conditions are applied to seven different

stability conditions based on the Høvsøre test site (Gryning et al., 2007). Simulations reach a quasi-equilibrium state at $\mathcal{T} = 21000s$ ($\sim 26\tau_* - 30\tau_*$) for the unstable PBL, $\mathcal{T} = 20000s$ ($\sim 18\tau_*$) for the neutral and $\mathcal{T} = 20000s$ ($\sim 11\tau_* - 14\tau_*$) for the stable PBL. Afterwards, LES simulations are continued $3\tau_*$ more for time averaging where τ_* denotes large-eddy turnover time given in Tab.2.3. It is defined to be $\tau_* = z_i/u_*$ for non-convective conditions while for the convective conditions as $\tau_* = z_i/w_*$ (Ayotte et al., 1996). Herein, u_* is the friction velocity and w_* denotes the Deardorff convective velocity and reads,

$$w_* = \left(\frac{g}{\theta_0}\, q_s\, z_i\right)^{1/3} \tag{2.26}$$

where g is the gravitational acceleration, θ_0 is the horizontally-averaged surface potential temperature, q_s is the surface kinematic heat flux.

Time step of the LES simulations, $\Delta t = 0.9s, 1.0s, 0.3s$ for the unstable, neutral, stable PBL respectively. The sampling frequency for the time averaged LES results are $f_s = 1.11\ Hz$ for unstable, $f_s = 1.00\ Hz$ for neutral and $f_s = 3.33\ Hz$ for stable PBL. In addition to the time averaging, a horizontal averaging Catalano and Moeng (2010) is executed in the horizontal directions to determine the turbulence statistics due to the existence of quasi-steady turbulence after a characteristic time.

Once all the computations finish, to ensure the convergence, the relative change in the friction velocity, u_*, Obukhov length scale, L_O and PBL height, z_i, are checked. Their relative errors are lower than $5x10^{-5}$ which can be considered as a satisfying convergence level. LES results are listed in Tab.2.3 in terms of the main PBL parameters. Here, u_* are calculated at the first grid center close to the ground, i.e. $z_{1/2} = 8, 5, 3.125\ m$ for unstable, neutral and stable conditions respectively. Tab.2.3 also includes the planetary boundary layer height, z_i. It is specified at the height where the vertical profile of resolved heat flux becomes minimum for the unstable conditions, contrarily, it corresponds to maximum resolved heat flux in case of stable conditions. For the neutral condition, PBL height is determined at the height when the kinematic heat flux being 0. As presented in Tab.2.3, the PBL height is highest for the very unstable case and lowest for the very stable case, consistently with the literature, e.g. Moeng and Sullivan (1994); Udina et al. (2016).

First, the wind speed predictions by LES are compared with the wind speed

Case	L_O [m]	$L_x \times L_y \times L_z$ [km^3]	$N_x \times N_y \times N_z$ [−]	$\Delta_x \times \Delta_y \times \Delta_z$ [m^3]	N_t [−]
LES-vu	−71	5.0 × 5.0 × 2.0	125 × 125 × 125	40 × 40 × 16	1.953.125
LES-mu	−142	5.0 × 5.0 × 2.0	125 × 125 × 125	40 × 40 × 16	1.953.125
LES-nu	−275	5.0 × 5.0 × 2.0	125 × 125 × 125	40 × 40 × 16	1.953.125
LES-n	3910	3.0 × 3.0 × 1.0	125 × 125 × 100	24 × 24 × 10	1.562.500
LES-ns	323	0.4 × 0.4 × 0.4	64 × 64 × 64	6.25 × 6.25 × 6.25	262.144
LES-ms	108	0.4 × 0.4 × 0.4	64 × 64 × 64	6.25 × 6.25 × 6.25	262.144
LES-vs	28	0.4 × 0.4 × 0.4	64 × 64 × 64	6.25 × 6.25 × 6.25	262.144

Table 2.2: The details of the computational domain and the grid resolution depending on the atmospheric stability.

measurements performed at the Høvsøre test site (Gryning et al., 2007). Time- and horizontal averaged wind speed profiles normalized by the reference friction velocity, $u_{*,ref}$, are plotted in the vertical direction up to 400 m altitude (Fig. 2.1). Herein, $\langle U \rangle = (\langle u \rangle^2 + \langle v \rangle^2)^{1/2}$ where the $\langle u \rangle$ and $\langle v \rangle$ denotes the x and y component of the time- and horizontal averaged mean velocity. Results

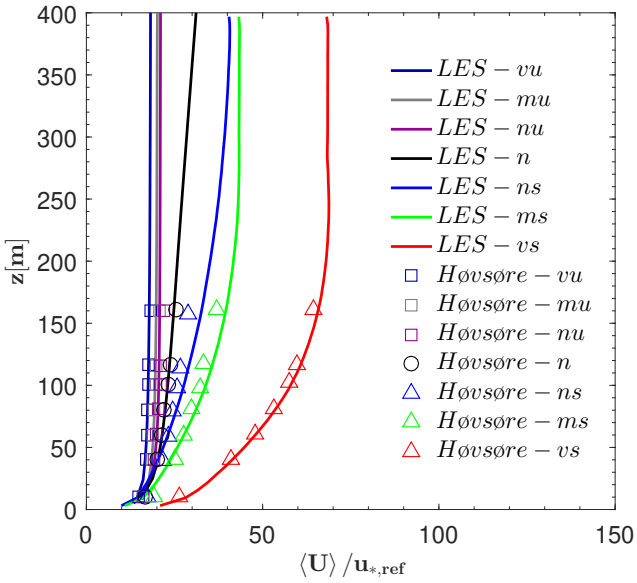

Figure 2.1: Horizontally-averaged wind speed profiles normalized by the reference friction velocity depending on the atmospheric stability. Solid lines refer to the LES results and open markers refer to the Høvsøre experiment (Gryning et al., 2007). (Subscripts, vu: Very unstable, mu: Moderate unstable, nu: Near-neutral unstable, n: Near-neutral, ns: Near-neutral stable, ms: Moderate stable, vs: Very stable)

Case	$L_O[m]$ [m]	u_* [m/s]	w_* [m/s]	τ_* [s]	(U_g, V_g) [m/s]	z_i [m]
LES-vu	−54	0.3371	1.1172	698	(6.63, 0)	780
LES-mu	−108	0.3641	0.8689	673	(8.09, 0)	585
LES-nu	−200	0.4009	0.8042	803	(9.27, 0)	646
LES-n	3094	0.3513	–	1039	(10.95, 0)	390
LES-ns	94	0.2576	–	1394	(11.51, 0)	347
LES-ms	30	0.1761	–	1613	(8.51, 0)	278
LES-vs	18	0.1458	–	1824	(8.49, 0)	266

Table 2.3: Main PBL parameters based on LES results.

indicate that the LES based wind profiles perform well and are consistent with the Høvsøre experiment. Furthermore, the normalized wind speed gradient increases from convective conditions through neutral and stable conditions, so that the strongest gradient exists once the atmosphere becomes strongly stable, i.e. very stable PBL, as in Fig. 2.1.

In Fig. 2.2, time- and horizontal averaged wind speed and potential temperature profiles are depicted in the vertical direction depending on various atmospheric stabilities. The altitude expressed herein is normalized by the PBL height, z_i. Averaged wind speed profiles show that the highest velocity gradient appears in case of the stable cases, as a result of the suppressed turbulence due to the negative buoyancy. Unlike the stable conditions, a weak velocity gradient appears for the unstable conditions thanks to the strong buoyancy and weaker winds. This leads to slightly varying wind speed in the surface layer and nearly-constant wind speed until the entrainment zone consistently with the previous studies, e.g. Moeng and Sullivan (1994); Degrazia et al. (2009). As can be expected, in comparison to stable cases, wind speed gradients are lower for the neutral case, revealing the well reported change of wind gradient from very stable conditions through weakly stable condition (Huang and Bou-Zeid, 2013). Furthermore, the averaged potential temperature profiles exhibit the typical behaviours related to the stability conditions, such as; positive and negative potential temperature gradients on the surface for stable and unstable conditions, as well as the capping inversion at the top of PBL at $z/z_i = 1.0$.

One of the most important features of the atmosphere is its turbulence kinetic energy that is the basis for mesoscale parameterizations of turbulence effects in the PBL,

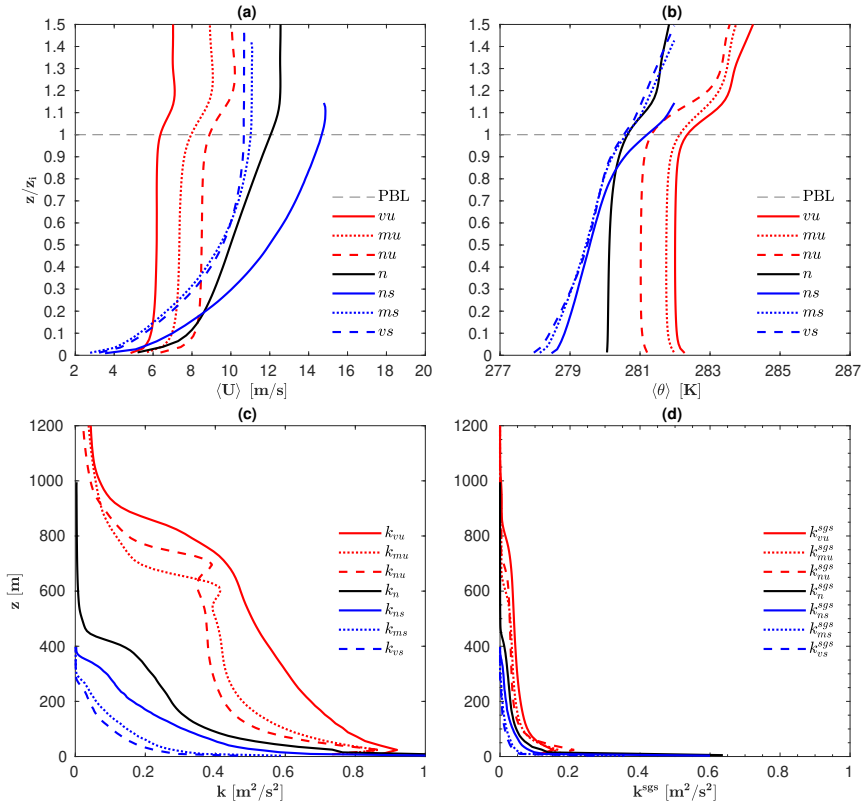

Figure 2.2: Vertical profiles of the time- and horizontal averaged wind speed (a), potential temperature (b), total TKE (c) and SGS TKE (d) for different atmospheric stabilities. Horizontal gray dashed lines show the PBL height. (Subscripts, vu: Very unstable, mu: Moderate unstable, nu: Near-neutral unstable, n: Near-neutral, ns: Near-neutral stable, ms: Moderate stable, vs: Very stable)

$$k = \frac{1}{2}\left\langle u_i' u_i' \right\rangle = \int_0^\infty E(\kappa)\, d\kappa \tag{2.27}$$

where k is the total turbulence kinetic energy and u_i' is the fluctuating velocity. Herein, $E(\kappa)$ denotes the energy spectrum in the wavenumber space, κ, and such that the integration of $E(\kappa)\, d\kappa$ along the wavenumber space also gives the total kinetic energy. In Fig. 2.2, the vertical variation of the total and SGS TKE are plotted for different stability conditions. It can be stated that the contribution of subgrid scales are negligible compared to resolved scales except

near the ground. Another observation is that the turbulence kinetic energy decays with the atmospheric stability, such that it is quite high because of the strong convective motions during the daytime. But it decays from the most unstable condition to neutral condition and towards the most stable condition. This is in fact the observation that gives an idea to model the turbulence length scale later on. By this way, TKE and its length scale can be linked similar to the modeling of MYNN scheme by Nakanishi and Niino (2009).

To ensure whether the spatial resolution is sufficient for well-resolved LES, the energy spectra is investigated on the basis that if it exhibits for a -5/3 cascade, i.e. $E(\kappa) \propto \kappa^{-5/3}$, within the inertial subrange in accordance with Kolmogorov -5/3 theory (Kolmogorov, 1941). Therefore, the one dimensional energy spectral density (or energy spectra) of resolved $\widetilde{u_1'u_1'}$, $\widetilde{u_2'u_2'}$, $\widetilde{u_3'u_3'}$ fluctuations are computed along the spanwise y-direction, i.e. $E_{ii}(\kappa_2)$ for $i = 1, 2, 3$. The energy spectra is averaged in the streamwise x-direction for all the x grid locations and then in time, similar to other LES studies, e.g. Muñoz-Esparza et al. (2014a). So that, in Fig. 2.3, the time- and streamwise averaged energy spectra along the spanwise wavenumber, i.e. κ_2, is presented for the very unstable, neutral and very stable conditions at two different vertical locations, i.e. $z/z_i = 0.05$ and $z/z_i = 0.80$. The energy spectra represents the spectral energy transfer from larger scales, i.e. low wavenumbers, to the dissipative smaller scales, i.e. high wavenumbers, via the energy cascading process. In Fig. 2.3, low wavenumbers correspond to the high-level spectral energy because of the turbulence kinetic energy production by larger scales while it decays steeply through the high wavenumbers due to the turbulence dissipation. In addition to this, all the LES computations exhibit the Kolmogorov spectral -5/3 slope within the inertial subrange which enables us to ensure the reliability of the LES. Besides that the averaged energy spectra is much higher at the altitude $z/z_i = 0.05$ than the altitude at $z/z_i = 0.80$ for all the conditions, this is because the fact that the turbulence kinetic energy is decaying towards the higher altitudes as depicted in Fig. 2.2. Energy spectral density is also effected by the effect of atmospheric stability, such that the spectra within the inertial subrange decreases from very unstable condition, i.e. $< \overline{E_{ii}} >_{z/z_i=0.05} \sim \mathcal{O}(10^1)$ and $< \overline{E_{ii}} >_{z/z_i=0.80} \sim \mathcal{O}(10^0)$, towards very stable condition, i.e. $< \overline{E_{ii}} >_{z/z_i=0.05} \sim \mathcal{O}(10^0)$ and $< \overline{E_{ii}} >_{z/z_i=0.80} \sim \mathcal{O}(10^{-1})$. And finally, the highest wavenumber increases from the very unstable condition, i.e. $\kappa_2 \sim 8e^{-2}$ to the very stable condition, i.e. $\kappa_2 \sim 5e^{-1}$, because of the fact

that we employ higher horizontal grid resolution for the stable atmosphere, i.e. $\Delta_{x,y}$ = 6.25 m, than the convective atmosphere, i.e. $\Delta_{x,y}$ = 40.0 m.

One of our main aims is to determine the length scale depending on the atmospheric stability to derive a new PBL scheme. The length scale can be obtained from the turbulence dissipation and TKE, employing according to Kolmogorov's hypothesis, by making use of the Eq. 2.4. Then, it becomes possible to determine the length scale, i.e. $l = k^{1.5}/(\epsilon\ B_1)$, by getting TKE and dissipation fields from our large-eddy simulations. Before this, we investigate the budget of total turbulence kinetic energy in order to see the relative importance of each term in this equation and to judge the effect of the atmospheric stability. To do this, as presented in the Appendix A, the one-dimensional total turbulence kinetic energy budget equation is derived as follows:

$$
\begin{aligned}
0 = \quad & \underbrace{-\langle\widetilde{w}\rangle \frac{\mathrm{d}\langle k\rangle}{\mathrm{d}z}}_{\mathcal{A}=0} \underbrace{-\frac{\mathrm{d}}{\mathrm{d}z}\langle kw'\rangle}_{T^T} \underbrace{-\frac{1}{\rho_0}\frac{\mathrm{d}}{\mathrm{d}z}\langle p'w'\rangle}_{T^P} \underbrace{-\frac{\mathrm{d}}{\mathrm{d}z}\left\langle \tau_{i3}^{D'}\widetilde{u_i'}\right\rangle}_{T^{sgs}} \\
& \underbrace{-\langle u'w'\rangle \frac{\mathrm{d}\langle\widetilde{u}\rangle}{\mathrm{d}z} - \langle v'w'\rangle \frac{\mathrm{d}\langle\widetilde{v}\rangle}{\mathrm{d}z}}_{P^S} + \underbrace{\frac{g}{\theta_0}\langle w'\theta'\rangle}_{P^B} + \underbrace{\left\langle \tau_{ij}^{D'} S_{ij}'\right\rangle}_{\epsilon}
\end{aligned}
\tag{2.28}
$$

where $\mathcal{A}$ denotes the advection, T^T, T^P, T^{sgs} denote the turbulence, pressure and SGS transport, respectively. P^S and P^B are the shear and buoyancy productions and ϵ stands for the dissipation. Note that, the advection term is negligible in Eq. 2.28 since the horizontally-averaged $\langle\widetilde{w}\rangle = 0$ as a consequence of the continuity equation. Since we aim to get the dissipation field for the determination of the length scale, we do not followed the modeled expression for the ϵ, which is based on Kolmogorov hypothesis in Eq. 2.4 and common in the literature, e.g. Sullivan and Patton (2011); Ramachandran and Wyngaard (2011); Kosović and Curry (2000). Instead, we determine as the double inner product of two second-rank tensors which are the fluctuating components of the deviatoric SGS stress tensor and the strain-rate tensor, $\epsilon =< \tau_{ij}^{D'} S_{ij}' >$.

Following the Eq. 2.28, the turbulence kinetic energy budget of very unstable, near neutral and very stable PBLs are presented in Fig. 2.4. It shows the relative contribution to the total turbulence kinetic energy term by term along the vertical direction. The positive and negative values of the

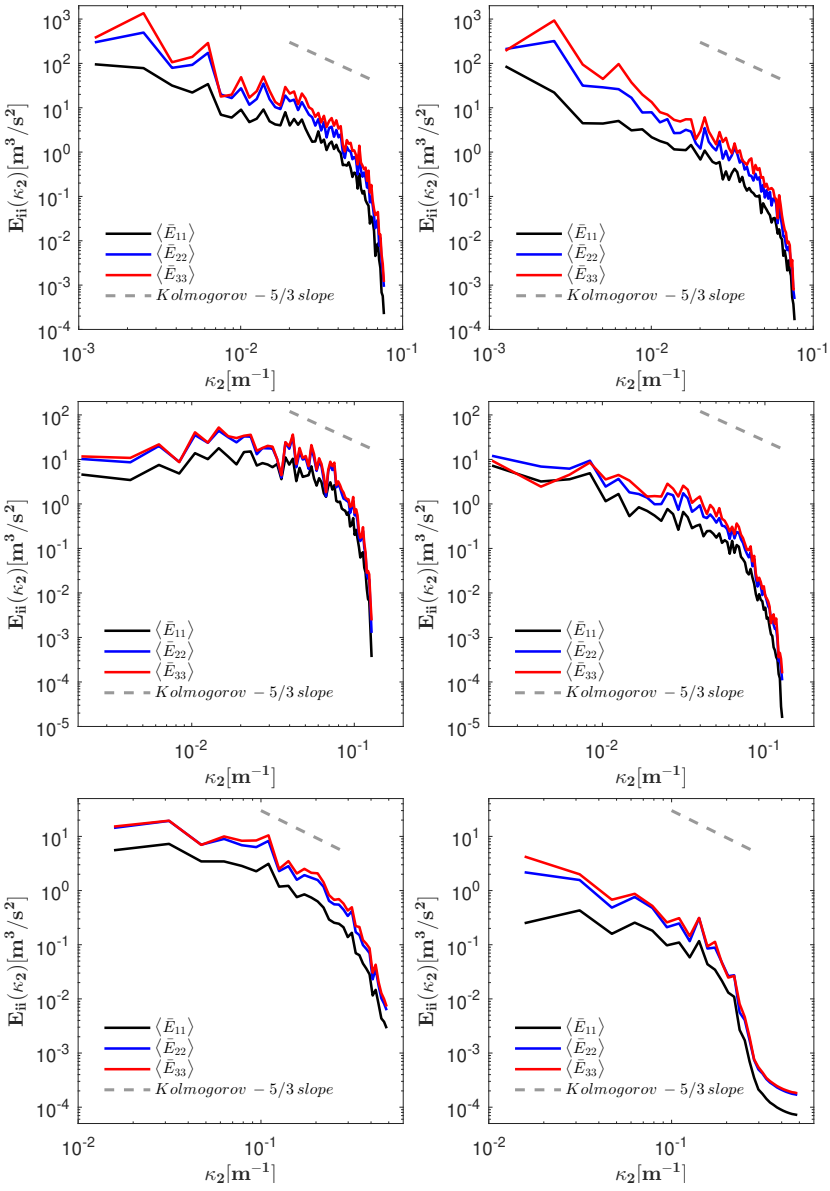

Figure 2.3: Time- and streamwise averaged energy spectra vs. spanwise wavenumber, κ_2, for very unstable (top), near neutral (middle) and very stable (bottom) conditions at two different altitudes, i.e. $z/z_i = 0.05$ and $z/z_i = 0.80$. Black, blue and red solid lines denote the averaged energy spectra of resolved $\widetilde{u_1'u_1'}$, $\widetilde{u_2'u_2'}$, $\widetilde{u_3'u_3'}$ fluctuations respectively. Gray dashed line denote the theoretical Kolmogorov -5/3 slope.

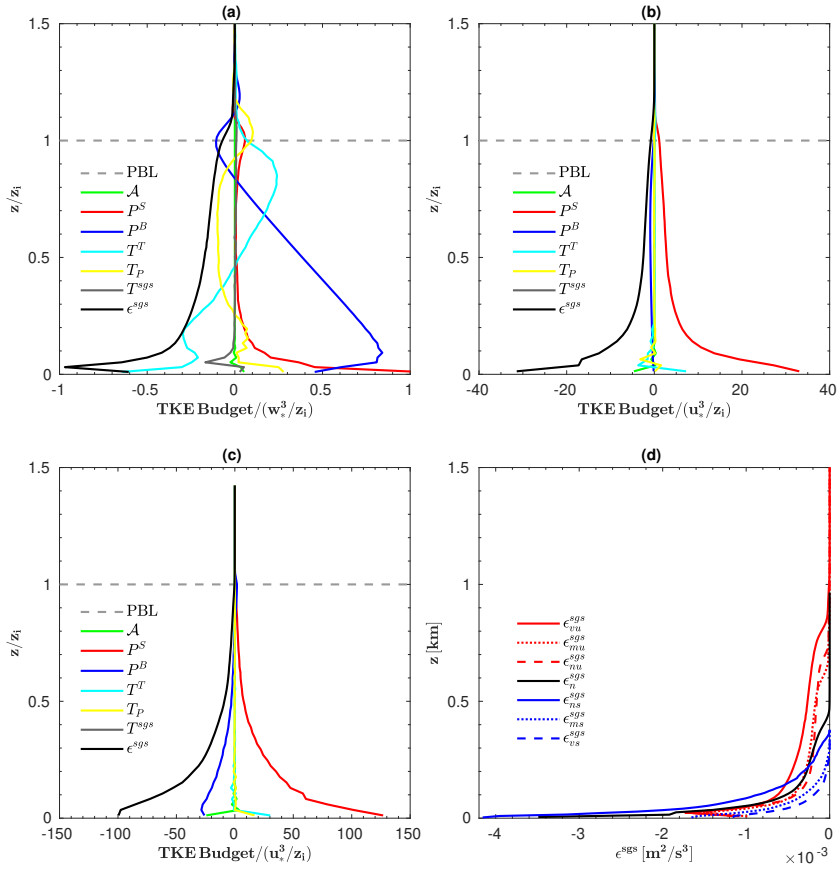

Figure 2.4: TKE budgets of very unstable (a), near neutral (b) and very stable (c) PBLs. Positive & negative signs of the budget denote TKE production & destruction. Horizontal gray dashed lines show the PBL height. Vertical profile of the dissipation (d) is given for unstable (red), near neutral (black) and stable (blue) conditions respectively.

turbulence kinetic energy budget indicate if the turbulence kinetic energy is produced or destructed respectively. Fig. 2.4 reveals that the the transport terms seem to be less important than the production and dissipation terms. Its effect is only evident in case of the convective condition. This is due to the transport of strong updraughts and downdraughts different from the neutral and stable conditions. And the integral of the transport term over the altitude goes to ~ 0 consistently with the earlier studies and the overall behaviour of both pressure and turbulent transport terms are in well agreement with the

LES results of Moeng and Sullivan (1994) for the convective and neutral PBL and Jiménez and Cuxart (2005) for the stable PBL. The main contribution to the turbulence kinetic energy arises from the existence of production and dissipation terms. Regarding the production term, the buoyancy production is the most sensitive term to the atmospheric stability. To illustrate, it becomes positive because of the upward buoyancy in convective conditions. It makes a first peak around $z/z_i = 0.1$ and decreases until the PBL height, $z/z_i = 1.0$, where it makes the second peak which is relatively small and negative because of the existence of stably stratified capping inversion. This feature of the buoyancy production is a well-known feature of the unstable atmosphere (Moeng and Sullivan, 1994; Catalano and Moeng, 2010). Under the convective condition, the buoyancy production dominates the total turbulence kinetic energy variation compared to the shear production that is only evident close to the ground due to the existence of wind shear, however it disappears above the surface layer, i.e. $z/z_i = 0.1$. After the sunset, convective motions dramatically weaken and the stable atmosphere take places. The buoyancy production is no longer a turbulence kinetic energy production in this condition and it pretends to be weakly destructive as can be seen in Fig. 2.4. If we look at the neutral atmosphere, there is neither a buoyancy production nor a buoyancy destruction, instead it is characterized by the high shear production due to the existence of strong wind shear. Besides the final observation is that the dissipation, ϵ, behaves as the most dominant source for the destruction of turbulence kinetic energy.

Fig. 2.4 also includes the vertical profile of the dissipation up to 1.5 km for all the stability classes. The dissipation takes its highest value close to the Earth's surface, then it goes down with the altitude since the dissipation mainly arises close to the ground where the mechanical energy transforms into the thermal energy produced by the smallest scales. Regarding the effect of the atmospheric stability, the dissipation decreases from unstable condition to neutral and stable conditions above the surface layer, however near the ground, this tendency become reversed. The main finding about the dissipation variation is that it decreases with the atmospheric stability. For the unstable atmosphere, the dissipation becomes less from very unstable to near unstable condition. For the stable atmosphere, similar to the observation of Huang and Bou-Zeid (2013), an increase in stability leads to a lower dissipation value.

Finally, the results of the proposed length scale model are depicted in

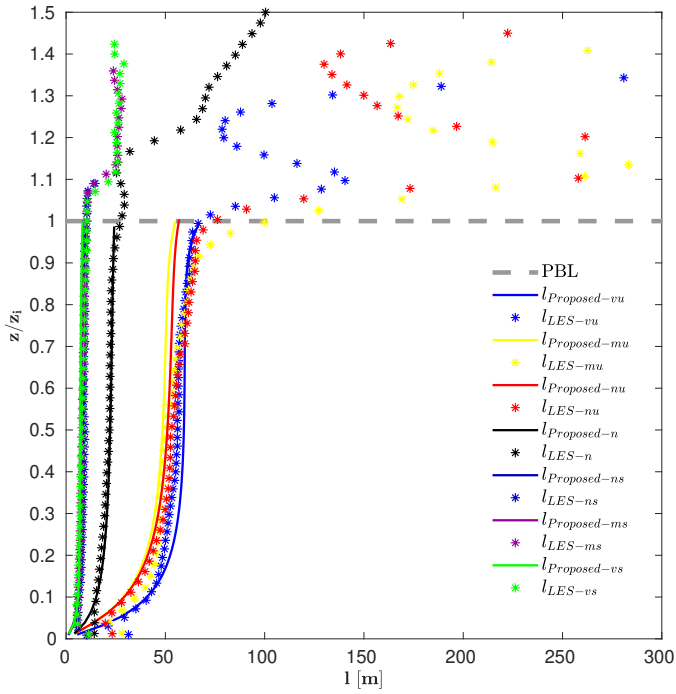

Figure 2.5: Vertical profiles of the proposed mixing length scale compared to LES results. Solid lines refer to the proposed model and circular markers refer to LES results. The gray dashed lines refer to the PBL height.

Fig. 2.5 in comparison to the Høvsøre LES results. The proposed length scale matches excelently with LES results from $0.02z_i$ until $0.90z_i$ for all the stability conditions. However, outside of which, a deviation initiates particularly for the convective PBL. This is because our model does not presently account for the entrainment and inversion effects that exist between the upper PBL and free atmosphere, in which high model resolutions are required to resolve particular physics of the entrainment processes including temperature inversion, intermittent turbulence and internal gravity waves. Therefore, for the altitudes higher than $0.90z_i$, the mixing length scale is determined based on the MYJ scheme Janjić (1994), as follows

$$l = 0.23\Delta z \tag{2.29}$$

where Δz corresponds to the vertical grid spacing. Note that the departures within the first few meters ($0.02z_i$) needs particular attention in terms of subgrid scale modeling.

2.2.3 Idealized PBL Simulations

In this section, we present the results of idealized PBL simulations in comparison to LES results, which are presented in Sec. 2.2.2. The idealized PBL simulations are performed by using an open-source numerical weather prediction code, i.e. the Weather Research and Forecasting (WRF) model version 3.5.1 (Skamarock et al., 2008a). The model forcing is conducted by imposing the surface heat fluxes presented in Tab.2.1. However, the momentum flux is calculated by using a surface layer scheme, MM5 similarity scheme (Beljaars, 1995). In this section, we make use of LES results to verify our proposed model. The concept of using high-fidelity simulations, such as LES, as a verification tool for PBL parameterization schemes, has been widely applied in the literature when a novel turbulence closure is initially designed (Bretherton and Park, 2009; Nakanishi and Niino, 2009; Efstathiou and Beare, 2015). Even if the LES and mesoscale models used for this comparison are different, a recent LES intercomparison study by Mirocha et al. (2017) has shown that both dynamical cores (SOWFA and WRF) provide comparable results in canonical ABL simulations. As described in Sec. 2.2.1, it is possible to state that our proposed PBL scheme has some similarities both with MYNN and BouLac schemes. The mixing length scale parameterization is based on three components as it is in case of MYNN scheme and the closure coefficient to determine turbulent viscosity is constant similar to the BouLac scheme. Therefore, idealized PBL simulations are also performed by using MYNN (Nakanishi and Niino, 2009) and BouLac schemes (Bougeault and Lacarrere, 1989b), enabling us to evaluate the performance of our model against these two state-of-the-art PBL schemes. As far as the computational details are concerned, the horizontal domain size is set to $L_{x,y} = 15km\ x\ 15km$ for unstable PBL, $L_{x,y} = 9km\ x\ 9km$ for neutral PBL, $L_{x,y} = 4km\ x\ 4km$ for stable PBL. The horizontal grid resolution is taken to be $1km$ in order to avoid passing the gray-zone. It is worth noting that the horizontal length of the mesoscale domain does not affect the results of idealized PBL simulations due to the idealized conditions. The vertical height is set to $2km$ where 80 grid points are

$MAE_{\langle\theta\rangle}$ $[K]$	*vu*	*mu*	*nu*	*n*	*ns*	*ms*	*vs*
VKI01	0.076	0.055	0.077	0.142	0.320	0.318	0.362
MYNN	0.117	0.089	0.105	0.190	0.377	0.294	0.309
BouLac	0.034	0.134	0.063	0.595	0.689	0.569	0.586
$MAE_{\langle U\rangle}$ $[m/s]$	*vu*	*mu*	*nu*	*n*	*ns*	*ms*	*vs*
VKI01	0.261	0.462	0.437	0.770	1.750	1.447	1.730
MYNN	0.445	0.754	0.727	1.695	1.212	1.695	1.223
BouLac	0.471	0.849	0.932	1.626	2.716	2.417	2.421

Table 2.4: Mean absolute errors of three PBL schemes compared to the Høvsøre LES results in terms of horizontally-averaged potential temperature and wind speed where $z \leq z_{i,LES}$. Bold values denote the best performance as the lowest MAE among the three PBL schemes.

located along this direction, by clustering near the ground. Time integration is conducted setting time step to $\Delta t = 5s$. The total simulation time is same as our LES computations, i.e. $\mathcal{T} = 23400s$ for unstable condition and $\mathcal{T} = 24000s$ for neutral and stable conditions. Note that, periodic boundary conditions are applied to lateral boundaries and the Coriolis force is accounted consistently with our Høvsøre LES database.

As noted before, the idealized PBL simulations are performed for the same stability conditions presented in Tab.2.3. Compared to the LES results, vertical profiles of horizontally-averaged potential temperature and wind speed, predicted by VKI01, MYNN and BouLac schemes, are presented in Fig. 2.6 and Fig. 2.7. As presented in Fig. 2.6, within the mixed layer of unstable PBLs, VKI01 and BouLac provide better predictions than the MYNN scheme. However, within the surface layer, potential temperature gradient is overestimated by VKI01 scheme compared to both schemes. Considering the mixed layer characteristics, VKI01 presents the best agreement in moderately unstable PBL where BouLac significantly overestimates the potential temperature. However, BouLac is slightly better than VKI01 for very and near-neutral unstable conditions. MYNN scheme underestimates the potential temperature in the mixed layer where it underestimates the potential temperature. In Tab.2.4, this behaviour is quantified with a performance metric, i.e. mean absolute error (MAE), against to the Høvsøre LES results. VKI01 produces the lowest error of potential temperature for moderately-unstable PBL, while BouLac is the best in case of very and near-unstable PBLs. For the stable PBL, although VKI01 and MYNN schemes perform very similarly, VKI01 stands slightly better than MYNN below the PBL

height except for near the ground. While VKI01 improves near-neutral stable PBL with the lowest MAE, MYNN is slightly better than VKI01 for moderately stable and very stable PBLs. For the BouLac scheme, it significantly overestimates the potential temperature all along the stable boundary layer. Note that, none of the PBL schemes is able to predict correctly the capping inversion, showing the intrinsic limitations of these PBL schemes for stably stratified boundary layer. Regarding the near-neutral condition, VKI01 performs superior than other two PBL schemes considering its mixing layer and PBL top behaviour. Its MAE is equal to 0.142 which is much lower than that of MYNN and BouLac schemes. The latter fails predicting correctly the potential temperature both below and above the PBL for the neutral conditions (Fig. 2.6-g). Along with the potential temperature profiles, predicted wind speed profiles for three PBL schemes in comparison to LES results are also given in Fig. 2.7. For all the stability levels, BouLac scheme fails to represent a good agreement with LES results. However, although VKI01 scheme overestimates the potential temperature gradient near the ground for convective cases, it provides better estimation for the wind speed compared to the MYNN scheme. VKI01 performs better also through the convective mixed-layer. Quantitatively, VKI01 gives the lowest mean absolute errors for all the stability levels except for near-neutral and very stable PBLs where MYNN improves the wind speed slightly better than VKI01.

2.2.4 Application to the XPIA field campaign

In the previous section, the proposed model is verified with the LES results to some degree that despite its simpler closure coefficient formulation, the new PBL scheme is able to provide similar predictions to MYNN scheme, which solves a set of algebraic equations to determine the closure coefficients. However, the validity of the newly proposed PBL scheme for a real-case study should also be tested based on a full-scale field campaign. In this section, we present the mesoscale simulations for the eXperimental Planetary boundary layer Instrumentation Assessment (XPIA) campaign (40.05°N, 105°W) conducted at the Boulder Atmospheric Observatory (BAO) from March 2^{nd} to May 31^{st} in 2015 (Lundquist et al., 2017). The BAO tower contains a total of 12 three-dimensional sonic anemometers (Campbell CSAT3) mounted on northwesterly (NW, 334°) and southeasterly (SE, 154°) pointing

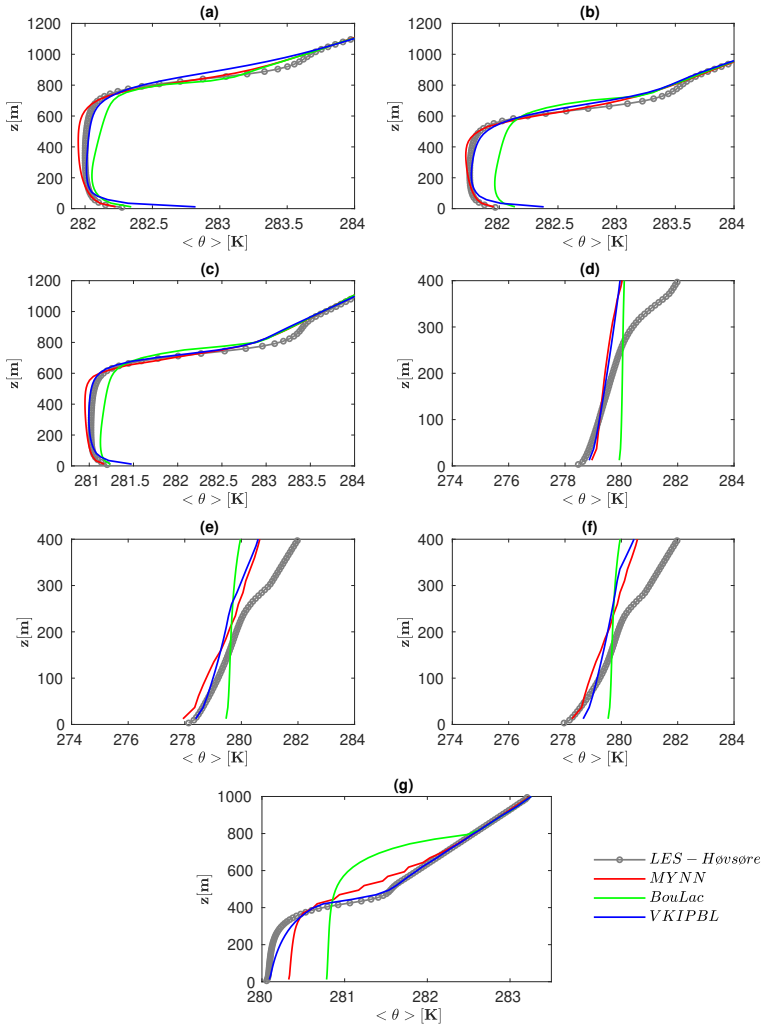

Figure 2.6: Horizontally-averaged potential temperature predictions. Gray line with circle markers denotes Høvsøre LES results. Red, blue and green lines show the MYNN, BouLac and VKI01 (VKIPBL) schemes. Panels refer to very unstable (a), moderately unstable (b), near-neutral unstable (c) near-neutral stable (d), moderately stable (e), very stable (f) and near-neutral (g) conditions from left to right.

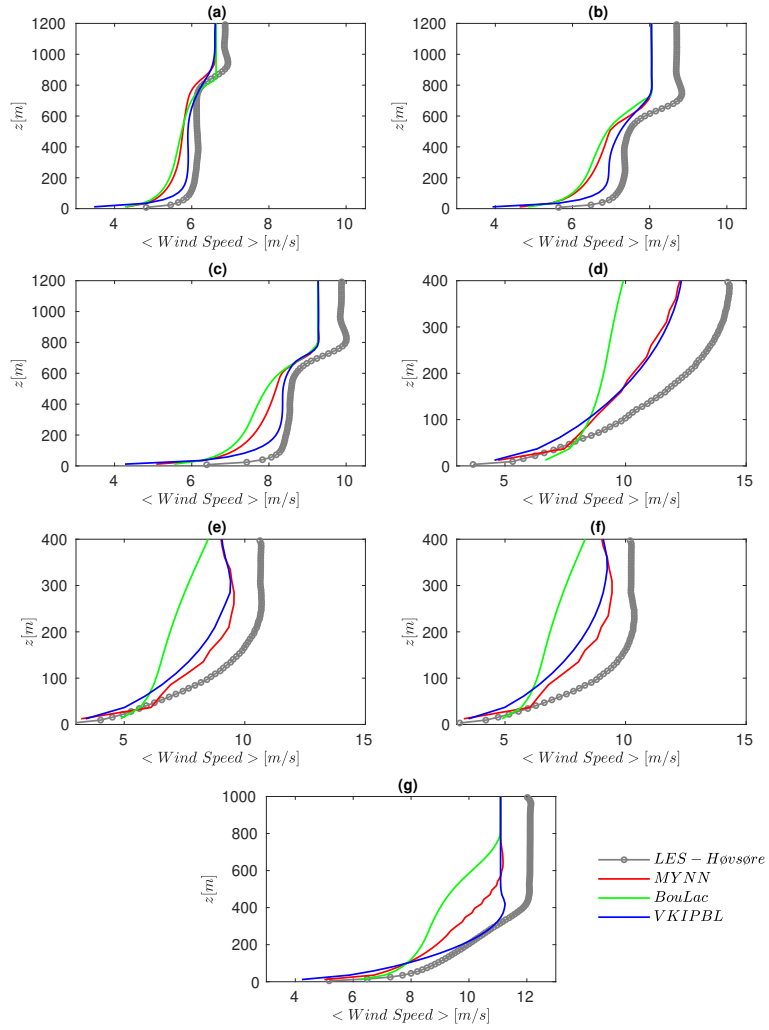

Figure 2.7: Horizontally-averaged wind speed predictions. Gray line with circle markers denotes Høvsøre LES results. Red, blue and green lines show the MYNN, BouLac and VKI01 (VKIPBL) schemes respectively. Panels refer to very unstable (a), moderately unstable (b), near-neutral unstable (c) near-neutral stable (d), moderately stable (e), very stable (f) and near-neutral (g) conditions from left to right.

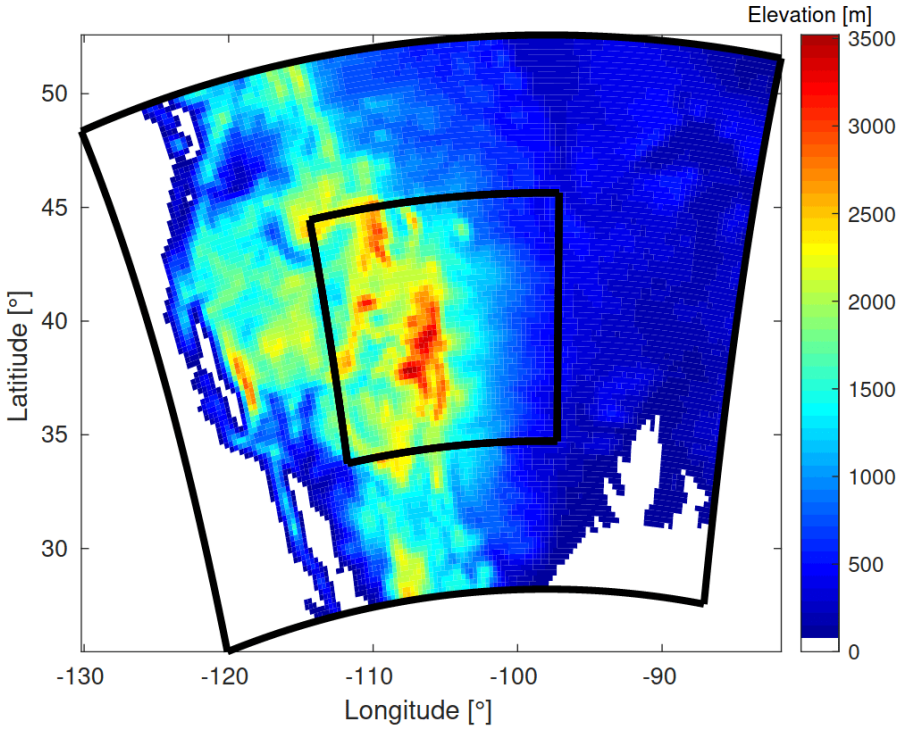

Figure 2.8: WRF domain for the mesoscale simulation with the terrain elevation [m] where it is located at the Boulder Atmospheric Observatory (BAO) in Colorado (40.05°N, 105°W). The outer black line encircles the outer zone with the resolution 27 km where the inner region demonstrates the inner zone with 9 km resolution.

booms every 50 m starting from 50 m above ground level up to 300 m, as well as temperature/relative humidity sensors. This experimental campaign involves high-frequency 20-Hz measurements of wind, temperature and relative humidity. Recently, Muñoz-Esparza et al. (2018) derived the turbulence dissipation rate, ϵ, within the planetary boundary layer using these mast measurements. These results are available at z = 50 m and they are classified into daytime/convective and nighttime/stable conditions.

These measurements will help us to validate mesoscale simulations, performed by the new PBL scheme and again compare with MYNN and BouLac schemes. The mesoscale domain depicted in Fig. 2.8 consists of two one-way nested domains, the largest domain has a horizontal resolution of 27 km with a domain size of 3375 x 2700 km^2. The smallest domain, on

the other hand, has a horizontal resolution of 9 km with a domain size of 1332 x 1197 km^2. For the vertical discretization, 53 grid points are used with the finest resolution of 2.5 m close to the ground, while the upper boundary is located at 15 km. Boundary and initial conditions are extracted from the National Centre of Environmental Prediction (NCEP) North American Regional Reanalysis (NARR) datasets. For the PBL parameterization, BouLac, MYNN and VKI01 schemes are used. In addition to the PBL schemes, the other physical parameterizations utilized for the WRF set-up are the longwave and shortwave Rapid Radiative Transfer Model (RRTM) (Iacono et al., 2008) for the radiation, the Thompson microphysics parameterization (Thompson et al., 2008), MM5 Similarity Scheme (Beljaars, 1995) for the surface layer parameterization and the Community Land Model version 4 (Lawrence et al., 2011) for the land surface coupling.

Nested mesoscale simulations are performed during the 6^{th}-9^{th} of March in 2015 at the XPIA field campaign for 72 hours, but the first 24 hours is discarded considering the model spin-up so that the results are presented between the 7^{th}-9^{th} of March. In Fig. 2.9, mesoscale simulations are compared against to mast measurements at $z = 50$ m. Fig. 2.9-a and Fig. 2.9-b present the time evolution of the turbulence kinetic energy and dissipation rate respectively. Compared to the MYNN and BouLac schemes, VKI01 matches well with the XPIA measurements presenting the best agreement where it is able to reproduce the diurnal evolution of the boundary layer. Both MYNN and BouLac significantly underestimate the turbulence kinetic energy and dissipation rate profiles during the first ($t = 7.0 - 7.5$ day) and second ($t = 8.0 - 8.5$ day) nighttime. Such that, VKI01 and XPIA profiles are $\sim \mathcal{O}(10^{-2})$ for turbulence kinetic energy and $\sim \mathcal{O}(10^{-4})$ for the dissipation rate. However, TKE for MYNN and BouLac are $\sim \mathcal{O}(10^{-3})$ and $\sim \mathcal{O}(10^{-4})$ where dissipation rate for MYNN and BouLac are $\sim \mathcal{O}(10^{-5})$ and $\sim \mathcal{O}(10^{-7})$, respectively. Although MYNN and BouLac schemes predict the TKE better during the daytime, VKI01 is much better for the dissipation rate in case of convective conditions. In Tab.2.5, in order to evaluate the performance of simulated PBL schemes, mean absolute errors (MAE) for TKE, its dissipation rate, temperature and wind speed are presented against to XPIA measurements from Muñoz-Esparza et al. (2018). VKI01 reproduces the dissipation rate better by reducing MAE compared to MYNN and BouLac schemes. However for the MAE of k, MYNN scheme produces slightly lower error than both PBL

PBL scheme	$RMSLE_k$ $[m^2/s^2]$	$RMSLE_\epsilon$ $[m^2/s^3]$	MAE_T $[^\circ C]$	MAE_U $[m/s]$	MAE_{WD} $[^\circ]$
VKI01	$0.5\ 10^{-1}$	$0.6\ 10^{-1}$	1.83	2.24	81.3
MYNN	$1.3\ 10^{-1}$	$1.1\ 10^{-1}$	1.20	1.90	84.6
BouLac	$1.4\ 10^{-1}$	$1.7\ 10^{-1}$	1.04	1.14	80.0

Table 2.5: Mean absolute errors of TKE, its dissipation rate, temperature wind speed and wind direction obtained by three PBL schemes in comparison to XPIA measurements at $z = 50m$ from Muñoz-Esparza et al. (2018). Bold values denote the best performance as the lowest error among the three PBL schemes.

schemes. On the other hand, Fig. 2.9-c and Fig. 2.9-d show the time evolution of wind speed and temperature at $z = 50$ m for three PBL schemes. Even though the wind speed profiles are able to capture the general behaviour of the diurnal pattern at the XPIA campaign, all the PBL schemes, particularly VKI01, overpredict the wind speed during nighttime conditions. While they underestimate it during the daytime condition (i.e. $t = 7.7 - 8.2$ day). But in general, BouLac scheme predicts the wind speed much better. In Fig. 2.9-d, the time evolution of the temperature acquired by three PBL schemes are depicted. It can be stated that all the PBL schemes are in good agreement except for the first night time till the first morning transition, i.e. $t = 7.0 - 7.5$ day. Eventually, if the mean absolute errors are concerned BouLac scheme improves both wind speed and temperature resulting in the lowest errors as $MAE_U = 1.14\ m/s$ and $MAE_T = 1.04\ ^\circ C$ respectively.

In Fig. 2.10, the time variation of the wind direction and vertical velocity are depicted compared to the mast measurements at $z = 50$ m. Unlike the wind speed trend, VKI01 matches well with the XPIA measurements along the whole period except for the peak around t=7.8day. Moreover, both stable and convective conditions as well as the morning/evening transitions in terms of the wind direction are well represented compared to the sonic measurements. On the other hand, MYNN scheme causes large biases for the wind direction at the first nighttime and around the first noon as well as during the morning and evening transitions. Even these biases appear similarly for the BouLac scheme, during the first nighttime and the morning/evening transitions, its overall performance in terms of MAE is slightly better than VKI01 (Tab.5). In addition to these, all the PBL schemes are able to reproduce the wind direction during the second morning transition. Fig. 2.10-d indicates the time evolution of the vertical wind component at $z = 50$ m. This result shows that all the

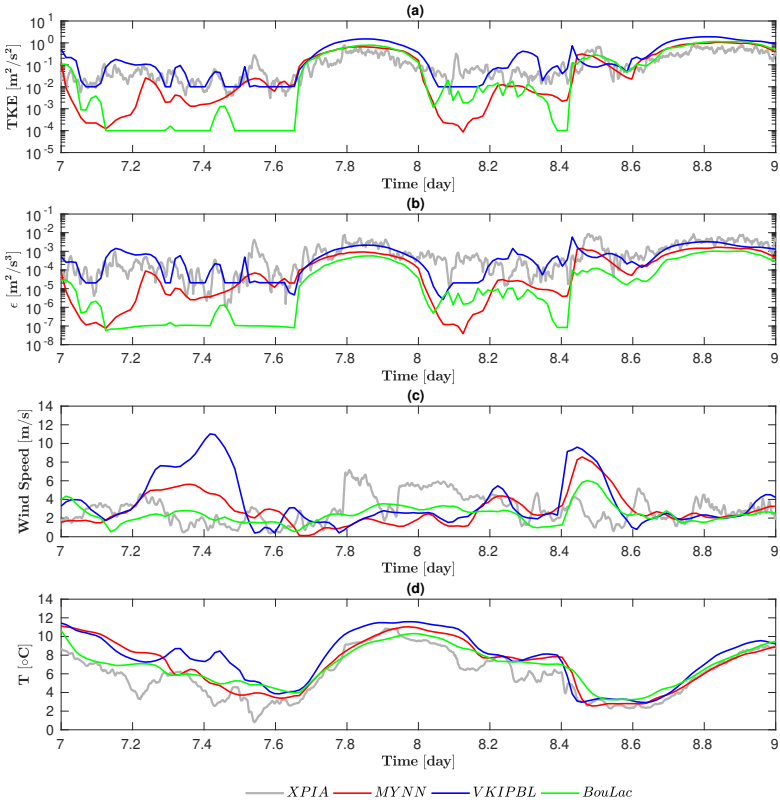

Figure 2.9: Time evolution of the turbulence kinetic energy, k, (top-left), dissipation rate, ϵ, (top-right), wind speed (bottom-left) and temperature (bottom-right) profiles at $z = 50\ m$ obtained from the VKI01 (VKIPBL) (blue line), MYNN (red line), BouLac (green line) schemes. Gray solid line denotes the mast measurements during March 7^{th}–9^{th} in 2015 at the XPIA field campaign from Muñoz-Esparza et al. (2018).

simulated PBL schemes agree each other, however, the measured vertical speed in the XPIA campaign is much higher than these predicted results.

Fig. 2.11 compares three PBL schemes to get more insights into their PBL characteristics. Fig. 2.11-a presents the time evolution of friction velocity at the surface. Despite the general agreement among the three PBL schemes, there are some unrealistic trends for the friction velocity. To illustrate, MYNN scheme continuously oscillates on an hourly basis for the whole period, and it approaches to zero during morning/evening transitions. During the second

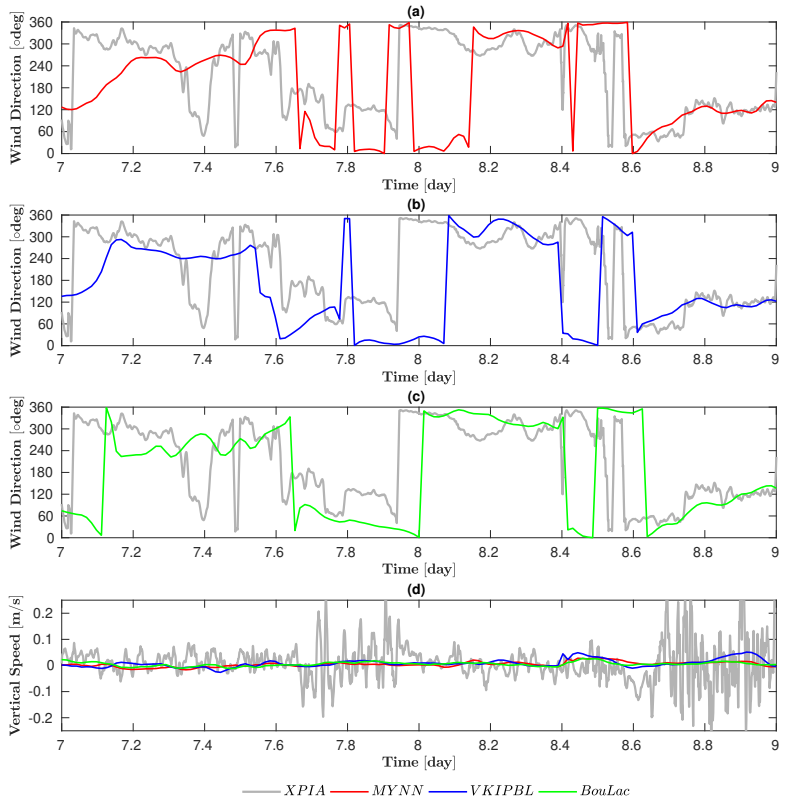

Figure 2.10: Time evolution of wind direction (top-left, top-right, bottom-left) and vertical speed (bottom-right) profiles at $z = 50$ m obtained from the VKI01 (VKIPBL) (blue line), MYNN (red line), BouLac (green line) schemes. Gray solid line denotes the mast measurements during March 7^{th}-9^{th} in 2015 at the XPIA field campaign from Muñoz-Esparza et al. (2018).

nighttime, both MYNN and BouLac makes a peak where this peak also exists in the wind speed profile, as can be seen in Fig. 2.9-c. Considering the overall behaviour of u_*, the evolution of VKI01 take places falling in the between MYNN and BouLac schemes. Fig. 2.11-b shows the PBL height variation where there is an agreement during the stable conditions. However, for the first nighttime, MYNN makes three instantaneous peaks until $z_i = 1000$ m that becomes unrealistic for the stable atmosphere. Another observation can be stated regarding the value of PBL height during the convective condition.

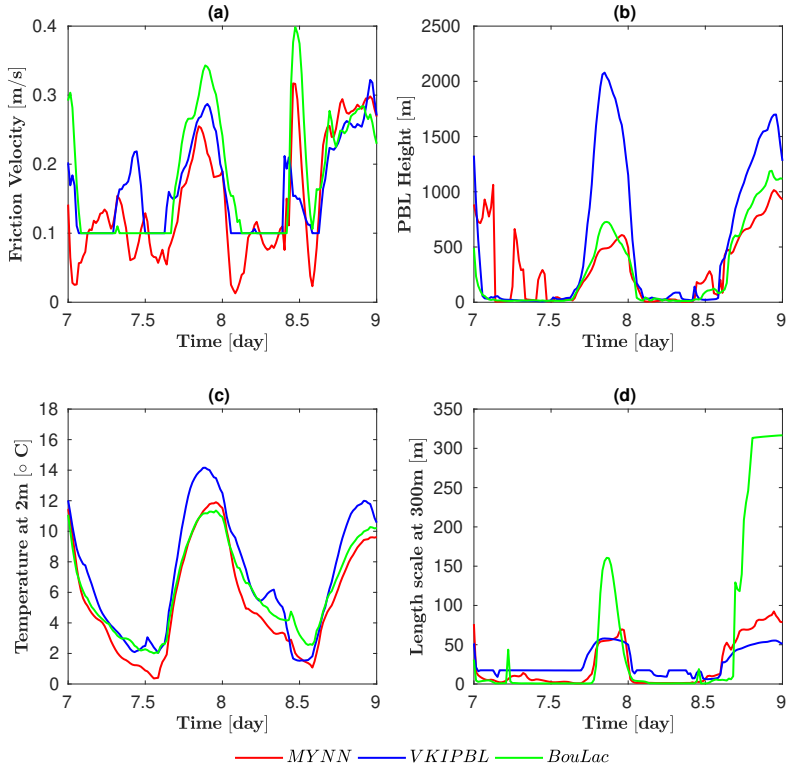

Figure 2.11: Time evolution of the friction velocity (top-left), PBL height (top-right), temperature at 2m (bottom-left) and mixing length scale at 300m (bottom-right) profiles obtained from the VKI01 (VKIPBL) (blue line), MYNN (red line), BouLac (green line) schemes.

Even the results of MYNN and BouLac are consistent at the first daytime as $z_i \sim 700$ m, VKI01 reaches to such a relatively higher altitude as of $z_i \sim 2000$ m. However these high difference disappears during the second daytime. In Fig. 2.11-c, time variation of the temperature at $z = 2$ m is demonstrated. Similar to the temperature profiles at $z = 50$ m, as shown in Fig. 2.9-d, the results acquired by PBL schemes at $z = 2$, more generally, are in good agreement between each other. Eventually, the final result is depicted in Fig. 2.11-d, which is the time evolution of the mixing length scale at $z = 300$ m. VKI01 matches generally well with the MYNN scheme in comparison to the BouLac scheme. Furthermore, the average value of the l is around 10 m for the stable condition while it rises to 50 m for the convective condition. These

values are in consistency with that obtained from the Høvsøre LES results, as can be seen in Fig. 2.5. Accordingly, it can be argued that the developed PBL scheme produces notably realistic mixing length scale profiles depending on the atmospheric stability getting more confidence to the ability of the proposed scheme. On the other hand, MYNN and BouLac models converge to the zero during the stable condition, which stands for quite unrealistic. Another unrealistic observation is that the BouLac model gives an high value of length scale corresponding to the 4 times of the VKI01 and MYNN schemes.

2.3 Discussion and conclusions

In the present study, we presented a new PBL scheme, VKI01. Our proposed scheme incorporates with a new formulation for the mixing length scale, which has been applied to idealized and real test cases, and benchmarked against two state-of-the-art PBL schemes (MYNN and BouLac PBL schemes).

For idealized cases, mesoscale simulations with a horizontal grid resolution, $\Delta_{meso} = 1\ km$, have been performed for three PBL schemes in the WRF framework. Results have been compared against reference large-eddy simulations performed over the Høvsøre test site in Denmark (Gryning et al., 2007). To account for the effect of atmospheric stability over a significant range, seven different stability levels have been employed from very-unstable regime through the very-stable regime based on the classification of Gryning et al. (2007). Considering the results of idealized mesoscale simulations, the proposed scheme performs overal better in terms of predicting horizontally-averaged wind speed and potential temperature profiles. For the convective atmosphere, VKI01 gives better predictions along the convective-mixed layer. However it overestimates the potential temperature inside the surface layer where the MYNN and BouLac schemes are tends to be better. On the other hand, for the wind speed predictions, VKI01 is superior for all the stability levels except for near-neutral stable (ns) and very stable (vs) PBLs where MYNN acts to be slightly better (Tab.2.4).

Regarding the real-case test, one-way nested mesoscale simulations with the horizontal grid resolutions of 27 km and 9 km have been performed for the eXperimental Planetary boundary layer Instrumentation Assessment (XPIA) campaign at the Boulder Atmospheric Observatory (BAO) in 2015. To evaluate the skill of the proposed PBL scheme in a real application, its performance

have been compared against to the mast measurements at the altitude of $z = 50$ m during 7^{th}-9^{th} of March. Our proposed scheme appears to exhibit improved skill in predicting turbulence kinetic energy and its dissipation rate except for the overestimation of turbulence kinetic energy during convective conditions. If the mean absolute errors are concerned, VKI01 produces the lowest error of ϵ whereas that of k is slightly higher than both schemes due to the overprediction in the convective regime. However, statistically robust analysis needs to be performed to further confirm this interpretation. In addition to k and ϵ, time evolution of wind speed and temperature profiles have been investigated. All the performed PBL schemes are able to reproduce the general behavior of XPIA measurements for the temperature while some large biases have been observed for the wind speed. However, MYNN and BouLac schemes bring an advantage over VKI01 estimating them better. To illustrate, BouLac scheme improves both wind speed and temperature resulting in the lowest errors. Unlike the wind speed and temperature profiles, in case the evolution of wind direction is concerned, VKI01 has a good agreement with the XPIA data together with BouLac scheme. Regarding the general PBL characteristics, all the PBL schemes fail to predict the PBL height during the stable conditions. Because the predicted z_i is around $\approx 10m$ for all the schemes. This is due to the failure in the algorithm that predicts the z_i. We believe that the way of the calculation for the PBL height needs to be a further investigation as a future study. Nevertheless, MYNN scheme makes three instantaneous peaks until $z_i = 1000$ m that stands unrealistic for the stable condition. For the convective convective, MYNN and BouLac are consistent with each other having $z_i \sim 700$ m at the first daytime while VKI01 rising to such a relatively higher altitude as of $z_i \sim 2000$ m. This high difference in terms of the PBL height disappears during the second daytime. Besides the trend of PBL height, time evolution of the mixing length scale at $z = 300$ m reveals that the VKI01 agrees well with the MYNN scheme in general. It can also be stated that the developed VKI01 PBL scheme leads to a realistic mixing length scale profiles depending on the atmospheric stability, providing more confidence with regards to the proposed scheme. This is because, MYNN and BouLac models unrealistically converge to the zero during the stable conditions. As well as the BouLac schemes results in a quite-high length scale values, corresponding to the 4 times of the VKI01 and MYNN schemes. In this context, even if the proposed PBL scheme performs well in predicting k

and ϵ except for the slight overestimation during daytime, the BouLac scheme seems better in terms of wind speed and potential temperature estimations. One reason may be the use of an existing parameterization, i.e. MYJ scheme, above $z/z_i > 0.9$ (see Eq. 2.29), while presently the proposed mixing length scale does not take into account the interaction between the upper PBL and the free atmosphere. The second reason for this mismatch might be caused by the parameterization of the non-local term given in Eq. 2.24 which is based on Therry and Lacarrère (1983). Moreover, another possibility for the mismatch between the observations and the predicted results might be resulted from either the definition of the PBL height or the physical parameterizations used by WRF, such as the microphysics, surface layer and land-surface coupling schemes. All these possibilities will be investigated in detail as a future study.

As a result, considering both idealized and real-case tests, the developed PBL scheme gives promising predictions despite some mentioned exceptions. Even though, it is possible to state that our objective has not been to propose an ultimately improved PBL scheme, but to develop a new formulation that can be considered as a baseline for further studies to develop a three-dimensional PBL scheme. Our proposed PBL scheme is based on the use of constant closure coefficients to determine eddy diffusivities, as opposed to the MYNN scheme. In this way, our proposed formulation stands as a baseline for a more straightforward extension to a three-dimensional PBL parameterization. However, it must be noted that the development of a three-dimensional parameterization will require further LES studies in order to quantify the contribution of horizontal turbulent fluxes in both horizontally-homogeneous PBLs as well as flow over complex terrain, including various stability conditions. Finally, these idealized PBL simulations are performed in order to verify the implementation of our new PBL scheme. And, as expected, our model performs mostly better than the other schemes thanks to the fact that its mixing length definition is derived from the LES dataset given in Sec. 2.2.2, which is also used to be compared. Therefore, the present results do not discard the applicability of the other PBL schemes. In order to perform a quantitative realistic inter-comparison study of various PBL schemes, long-term mesoscale simulations must be performed and compared with near-surface meteorological observations (Hu et al., 2010), which is beyond the scope of the present study.

Chapter 3

From large-eddy simulations to a new 1D PBL model for Mars[1]

3.1 Introduction

The Martian planetary boundary layer is one of the most important components of the Martian climate. Turbulent motions in the lowest kilometers of the Martian atmosphere affect the amount of the dust lifted from the ground (Spiga and Lewis, 2010; Toigo et al., 2003), and the changes in the atmospheric dust content lead to sol-to-sol, seasonal and inter-annual changes in the atmosphere of Mars (Montabone et al., 2015). It shares significant similarities with the planetary boundary layer of the Earth, including the formation of low-level jets (Joshi et al., 1997), convective clouds (Colaprete et al., 2003) and dust devils (Fenton and Lorenz, 2015). Mars, having a thinner atmosphere compared to Earth exhibits stronger diurnal variations in its atmospheric boundary layer. The thinner atmosphere also causes a stronger radiative heat forcing; as such, the Martian planetary boundary height can rise to upwards of 4 km based on large eddy simulations (LES) (Sorbjan, 2007; Gheynani and Taylor, 2010), 5-6 km from mesoscale simulations and even up to 10 km based on radio occulation measurements (Hinson et al., 2008). Investigations on the heights of dust devils, which can be considered as an

[1]This chapter is written based on the published article: Temel, O., Senel, C. B., Porchetta, S., Muñoz-Esparza, D., Mischna, M. A., Van Hoolst, T., van Beeck, J. & Karatekin, Ö. (2021). Large eddy simulations of the Martian convective boundary layer: towards developing a new planetary boundary layer scheme. Atmospheric Research, 250, 105381. Here, Cem Berk Senel, as the second co-author of the paper, contributed to the research conceptualization, performing MarsWRF large-eddy simulations, energy spectra analysis, development of the turbulent mixing length scale formulation and the Mars-specific PBL scheme, post-processing the GCM and mesoscale simulation results, and the writing of the manuscript.

indicator of the convective boundary layer height, also show similar altitude ranges (Balme and Greeley, 2006; Toigo et al., 2003). By contrast, the height of the Earth's planetary boundary layer only reaches 2 km for tropical conditions (Wood and Bretherton, 2004). The turbulence in the boundary layer is driven by the temperature and wind speed gradients, or, in other words, by the buoyancy production/destruction and shear production of turbulence. During the nighttime, the positive effect of buoyancy on the turbulence generation, which is present during daytime, is reversed, resulting in a shallower planetary boundary layer. Under such conditions, the boundary layer is dominated by shear production, and resembles the very stable boundary layer developed in the polar regions or over sea ice on Earth (Grachev et al., 2005). In general, the budgets of turbulence kinetic energy showed that the turbulence characteristics within the boundary layer of Mars and Earth share remarkable similarities (Spiga et al., 2010). Thanks to the similarity between the budget of turbulence kinetic energy within the PBLs of Mars and Earth, atmospheric models used to predict the meteorological conditions on Mars, employ the same turbulence modeling methodology as for Earth applications. Depending on the spatial resolution of the atmospheric model, turbulent transport can either be parameterized using a PBL scheme or largely resolved by performing LES. Due to the computational cost, LES can only be used as a research tool in limited-area models, mostly to investigate microscale meteorological events, but not for long-term weather forecasting with global or mesoscale models.

In this study, our main goal is to make use of LES to provide a dataset for the Martian convective boundary layer to investigate the turbulent transport in the PBL, such as vertical velocity updrafts and downdrafts, and to quantify the turbulence statistics, including the velocity and temperature variances, turbulent scalars (turbulence kinetic energy and its dissipation rate) and energy spectra. Apart from the Martian PBL's importance to fundamental boundary-layer meteorology research, the investigation of the Martian PBL with a high-fidelity LES is essential for various planetary science applications. For instance, the determination of turbulent scalars within the PBL is crucial for the quantification of atmospheric refractive index variations (He and Basu, 2016), an important physical phenomenon for the future manned missions on Mars.

Additionally, LES results can be used to develop PBL schemes for Mars GCMs and mesoscale models, as has been done for Earth-based modeling

(Nakanishi and Niino, 2006). In contrast to LES, PBL schemes only provide the mean state of the atmosphere based on the assumption that the turbulent fluxes can be approximated in terms of vertical gradients of physical quantities (velocity, temperature, humidity). The effect of these turbulent fluxes is taken into account by solving a one-dimensional vertical diffusion equation in atmospheric models, neglecting the horizontal contribution of turbulent fluxes. This one-dimensional diffusion equation has the following generic form for any transported atmospheric variable:

$$\frac{\partial c}{\partial t} = -\frac{\partial \overline{c'w'}}{\partial z} = \frac{\partial}{\partial z}\left(K\left(\frac{\partial c}{\partial z} - \gamma\right)\right) \tag{3.1}$$

Here, c being a generic variable (u,v or θ), $\overline{c'w'}$ is the turbulent flux, can not be explicitly resolved by a PBL scheme due to insufficient spatial resolution. However, this turbulent flux can be parameterized. This is done by relating the turbulent flux to local vertical gradient of mean flow quantities, c, using an eddy diffusivity coefficient, K. The term γ represents the contribution of turbulent mixing due to large-scale eddies (Hong et al., 2006) (see Sec. 4 for details).

The main purpose of PBL schemes in atmospheric models is to calculate eddy diffusivity coefficients, which is done either using an algebraic relationship (Pleim, 2007) or in terms of turbulent-related quantities, the turbulence kinetic energy (turbulence kinetic energy, $e = 0.5\sum u'^2$) and a mixing length scale, l (Janjić, 1994). PBL schemes, based on a turbulence kinetic energy formulation, compute the eddy diffusivity as follows:

$$K = lS_m e^{0.5} \tag{3.2}$$

The difference among PBL schemes comes from the definition of the model constant, S_m, and empirical determination of l. However, all TKE-based PBL schemes solve the same one-dimensional diffusion equation for e, which has the following generic form:

$$\frac{\partial e}{\partial t} = D + P_s + P_b - \frac{e^{1.5}}{B_1 l} \tag{3.3}$$

Terms on the right hand side of Eq. 3.3 represent the diffusion of turbulence kinetic energy, D, production of turbulence by wind shear, P_s, production or destruction of turbulence by buoyancy, P_b and its dissipation,

$\epsilon = e^{1.5}/B_1 l$. Similar to S_m, B_1 is another model constant. (see Sec. 4 for detailed explanation of these terms). Given the high level of boundary layer observations on Earth, several different one-dimensional, Earth-specific planetary boundary layer schemes have been proposed in the literature, such as the Bougeault-Lacarrere (BouLac) scheme (Bougeault and Lacarrere, 1989a), the Mellor-Yamada-Janjic (MYJ) scheme (Janjić, 1994) and the Mellor-Yamada-Nakanishi-Niino (MYNN) scheme (Nakanishi and Niino, 2006). Each of these planetary boundary layer schemes uses a different set of closure coefficients and a different turbulent mixing length scale formulation. The differences between the distinct closures are either based on observations combined with theoretical calculations (Sukoriansky et al., 2005), solely based on theoretical calculations (Janjić, 2001), or based on the the results of LES (Nakanishi and Niino, 2009). For terrestrial applications, studies show that a better representation of the atmospheric boundary layer is obtained when the closure coefficients, first determined by theoretical calculations, are modified based on LES results (Nakanishi and Niino, 2009). Considering the fact that the planetary boundary layer on Mars exhibits more extreme conditions than the boundary layer on Earth, the closure coefficients and mixing length formulations proposed for Earth should thus be re-evaluated for application to Mars. However, in previous studies (Temel et al., 2019; Pla-Garcia et al., 2016; Newman et al., 2017; Fonseca et al., 2018; Spiga and Forget, 2009), planetary boundary layer schemes, that have been developed for Earth, are nevertheless used, unmodified, for Mars. Currently, turbulence mixing lengths and parameterization of turbulence fluxes is based on the Earth-specific Mellor-Yamada-Janjic (MYJ) scheme (Janjić, 1994). Despite attempts to improve the parameterization of vertical updrafts and downdrafts within the planetary boundary layer of Mars by means of LES results (Colaïtis et al., 2013), a PBL scheme, solely developed according to the physics of the Martian planetary boundary layer, does not currently exist. As a first attempt to establish a new PBL scheme for Mars, we make use of LES results to compute the dissipation term in Eq. 3.1 and propose a generic mixing length formulation. LES computations are conducted with different positive sensible heat fluxes at the surface, producing different amounts of convective instability in the atmosphere. Note that, by definition, a positive sensible heat flux means net heat transport out of the surface. We present the first attempt to develop a Mars-specific PBL scheme, based on a turbulence kinetic energy diffusion

equation and a mixing length scale formulation. Finally, the proposed PBL scheme is tested both for GCM and mesoscale simulations. Despite several LES studies on the convective PBL of Mars, turbulence spectra are investigated for the first time. Our LES results can also be used as a benchmark for the verification of future LES studies, thanks to the comprehensive turbulence statistics that we present for different sensible heat forcings.

It must be noted that our focus in this study is on the daytime Martian boundary layer. Despite the same methodology being applicable for nighttime conditions, simulating the nighttime planetary boundary layer exhibits more challenges compared to daytime boundary layer. This is because of the limited turbulence by thermal stratification, leading to smaller eddy sizes, and this requiring higher grid resolutions. Moreover, intermittent turbulence during the nighttime increases the level of complexity, requiring a slightly different methodology for the large eddy simulation of nocturnal boundary layers (Kosović and Curry, 2000). Currently, such a dedicated methodology for the Martian nighttime boundary layer does not exist. Therefore, in this study, we only focus on the daytime boundary layer and propose modifications for turbulence parameterization solely for the convective conditions.

It is worth mentioning that our objective is neither to perform an intercomparison study across several different PBL schemes, nor to develop an ultimate single PBL scheme for Mars surpassing all the Earth-based PBL schemes. Such an extensive intercomparison study could only be conducted by performing a quantitative comparison with an observational dataset consisting of the temporal and vertical variations of turbulent fluxes, wind speed and its direction along the PBL. To date, such an observational dataset does not exist for Mars. Moreover, studies of the Earth PBL show that by using different PBL schemes, surface and near-surface temperature predictions can vary up to 6 – 7 K (Shin and Hong, 2011), which corresponds to the uncertainty of surface and near-surface temperature measurements on Mars (Pla-Garcia et al., 2016). This is also another reason, why an intercomparison study of PBL schemes for Mars is currently impractical using only limited observational datasets. Nevertheless, it is possible that realistic LES studies, validated using radio occultation data and driven by heating appropriate to the time and location of each observation, could be used to evaluate the performance of different PBL schemes. However, this is beyond the scope of this paper and will be the subject of a subsequent study.

The rest of the paper is organized as follows: Sec. 3.2.1 presents a brief description of the multiscale atmospheric code, the Mars implementation of the Weather Research and Forecasting (WRF) model, which is followed by a discussion of results obtained by the LES simulations in Sec. 3.2.2. Then, the new PBL scheme is described in Sec.3.2.3–3.2.5, and Sec. 3.2.6 is devoted to the application of the new PBL scheme. Finally, Sec. 3.3 presents the discussions and conclusions, respectively.

3.2 Theory & Modeling

3.2.1 MarsWRF and large-eddy simulation methodology

In this study, both GCM/mesoscale and LES computations are performed using the Mars implementation of the planetWRF (Richardson et al., 2007) model, i.e., so-called the MarsWRF model, which is a multiscale model based on a terrain following sigma-coordinate and the Arakawa-C grid (Arakawa and Lamb, 1977). In atmospheric models, several physical processes, including water microphysics, CO_2, and water and dust cycles interacting with radiative heat transfer, must be parameterized. In MarsWRF, longwave and shortwave radiation parameterization is based on a single scattering, two stream, k-distribution model (Mischna et al., 2012). Atmospheric dust content is prescribed in the present work using the Mars Climate Database's Mars Global Surveyor (MGS) dust scenario, the so called MCD/MGS scenario (Montmessin et al., 2004). Surface topography, thermal inertia and albedo are obtained from Mars Orbiter Laser Altimeter (MOLA) (Smith et al., 2001) and Thermal Emission Spectrometer (TES) (Christensen et al., 2004) data, respectively. Surface roughness is set to according to Garvin et al. (1999) and dust properties for radiative transfer are selected as suggested by Wolff and Clancy (2003). Finally, the lower boundary conditions for the vertical transport of state variables are computed by using a surface-layer parameterization scheme (Jiménez et al., 2012). The latter is important to have a realistic exchange of momentum, heat and moisture between the surface and the first 10% of the planetary boundary layer (Stull, 2012). More specifically, it determines the exchange fluxes of momentum, τ, heat, H, and moisture, E, from the exchange coefficients (momentum, C_d, heat, C_h, and moisture, C_q), as well as the gradient of physical quantities (i.e. wind speed, potential temperature and specific humidity respectively) between the ground and air.

To develop a Mars-specific PBL scheme, we perform LES computations for the convective boundary layer by using the LES implementation of the MarsWRF model (Richardson et al., 2007). In order to represent different amounts of convective instability, we considered different sensible heat flux values out of the surface. Periodic boundary conditions are used in both horizontal directions over a flat terrain similar to Sorbjan (2007) and Gheynani and Taylor (2010). The LES technique is based on the idea of decomposing a flow quantity, ϕ, into resolved scales, $\widetilde{\phi}$, and subgrid scales (SGS), ϕ^{sgs}. The large and energetic scales are resolved explicitly by the dynamical solver operating on the model grid, while small and dissipative scales are represented via SGS schemes within the MarsWRF model. Considering the similarities of daytime turbulence on Earth and Mars (even though the latter is more extreme due to its vigorous convection), it can be assumed that the same SGS schemes applied for Earth can also be applied to Mars, in accordance with the other Martian LES studies (Sorbjan, 2007; Tyler et al., 2008; Gheynani and Taylor, 2010; Spiga et al., 2010). Similar to PBL schemes, SGS schemes are also based on the eddy-diffusivity concept, such that, for both approaches, turbulent fluxes are computed using an eddy diffusion coefficient of momentum and heat. The difference is related to the spatial resolution. In LES, the spatial resolution is sufficiently small to resolve the larger and energetic scales. On the other hand, when PBL schemes are used for mesoscale (or lower resolution) simulations, the spatial resolution is not high enough to resolve even the large eddies, thus the turbulence parameterization is performed for all scales.

In MarsWRF, there are two standard SGS schemes available: the Smagorinsky (Smagorinsky, 1963), and the 1.5-order turbulence kinetic energy (Deardorff, 1980) schemes. Both are based on the linear eddy-diffusivity assumption, i.e.,

$$\tau_{ij} = -2K_m\widetilde{S}_{ij}, \tag{3.4}$$

postulating a linear relation between the SGS stress tensor, τ_{ij}, and the resolved shear strain-rate tensor, $\widetilde{S}_{ij} = \frac{1}{2}(\partial\widetilde{u}_i/\partial x_j + \partial\widetilde{u}_j/\partial x_i)$ where $\widetilde{u}_i$ is the resolved velocity and x_i denotes the spatial location in Cartesian coordinates, i and j are the two orthogonal horizontal directions. The proportionality parameter is the eddy-diffusivity coefficient, K_m. For the Smagorinsky scheme (Smagorinsky, 1963), K_m is expressed as

$$K_m = (C_s l)^2 \; max \left[0, (\widetilde{S}_{ij}\widetilde{S}_{ij} - Pr^{-1}N^2)^{1/2}\right], \tag{3.5}$$

where $C_s = 0.25$ is the Smagorinsky constant, $l = (\Delta x \Delta y \Delta z)^{1/3}$ is the length scale, which is the geometric average of the grid sizes in all directions, $Pr = 1/3$ is the turbulent Prandtl number (Skamarock and Klemp, 2008) and N is the Brunt-Väisälä frequency,

$$N = \sqrt{\frac{g}{\theta}\frac{\partial \theta}{\partial z}}, \tag{3.6}$$

where θ is the local potential temperature, $\partial\theta/\partial z$ is the vertical gradient of potential temperature, and g is the gravitational acceleration. The eddy-diffusivity coefficient in the 1.5-order turbulence kinetic energy scheme (Deardorff, 1980), reads

$$K_m = C_e l \sqrt{e}, \tag{3.7}$$

where $C_e = 0.10$ is a model constant and e is the turbulence kinetic energy, which is determined prognostically by solving an additional diffusion equation.

Despite the wide usage of these linear SGS schemes, they bring about some major disadvantages. The first drawback is the assumption of local equilibrium in small scales between the production and dissipation of turbulence kinetic energy (Germano et al., 1991), leading to an overly dissipative behavior. Such an assumption neglects the local contribution of transport terms, i.e. pressure, turbulence and subgrid scale transport (see the turbulence kinetic energy budget equation in Moeng and Sullivan (1994)), and relates the energy production solely to the dissipation. The hypothesis of local balance is employed by the use of $C_s = 0.25$ in Eq. 5 for the Smagorinsky scheme. However, it is taken into account in the dissipation term for the 1.5-order turbulence kinetic energy scheme (see the Eq. 6, 11a, 11b in Deardorff (1980)). The second weakness is the linear character of these eddy-viscosity models. Hence, they can not model any nonlinearities such as the energy that cascades backwards from the unresolved to the resolved scales, called the backscatter of energy. The final weakness is that these models are not able to account for shear anisotropy which requires an appropriate representation of the normal stresses (Muñoz-Esparza et al., 2014b). In order to overcome the aforementioned deficiencies of linear SGS models, we apply the nonlinear backscatter and anisotropy (NBA) SGS model of Kosović (1997) to Mars for the first time. It is

worth noting that this model is an updated version of the linear Smagorinsky model but now in a nonlinear framework. It builds the nonlinear SGS stress tensor as,

$$\begin{aligned}\tau_{ij} = &-(C_s l)^2 \left[2\left(2\widetilde{S}_{mn}\widetilde{S}_{mn}\right)^{1/2}\widetilde{S}_{ij}\right] \\ &-(C_s l)^2 \left[C_1\left(\widetilde{S}_{ik}\widetilde{S}_{kj} - \frac{1}{3}\widetilde{S}_{mn}\widetilde{S}_{mn}\delta_{ij}\right) + C_2\left(\widetilde{S}_{ik}\widetilde{R}_{kj} - \widetilde{R}_{ik}\widetilde{S}_{kj}\right)\right],\end{aligned} \tag{3.8}$$

where $\widetilde{R}_{ij} = \frac{1}{2}(\partial\widetilde{u}_i/\partial x_j - \partial\widetilde{u}_j/\partial x_i)$ denotes the resolved rotation rate tensor, $\widetilde{S}_{ij} = \frac{1}{2}(\partial\widetilde{u}_i/\partial x_j + \partial\widetilde{u}_j/\partial x_i)$ is the resolved shear strain rate tensor, δ_{ij} is the Kronecker delta. Note that Eq. 3.8 contains model coefficients as follows: $C_s = \left[8(1+C_b)/27\pi^2\right]^{1/2}$, $C_1 = C_2 = 960^{1/2}C_b/7(1+C_b)S_k$, with $S_k = 0.5$, and the backscatter coefficient, $C_b = 0.36$. Our chosen set of coefficients (Kosović, 1997) were then updated as in the form used by Muñoz-Esparza et al. (2014a). We carried out our calculations using the previous set of coefficients. Nevertheless, as shown in Appendix B1, we compare the vertical profiles of flow and turbulence quantities by both coefficient configurations and find that its effect is negligible. However, this does not rule out the possible differences that might arise using different SGS models. For terrestrial applications, the details of these model coefficients and their effects on turbulence characteristics are discussed in Kosović (1997) and Mirocha et al. (2010). The effect of SGS models on the accuracy of LES computations has been widely investigated for the Earth's PBL, with the NBA scheme found to reproduce the boundary layer turbulence better than other schemes thanks to its nonlinear framework (Mirocha et al., 2010). Unlike the standard linear SGS models, taking into account the backscatter of energy together with correct turbulence anisotropy presents better agreement with the theoretical similarity solutions within the surface layer.

3.2.2 Martian LES configuration

We investigate the Martian daytime PBL (i.e, convective boundary layer) for five different convective instability levels utilizing the LES model. To set up the LES model, the main parameters are the surface sensible heat flux, the dust content and the geostrophic wind. As the convective instability of the boundary layer is controlled by the imposed surface sensible heat flux, the

Case	q_s $[W/m^2]$	L_O $[m]$	u_* $[m/s]$	w_* $[m/s]$	z_i $[km]$	θ_0 $[K]$	$\langle e \rangle_{max}$ $[m^2/s^2]$	$\langle \epsilon \rangle_{max}$ $[m^2/s^3]$
LESq10	10	-29.6	0.533	3.40	3.06	235.0	8.0	0.012
LESq15	15	-23.8	0.566	4.08	3.57	236.8	9.8	0.015
LESq20	20	-17.2	0.558	4.63	3.93	238.1	13.0	0.018
LESq25	25	-13.6	0.555	5.16	4.39	239.1	15.0	0.021
LESq30	30	-11.2	0.551	5.63	4.77	240.2	17.3	0.028

Table 3.1: Main PBL parameters acquired from the LES simulations for different surface sensible heat flux, q_s. Here, L_o is the Obukhov length, u_* is the friction velocity, w_* is the Deardorff convective velocity, z_i is the PBL height, and θ_0 is the potential temperature near the ground. e_{max} and ϵ_{max} are the maximum values of horizontally averaged turbulence kinetic energy and its dissipation rate along the vertical direction. The angle bracket, $\langle\rangle$, denotes horizontally averaged values. These values are averaged over 500 seconds following a 2-hours simulation period.

range is specified as $q_s = 10, 15, 20, 25, 30\ W/m^2$. Note that the different q_s values are intended to reproduce the convective forcing at different times of day; hence, the resultant PBL scheme can be tuned to work for the whole of the daytime PBL. Moreover, the specified range of $q_s = 10 - 30\ W/m^2$ covers the reported values in Sutton et al. (1978) from in-situ measurements by the two Viking Landers. The latter study reported that the maximum sensible heat flux values around the local noon are estimated within the range of 15-20 W/m^2 by Viking 1 (47°W, 23°N) and of 10-15 W/m^2 by Viking 2 (227°W, 48°N) during the Northern summer. Moreover, this range is reported to be 15-30 W/m^2 in (Ye et al., 1990) for Martian daytime in summer from their numerical simulations. More recently, Martian LES modeling of Spiga et al. (2010) showed that the diurnal variation of surface sensible heat flux varies between $Q_s = 0.8 - 2.7\ Km/s$ (i.e. $q_s \sim 10 - 34\ W/m^2$) for Amazonis Planitia, Tharsis and Nili Fossae around local noon (11-15 h).

Another important parameter affecting the dynamics of the convective boundary layer is the dust content and its vertical distribution. For the LES model, the atmospheric dust content is prescribed, with a dust opacity of 0.3, similar to Michaels and Rafkin (2004). Simulations are initialized with a constant geostrophic wind speed along the x direction, i.e., $u_G = 10\ m/s$, $v_G = 0$, $w_G = 0$. The reason is to force the convective boundary layer (CBL) with a strong shear, which is the case for the typical Martian CBL, leading, in turn, to a shear-driven CBL. The value of u_G is taken as $10m/s$

similar to another LES study on the Martian PBL by Tyler et al. (2008). In addition to the initial geostrophic wind forcing, the initial temperature field is imposed according to the Mars Climate Database (MCD) v5.3 (Forget et al., 1999; Millour et al., 2018) for the mid latitudes at the local sunrise. The initial potential temperature profile gradually increases from 214 K at the surface to 216 K at the top of boundary layer where the initial PBL height is $z_{i,0} = 870\ m$. Above which, potential temperature increases linearly with the free-atmospheric stratification rate, i.e. $\Gamma = 4.7\ K/km$ similar to Petrosyan et al. (2011).

For the LES simulations, the domain size is set to be $L_x = L_y = 10$ km and $L_z = 12$ km with $100 \times 100 \times 120$ grid points along (x, y, z). This setting provides a relatively high grid resolution of $100\ m \times 100\ m \times 100\ m$, similar to the earlier LES studies for Mars such as Gheynani and Taylor (2010) and Spiga et al. (2010). The simulation domain is periodic at the lateral boundaries. The bottom surface is a flat terrain with an aerodynamic roughness height, $z_0 = 0.01$ m. At the top boundary, implicit Rayleigh damping for the vertical velocity (Klemp et al., 2008) is applied to prevent unphysical wave breaking or reflections at the model top. The surface layer parameterization is based on the revised MM5 scheme of Jiménez et al. (2012) as described in Sec. 3.2.1.

Similar to global or mesoscale models, LES models need to be run for an initial time period to allow the state variables to reach a valid physical state, the so-called the spin-up time. For LES studies,the flow field is initially not turbulent. Therefore, a spin-up time is required for the flow to become turbulent. The recommended spin-up time for the Martian LES is $t_{spin-up} = 0.5 - 1.0$ hour in Spiga and Forget (2009) and Spiga et al. (2018). This initial state corresponds to the $\sim 2 - 4$ large-eddy turnover time, τ_*, which can be defined as

$$\tau_* = \frac{z_i}{w_*} \tag{3.9}$$

Here, z_i is the PBL height, defined as the height when the time- and horizontally averaged eddy heat flux, $w'\theta'$, goes to its minimum value, and w_* denotes the Deardorff convective velocity (Deardorff, 1970), which is defined as

$$w_* = \left(\frac{g}{\theta_0}\ q_s\ z_i \right)^{1/3} \tag{3.10}$$

where θ_0 is the time- and horizontally averaged potential temperature near the ground, i.e, at 1.5 m above ground level.

In our study, the LES experiments are performed for 2 hours ($\sim 8\tau_*$) ensuring we achieve a well-mixed turbulence state similar to Sorbjan (2007) and Gheynani and Taylor (2010). It is worth noting that the computed large-eddy turnover time ranges from $\tau_* = 900\ s$ to $\tau_* = 850\ s$ from $q_s = 10\ W/m^2$ to $q_s = 30\ W/m^2$ (see Table. 1 to compute τ_* in terms of given z_i and q_s values). In order to compute the time-averaged turbulence statistics, all the simulations are continued for 500 seconds ($\sim 0.5\tau_*$) more for time-averaging. An insufficiently short time period can lead to noise in the averaging process; hence, this period is chosen by considering the number of samples needed to acquire smooth turbulence statistics. Regarding our LES results presented below, selection of $\sim 0.5\tau_*$ for the time-averaging reveals a smooth behaviour in turbulence profiles and energy spectra.

In Tab. 1, time- and horizontally averaged PBL parameters are listed. In addition to the sensible heat flux, the convective instability of the boundary layer is also expressed by the Obukhov length, which is calculated as:

$$L = -\frac{u_*^3 \theta_0}{\kappa g Q_s} \tag{3.11}$$

Here, u_* is the friction velocity, θ_0 is the reference potential temperature, κ is the von Karman constant and Q_s is the kinematic temperature flux, defined as:

$$Q_s = \frac{q_s}{\rho C_p} \tag{3.12}$$

where, q_s is the sensible heat flux, ρ is the air density, and C_p is the specific heat capacity of air.

By convention, the surface sensible heat flux, q_s, in Eq. 3.12 is positive when heat is added to the atmosphere from the surface during daytime, and negative during nighttime. During daytime conditions, when the boundary layer is convective, the Obukhov length becomes negative. By its definition, the Obukhov length represents the relative importance of shear and buoyancy fluxes as a measure of the atmospheric stability. In Tab. 1, apart from the Obukhov length, surface sensible heat flux, friction velocity and convective velocity, the maximum turbulence kinetic energy and its dissipation rate, $\overline{e}_{max}$ and $\overline{\epsilon}_{max}$, are given. The dissipation rate is calculated based on Senel

et al. (2019). As shown in Tab. 1, the imposed sensible heat flux enhances the magnitude of convective characteristics, such that the Obukhov length increases from -29.6 m to -11.2 m between the lowest and highest values of q_s. Consistent with this, the convective velocity increases from 3.40 m/s to 5.63 m/s and the PBL height rises from 3.06 km to 4.77 km. These values for the Martian CBL are significantly higher compared to those observed in Earth's atmosphere. To illustrate, in Earth's CBL, the convective velocity over land, at the time of peak convective activity, i.e., late afternoon, is typically $\sim 1-2\ m/s$ while the boundary layer height is around 1 km from observational and numerical studies (Kaimal et al., 1976; Schmidt and Schumann, 1989; Moeng and Sullivan, 1994; Shin and Hong, 2013; Degrazia et al., 2018). Regarding the turbulence kinetic energy, we observe relatively higher turbulence kinetic energy values for the Martian CBL reaching up to 17.3 m^2/s^2 consistent with the finding of Spiga et al. (2010). On the other hand, the maximum value of the dissipation rate is found to be 0.028 m^2/s^3 for the highest, $q_s = 30\ W/m^2$m, value. These higher values of daytime CBL verify the fact that the Martian boundary layer is much deeper than Earth's boundary layer (Spiga et al., 2010). For the Earth's convective PBL, turbulence kinetic energy and its dissipation rate can reach up to $\sim$ 1.0 m^2/s^2 and $\sim$ 0.02 m^2/s^3 over a flat terrain (Senel et al., 2019).

Before investigating the results of LES, it is worth noting that the convective boundary layer is composed of three distinct vertical regions, the surface layer, mixed layer and entrainment zone. Surface layer is roughly defined as the first 10% of the CBL, i.e., $0 < z/z_i \leq 0.10$, where the surface forcings (wind shear and buoyancy) are dominant (Schmidt and Schumann, 1989; Shin and Hong, 2013). The surface layer is topped by the mixed layer extending from 10% to 85% of the CBL height, in which the turbulence is quite actively mixing the physical quantities (velocity, temperature, moisture and tracers) in the vertical direction (Stull, 2012; Zhang et al., 2018). The growth of the mixed layer is capped by the entrainment zone with an intense temperature inversion, at which the stably-stratified free atmosphere is entrained into the top of mixed layer (Brooks and Fowler, 2012). This entrainment (i.e. the penetration of air from free-atmosphere down to the top part of mixed layer) takes place around 85% of height of the CBL, rising up to 110% of the CBL, i.e. $0.85 \leq z/z_i \leq 1.10$ (Honnert et al., 2011). The results of LES are depicted in terms of vertical profiles of time- and horizontally averaged wind speed,

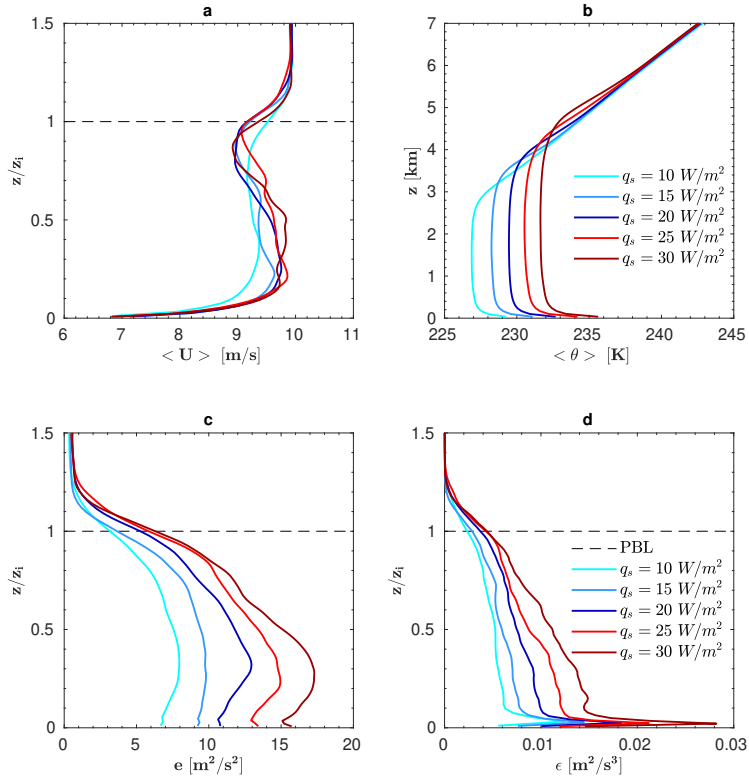

Figure 3.1: Vertical profiles of time- and horizontally averaged wind speed (a), potential temperature (b), turbulence kinetic energy (c) and dissipation rate (d). Black dashed line denotes the normalized PBL height. All the LES computations are scaled by its own PBL height listed in Tab. 3.1 as z_i.

potential temperature, turbulence kinetic energy and dissipation rate in Fig. 3.1. Although these vertical ranges are generally reported for Earth's CBL, the altitude range of the vertical regions agree with the results of Sorbjan (2007); Spiga et al. (2010) inferred from LES of Martian CBL. Besides the latter studies, our LES results, presented below, will confirm the range of vertical regions of Martian CBL over a significant range of convective instability.

The results of LES are presented in Fig. 3.1 in terms of vertical profiles of time- and horizontally averaged wind speed, potential temperature, turbulence kinetic energy and dissipation rate. Note that the vertical axis is given in terms

of z/z_i to interpret the vertical regions of the CBL. The physical quantities plotted in Fig. 3.1 increase with higher surface heating indicating a more vigorous convection. More specifically, the vertical profiles of wind speed (Fig. 3.1a) indicate that the wind speed is substantially affected by the surface heating above the surface layer until the free-atmosphere; however, there is no considerable difference occurring within the first half of the surface layer ($0 < z/z_i \leq 0.05$). This is due to the fact that this part of surface layer is more governed by shear forces rather than buoyant forces (see the horizontal shear fluxes, $\widetilde{u'u'}$ and $\widetilde{v'v'}$ in Fig. 3.3c-d). Besides these, it is worth mentioning that the existence of turbulence tends to vanish above the convective boundary layer as can be seen from the turbulence kinetic energy, e, and the dissipation rate, ϵ, profiles (Fig. 3.1c-d). This is because of the intense temperature inversion arising between $0.85 < z/z_i \leq 1.10$ (Fig. 3.1b) because the presence of the entrainment zone. Furthermore, the sharp peak occurring in dissipation rate, within the surface layer ($0 < z/z_i \leq 0.1$), is due to energy-dissipation is mainly produced near the planetary surface where the dissipative eddy scales destroy the turbulence kinetic energy more drastically.

In Fig. 3.2, spanwise energy spectra of resolved $\widetilde{u_1'u_1'}$, $\widetilde{u_2'u_2'}$, $\widetilde{u_3'u_3'}$ fluctuations vs. spanwise wavenumber, κ_2, are presented. Here, the subscript $i = 1, 2, 3$ refers to the x (streamwise), y (spanwise), z (vertical) components of the velocity, i.e. $u_1 = u$, $u_2 = v$, $u_3 = w$. Furthermore, the energy spectra are averaged both in time and streamwise direction to make them smoother. The spectra are plotted for $q_s = 10\ W/m^2$ (top), $q_s = 20\ W/m^2$ (middle) and $q_s = 30\ W/m^2$ (bottom) conditions at two different altitudes: $z = 230\ m$ (within the surface layer) and $z = 7.7\ km$ (above the PBL in free-atmosphere). The results show that the LES computations exhibit the theoretical -5/3 cascade, i.e, $E(\kappa) \propto \kappa^{-5/3}$. This demonstrates, for the first time, that the eddies in the inertial subrange appearing inside the Martian convective boundary layer match well with Kolmogorov's theory of turbulence (Kolmogorov, 1941). This suggests that the chosen spatial resolution of the LES is sufficient to resolve the most energetic eddies producing the most turbulence kinetic energy. The results of the energy spectra in Fig. 3.2 also indicate that the surface layer (left panels) is more energetic than the free-atmosphere (right panels). This is due to the fact that the turbulence kinetic energy decays with altitude as can be clearly seen from the profiles of turbulence kinetic energy presented in Fig. 3.1c.

Moreover, within the surface layer, the part of the energy spectra

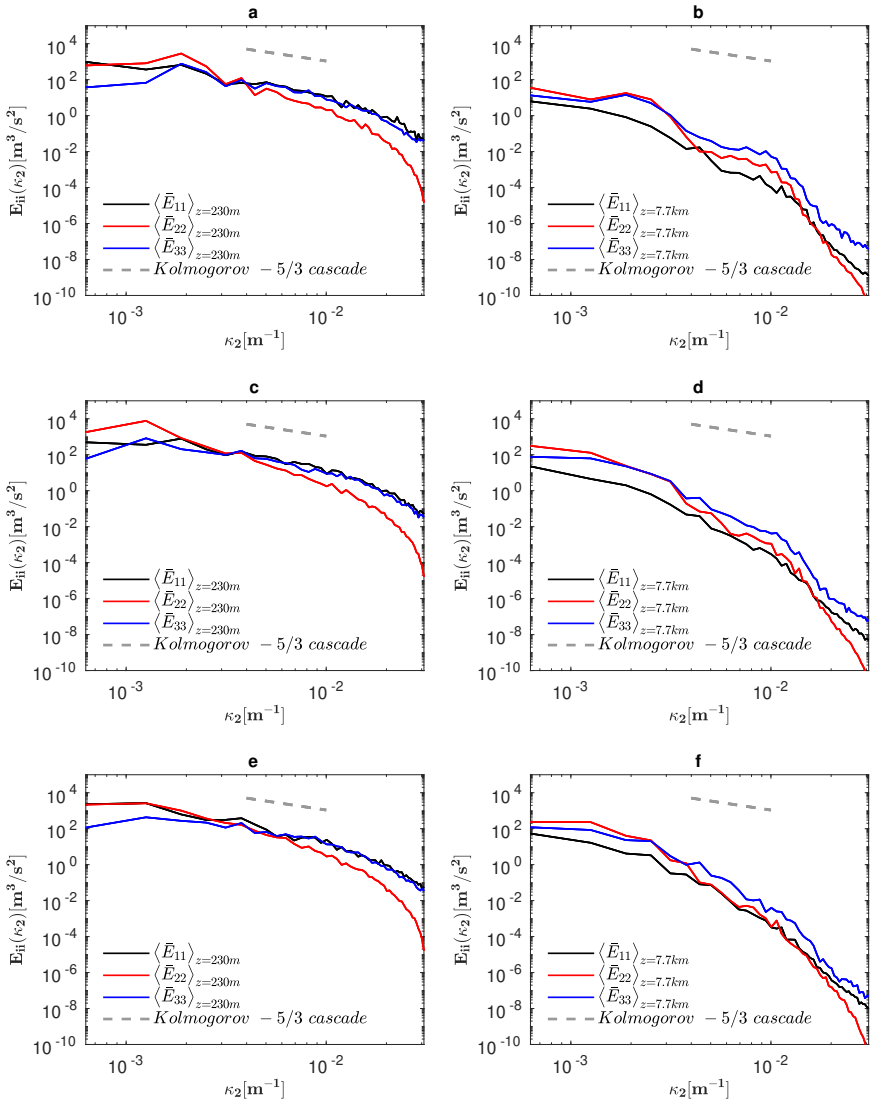

Figure 3.2: Time- and streamwise-averaged energy spectra vs. spanwise wavenumber, κ_2, for $q_s = 10\ W/m^2$ (top), $q_s = 20\ W/m^2$ (middle) and $q_s = 30\ W/m^2$ (bottom) conditions at two different altitudes, $z = 230\ m$ (left) and $z = 7.7\ km$ (right). Black, blue and red solid lines denote the averaged spectra of resolved $\widetilde{u_1'u_1'}$, $\widetilde{u_2'u_2'}$, $\widetilde{u_3'u_3'}$ fluctuations, respectively. Gray dashed line denotes the theoretical Kolmogorov -5/3 slope.

corresponding to dissipative scales still follows the Kolmogorov cascade. Above the PBL, small eddies deviate from this theory; hence, the inertial subrange,

in which the major energy process is the transport of energy from large to small eddies, terminates at lower wavenumbers. Therefore, it might be possible that during nighttime conditions (stable boundary layer) for which the energy cascade might resemble the case of the free-atmosphere characterized by a stable stratification, energy spectra might not follow the Kolmogorov slope.

The vertical variation of time- and horizontally averaged turbulence statistics is given in Fig. 3.3. For all the q_s values, non-dimensional eddy heat flux, i.e, $\langle w'\theta' \rangle / \langle w'\theta' \rangle_{max}$, profiles are nearly identical. They have a large positive peak near the ground resulting from the strong buoyancy generation, besides a small negative peak near the top of the PBL due to the capping inversion, which is a stable layer that restricts the growth of the convective boundary layer. The ratio between these minimum and maximum peaks is -0.2/1.0, which fits the general characteristics of the Earth's convective PBL very well (Moeng and Sullivan, 1994). Fig. 3.3 shows that the turbulent heat flux reaches zero, close to the top of PBL, confirming that the buoyancy generation of turbulence kinetic energy, which is significant in the PBL, does not occur above it in the free atmosphere. Fig. 3.3 also shows the time- and horizontally averaged variances of streamwise, spanwise and vertical velocities. While the horizontal variances ($\langle u'u' \rangle$ and $\langle v'v' \rangle$) decrease with altitude (Fig. 3.3b-c), the increase in surface heating from $q_s = 10\ W/m^2$ to $q_s = 30\ W/m^2$ grows the horizontal variances in general. However, there exists a slight increase in $\langle v'v' \rangle$ by $q_s = 25\ W/m^2$ with respect to $q_s = 30\ W/m^2$ near the surface (which is also the case for the horizontal wind speed profiles in Fig.3.1a). Even though the surface heating increase enhances the buoyancy production systematically, this does not guarantee that the shear production should present monotonic behavior with the increase in surface heating. This can be caused by the local balance/imbalance between the buoyancy and shear production. However, a detailed understanding can be obtained by means of a turbulence kinetic energy budget analysis, in order to evaluate the relative contribution of each sub-component to the total turbulence kinetic energy.

Furthermore, the eddy momentum flux of vertical velocity, or the vertical variance, in other words, grows until $z/z_i \sim 0.4$ then decays as displayed in (Fig. 3.3d). This is due to the existence of stronger updrafts accelerated by the surface heating, reaching their maximum momentum. Their intensity is damped in the upper boundary layer due to the capping inversion, resulting in a maxima around the mid-altitudes. This behaviour of vertical eddy

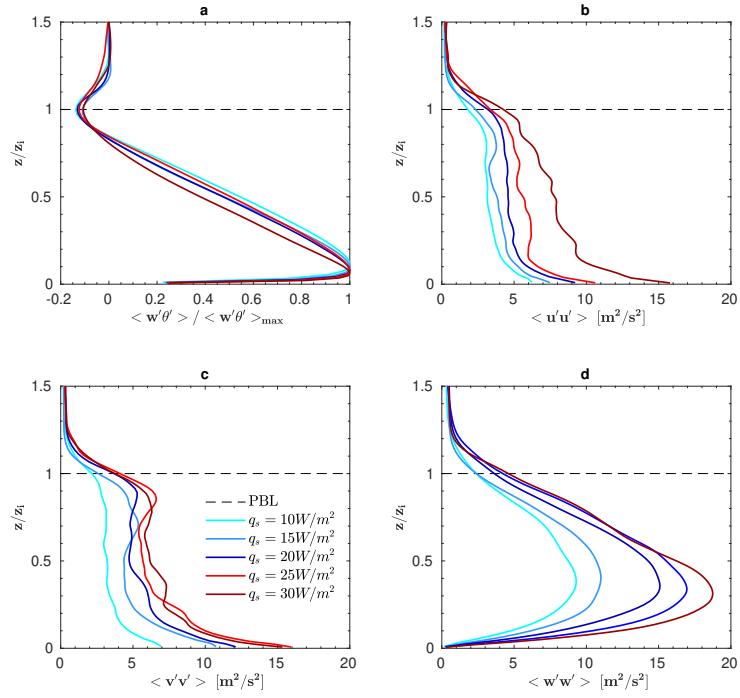

Figure 3.3: Vertical profiles of time- and horizontally averaged non-dimensional eddy heat flux (a), eddy momentum fluxes of streamwise (b), spanwise (c) and vertical (d) velocities. Black dashed line denotes the PBL height. All the LES computations are scaled by its own PBL height listed in Tab. 3.1 as z_i.

momentum makes the turbulence kinetic energy reach its maximum value around $z/z_i \sim 0.4$ in Fig. 3.1. Here, the increase in vertical momentum is due to the enhancement in buoyancy production near the surface.

To illustrate the updrafts, an instantaneous contour plot of the vertical velocity is presented at $z/z_i \sim 0.05$ and $z/z_i \sim 0.40$ at the start of the averaging period (Fig. 3.4). The maximum value of the updrafts increases from 9.3 m/s to 15.3 m/s between the lowest and highest q_s values at $z/z_i \sim 0.40$. Note that Fig. 3.4 also shows the largest horizontal size of the turbulent structures to be ~ 3 km, and Fig. 3.3b and Fig. 3.3d show the maximum predicted horizontal and vertical variances to be ~ 15 m^2/s^2, which are all consistent with the simulations of Spiga et al. (2010).

Similar to previous LES studies on the Martian CBL, we perform our

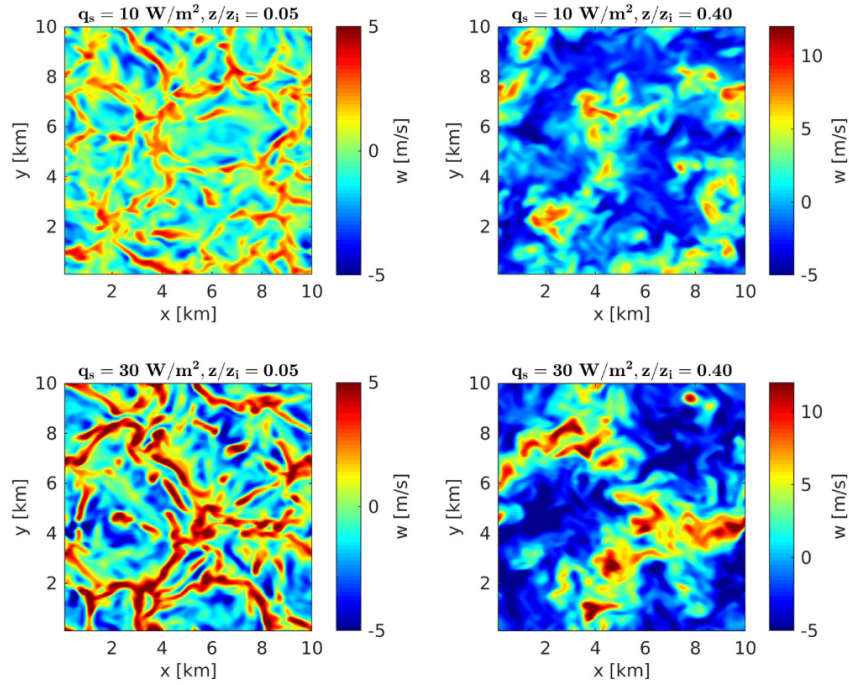

Figure 3.4: Instantaneous fields of the vertical velocity at $z/z_i \sim 0.05$ and $z/z_i \sim 0.40$ when $t = 2h$ for value of q_s between $q_s = 10$ (top) and 30 W/m^2 (bottom).

simulations for a dry atmosphere (Michaels and Rafkin, 2004; Gheynani and Taylor, 2010; Spiga et al., 2010). However, terrestrial studies showed that the vertical transport of water vapor can affect the momentum and heat transport between the top of PBL and free atmosphere, the so-called entrainment zone (Canut et al., 2012), along with other possible parameters such as the capping inversion gradient, the inversion height (Stevens et al., 1999; Brooks and Fowler, 2012; Kurowski and Teixeira, 2018). The effect of these parameters on the dynamics of the daytime Martian boundary layer is currently unknown and out of scope for this study.

3.2.3 Description of the new Mars-specific PBL scheme

In this section we make use of our database of LES results to derive a turbulent mixing length scale formulation and incorporate it into a turbulence kinetic energy-closure based PBL scheme. As noted before, turbulent fluxes are computed using Eq. 3.1 and the counter-gradient term, γ which represents

the contribution of the large-scale eddies (Hong et al., 2006) is calculated as:

$$\gamma_{cg} = \frac{g}{\theta_0} \frac{\overline{\theta'\theta'}}{\overline{w'w'}} \tag{3.13}$$

The counter-gradient term is only included for potential temperature and computed as suggested by Therry and Lacarrère (1983) (see Sec. 4.2, Eq. 40), i.e., where θ_0 is the reference potential temperature computed at the first grid layer, $\overline{\theta'\theta'}$ and $\overline{w'w'}$ are the variances of potential temperature and vertical velocity., which corresponds to the vertical turbulent thermal flux. For the computation of turbulent fluxes, an algebraic relationship, including the turbulence kinetic energy, e, and the mixing length is needed as shown by Eq. 3.2. In order to obtain the turbulence kinetic energy, Eq. 3.3, was solved, which has the following exact form:

$$\frac{\partial e}{\partial t} = \frac{\partial}{\partial z}\left[le^{0.5} S_e \frac{\partial e}{\partial z}\right] + P_s + P_b - \epsilon \tag{3.14}$$

where S_e denotes the diffusion coefficient of turbulence kinetic energy, set same as in (Bougeault and Lacarrere, 1989a). As noted before, source and sink terms on the right-hand side of Eq. 3.14 are, respectively, shear production, P_s, buoyancy production/destruction, P_b, and the dissipation of turbulence kinetic energy. These terms denote the contribution of wind shear and thermal gradients on the production/destruction of turbulence kinetic energy and its destruction by dissipation within the PBL. These are defined as,

$$P_s = K\left[\left(\frac{\partial u}{\partial z}\right)^2 + \left(\frac{\partial v}{\partial z}\right)^2\right] \tag{3.15}$$

$$P_b = -\beta g K \frac{\partial \theta_v}{\partial z} \tag{3.16}$$

$$\epsilon = \frac{e^{1.5}}{B_1 l} \tag{3.17}$$

where β is the thermal expansion coefficient.

3.2.4 Determination of the closure coefficients

As can be seen in Eq. 3.17, the dissipation rate of turbulence kinetic energy is a function of the mixing length scale, turbulence kinetic energy itself, and, a proportionality coefficient, B_1. turbulence kinetic energy and its dissipation

rate are computed in the LES and presented in Sec. 3.2.2. Therefore, it is possible to calculate the $B_1 l$ term using the LES results. Theoretical studies on the determination of the mixing length scale for the Earth's atmosphere show a ratio of ~ 0.2 between the maximum length scale within the PBL and its height (Degrazia et al., 1996), (see their Eq. 15). This ratio was found based on theoretical calculations using an energy spectrum, following the Kolmogorov theory of turbulence, which is the case for our results inside the PBL, presented in Sec. 3.2.2. Therefore, despite this ratio being initially suggested for the Earth's PBL, here, we also apply a similar ratio in order to avoid unrealistic mixing length scale values, exceeding the PBL height. So, the B_1 coefficient is set to 6.0, which falls within a range for its conventional values used by terrestrial PBL schemes, such as 1.4, 11.88 and 24 in BouLac, MYJ and MYNN schemes.

Another important term of any PBL scheme is the turbulent exchange coefficient, S_m. PBL schemes can be designed to work with either a constant (Bougeault and Lacarrere, 1989a) or varying, S_m coefficient (Janjić, 2001). As suggested by Senel et al. (2019), a further extension towards 3D PBL schemes, which may be important as a possible improvement given the complex topography of Mars, will be more straightforward by using a constant S_m coefficient. We follow this approach and introduce a new definition of a turbulent exchange coefficient that can be derived in terms of the dissipation rate of turbulence kinetic energy from Eqs. 3.2:3.17.

$$K = \frac{S_m}{B_1} \frac{e^2}{\epsilon} \tag{3.18}$$

As discussed by Temel et al. (2018b), the ratio of S_m/B_1 corresponds to the equivalent turbulent exchange coefficient for two-equation turbulence models. In that study, it was found that high values of S_m/B_1, e.g., higher than 0.09 for Earth's PBL, can lead to unrealistic estimations for the turbulence kinetic energy. In the present study, S_m is therefore set to 0.2, corresponding to $S_m/B_1 = 0.033$.

3.2.5 Turbulent mixing length scale formulation

In this section, we propose a generic formulation for the mixing length scale, l, using the LES calculations of the turbulence kinetic energy, e, its dissipation rate, ϵ, and the closure coefficient, B_1, determined previously. For the variation

of the mixing length scale in the PBL, we utilize a formulation based on three sub-components, which are the surface layer length scale, l_s, asymptotic length scale, l_λ, and upper layer length scale, l_u, as follows:

$$\frac{1}{l} = \frac{1}{l_s} + \frac{1}{l_\lambda} + \frac{1}{l_u} \tag{3.19}$$

This approach is also adapted by terrestrial PBL schemes, such as the MYJ and MYNN schemes. Similarly, we also fit functions to these length scales based on our LES computations. In Eq. 3.19, the l_λ component governs the mixed layer of the CBL between $0.10 < z/z_i < 0.85$. Below $z/z_i = 0.10$, the turbulence characteristics of the surface layer are taken into account thanks to the use of surface layer length scale, l_s, as $1/l_s \gg 1/l_\lambda$ within the surface layer. We formulate l_s as

$$l_s = \kappa z\,(1 - \alpha\,\zeta)^p \;\; \{\alpha = 80,\; p = 1/4 \mid L_O < 0\} \tag{3.20}$$

The α and p given in Eq. 3.20 are determined by applying nonlinear curve fitting to the reference LES data. Regarding the functional form of asymptotic length scale, we let l_λ be a function of the PBL height, z_i, and the non-dimensional stability parameter, ζ_1, where $\zeta_1 = z_1/L_O$, at the first vertical grid layer. Hence,

$$l_\lambda = f(z_i, \zeta_1) \tag{3.21}$$

This functional form is based on another terrestrial PBL scheme used in the Earth WRF model, called as the University of the Washington (UW) (Bretherton and Park, 2009) scheme. In that scheme, the length scale $l_{\lambda,UW} = z_i\eta$ where $\eta = 0.085\left(2 - e^{[min(Ri^{CL},0)]}\right)$ from their own LES results. Applying a linear regression analysis to the present LES results and accounting for the quasi-linear characteristics of the asymptotic length scale in the mixed layer (the portion of CBL distant from the surface and upper layer, forming between $z/z_i =\sim 0.10 - 0.85$), we end up with the final form as,

$$l_\lambda = \lambda\, e^{0.1\zeta_1} z_i \;\; \{\lambda = 0.43 \mid L_O < 0\} \tag{3.22}$$

where λ denotes the model parameter of asymptotic length scale, l_λ, obtained from the linear regression analysis. Note that the derivation of this functional form is based on Senel et al. (2019) (for its details see Sec. 2, Eq. 17-20).

As discussed earlier, the upper part of the boundary layer, $0.85 \leq z/z_i \leq$

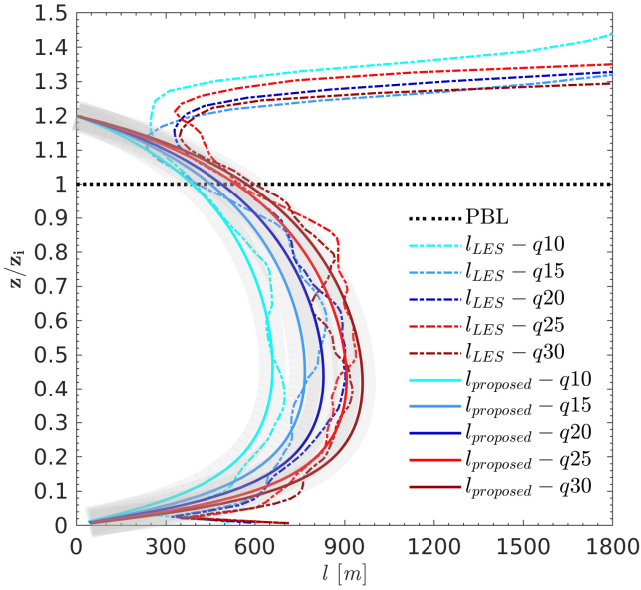

Figure 3.5: Vertical profiles of time- and horizontally averaged mixing length scale profiles for different amount of convective instability. Dashed lines display the results of LES computations and solid lines refer to the proposed model. The gray highlight marks the region where the minimum and maximum values of the proposed l appears. Black dotted line denotes the convective PBL height. Note that all the LES computations are scaled by its own PBL height listed in Tab. 3.1 as z_i.

1.10, requires particular attention to its modeling aspect. This is because of the dynamic structure of air entrainment from the free-atmosphere down to the top of the boundary layer. Despite its complexity, the turbulence in the entrainment-zone can be approximated through the mixing length theory by incorporating a complimentary term into Eq. 3.19, as follows:

$$l_u = \gamma z_i - z \tag{3.23}$$

where l_u refers to the upper layer length scale. The functional form of l_u follows the description of Gryning et al. (2007) where they assume $\gamma = 1$ as a linear relation between l and z for the Earth's CBL. However, we set γ to 1.20 by means of the regression analysis with respect to the reference LES data presented in Sec. 3.2.2.

Results of the proposed mixing length scale are presented in Fig. 3.5. The proposed model agrees good with the LES results in all the vertical regions of

convective boundary layer for different amounts of convective instability. It is worth noting that the LES-based mixing length is calculated from Eq. 3.17 as, $l_{LES} = \frac{e_{LES}^{1.5}}{B_1 \epsilon_{LES}}$. Despite the good agreement between the proposed and LES-based mixing length within the boundary layer, it tends to deviate through the free-atmosphere, i.e. especially over $\sim 1.1 z_i$. Since our interest focuses mainly on the boundary-layer representation, the proposed formulation inferred from the LES computations fits well from surface up to the free-atmosphere, i.e., $\sim 1.1 z_i$. Finally, the mixing length scale must also be defined above the PBL height, in which we use the conventional mixing length scale definition for the free atmospheric diffusion similar to Janjić (2001) and Mason (1989):

$$l = 0.23\ \Delta z \tag{3.24}$$

where Δz is the vertical grid spacing above the PBL height.

In the present study, the mixing length formulation is solely derived for the daytime convective turbulence inferred from high-resolution LES computations. Considering the aforementioned challenges for modeling the stable atmosphere boundary layer of Mars, the mixing length scale is simply treated by incorporating the mixing length definition of MYJ scheme (Janjić, 1994) in accordance with the classical Blackadar formulation (Blackadar, 1962b). Hence, it is defined as given, i.e., $l_{stable} = (1/l_s + 1/l_\lambda)^{-1}$ where the surface layer length scale is set to $l_s = \kappa z$ and the asymptotic length scale is $l_\lambda = 150$ m.

Briefly, our PBL scheme is based on solving turbulence kinetic energy in Eq. 3.14, with the source and sink terms given in Eqs. 3.15 and 3.16. The turbulent exchange coefficients are calculated using Eq. 3.18. The mixing length scale below the PBL height is obtained by Eqs. 3.19, 3.20 and 3.22. Finally, the closure coefficients, S_m and B_1, are set to 0.2 and 6.0. As noted before, we use the revised MM5 surface-layer scheme (Jiménez et al., 2012) for our PBL formulation. However, for the determination of surface momentum flux to calculate the vertical transport of velocity components, we follow a similar approach to Angevine et al. (2010).

3.2.6 Mesoscale simulations in comparison with in-situ observations of NASA's InSight Mars Lander

In this section, we illustrate the applicability of our new PBL scheme for predicting the surface meteorological conditions at the InSight landing site using the Martian mesoscale simulations. We compare the near-surface meteorological predictions with the in-situ observations by the InSight rover, (landing site 4.5° S, 135.6° E) (Banfield et al., 2020) (data is available https://pds-geosciences.wustl.edu/missions/insight/index.htm). Before the Martian mesoscale simulations, we also assess the accuracy of convective PBL height predictions of the proposed scheme in comparison the estimated PBL heights based on radio occulations of Mars Express (MEX) (Hinson et al., 2008), running MarsWRF in global mode, with a spatial resolution of 5° (298 km on the equator). Global simulations were performed for two Mars years, where the first year of the simulation was the spin-up year to remove all initial model transients. The model parameters for GCM simulations are as given in Sec. 3.2.1.

As stated before, the proposed scheme is compared with an already existing PBL scheme in the MarsWRF model, which is the Medium-Range Forecast (MRF) scheme. The MRF scheme is an algebraic PBL scheme, in which the turbulent diffusivity coefficients are evaluated based on empirical relationships (Hong and Pan, 1996). Like any other PBL scheme, determination of the planetary boundary layer height is an important diagnostic process, which has an impact on the correct representation of the mixed layer. For the MRF scheme, the PBL height is estimated depending on the critical bulk Richardson number, $Ri_{b,cr}$. As such, the PBL height is defined as the first grid level where Ri_b becomes larger than a critical value, $Ri_{b,cr} = 0.5$. Our proposed model, instead, determines the PBL height from the potential temperature (θ) as the first grid level where the local θ exceeds the mixing layer θ by a threshold value of 0.5 K. This approach is similar to the θ-increase method of Hu et al. (2010).

The vertical profiles of the potential temperature are depicted for the proposed and MRF schemes at the local time 17.0h (Fig. 3.6). The locations for these profiles are 27.5° N, 107° W at $L_s = 44.5°$ and 21.8° N, 205° E at $L_s = 47.1°$ (Tab. 2) based on the MEX radio occultation locations (Hinson et al., 2008). Considering the potential temperature gradient between the near surface and mixed layer, the proposed scheme results in a more convective behaviour than

the MRF scheme. This is because the new model accounts for the daytime turbulence over a significant range of convective instability (see Sec. 3.2.2). Besides, the new model produces more realistic PBL height estimations as can be seen in Fig. 3.6. For instance at the second location (21.8° N, 205° E), boundary layer height predicted by the MRF scheme reaches 11.5 km which is double that of the MEX observation (5.1 km).

The second application deals with mesoscale simulations using the two PBL schemes for the InSight landing site. GCM results, corresponding to L_s = 70°, are used to initialize multiscale simulations, in which three nested domains are used. The nesting technique is based on introducing high-resolution "child grids" to the coarser grid that covers a larger region. Each "child grid" has a "parent grid", which provides boundary conditions for each time step. The model time step and grid spacing are reduced by a factor of three in each nest compared to its parent. The configuration of the nested domains is presented in Fig. 3.7, where the resolution of the finest grid is 33 km.

It should be noted that our purpose here is to illustrate the applicability of our new PBL scheme by reproducing near-surface observations, but not to investigate the micro-meteorological events at the InSight landing site. Along with horizontal resolution, vertical resolution also plays an important role in

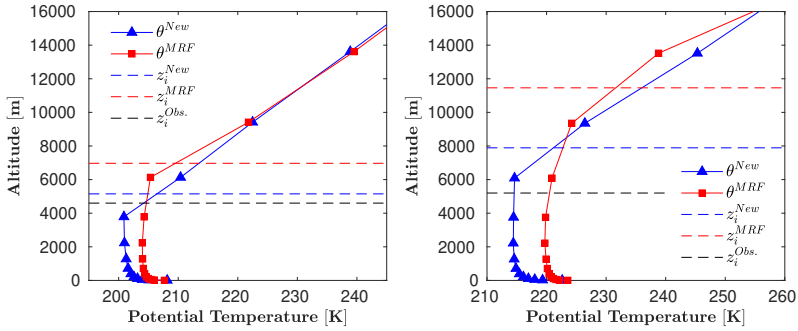

Figure 3.6: Vertical profiles of the potential temperature at 27.5° N, 107° W (left) and 21.8° N, 205° E (right), the reported locations of two radio occultations of MEX (Hinson et al., 2008). Blue and red solid lines with markers denote the θ predictions from our new scheme and the MRF scheme, respectively. Blue and red dashed lines show the PBL height estimations of our new scheme and the MRF scheme. Black dashed lines show the altitude above the surface, where the PBL height is diagnosed based on the MEX observations from Hinson et al. (2008). Note that the local time is 17.0h.

Layer	z [m]	Layer	z [km]	Layer	z [km]	Layer	z [km]
1	23.9	14	1.8	27	23.0	40	57.5
2	83.7	15	2.1	28	25.6	41	60.2
3	180.2	16	2.5	29	28.2	42	62.9
4	301.6	17	3.1	30	30.8	43	65.6
5	424.3	18	4.4	31	33.5	44	68.3
6	548.2	19	5.8	32	36.2	45	71.2
7	673.3	20	7.4	33	38.9	46	74.2
8	799.7	21	9.2	34	41.6	47	77.3
9	927.3	22	11.2	35	44.2	48	80.7
10	1056.3	23	13.3	36	46.9	49	84.5
11	1219.6	24	15.5	37	49.5	50	88.9
12	1418.2	25	17.9	38	52.2	51	94.0
13	1620.0	26	20.4	39	54.8	52	101.1

Table 3.2: Vertical grid configuration of MarsWRF: altitude of the center of the vertical layers above the ground level.

the representation of the planetary boundary layer. Vertical grid spacing is the same for each domain, and the altitudes of the centers of each vertical level are presented in Tab. 3.2. Within the first 3 *km*, which corresponds to the reported minimum daytime planetary boundary layer height (in Tab. 3.2), there are 16 vertical model levels located. Another important model parameter is the height of the first vertical layer. As PBL schemes use surface-layer parameterizations to determine turbulent fluxes for the first model layer, the first model layer must be located within the surface layer. As a rough approximation, the surface layer can be regarded as 10% of the boundary layer thickness. Based on radio occultations Hinson et al. (2008), minimum CBL height is around 300 m. In the present study, the first vertical layer is located at 24 *m*. Therefore, the vertical grid is sufficiently fine to resolve the convective atmospheric surface layer. However, for nighttime conditions, terrestrial studies show that the nocturnal boundary layer can be as shallow as 10 m Grachev et al. (2005). Therefore, for studies focused on the nighttime boundary layer, a much higher vertical resolution would be needed.

We compare a full diurnal cycle at the InSight landing site during Northern Hemisphere summer (L_s = 70°). Observed and predicted diurnal variations of air temperature and wind speed are shown in Fig. 3.8. Air temperature and wind speed observations from InSight are acquired at 1.2 *m* above ground level (AGL). It must be noted that the uncertainty of air temperature observations

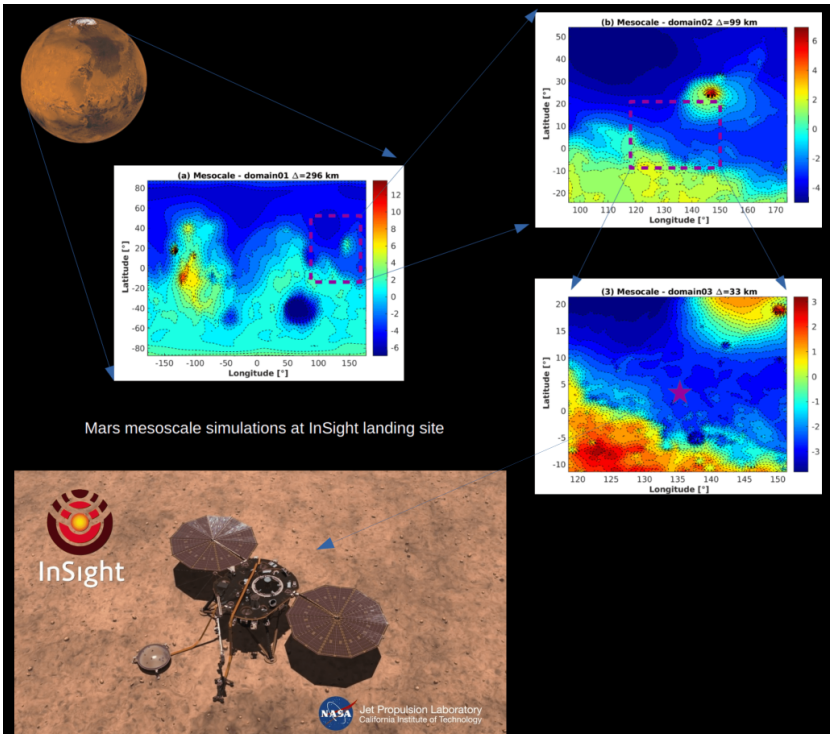

Figure 3.7: Global and mesoscale domains with terrain altitude (in km): d1 (Resolution: 298 *km*), d2 (Resolution: 99 *km*), d3 (Resolution: 33 *km*). The purple star at the center of innermost domain, d3, stands for the location of NASA's InSight lander, which is displayed at bottom-left (Credit: NASA Jet Propulsion Laboratory).

can be up to 10–15 K as a result of the interaction between the lander and sensors (see (Banfield et al., 2020) for details). The overall accuracy for temperature and wind speed observations are reported to be 5 K and 1 m/s (Banfield et al., 2020). As presented in Tab. 3.2, the first model layer of MarsWRF is located at 23.9 m. Similar to (Newman et al., 2017), air temperature model predictions are extrapolated to 1.2 *m* AGL, using the empirical relationships of the revised MM5 surface layer parameterization scheme, which is also the parameterization scheme used in our proposed turbulence closure to compute turbulent mixing in the planetary boundary layer.

The results show that the PBL scheme does not play an important role either in terms of near-surface temperature estimations. According to Earth-based studies (Gilliam and Pleim, 2010), it is found that the surface-layer and

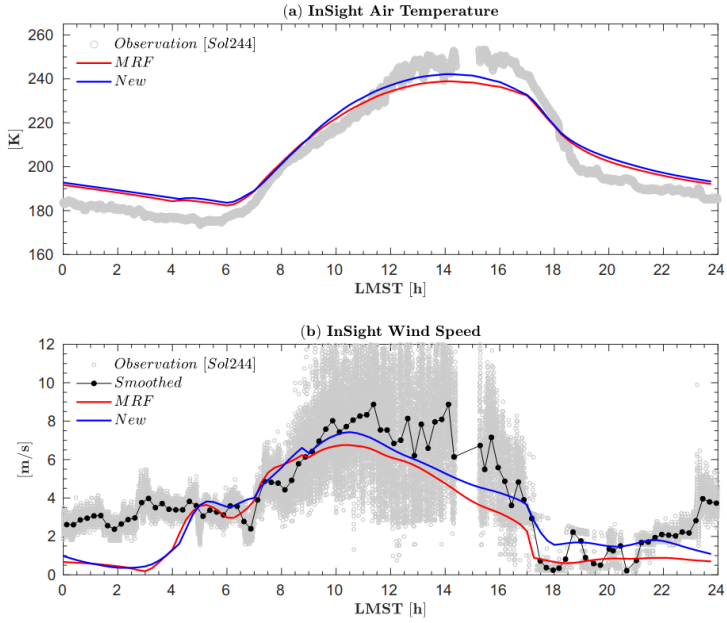

Figure 3.8: Observed and computed diurnal variations of air temperature (a) and wind speed (b). InSight observations, which are obtained each second, are smoothed by averaging for 15 min. MarsWRF output is for each 15 min. T_{air} and wind speed corresponds to the temperature and wind speed at the rover height (1.2 m).

subsurface models play an important role on the surface and near-surface temperature estimations, rather than the PBL schemes. Given the fact that the air density on Mars is much lower than on Earth, near-surface turbulent fluxes are also much lower; hence, the surface radiative heat balance, which is mainly influenced by the atmospheric dust content, plays a more important role in the prediction of surface temperatures on Mars. The only slightly significant difference is in the wind speed predictions. Soon after the sunrise at 7.0h LST, near-surface winds start to increase with the enhanced daytime convection. Between 08-10.0h LST, both schemes are able to predict the wind speed correctly at the InSight landing site. After reaching noon, the wind speed is underestimated by both schemes. However, for this time period (between 10-18.0h LST), the new proposed scheme works better than the MRF scheme. Despite the reasonable agreement with the observations, both schemes fail to correctly predict the wind speed before sunrise, when the boundary layer is stably stratified. Based on terrestrial studies, under stable

stratification, boundary layer can become as shallow as 10 m (Grachev et al., 2005). This might require a higher grid resolution close to the ground, which is not the case for this present study as the main focus is on the daytime Martian boundary layer.

3.3 Discussion & Conclusions

We present a parametric investigation of the Martian convective boundary layer using a set of LES results. Using the turbulent statistics acquired from the LES, a generic formulation for the turbulent mixing length scale is derived and incorporated within a PBL scheme. This study is devoted to illustrating the applicability of LES to better understand the turbulent processes within the PBL and generating datasets to inform the development of Mars-specific parameterization schemes. It must be noted that the investigation of stable (i.e., nighttime) atmospheric regimes are out of the scope of this study since it requires particular attention due to the existence of complex turbulence structures, e.g., low-level jets (Mahrt, 1998), shear instabilities (Holtslag, 2006) and strong intermittency of turbulence (Mahrt, 2014). Another difficulty in modeling stable boundary layers is correctly defining the surface boundary condition in order to properly reproduce small-scale structures. As another possible difficulty, it was suggested that imposing a sensible heat flux at ground level instead of a cooling rate becomes problematic, particularly for strongly stable conditions (Basu et al., 2008). Even though there are comprehensive LES investigations of the Earth's stable boundary layer, to the best of our knowledge, no LES studies have addressed the Martian stable boundary layer yet. Considering all these challenges for the stable atmosphere of Mars, this specific topic will be studied in-depth in future research.

Results of Martian LES reveal that the Martian daytime PBL is more vigorously convective (and produces more turbulence) than its terrestrial counterpart, leading to a deep convective boundary layer, reaching up to nearly 5 km over flat terrain during conditions of the maximum surface heating, i.e., 30 W/m^2. This surface heating rate can be considered as the mean value around the local noon (11-15 h) at Amazonis Planitia during Northern spring (see (Spiga et al., 2010)). However, the PBL height can be higher values for regions where the topography is complex, as observed by Hinson et al. (2008) from radio occultation measurements. They recorded that the Martian

CBL becomes deeper over complex terrains, e.g., in Tharsis, compared to 4-6 km over Northern plains, e.g. Amazonis Planitia. These values of CBL depth on Mars are significantly higher than the corresponding values for Earth over land ($\sim 1\ km$).

Our simulations show that the daytime convective velocity scale, as an indicator of the level of convection, is at about 6 m/s, which is 4 times stronger than a typical CBL on Earth in the late afternoon (time of peak convective activity). Moreover, we observe relatively higher turbulence kinetic energy values rising up to 17.3 m^2/s^2, around $z/z_i \sim 0.4$ on Mars, consistent with the simulations of Spiga et al. (2010). Higher turbulence kinetic energy recorded for the Martian daytime is related to its vigorous turbulence activity, stirring the air continuously due to the strong updrafts with vertical velocities up to 15 m/s. It is shown that these updrafts are not only active vertically, but also energetic in the horizontal direction spanning around 3 km in diameter. Furthermore, the turbulence dissipation rate reaches $\epsilon = 0.028\ m^2/s^3$ for the highest value of sensible heat flux we use.

For the first time, we investigate the energy spectra within the Martian PBL by making use of LES results. Within the surface layer, the LES for Martian CBLs display a spectral slope that matches well with the Kolmogorov's theoretical $-5/3$ cascade, i.e., $E(\kappa) \propto \kappa^{-5/3}$. However, above the PBL, we demonstrate that the portion of the energy spectra corresponding to small and dissipative eddies deviates from the theoretical slope. Therefore, in the case of intermittency (or the irregular alteration of turbulence) due to the low atmospheric density and strong buoyancy suppression due to the surface cooling, either for the nighttime stable PBL or for the free-atmosphere, the energy spectra might not be consistent with Kolmogorov's turbulence theory.

In the application phase, a planetary boundary layer scheme, based on a prognostic turbulence kinetic energy equation, is incorporated with the new turbulent mixing length scale. The new PBL scheme is implemented as a non-local turbulence kinetic energy closure in the MarsWRF model. The new length scale definition is built from a set of LES computations forced by a sensible heat flux from the ground in the convective regime. Despite the similar performance of the proposed Mars-specific and Earth-based PBL scheme for determining surface and near-surface meteorological conditions, the convective boundary layer heights are better estimated by the proposed scheme when compared to radio occultation results from orbiting spacecraft.

Chapter 4

General circulation modeling of Martian convective PBL with a new semi-interactive dust transport model[1]

4.1 Introduction

The Martian planetary boundary layer (PBL) is a vital component of climate dynamics, in which its dynamics are strongly affected by radiative, microphysical, and surface processes (Petrosyan et al., 2011). It is the lowermost and likely most active layer of the atmosphere (Spiga, 2019), in which turbulent motions govern the transport of momentum, heat, dust and volatiles between the surface and atmosphere (Michaels and Rafkin, 2004). This transport is mainly controlled by the diurnal variation in surface radiative forcing. During the daytime, surface radiative heating enhances the convective activity via buoyancy production, which is the production of turbulent convection. It results in a well-mixed boundary layer, referred to as the daytime PBL or convective boundary layer (CBL), composed of large convective eddies and deep thermal plumes (Stull, 2012). On the other hand, this process is reversed during the nighttime as the turbulent convection is suppressed by surface radiative cooling. It forms a very shallow layer on the order of tens of meters (Mason and Derbyshire, 1990; Smith et al., 2004), characterized by local shear instabilities (Banta, 2008) and intermittent turbulence (Sun et al., 2012). We see the signatures of the latter on Mars as detected by the InSight lander in

[1] This chapter is written based on the published article: Senel, C. B., Temel, O., Lee, C., Newman, C. E., Mischna, M. A., Muñoz-Esparza, D., ... & Karatekin, O. (2021). Interannual, seasonal and regional variations in the Martian convective boundary layer derived from GCM simulations with a semi-interactive dust transport model. Journal of Geophysical Research: Planets, 126(10), e2021JE006965. Here, Cem Berk Senel led the research conceptualization, model development and validation, formal analysis, simulations and visualization of results, and the writing of the manuscript.

Banfield et al. (2020), to be like the boundary layer formed over polar regions on Earth (Grachev et al., 2005). Unlike the quieter mode at night, the Martian convective boundary layer becomes highly turbulent, particularly in the local afternoon, in which the depth of the CBL can rise to in excess of 10 km (above the local surface) (Hinson et al., 2008). This is one order of magnitude deeper than a typical convective boundary layer formed on Earth, which is only on the order of ~1 km (Moeng and Sullivan, 1994; Gheynani and Taylor, 2010). This implies, accordingly, a more intensified diurnal contrast between daytime and nighttime on Mars than is encountered on Earth, as a consequence of the fact that Mars has a lower atmospheric density (Wilson and Hamilton, 1996; Larsen et al., 2002) and lower surface thermal inertia (Putzig and Mellon, 2007).

In addition to the intense diurnal variability, the Martian PBL exhibits seasonal and inter-annual changes, likely influencing the circulation dynamics and thermal composition of the atmosphere from the surface to the free atmosphere (i.e., the region above the PBL that is a stably stratified layer preventing the further growth of the PBL (Brooks and Fowler, 2012)). This variability is possibly modulated by the dust cycle on Mars (Haberle et al., 1982; Newman et al., 2002; Liu et al., 2003; Heavens et al., 2011b; Wolkenberg et al., 2018; Kass et al., 2020). In the meanwhile, the exchange of dust content between the surface and atmosphere is strongly influenced by PBL dynamics (Spiga, 2019). For instance, a stronger production of daytime turbulent convection exerted by strong radiative heating would impact the vertical dust distribution, injecting dust particles into the upper layers of the PBL (Guzewich et al., 2013a). This process is further enhanced, locally, by the presence of dust devils (Rennó et al., 2004; Spiga et al., 2016), which is one of the two main contributors of dust lifting besides the lifting by near-surface winds (Newman and Richardson, 2015). Such enhancement in lifting via dust devils and near-surface winds occurs in both hemispheres in local summer, as a consequence of high solar forcing and strong winds (Newman et al., 2019b). Besides, the Martian dust cycle features stronger dust events, such as regional and planet-encircling dust storms (Martin and Zurek, 1993). The latter are also known as Global Dust Storms (GDS), affecting the entire thermal and circulation structure of the planet from the lower atmosphere (Basu et al., 2006; Aoki et al., 2019) to the upper atmosphere (Fedorova et al., 2020; Liuzzi et al., 2020; Neary et al., 2020). GDS originate around southern spring equinox or summer solstice, lifting a large mass of dust and entraining it into the upper

layers of the atmosphere (Montabone et al., 2020), reaching nearly 80 km during a GDS's mature phase, as observed by the Mars Climate Sounder (MCS) (Kass et al., 2020). These storms encircle the planet, sustaining the transport of dust for a long period, from weeks to months (Guzewich et al., 2019). In such a way, GDS have a profound effect on PBL dynamics (Haberle et al., 1993), because the long-term presence of a global dust storm tends to continuously attenuate the surface net radiative heating as most of the incoming sunlight is absorbed by dust particles (Spiga, 2019). Three major GDS have been observed in the last 10 Mars years. These are recorded in Mars Years (hereafter MY) 25, 28, and recently, in MY 34 (Kleinböhl et al., 2020).

Moreover, the Martian PBL exhibits significant regional variabilities due to the complexity in geophysical properties of the terrain (i.e., thermal inertia and albedo) and elevation of Mars' topography. Mars, having steep mountains, deep canyons and large impact craters, has a severe surface heterogeneity. For instance, Olympus Mons is almost 25 km in height (Milkovich et al., 2006) and Valles Marineris is a canyon, that spans around 4000 km (Fueten et al., 2005). Such extremes in Martian topography make the local PBL exhibit more irregular spatial variability, producing highly turbulent gradients in near-surface winds such as katabatic and anabatic winds that are by two to three times more intense than the same winds on Earth (Spiga and Lewis, 2010). Here the anabatic winds refer to the upslope convective winds over mountains, craters and canyons (Newman et al., 2017), resulting in less turbulent convection at the onset of upslope winds, e.g., in the center of canyons (Spiga and Forget, 2009; Moores et al., 2015). As acquired by the Navigation Cameras (Navcams) onboard the Mars Science Laboratory (MSL), rover assisted by mesoscale simulations, Moores et al. (2015) found observational evidence for a severe suppression in the CBL along northern Gale crater in which fewer dust devils appear. This suppression was quantified with mesoscale simulations over Gale crater (Tyler and Barnes, 2013), showing CBL depth as shallow as 1–2 km within the crater unlike the exterior plains for which the CBL could reach depths of 10 km. More recently, Guzewich et al. (2017) determined the annual variation of the diurnal peak in CBL depth from MCS profiles, ranging between 2–5.5 km within Gale crater due to the suppression by daytime upslope winds. Newman et al. (2019a) use MarsWRF to show that, while the CBL is suppressed in the crater trench for about half the Mars year (including the landing period, L_s ~150°), the peak CBL depth is

actually predicted to be enhanced in the crater trench, compared to Mt. Sharp, during southern summer and surrounding period. Newman et al. (2019a) also suggest that it is the sensible heat flux, based on the near-surface temperature gradient and wind stress, not the CBL depth, that has the biggest impact on finding more dust devils as one moves up the slopes, while the CBL depth appears to have a larger impact on seasonal variations.

On the other hand, the depth of the CBL on Mars is also influenced by the elevation of the topography (Pätzold et al., 2016). Hinson et al. (2008) determined the CBL depth from radio occultation (RO) measurements by the Mars Express (MEX) orbiter with a horizontal resolution of 400 km (i.e., nearly 7° resolution in the longitudinal direction along the equator). These radio occultations cover the latitudes between 15°S and 54°N at 38 locations during the northern mid-spring of MY 27 (L_s = 34.7° – 69.2°). By these experiments, they found a significant correlation between the terrain elevation and CBL depth with shallow CBL formations in Utopia and Amazonis Planitia (e.g., 4-6 km) becoming deeper at higher terrains, for instance around Syrtis Major and Tharsis Montes (e.g., 8-10 km). Hinson et al. (2019) later relate this dependence to the surface potential temperature, combining radio occultations with infrared sounding. Their results indicate that the CBL depth exhibits high spatial variability ranging from a few kilometers up to in excess of 9 km between lower and higher terrains, while a gradual variability appears in terms of seasonal change (e.g., ~1 km increase in CBL depth) as these measurements are collected during the northern mid-spring and late winter of MY 27 as well as in the early spring of MY 28 (in early to late afternoon at 118 locations).

To date, studies addressing the Martian planetary boundary layer have presented crucial insights into its depth (Hinson et al., 2008, 2019), turbulent circulations (Paton et al., 2018), thermal structure (Hamilton et al., 2014) and dust activity (Banfield et al., 2020; Perrin et al., 2020), inferred from either in-situ or orbiting satellite observations. Using ground-based observations in combination with similarity theory, the Martian PBL depth was estimated at the Viking and Phoenix landing sites in Martínez et al. (2009). Meanwhile, there have been numerical efforts using turbulence-resolving large-eddy simulations (LES) at microscale grid resolutions (Michaels and Rafkin, 2004; Spiga and Lewis, 2010; Temel et al., 2020), mesoscale simulations on regional domains (Tyler and Barnes, 2013; Guzewich et al., 2017; Fonseca et al., 2018) and the general circulation model (GCM) simulations of CBL at

planetary scales (Colaïtis et al., 2013). However, all these efforts are limited to either specific locations or particular time episodes in a given season or year, due to the observational limitations or high computational demand of the numerical simulations. Therefore, in the present study, our aim is to conduct a comprehensive investigation of the spatial and temporal variability of the Martian CBL derived from GCM simulations. More specifically, this variability is examined on inter-annual, seasonal and regional spatio-temporal scales over the last decade of Martian Years (from MY24 to MY34). Thus, our study focuses into dust-CBL interactions while GDS encircle the planet. It is worth noting that the current study is primarily devoted to the daytime convective boundary layer. The reason is that the whole representation of the nighttime stable PBL (i.e., SBL) ranging between the order of tens to hundreds of meters in depth (Spiga, 2019; Davy et al., 2010), is likely to require turbulence resolving large-eddy simulations due to the presence of smaller eddy sizes as well as the complexity of stably stratified intermittent turbulence (Kosović and Curry, 2000; Senel et al., 2019; Temel et al., 2020). However, the effect of nocturnal turbulence can be implicitly parameterized, so that our Martian PBL scheme switches to the SBL mode, by incorporating the SBL mixing length definition of MYJ scheme (Janjić, 1994) based on classical Blackadar formulation (Blackadar, 1962b). However, a Mars-specific nighttime SBL model is essential for more advanced representation of the nocturnal turbulence, which will be studied in-depth in future research.

In Sec. 4.2.1-4.2.2, we present the methodology, describing the MarsWRF GCM (Richardson et al., 2007) and details of the physical models used. We also validate the model's dust processes by comparing the simulated dust distribution to that observed by MCS. Sec. 4.2.3 describes the GCM experiments giving computational details, then the results in terms of inter-annual, seasonal and regional variations in the Martian CBL, and a comparison between the modeled CBL depths by comparing with MEX radio occultation (RO) measurements. Finally, Sec. 4.2.4 presents our conclusions and discussions.

4.2 Theory & Modeling

4.2.1 Description of the MarsWRF general circulation model

To perform GCM simulations, we utilize the MarsWRF model, which is the Mars version of the planetWRF model (Richardson et al., 2007; Toigo et al., 2012; Newman and Richardson, 2015) based upon the terrestrial Weather Research and Forecast (WRF) model (Skamarock et al., 2008b). In MarsWRF, we use the two-stream correlated k-distribution scheme for the shortwave and longwave radiative transfer (Mischna et al., 2012). To model the turbulent mixing of momentum, heat, dust and aerosols between the surface and atmosphere, we use our recent implementation of a Mars-specific PBL scheme (Temel et al., 2020), using a local and 1.5-order turbulence kinetic energy (TKE) closure scheme, in which the nonlocal transport of buoyant plumes is treated based on the scheme presented in Therry and Lacarrère (1983). Our model incorporates a generic formulation for the mixing length scale in Mars-specific conditions, over a wide range of convective instabilities. For the physical description and its performance compared to a terrestrial scheme with respect to MEX radio occultation observations (Hinson et al., 2008) and near-surface wind measurements from the InSight lander (Banfield et al., 2020), the reader is referred to Temel et al. (2020). The MarsWRF model has also been widely validated against remote-sensing and in-situ pressure and temperature observations (Guo et al., 2009; Temel et al., 2019; Toigo et al., 2012; Newman and Richardson, 2015). The vertical exchange of momentum, heat and tracers at the surface is treated by the MarsWRF implementation of the revised MM5 scheme (Jiménez and Dudhia, 2012). Moreover, surface properties of the MarsWRF model, such as the topography, albedo, emissivity and thermal inertia, are acquired from the datasets of the Mars Orbiter Laser Altimeter (MOLA) (Smith et al., 2001) and Thermal Emission Spectrometer (TES) (Christensen et al., 2004) observations, where the details are presented in Richardson et al. (2007).

4.2.2 Development of a new semi-interactive dust transport scheme

The dust cycle is the most profound driver of the Martian climate; thus, capturing the time-evolving dust distribution correctly is extremely important for simulating a realistic climate. One approach is fully-interactive dust

modeling (Newman and Richardson, 2015; Lee et al., 2018) in which the dust transport is freely sustained without any observation-based constraints. This way would reproduce the dust cycle realistically, even when there are no observational data to guide the GCM. However, it brings limitations in properly predicting the onset time, period, intensity and location of dust storms, in comparison with observations. To handle this incompatibility, recently, Newman et al. (2019b) made an initial assessment of a GCM simulation including orbit-spin coupling on Mars. Even though the coupling term acceleration leads to an increase in the inter-annual variability of global dust storms, further refinement is still needed to capture the onset and size of global dust storms consistently.

As yet, no Mars GCM can spontaneously generate all types of observed dust storms (in terms of onset timing, location, evolution, etc.), let alone the occurrence of a particular type and size of large dust storm in the Mars year it was observed. Attempts to improve this are ongoing, and include considering the limited availability of surface dust where the surface dust abundance is imposed as finite unlike an infinite dust source (Newman and Richardson, 2015), orbit-spin coupling (Newman et al., 2019b), and coupling of the dust and water ice cycles (Kahre et al., 2011, 2015; Madeleine et al., 2011, 2012; Navarro et al., 2014; Lee et al., 2018). But, it is necessary to guide GCMs using observations in some way, if the impact of dust storms in a given Mars year is to be as realistic as possible. Possible approaches include: prescribing a 2D dust distribution based on 2D dust observations and using a modified Conrath profile (hereafter referred to as a prescribed dust scheme) to determine the vertical variation (Conrath, 1975; Forget et al., 1999); prescribing the 3D dust distribution using TES limb and nadir dust observations (Guzewich et al., 2013b); data assimilation of observed temperatures or radiances (Lewis et al., 1999; Greybush et al., 2012; Lee et al., 2011); prescribing dust lifting based on observations (Kahre et al., 2009; Bertrand et al., 2020); and just as the present work, the semi-interactive scheme in Madeleine et al. (2011) involves rescaling the dust column based on opacity maps. It is worth noting that the semi-interactive approach differs from models in which dust is not transported in the atmosphere. In such models (e.g., the prescribed dust scheme), the vertical distribution of dust must be prescribed assuming a spatially uniform dust distribution, such that the dust opacity monotonically decreases with altitude. Nevertheless, such a prescribed dust scheme is unable to reproduce

well the enhanced dust layers at high altitudes, i.e., 15–25 km, over the tropics as observed from the MCS (Heavens et al., 2011b,a), or the detached dust layers due to rocket dust storms (Spiga et al., 2013; Wang et al., 2018). This motivates our approach of allowing dust to be advected by model winds, mixed by turbulent processes, and sedimented out.

To accomplish this, we adapt the existing dust transport scheme of MarsWRF (i.e., a two-moment dust transport scheme) by Lee et al. (2018) to a semi-interactive mode. The original scheme treats the atmospheric dust transport by means of a two-moment approach based upon the terrestrial Morrison and Gettelman (2008) microphysics scheme. The two-moment framework of Lee et al. (2018) enables us to transport the dust advecting and diffusing in the atmosphere as two independent tracers: the mass density (q) and number density (N) of dust, where the dust particles are considered to follow a gamma function (Lee et al., 2018). The original scheme treats these tracers as $q = \frac{\pi\rho_p}{6}M_3$ and $N = M_0$, where ρ_p is the dust particle density and M_p denotes the p^{th}-order moment of the gamma size-distribution as

$$M_p = \int_0^\infty D^p N(D) = \frac{N_0}{\lambda^{\mu+p+1}}\Gamma(\mu + p + 1) \tag{4.1}$$

where $N(D)$ is the gamma distribution of number density as a function of the particle diameter, D. In Eq. 4.1, Γ refers to the integral of the gamma function in terms of intercept (N_0), shape (μ) and slope (λ) parameters as described in Lee et al. (2018). As the gamma size-distribution requires the value of μ, we set $\mu = 1$ following Lee et al. (2018), leading to a corresponding value for the effective variance of the gamma size-distribution, i.e., such that $v_{eff} = (\mu+3)^{-1} = 0.25$, which satisfies the range ($0.2 < v_{eff} < 0.8$) given in Wolff et al. (2006).

The two tracers in the two-moment framework of Lee et al. (2018), i.e., q and N, are related as

$$q = N\frac{4\pi\rho_p r_{eff}^3}{3}\frac{(\mu+2)(\mu+1)}{(\mu+3)^2} \tag{4.2}$$

in terms of the dust effective radius of the gamma-size distribution, $r_{eff} = M_3/2M_2 = (\mu+3)/(2\lambda)$, where the initial value of r_{eff} is set to 2 μm as in Lee et al. (2018).

After having the mass density of dust, q, or, alternatively, the dust mixing ratio, in Eq. 4.2, the distribution of the dust optical depth field, τ_d, is computed following Forget et al. (1999) and Wang et al. (2018).

$$d\tau_{d,si} = \frac{3}{4}\frac{Q_{ext,\lambda} q}{\rho_p r_{eff} g} dp \tag{4.3}$$

where $\rho_p = 2500$ kg/m^3 is the dust particle density, $g = 3.72$ m/s^2 is the gravitational acceleration, dp is the pressure gradient between vertical model layers and $Q_{ext,\lambda}$ refers to the dust extinction efficiency at the particular wavelength under consideration.

Applying a column integration to the $d\tau_{d,si}$ in Eq. 4.3 field returns

$$\widehat{\tau}_{d,si} = \int_{column} d\tau_{d,si} \tag{4.4}$$

where $\widehat{\tau}_{d,si}$ is the column integral of dust opacity. Up to this point, the dust distribution is self-consistently determined by the modeled circulation and parameterized dust processes. However, we now scale this opacity using the column dust climatology observations of Montabone et al. (2015, 2020) (which is based on TES (Christensen et al., 2001), Thermal Emission Imaging System (THEMIS) (Christensen et al., 2004) and MCS (McCleese et al., 2007) observations available between MY 24 and MY 34), to find a scaling ratio as follows

$$\alpha_{scale} = \frac{\widehat{\tau}_{d,obs}}{\widehat{\tau}_{d,si}} \tag{4.5}$$

This is used to scale the dust opacity field in each radiative transfer time-step, which is $\Delta t_{ra} = 15$ min for the present GCM simulations. As the reference observations of Montabone et al. (2015, 2020) are two-dimensional maps of the daily column-integrated dust opacity, rescaling to observations at a given instant within the day is determined by the linear interpolation between two successive days. It results in the scaled semi-interactive dust opacity field

$$\widetilde{\tau}_{d,si} = \alpha_{scale}\, d\tau_{d,si} \tag{4.6}$$

which is then used by the model radiative transfer scheme. Here, the dust transport model we use is coupled to the correlated k-distribution radiation scheme of Mischna et al. (2012). The size-dependent extinction efficiencies, $Q_{ext,\lambda}$ as well as radiative scattering properties needed for radiatively active transport of dust particles, are treated by the two-moment framework of Lee et al. (2018).

In addition to the rescaling of the dust opacity field in Eq. 4.6, we guide two

transported tracers, q and N, using the computed scaling ratio α_{scale} (Eq. 4.5), in each radiative transfer time-step as follows

$$\begin{aligned} \widetilde{q}_{si} &= \alpha_{scale}\, q \\ \widetilde{N}_{si} &= \alpha_{scale}\, N \end{aligned} \tag{4.7}$$

where $\widetilde{q}_{si}$ and $\widetilde{N}_{si}$ are the scaled semi-interactive tracers, then being used by the radiative transfer scheme. This final step, i.e., scaling of q and N, is quite essential to be able to consistently reproduce the dust storm onset and occurrence.

It is worth adding that the process of dust lifting, by either dust devils or near-surface winds, follows the method of Newman and Richardson (2015).

4.2.3 Verification of the new dust transport model

The proper modeling of the dust cycle is of particular importance in terms of having more realistic CBL-dust interaction, especially within the lower atmosphere. Thus, the validity of the presented dust transport scheme is investigated, comparing the current GCM simulations to the MCS observations from Forget and Montabone (2017) and Kleinböhl et al. (2009) (from 12:00h-16:00h local time). To this end, Fig. 4.1a-b displays the vertical evolution of daytime dust mixing ratio at Oxia Planum (i.e., the landing site for ExoMars 2022) (335.45°E, 24.55°N) from our GCM simulations against the MCS retrievals, during the northern late winter (L_s ~320°) in Mars years 31 and 32.

In both simulated Martian years, our MarsWRF GCM simulations match well with MCS observations of dust mixing ratio from the CBL (below ~10 km in altitude) to the upper atmosphere (~60 km). Within the convective boundary layer in MY 31 and MY 32, the predicted dust mixing ratios in the GCM are consistent with those retrieved from MCS observations. In addition, the GCM simulations of MY 31 and MY 32 reproduces a high altitude tropical dust maximum (McCleese et al., 2010; Heavens et al., 2011a), which originates at ~30 km. Moreover, in Fig. 4.1c-f, we compare our GCM results with the available MCS observations (Heavens et al., 2011b) at different locations and seasons, such as in north of Valles Marineris (MY29, L_s ~163°), southwest of Amazonis Planitia (MY29, L_s ~165°), west of Huygens Crater (MY29, L_s ~166°) and southwest of Gusev Crater (MY30, L_s ~90°). For

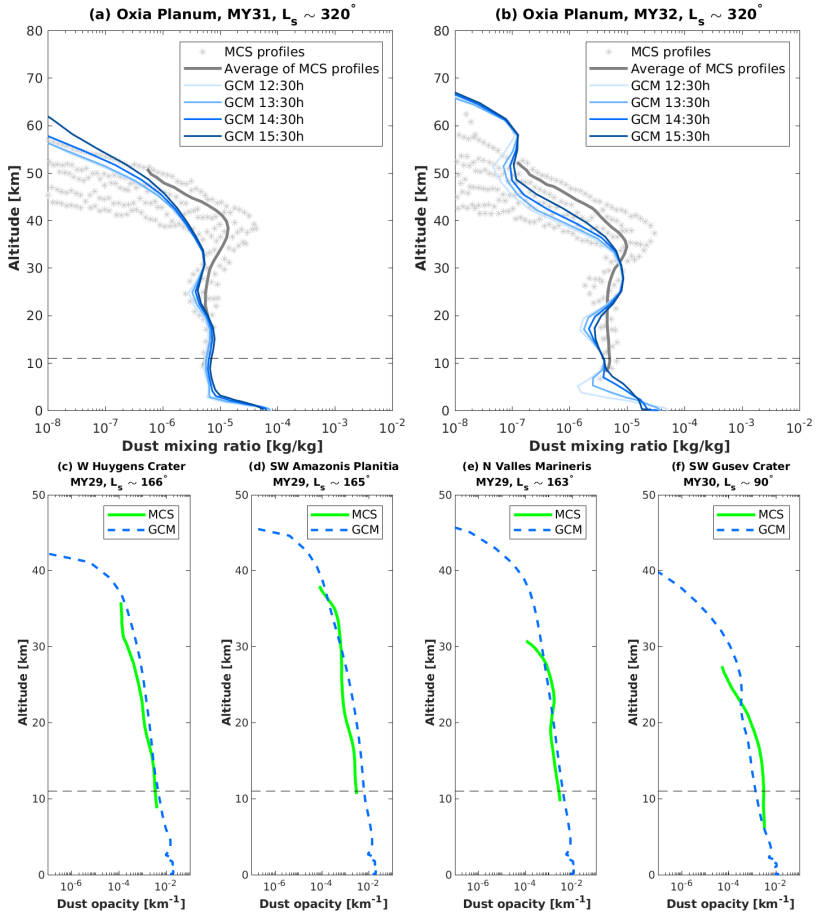

Figure 4.1: Vertical profiles of dust mixing ratio $[kg/kg]$ at Oxia Planum (335.45°E, 24.55°N) in the northern late winter for Mars years **(a)** 31 and **(b)** 32. Colored solid lines indicate results from GCM simulations at local afternoon, from 12:30h to 15:30h. Gray markers refer to the whole available vertical MCS observations falling into local time between 12:00h–16:00h as reported in Forget and Montabone (2017), while the gray solid lines correspond to the mean of given vertical profiles having relative uncertainties in the dust opacity lower than 1 (see the details in Forget and Montabone (2017)). Vertical profiles of daytime dust opacity $[km^{-1}]$ from GCM (blue dashed lines) and MCS observations (Heavens et al., 2011b) (green solid lines) at following locations and seasons: **(c)** West of Huygens Crater (MY29, L_s ~166°), **(d)** Southwest of Amazonis Planitia (MY29, L_s ~165°), **(e)** North of Valles Marineris (MY29, L_s ~163°), **(f)** Southwest of Gusev Crater (MY30, L_s ~90°). The horizontal dashed line in each panel displayed is the reference scale-height of Mars, i.e., 11 km.

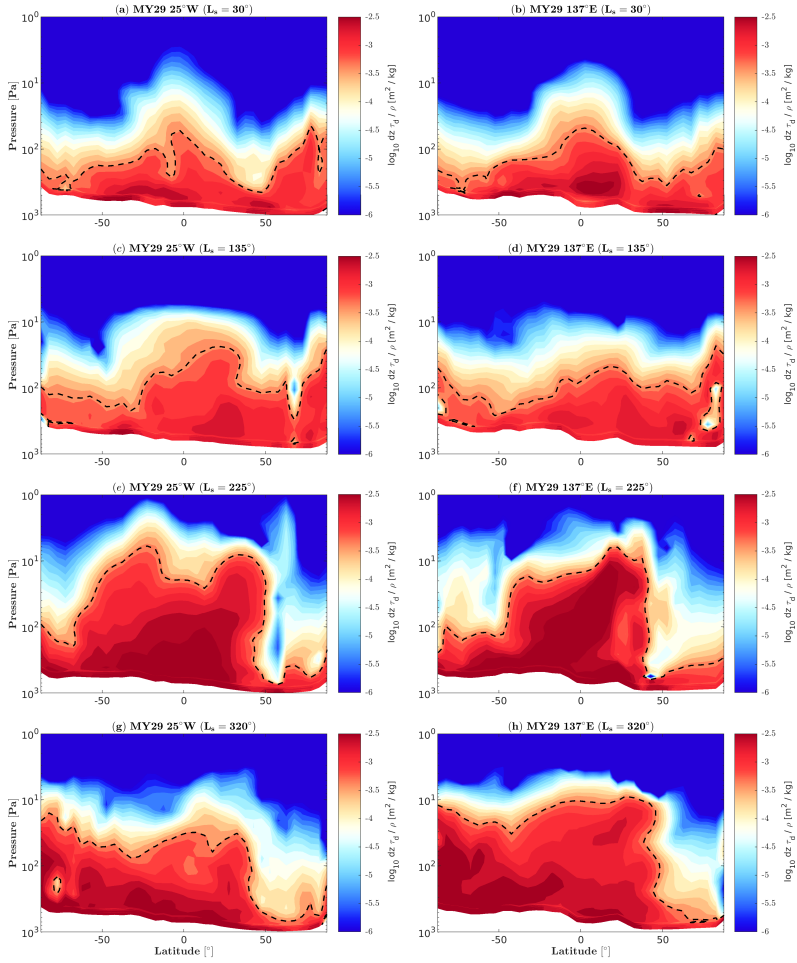

Figure 4.2: Seasonal variation of density-scaled dust opacity, $log_{10}\ dz\tau_d/\rho\ [m^2/kg]$ in MY 29 at $t = 15h$ (LMST). Latitudinal and vertical cross-sections are plotted at two longitudinal locations over $25°W$ (left panels) and $137°E$ (right panels). Black dashed lines represent the dust-top height, calculated at the altitude where the $\bar{\tau}_d = -3.3$, following Wu et al. (2020).

these additional profiles, vertical variation of simulated dust opacity values are consistent with the MCS retrievals.

Fig. 4.2 shows the seasonal variation of density-scaled dust opacity, calculated as follows

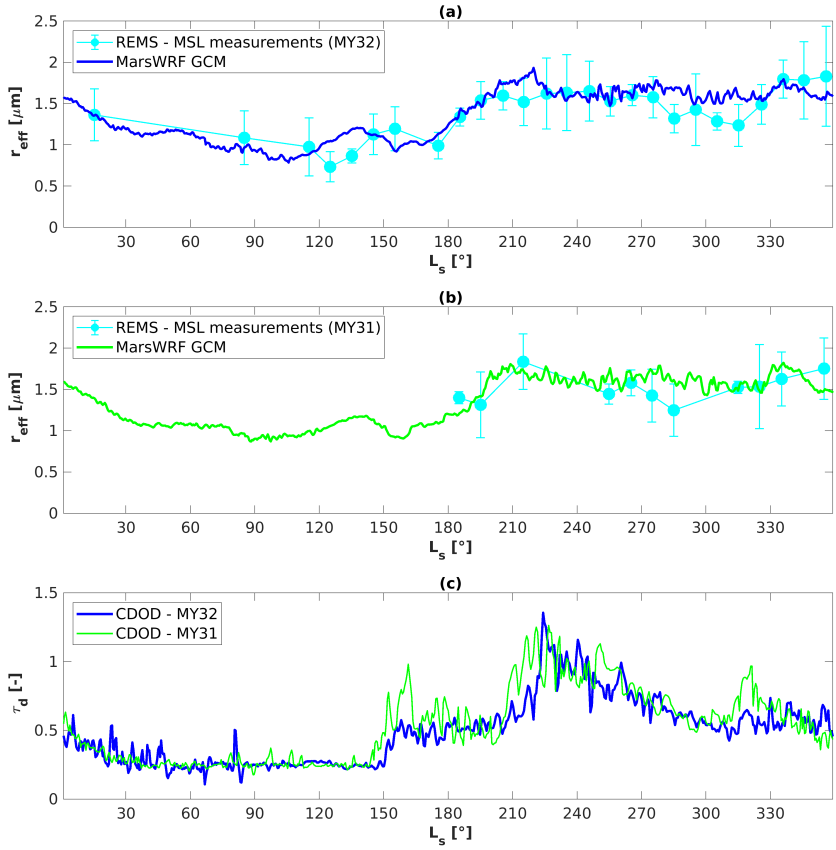

Figure 4.3: Seasonal evolution of dust particle effective radius through MY 32 **(a)** and MY 31 **(b)** above Gale crater. Blue (MY 32) and green (MY 31) solid lines show our GCM simulations with semi-interactive dust transport model. Light-blue solid lines with error bars refer to the rover measurements using the UV sensor (UVS) of the Rover Environmental Monitoring Station (REMS) and the Mastcam instrument, from Vicente-Retortillo et al. (2017). **(c)** Seasonal variation of column dust optical depth (CDOD) referenced to 700 Pa based on the dust climatology observations of Montabone et al. (2015) in MY 31 and MY 32.

$$\overline{\tau}_d = log_{10}\, dz\tau_d/\rho \;\; [m^2/kg] \tag{4.8}$$

where τ_d is the dust opacity, ρ is the atmospheric density and dz refers to the vertical thickness of the atmospheric layer (McCleese et al., 2010).

The latitude-height cross-sections are computed locally at 15h (LMST) for two longitudes: 25°W (passing through Oxia Planum) and 137°E (along Gale crater and Elysium Planitia, landing sites of MSL rover and InSight lander). For both longitudes, dust distribution contours confirm the enhancement in dust content during the dust storm season (L_s ~225°) compared to the northern spring (L_s ~30°) and summer seasons (L_s ~135°). To illustrate, the dust height maximum is at nearly 25 Pa (~32 km) before the dust storm season; however, it grows to as deep as 6 Pa (~47 km) due to the regional dust storms after L_s ~180°. The seasonal evolution of dust-top height is consistent with MCS retrievals of the dayside density-scaled dust opacity (see their Fig. 11 in McCleese et al. (2010)).

Furthermore, not only the dust-top altitude, but also the dust loading increases around L_s ~225°, where the dust cycle reaches nearly its peak activity as can be seen in column dust climatology observations (Montabone et al., 2015). Our GCM results during this period exhibit a sudden drop in dust content in the vicinity of 50°N. This structure, which can be interpreted as an abrupt dust content deficit, is also present at the same location in the Mars Climate Sounder (MCS) observations of McCleese et al. (2010).

In Fig. 4.3, we compare the seasonal evolution of dust effective particle radius retrieved from our GCM simulations, with respect to rover measurements at Gale crater. The measurements are obtained during the dust storm season of MY 31 and over a complete period of MY 32 using the UV sensor (UVS) of the Rover Environmental Monitoring Station (REMS) and the Mastcam instrument (Vicente-Retortillo et al., 2017). Results show that our GCM estimates exhibit a clear seasonal pattern matching well with the rover measurements, in which both GCM and measurements decrease from 1.4 μm in northern early spring to 0.9 μm in northern summer when the column-integrated dust opacity is as low as $\tau_d = 0.3$ (before the dust storm season). However, dust r_{eff} values are considerably enlarged with the growing dust activity in dust storm season where the column-integrated dust opacity exceeds ~ 1.

4.2.4 Martian GCM results: Seasonal and inter-annual variations

Thanks to observations by recent in-situ and orbiter missions, current knowledge of the Martian convective boundary layer has been progressing

in terms of observing day-side characteristics for particular locations. Nevertheless, long-term variations (i.e., seasonal and year-to-year) on a more global scale are less well constrained. To probe the long-term behavior of Martian boundary layer activity, we assess a decade-long GCM simulation from MY 24 through MY 34, using our Mars-specific PBL scheme (Temel et al., 2020) and the present semi-interactive dust transport model. Note that we use a 5°x5° spatial grid resolution with 52 vertical sigma layers extending up to a model top of ~100 km. As this decade has three GDS in MY 25, MY 28 and MY 34, particular attention is given to the impact of GDS on the planetary boundary layer.

We investigate first the seasonal and inter-annual trends in convective boundary layer activity by discussing two recent Martian years, MY 33 and MY 34. Given the fact that the global dust storms are an important perturbing force in the present Martian climate, the chosen years, MY 33 (without a GDS) and MY 34 (with a GDS), allow us to deduce the extent of the CBL response to the GDS. Therefore, in Fig. 4.4, the annual variation of CBL diagnostics are illustrated for MY 33 over the full span of latitudes.

In Fig. 4.4a, the zonal averaged CBL depth evolution is displayed through MY 33, which is one of the key parameters characterising CBL dynamics. Here, the depth of CBL refers to the altitude that marks the transition from a highly turbulent convective atmosphere below, to the non-turbulent, stable, free-atmosphere above. In other words, the depth of the CBL marks the upper boundary of a highly turbulent region, being well-mixed by means of highly-energetic eddies and deep convective plumes. We determine the top of CBL in the GCM, via our PBL scheme implementation (Temel et al., 2020), as the first vertical sigma level where the local potential temperature, θ_σ, surpasses the potential temperature of the mixed-layer, θ_m, by a threshold of $\Delta\theta_t = 0.5$ K. The given approach is referred to as the θ-increase method, derived from terrestrial assessments (Heffter, 1980; Nielsen-Gammon et al., 2008; Hu et al., 2010). Note that the mixed-layer here corresponds to the major portion of CBL, i.e., from about 10% to 85% of the CBL depth, where the turbulence leads to well-mixed exchange of momentum, heat and aerosols (Stull, 2012; Hinson et al., 2019; Senel et al., 2020b). The mixed-layer lies over the atmospheric surface layer (i.e., the lowermost portion of the CBL, up to 10% of CBL depth), with an almost uniform θ that is nearly equivalent to the base potential temperature of the surface layer. Note that the atmospheric surface

layer refers to the lowermost portion of the CBL, extending from the surface up to the Monin-Obukhov length, which is typically of the order of tens of meters (Martínez et al., 2009; Davy et al., 2010). Separate from the θ-increase method, the depth of the CBL is calculated in the RO experiments based upon the vertical gradient of potential temperature, i.e., the static stability method. This approach treats the CBL depth as the first model layer when the local vertical gradient of potential temperature reaches a threshold lapse rate of 1.5 K/km.

Fig. 4.4a, more specifically, shows the CBL depth evolution for the local afternoon at t=15h, when the convective boundary layer activity can nearly reach its peak activity (Spiga et al., 2010; Martínez et al., 2009). Note that the results here are displayed in terms of zonally averaged values (i.e., averaging the values in the longitudinal direction at a fixed local time, t=15h), to see the CBL depth variabilities through the meridional direction over different seasons. For detailed spatial variations towards both zonal and meridional directions in CBL characteristics, see Sec. 4.2.5. In Fig. 4.4a, the peak CBL depth has a seasonal pattern that is roughly symmetric about the equator, propagating to the northern tropics (~20-30°N) during northern summer and then back to the southern tropics (~20-30°S) during the northern winter. This seasonal variation results in two seasonal maxima in CBL depth, of up to ~9 km, which correspond to the peak convective heating of the surface during local summer. The latitudinal variation of the peak CBL depth as a function of season coincides nearly with the location of Hadley cell convection, shifting up and down toward the tropics during northern summer and winter seasons (i.e., in line with the surface temperature evolution in Fig. 4.4d). As the convective boundary layer deepens more, which is enhanced by the abundance of turbulent convection (see Sec. 4.1), these two maxima represent the extremity of production rate in terms of turbulent convection, where the boundary layer rises to in excess of 9 km in depth.

To clarify this better, the annual variation of surface kinematic heat flux, q_s is presented in Fig. 4.4c and Deardorff's convective velocity scale (also known as the convective velocity), w_*, is shown in Fig. 4.4e. The first parameter, $q_s = \mathscr{H}_s/(\rho_a C_p)$, is the measure of convecting heat flux from the surface, defined as the surface sensible heat flux, $\mathscr{H}_s$, normalized by the specific heat capacity, $C_p = 740\ JK^{-1}kg^{-1}$ and the surface air density, ρ_a, (Petrosyan et al., 2011). The second parameter, $w_* = [(g/T_s)q_s z_i)]^{1/3}$, is Deardorff's velocity

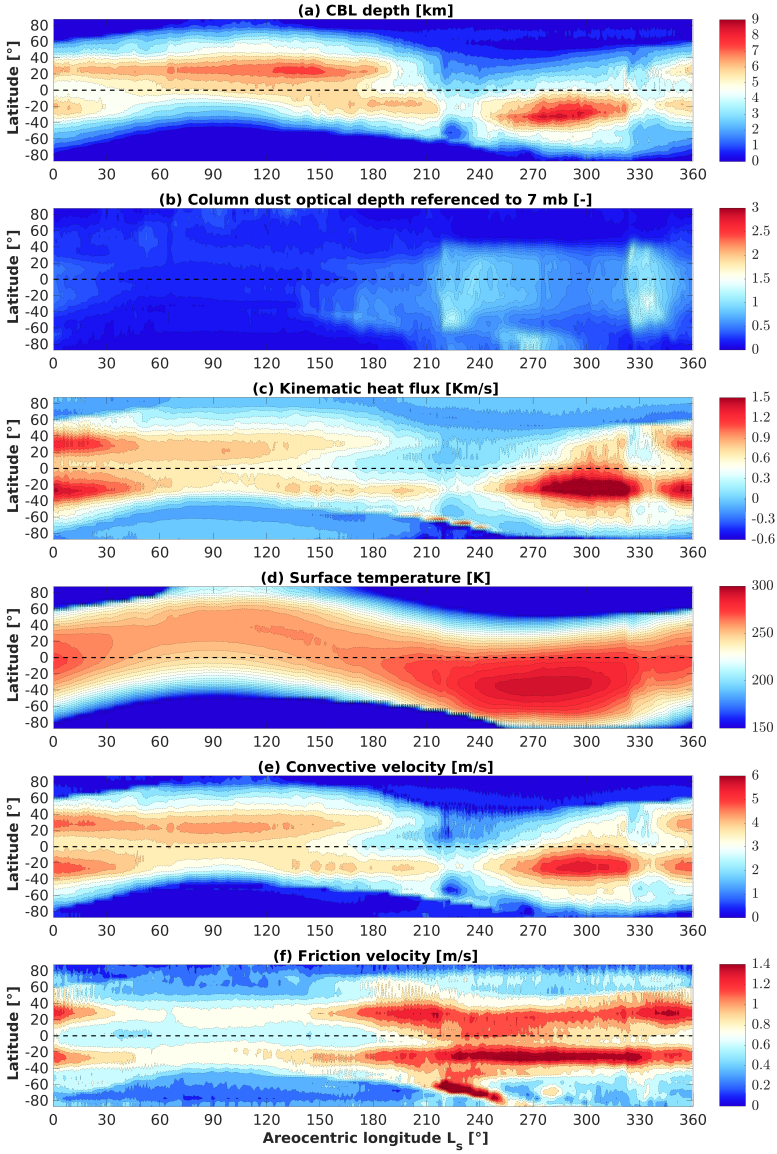

Figure 4.4: Annual variation of the zonally averaged **(a)** CBL depth, **(b)** column dust optical depth referenced to 7 mb, **(c)** surface kinematic heat flux, **(d)** surface temperature, **(e)** Deardorff's convective velocity, **(f)** friction velocity. Here, the simulated case is Mars Year 33 in the local afternoon, $t = 15h$ (LMST). Note that the colorbar limits are set to same range as in Fig. 4.5.

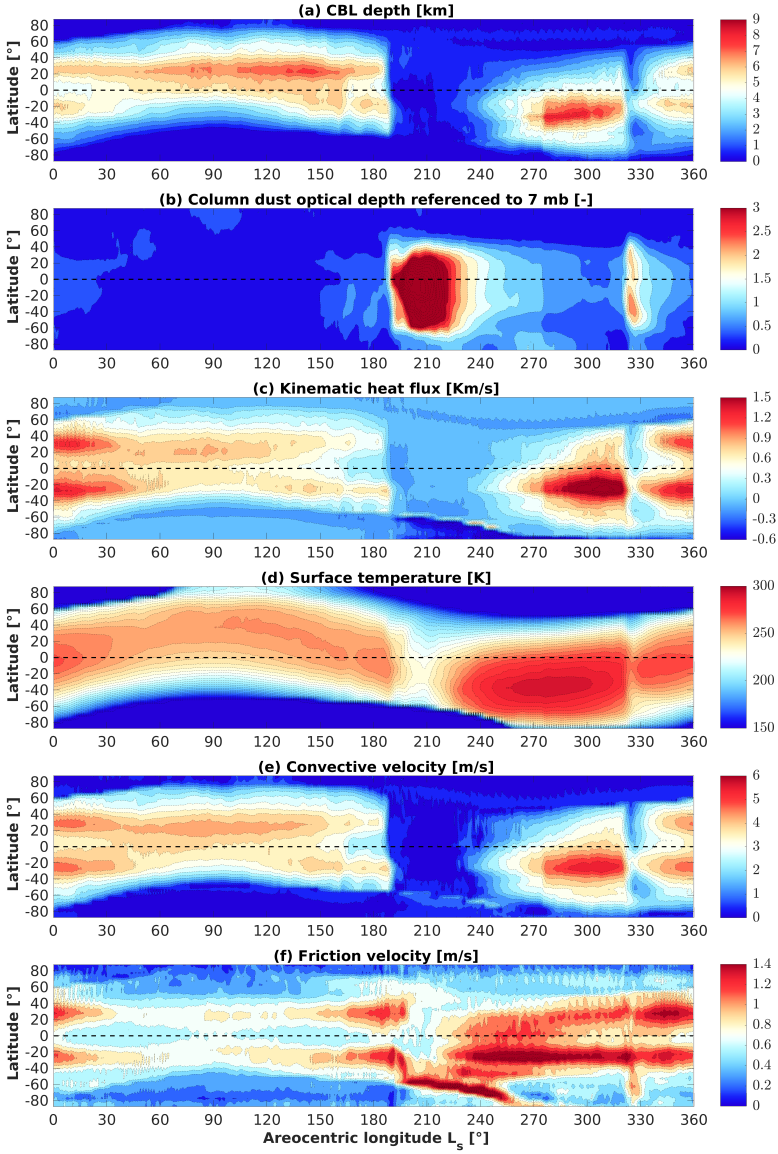

Figure 4.5: As in Figure 4 but now showing results for Mars Year 34

scale, which represents the speed of turbulent convection (Deardorff, 1970), where $g = 3.72$ m/s^2 is the average gravitational acceleration on Mars, T_s is the surface temperature, and z_i is the CBL depth.

Remembering that the planetary boundary layer is exposed to growing surface solar heating especially around the local noon (Newman et al., 2019a; Ordonez-Etxeberria et al., 2018), this tends to intensify the surface heat flux of rising convective plumes, q_s, which moves upward faster as given by the convective velocity, w_*. Therefore, the depth of the CBL, z_i, is positively correlated with the enhancement in q_s and w_*. In other words, the lower (higher) q_s and w_* are, the shallower (deeper) the planetary boundary layer is.

In Fig. 4.4a, the CBL depth during MY 33 is as shallow as a few kilometers at higher latitudes and in the vicinity of the polar caps. Yet, it is as deep as ~9 km around the tropics, even exceeding 9 km in depth around the northern mid-summer. This broad range is consistent with the radio occultation measurements of Hinson et al. (2008, 2019) in which the daytime CBL depth ranges between 1-10 km. In these measurements, the depth of CBL ranges from a few kilometers in high latitudes (i.e., z_i = 1.5 km) up to depths as deep as z_i ~9-10 km through the tropics. This significant change is largely driven by the inter-relation of turbulent convection and shear forcing, as explained below.

Given the seasonal evolution of turbulent convection in Fig. 4.4c-e, it likely confirms the positive correlations of q_s and w_* with the CBL depth. However, the periods of northern early spring (L_s ~0-30°) and from the northern late summer to the early autumn (L_s ~150-210°) are an exception, due to the negative feedback of high shear production on the growth of convective boundary layer. The latter is given in terms of friction velocity, u_*, (Fig. 4.4f), indicating high friction velocities in these two particular periods, i.e., compared to the typical mean daytime value of the Martian CBL, being approximately 0.4 m/s (Petrosyan et al., 2011). Note that the influence of shear production on the CBL will be discussed with more detail below. In addition, the convective velocity field in Fig. 4.4e ranges from nearly 3 m/s to 6 m/s, corresponding to the regions where a shallow and deep CBL form, respectively. This range in w_* from our GCM simulations agrees well with the turbulence-resolving large-eddy simulations of Spiga et al. (2010) where w_* ~3-6 m/s around $t = 15h$ (LMST), also with values obtained using ground-based observations in combination with similarity theory by (Martínez et al., 2009). Note that the value of w_* is nearly 1 – 2 m/s for a typical CBL on Earth (Kaimal et al., 1976; Moeng and Sullivan, 1994). Furthermore, as with the seasonal variation of w_*, Spiga et al. (2010) retrieve a surface kinematic heat

flux as high as q_s = 2 Km/s around $t = 15h$ (LMST), as is the case in our GCM simulations presented in Fig. 4.4c.

Regarding the deepest CBL formation (i.e., above 7 km), there exist two seasonal maxima. The first maximum evolves continuously between L_s ~125-150° over the northern tropics (~20-30°N). It is associated with a higher rate of turbulent convection (Fig. 4.4e) and surface temperature (Fig. 4.4d) augmented by radiative heating (Fig. 4.4c) during the northern summer season. Later the second maximum forms, extending from the northern late autumn towards the northern early winter (i.e., L_s ~255-310°). A sudden drop in CBL depth over southern tropics takes place between L_s ~210-240°, which marks the occurrence of regional dust storm activity, as is observed in the annual evolution of column dust optical depth (CDOD) referenced to 700 Pa (Fig. 4.4b). As MY 33 did not experience a GDS event, it can be considered a quiescent year in terms of dust abundance. However, two particular periods within the dust season (the northern late autumn and late winter, respectively) perturb the convective boundary layer via regional dust storms, during which the normalized CDOD of the planet reaches nearly 1. The presence of increased dust loading reduces surface-to-atmosphere temperature contrasts, producing a more stable lower atmosphere that weakens the convective activity, lowering the CBL depth by ~2 km.

Despite the high rates of surface heating and temperature over southern tropics (Fig. 4.4c-d) from late spring until early summer (L_s ~240-320°), this does not ensure further enhancement in CBL activity of extremely deep layers exceeding 9 km. To illustrate, Fig. 4.4a indicates that the second CBL maximum (occurring between L_s ~255-310°) exhibits similar CBL depths compared to the first CBL maximum (in the northern summer L_s ~125-150°). This is due to the high rates of shear forcing in the southern tropics (Fig. 4.4e), amplified by the regional dust storm of MY 33 commencing at L_s ~210° (Fig. 4.4b). Fig. 4.4f demonstrates the friction velocity, u_*, which is the velocity scale of surface shear forcing. In other words, the friction velocity, $u_* = (\tau_s/\rho_a)^{1/2}$, denotes the surface shear flux, τ_s, which is normalized by the air density, ρ_a. Growing friction velocity implies higher shear production, originating from the shear instabilities which can be augmented by local dust events or the Hadley circulation strength. That inhibits, in turn, the convection, and caps the growth of the CBL. Such a type of boundary layer is called shear-dominated CBL, unlike the purely buoyant CBL. To illustrate

the difference on Earth (Moeng and Sullivan, 1994), a typical purely-buoyant CBL doubles in depth (z_i ~1 km), with respect to a shear-dominated CBL (z_i ~0.5 km) via the shear/buoyancy interaction. This could explain why the second CBL maximum during the northern winter (Fig. 4.4a) is not capable of growing further in depth, as it is capped by the dust-induced shear instabilities.

Unlike the relatively quiescent MY 33, MY 34 exhibits extreme dust activity (Kass et al., 2020). As illustrated in Fig. 4.5b, MY 34 has one large/massive peak in dust opacity, northern autumn starting shortly after northern autumn equinox, corresponding to the planet-encircling GDS, which is followed by a smaller peak during northern late winter, corresponding to a large regional storm. Here, as can be seen, the present semi-interactive dust transport model performs adequately to capture the onset and occurrence of dust storms (being either a global or regional dust storm event). More specifically, the first peak shows the trace of an extreme dust event engulfing almost the whole planet for a long period. The global dust storm of MY 34, hereafter GDS-34, lasts more than 100 sols between L_s ~185-250°. Moreover, its intensity rises to in excess of 3 in terms of CDOD referenced to 700 Pa, covering most of the planet from the southern high latitudes to northern mid-latitudes. As the dust particles block the incoming sunlight, such a long-term residency of a much higher dust abundance implies a severe consequence in terms of radiative heating inhibition. Accordingly, a strong internal cooling occurs within the CBL and a drastic reduction of radiative heating (Fig. 4.5c) and surface temperature (Fig. 4.5d) during L_s ~185-250°.

The effect of global dust storms can also be seen in Fig. 4.6a-b, showing the inter-annual variability of globally averaged surface kinematic heat flux and temperature throughout the last decade on Mars. Results indicate that the surface daytime radiative flux is exposed to long-lasting attenuation while massive dust storms hit the planet, even in the afternoon, despite the peak rate of convective activity. Our GCM results show that surface level daytime solar fluxes are strongly attenuated during the larger dust storms, offsetting the increased convective activity for all the GDS events recorded during MY 25, MY 28 and MY 34. Nevertheless, only the events of GDS-25 and GDS-34 were able to drastically diminish thermal convection, reversing the thermal process as a prolonged surface cooling. Results show that the global average daytime surface kinematic heat flux, q_s, drops from ~0.35 Km/s (at the onset of the storm) to below 0 Km/s by the time the mature phase is reached (at L_s ~210°).

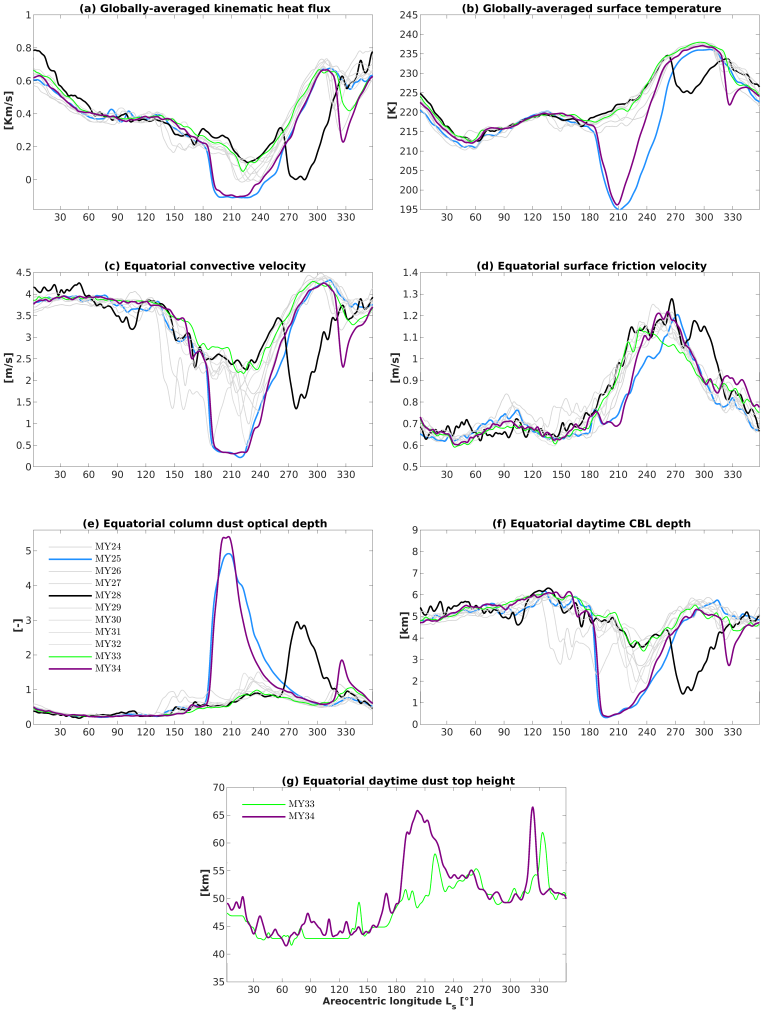

Figure 4.6: Inter-annual variation of simulated globally averaged **(a)** surface kinematic heat flux, **(b)** surface temperature; and equatorial **(c)** Deardorff's convective velocity, **(d)** friction velocity, **(e)** column dust optical depth (CDOD) referenced to 7 mb, **(f)** daytime CBL depth, **(g)** daytime dust top height, shown for MY 24 through 34 in the local afternoon, $t = 15h$ (LMST). Note that the Deardoff's convective velocity, by definition $w_* = [(g/T_s)q_s z_i)]^{1/3}$, physically sounds when convection occurs. Here, we computed the Deardroff's convective velocity at local afternoon, therefore, even global dust storms block the sunlight, very weak conditions can occur between L_s ~185-250°.

The period of surface cooling lasts for at least 95 sols (i.e., L_s ~189–249°) during GDS–25 and for nearly 82 sols (i.e., L_s ~191–242°) during the most recent global dust event on Mars, i.e., GDS–34 (Fig. 4.6a). Related to the extreme surface cooling, the global average surface temperature (Fig. 4.6b) drops by nearly 22 K in GDS–25 and nearly 20 K in GDS–34.

As a consequence of higher cooling rates within the boundary layer, the production rate of turbulent convection is drastically diminished during GDS–25 and GDS–34, relative to the quiescent years. For instance, in Fig. 4.6c, the velocity scale of turbulent convection, w_*, is depicted in terms of an equatorial time series for each simulated Martian year. For both GDS–25 and GDS–34, the global average of w_* drops from ~3 m/s at the onset of the storm to as low as ~0.5 m/s around during the mature phase of the storm. Similarly, w_* drops from ~3.5 m/s to ~1.5 m/s between the onset and mature phase of the GDS–28 storm, which occurs later in the year.

Besides the key effect of a GDS on the boundary layer, i.e., blocking the surface radiative heating thus a global weakening in convective activity, a secondary effect is the shear forcing alteration, in which a minor weakening of friction velocity occurs during the onset of GDS–34 (L_s ~180–210°) and re–strengthening afterwards (L_s ~210–270°), as shown in Fig. 4.5f. Moreover, for the friction velocity, we report strong seasonal variations, as high as 50% during the dust storm season (after L_s ~180°), by inducing enhanced shear instabilities within the boundary layer. To illustrate, the equatorial friction velocity grows from ~0.75 m/s (prior to storm onset) up to ~1.1–1.2 m/s within the dust storm season for each simulated Martian year (Fig. 4.6d).

So far, we have outlined the key and secondary effects of a GDS, acting negatively on the turbulent convection. Due to extreme dust abundance and the ensuing highly turbulent surface winds, a global dust storm massively inhibits convective activity. To deduce its effect on the convective boundary layer, we examine the annual evolution of CBL depth through MY 33 and MY 34, retrieved from the GCM results in Figs. 4.4a and 4.5a. Unlike the quiescent MY 33, a large amount of dust was injected into the atmosphere during GDS–34 (Fig. 4.5b), causing extremely shallow boundary layers. It becomes as shallow as a few hundred meters, covering the entire planet from the equator towards the polar caps (Fig. 4.5a). This results in a planet–wide boundary layer with the same depth as an extremely shallow daytime boundary layer, hence we describe it as a "global–darkness" state of the Martian CBL,

persisting for nearly 100 sols, i.e., L_s ~185–250°.

The inter-annual variability in equatorial (Fig. 4.6f) and zonally averaged (Fig. 4.7) CBL depth is illustrated from MY 24 to MY 34. The main inter-annual variability occurs especially during global dust storms. To illustrate, while passing through GDS-34, the depth of the CBL experiences an excessive drop from 6 km down to as shallow as 0.5 km; the same is true for GDS-25. The impact of GDS-28 differs from that of GDS-25 and GDS-34 in a way such that GDS-28 could not globally negate surface kinematic heat flux (Fig. 4.6a), since GDS-28 has nearly half the CDOD in terms of storm intensity (Fig. 4.6e). Thus, GDS-28 still features a relatively higher convective boundary layer with a depth around 1.5–2 km, even at the most mature phase of the storm (Fig. 4.6f). Therefore, in contrast to GDS-25 and GDS-34, GDS-28 could not form an extremely shallow daytime boundary layer near the equator. Even though extremely shallow daytime boundary layers form especially over southern mid-latitudes in GDS-28, they are not as long-lasting as in GDS-25 and GDS-34 events (Fig. 4.7).

Finally, we also examine the annual evolution of daytime dust-top altitude near the equator, determined as following Wu et al. (2020). This is shown in Fig. 4.6g for Mars years 33 and 34. The daytime dust-top altitude remains nearly constant at z_{max} ~ 43 km before the dust storm season, without any significant inter-annual variability. Following the start of the dust storm season, however, the daytime dust top is substantially raised in line with the growing dust activity (which is properly reproduced by the new semi-interactive dust transport model). The daytime dust top height rises to ~57 km for the quiescent year (MY 33) when there is no global dust storm. Yet, it extends up to ~65 km during GDS-34.

4.2.5 Martian GCM results: Regional variations

In addition to the seasonal and inter-annual variations presented above, Martian surface meteorology is also affected by the various complex features on its surface. To better understand CBL dynamics induced by regional effects, we show the variability of CBL depth, z_i, in northern (Fig. 4.8a) and southern (Fig. 4.8b) early-summer seasons for MY 33, in the local afternoon, $t = 15h$ (LMST) at all locations. Besides, the velocity scales of turbulent convection, w_*, and shear forcing, u_*, in northern early-summer are depicted in Fig. 4.8c-d

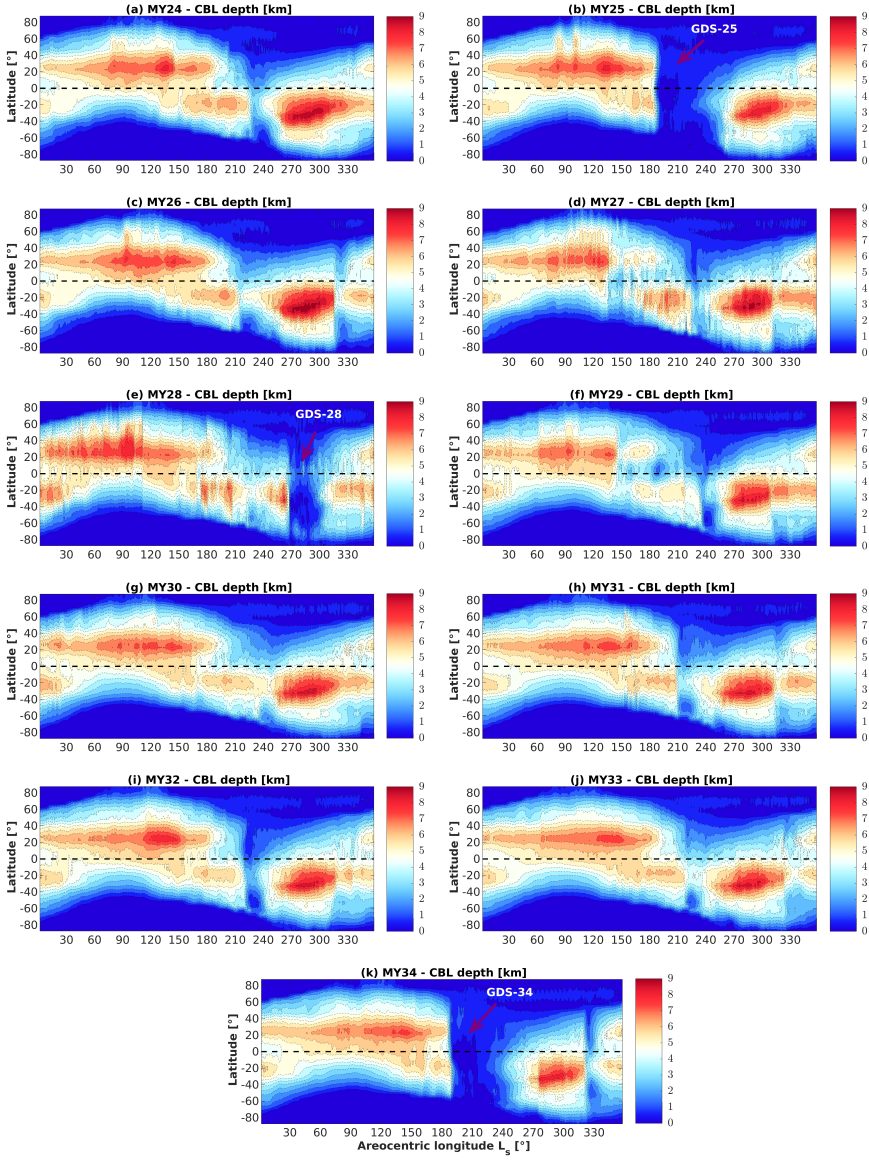

Figure 4.7: The decade-long evolution of zonally averaged CBL depth from MY 24 to MY 34, in the local afternoon, $t = 15h$ (LMST). GDS-25, GDS-28 and GDS-34 are the global dust storm events occurring in MY 25, MY 28 and MY 34, respectively.

respectively. First, the evolution of the polar caps is evident on the geographical variations of CBL depth (Fig. 4.8a-b), by altering the turbulent convection (i.e., in terms of Deardorff's convective velocity, w_*, in Fig. 4.8c). The polar ice caps are the result of the Martian CO_2 and water cycles, driven by the planet's orbital eccentricity and obliquity. For instance, during the northern winter season, water and CO_2 ice will be accumulated on the surface of the northern polar region. The accumulation of water as well as the increase in areal coverage of CO_2 will increase the surface albedo. Therefore, the more reflective surface will lead to negative surface kinematic heat fluxes (referring to the surface cooling) and a decrease in the level of turbulence within the planetary boundary layer. Consistently, very low CBL depths (up to only a few 100 m) are estimated in northern winter around the northern polar cap (Fig. 4.8b) and in southern winter around the southern polar cap (Fig. 4.8a) (see the zonally averaged CBL depths over polar caps in Fig. 4.9). In other words, the Martian PBL poleward of 80°N-S is stably stratified, which is mostly observed during night-time conditions (Petrosyan et al., 2011). Such a shallow formation of a stably stratified PBL, even during daytime conditions (Fig. 4.8a-b), is associated with very low values of surface kinematic flux around the polar caps (see Fig. 4.5c). In addition to high cooling rates, the polar caps show low friction velocities (u_* ~0.3 m/s) (Fig. 4.8d). Given the fact that the stably stratified PBLs with weak near-surface winds, i.e., the so-called very stable boundary layers (vSBL), are observed on Earth (Grachev et al., 2005), a similar type of PBL may occur in the northern polar region of Mars.

For mid-latitude and equatorial regions in the northern mid-summer season, the highest CBL depths, in excess of 9 km (Fig. 4.8a), occur in the vicinity of Tharsis Montes, Olympus Mons, Alba Mons and Elysium Mons (see the locations of this regions in Fig. 4.8f). The higher the elevation, the lower the surface pressure and the surface atmospheric density. This implies that the turbulent mixing in the CBL will be deeper with the same amount of turbulent flux, for the case where the planetary boundary layer develops in lower-pressure regions, consistent with Spiga et al. (2010). This effect on the CBL can also be seen in such locations as the Hellas basin and Argyre Planitia (as in Fig. 4.8b). Both regions are located below the MOLA reference elevation (Smith et al., 2001) and thus have higher surface pressures compared to other equatorial and mid-latitude regions. Therefore, for these regions, CBL depth can be as low as 3-4 km, as shown in Fig. 4.8b.

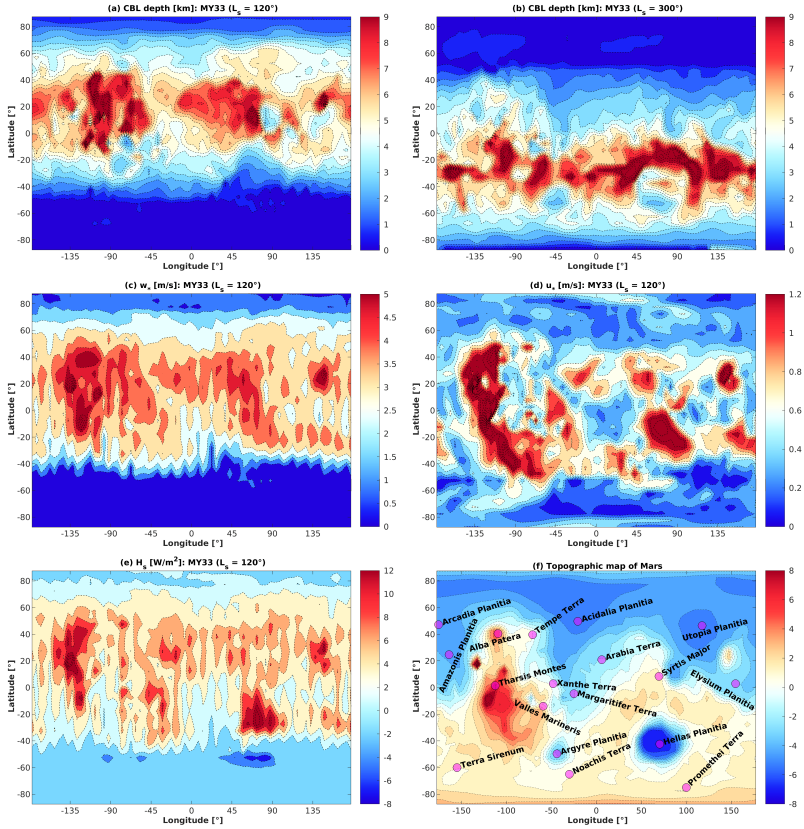

Figure 4.8: The regional variability in MY 33, in terms of the CBL depth in the northern early-summer (L_s=120°) **(a)** and southern early-summer (L_s=300°) **(b)**, in the local afternoon, $t = 15h$ (LMST) at all locations. Deardorff's convection velocity, w_*, **(c)**, the friction velocity, u_*, **(d)** and surface sensible heat flux, $\mathcal{H}_s$, **(e)** are depicted in the northern early-summer season. Locations of some particular regions addressed in the present study, marked on the topographic map of Mars **(f)** based on Mars Orbiter Laser Altimeter (MOLA) data (Smith et al., 2001).

In addition to terrain elevation, surface thermal inertia also plays an important role in surface meteorological conditions and thus CBL dynamics on Mars. For the northern mid-summer map of CBL depth in Fig. 4.8a, similar to Tharsis Montes, we find that deep CBLs form in the Amazonis Planitia, Arabia Terra, Alba Patera and Elysium Mons regions, which have lower thermal inertia compared to other mid-latitude regions (see Fig. 5 of

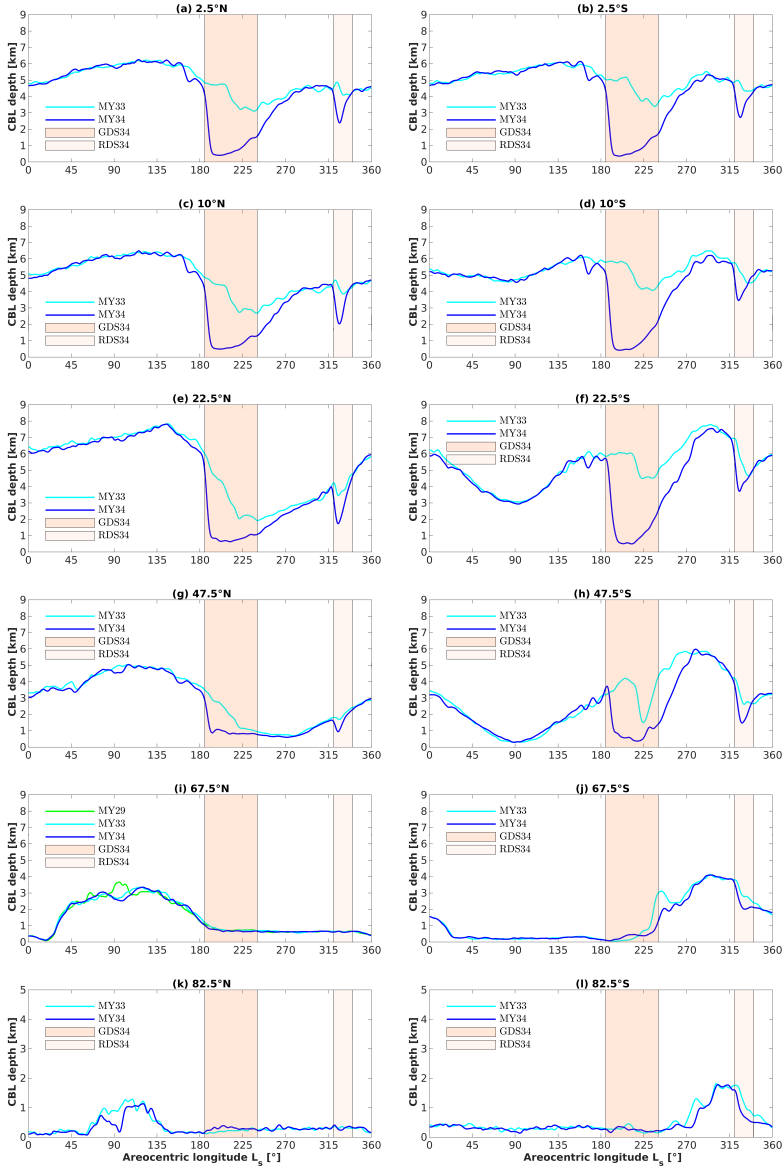

Figure 4.9: The annual evolution of the zonally averaged daytime CBL depth in the northern (left panels) and southern (right panels) hemispheres. The cyan and blue solid lines denote the simulated cases MY 33 and MY 34, respectively. The shaded areas refer to the GDS in MY 34 (GDS-34) and RDS in MY 34 (RDS-34).

Putzig et al. (2005) for the thermal inertia map of Mars). Thanks to their lower surface thermal inertia, temperature variations from night to day are greater in those regions. Thus, turbulent convection is enhanced and leads to a deeper CBL. Likewise, higher surface thermal inertia values mark relatively shallower CBL formation over the tropics, with a CBL depth of ~5 km, such as in the Elysium Planitia, Xanthe Terra and Valles Marineris regions (Fig. 4.8a). Another important effect of surface thermal inertia is related to the near surface winds. Stanzel et al. (2006) reported that high near-surface winds can be observed in Amazonis Planitia. We show that the heterogeneous thermal surface forcings, as a result of the spatial gradients of the thermal inertia with respect to its neighbouring regions, can amplify the near-surface winds (similarly to slope winds or cap-edge winds driven by horizontal contrasts in surface properties). It is worth noting that the presence of heterogeneous thermal surface forcings is noticeable in terms of surface sensible heat flux (Fig. 4.8e), exhibiting a high zonal variation, which accordingly causes high zonal variability in convection velocity (Fig. 4.8c).

We examine the zonally averaged depth of the CBL at different latitudes, from the equator up to the polar caps in both hemispheres, for both MY 33 and MY 34 as a function of season (Fig. 4.9). The predicted latitudinal variability in CBL depth indicates that GDS-34-induced suppression in boundary layer activity occurs mostly over the southern hemisphere, which had higher dust opacities during GDS-34. We obtain a decrease in CBL depth by as much as 5.8 km at 22.5°S and 4.8 km at 2.5°S for MY 34 (Fig. 4.9f-b), as compared to a reduction of 5.3 km at 22.5°N and 4.3 km at 2.5°N (Fig. 4.9e-a). As GDS-34 drives the tropics more actively, CBL evolution during MY 34 is less affected over the high latitudes, especially in the northern hemisphere. For instance, we observe that at 47.5°N the CBL drops by 1.9 km (Fig. 4.9g), while it decreases by 3.2 km over 47.5°S (Fig. 4.9h). It is worth noting that our CBL depth estimation at the latitude of 67.5°N (passing through the Phoenix landing site) is around 3.5 km in northern early-summer (L_s ~100°), as displayed in Fig. 4.9i for MY29. This prediction is consistent with the light detection and ranging instrument (LIDAR) observations of NASA's Phoenix Mars Lander, in which the daytime CBL depth is obtained to be around 4 km (Whiteway et al., 2009).

Regarding CBL evolution around the polar caps, we compare MY 33 and MY 34 poleward of 80° in Fig. 4.9k-l. Our results indicate that very shallow boundary layers surround the polar caps in both hemispheres (i.e., up to only

a few tens of meters), implying the existence of vSBL formation similar to what is observed in terrestrial polar regions (Grachev et al., 2005), associated with very weak turbulence and strong stratification (Mahrt and Vickers, 2006; Banta, 2008), which, in turn, excessively weakens the depth of CBL. In terms of the CBL maxima, Fig. 4.9k-l reveal that the CBL depth around the northern polar cap reaches to nearly 1.1 km in the northern early summer, while for the southern polar cap, it extends somewhat higher, to ~1.9 km during the southern late-summer. Lastly, even though the dust activity has no effect on the boundary layer over the northern polar cap (Fig. 4.9k), the regional dust storm in MY 34 (RDS-34) produces a gradual response on the extent of boundary layer formation around the southern polar cap. Fig. 4.9l shows that the PBL in MY 34 is lowered by nearly 0.5 km, by the impact of RDS-34.

4.2.6 Comparison with Mars Express (MEX) radio occultations

We compare the GCM predictions with available MEX radio occultation (RO) measurements of CBL depth (Hinson et al., 2008, 2019). For the comparison of CBL depth, the reference experiments consist of 118 RO profiles overall, collected during the northern mid-spring (L_s = 34.7 – 69.2°) and late winter of MY 27 (L_s = 357.1 – 359.9°), through the early spring of MY 28 (L_s = 0.1 – 42.3°). The latitude, ϕ, longitude, λ, solar longitude, L_s, local terrain elevations, z_s, based on MOLA (Christensen et al., 2001) and in the GCM, as well as local true solar time (LTST), t_l of these RO measurements are listed in Tab. C1-C2, while the spatial distribution is marked on a topographic map of Mars based on Mars Orbiter Laser Altimeter (MOLA) (Smith et al., 2001) in Fig. 4.10e.

Tab. C1-C2 lists the GCM-based CBL depth predictions, $z_{i,GCM}$, with respect to the RO measurements, $z_{i,RO}$, including the mean absolute error (MAE) values at each given RO location. Results indicate that the CBL predictions of the GCM are consistent with the RO measurements, in which the average MAE of z_i is 1.41 km among the 118 RO profiles with a standard deviation of 1.01 km. Indeed, 100 of 118 RO locations exhibit a good agreement with an average MAE of ~1.1 km in terms of CBL depth. Here, the high MAEs appear around northern Xanthe and Margaritifer Terra regions, in which the GCM underpredicts the depth of CBL as being ~5.7 and 6.1 km compared to a depth of ~8.8 and 8.3 km in RO measurements. This can be

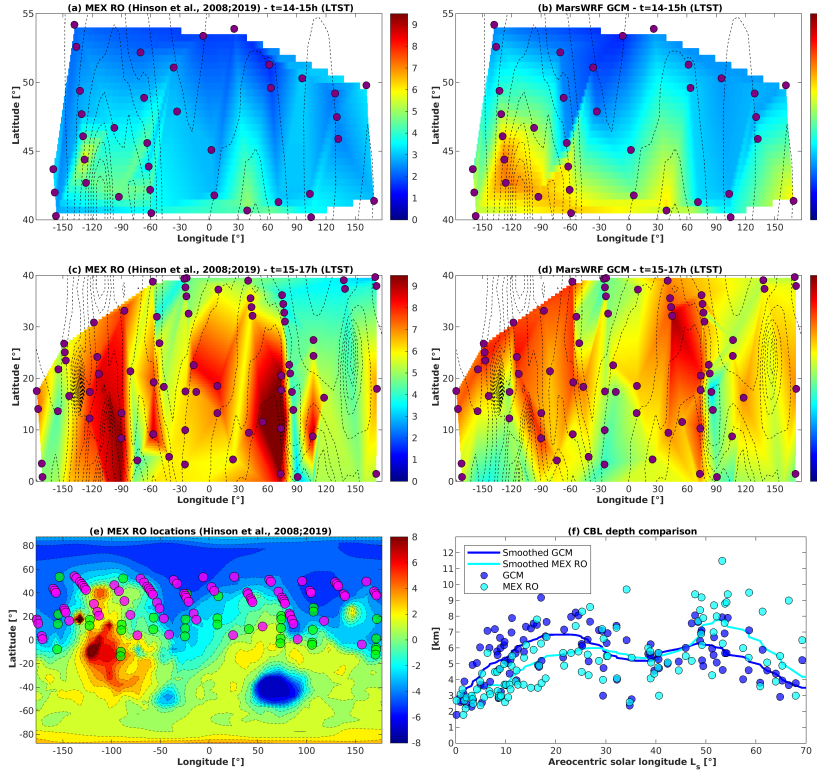

Figure 4.10: Regional distribution of CBL depth retrieved from MEX RO measurements (Hinson et al., 2008, 2019) at (a) t=14-15h (LTST), (c) t=15-17h (LTST) and MarsWRF GCM simulations at (b) t=14-15h (LTST), (d) t=15-17h (LTST) for given RO profiles as listed in Tab. C1-C2. The locations of RO experiments are marked with purple circles. The black dashed lines display the contour lines of topographic map of Mars retrieved by the datasets of Mars Orbiter Laser Altimeter (MOLA) (Smith et al., 2001). (e) The RO locations are also depicted together with the MOLA map. Here the green and magenta circles mark the RO profiles collected at MY 27 and MY 28 respectively. (f) The temporal variation of CBL depth is displayed at all available RO locations during northern early and late spring of MY 27 and MY 28. The dark and light blue markers show the GCM and RO results respectively, while the solid lines display their smoothed behaviour via Gaussian smoothing.

caused by the reason that both locations are heavily cratered and irregular regions (Dohm et al., 2007; Sato et al., 2010; Thomas et al., 2017), which can induce extensive mesoscale circulations or convective slope winds over the rim slopes. Similarly, under-predictions in CBL depth are also produced over

locations, for instance, western and eastern rims of Isidis Planitia (i.e., a large impact basin) as ~3.2–3.6 km, and the Valles Marineris rims as ~5.3 km. Along these regions, high CBL depth values in RO measurements can be related to the well-mixed turbulence enhanced over steep rims. Thus, the presence of strong topographical circulations through Isidis rims (Hinson et al., 2019) and canyon rims of Valles Marineris (Spiga and Forget, 2009) can necessitate high resolution mesoscale modeling with respect to the GCM approach. Another possible reason is that the terrain elevations can be different between the observation and the model (as listed in Tab. C1-C2), and also that even for identical elevations may exhibit differences due to the thermal inertia assumed at the regionally smoothed GCM mesh in comparison with the actual one at the location of the measurement.

Fig. 4.10 shows the spatial variation in observed and modeled CBL depths at the times of the RO observations using the results shown in Tab. C1-C2. Note that the sharp edges here are due to variations in the L_s and LTST of different RO observations, as well as the lack of RO profiles, especially in the southern tropics. The RO locations are scattered mostly around the northern mid-latitudes (Fig. 4.10a-b) at t=14–15h (LTST) and through the northern tropics (Fig. 4.10c-d) at t=15–17h (LTST). The contours of CBL depth predictions derived from the GCM show a spatial variation generally consistent with that of the RO measurements.

The deep CBL formations around the high terrains over northern tropics exist in both GCM and RO results. To illustrate, deeper layers mostly appear in the vicinity of Olympus Mons, Tharsis Montes, Valles Marineris and Syrtis Major, increasing to a depth as great as ~7–9 km (Fig. 4.10c-d). By contrast, relatively shallower layers form in the northern mid-latitudes (e.g., λ ~40–54°N), largely due to all RO observations being made during northern late winter and early to mid spring, when surface heating is lowest at these latitudes (see Sec. 4.2.4). The depth of the observed CBL in this region varies from ~3–7 km with the GCM predicting ~1.5 km greater depths, but, overall, the general spatial variation here matches well between the GCM and RO results, such as in Arcadia Planitia, Tempe Terra, Acidalia Planitia and Utopia Planitia (Fig. 4.10a-b).

Furthermore, in Fig. 4.10f, we compare our GCM estimations with MEX RO measurements in terms of the temporal variation from early to late northern spring (L_s = 0.1 – 69.7°). Note that in this figure we combine the

RO profiles of MY 27 and MY 28, as there is little inter-annual change in the northern spring season due to the lack of strong dust storms or planetary wave activity. For this season, Hinson et al. (2008) reports that the MGS TES observations of dust column opacity (at 9 μm wavelength) in the southern and northern tropics are as low as ~ 0.05 and 0.1, respectively. The profiles in Fig. 4.10f show very general agreement between the seasonal variation of predicted and observed CBL depths in northern spring, insofar as both increase rapidly after equinox, have some briefly smaller values midway through the period shown, then increase again before decreasing rapidly towards L_s ~70°. However, as shown by the smoothed curves (via Gaussian-weighted moving averaging (Horová et al., 2012) -based on Gaussian distrubition- with a window length of 30, in which the window slides through 30 neighboring elements for a given element), the GCM appears to have a positive bias of nearly 1.0-1.5 km magnitude in northern early spring ($L_s = 0 - 30°$), which reverses to a negative bias of nearly 1.5-2.0 km magnitude in around northern mid-spring ($L_s = 40 - 70°$). It is worth noting that the latter bias is caused by the local true solar times of corresponding RO observations. To illustrate, most of RO profiles within this period are retrieved after t=17h (LTST), standing for the "early-evening transition" period, which is challenging to model adequately (Nadeau et al., 2011). This is because, during the early-evening transition, convective boundary layers (characterized by positive surface buoyancy fluxes, i.e., unstable regime) begin to convert into stable boundary layers (i.e., surface buoyancy fluxes are reversed to be negative). From terrestrial studies (Pino et al., 2006; Busse and Knupp, 2012; Lampert et al., 2016), early-evening transition of unstable to stable regimes (i.e., large-scale turbulent convections into small-scale sporadically turbulent stratification (Stull, 2012)) are quite dynamic processes where the convective turbulence and radiative heating decays substantially in short periods. Thus, capturing well this time-varying process in GCM can be possible by either implementing external parameterization (Nadeau et al., 2011) or refining model resolutions, which will be taken into account as a future work. In addition, considering the possible model-based or experimental uncertainties and recalling that 100 of 118 RO locations give an average MAE of ~1 km in terms of CBL depth, the GCM appears to be largely consistent with the radio occultation measurements at the observation times and locations. Lastly, as the available datasets for MEX radio occultation measurements are limited, we can not examine the potential

inter-annual variabilities in this comparison.

4.3 Discussion and Conclusions

The present study addresses decade-long spatio-temporal variabilities (inter-annual, seasonal and regional) in the Martian convective boundary layer. During this period, from MY 24 to MY 34, there have been three major planet-encircling dust events recorded. To examine their impact on CBL characteristics as well as the spatio-temporal variations occurring in the convective boundary layer, we performed a decade-long general circulation model (GCM) simulation using the MarsWRF model (Richardson et al., 2007). As the dust cycle is the main driver of boundary layer dynamics, we built a new dust transport scheme in order to correctly represent the time-evolving dust distribution. In our scheme, the dust is transported freely, then corrected by the observed column dust opacity measurements from Montabone et al. (2015, 2020) as a novel semi-interactive framework. As noted before, several different atmospheric models use different dust interaction schemes, ranging from simple prescribed dust opacity forcings (Forget et al., 1999) to orbit-spin coupling methods using fully-interactive dust transport (Newman et al., 2019b). Here, we did not quantify the possible consequences of using different dust schemes on the boundary-layer meteorology of Mars, which would require extensive high-resolution in-situ near-surface meteorological observations. Currently, such a meteorological dataset is available by the InSight lander and will be available by the Perseverance rover. A multi-model intercomparison study, covering different dust schemes, is essential as a future work to further improve our understanding of the Martian dust cycle and boundary-layer meteorology. However, for this study, such an extensive study is out of our current scope.

Results of our GCM simulations reveal that enhanced dust content in the Martian atmosphere (especially during global dust storms) has significant impacts on the seasonal and inter-annual variability in CBL dynamics. We find that a strong reduction in surface convective heat flux occurs for all the global dust storm events recorded during MY 25, MY 28 and MY 34, which is quite unlike the intervening, quiescent Martian years. However, only the global dust storms of MY 25 and MY 34 were able to terminate the convective heat production at a global level. In this manner, both planet-encircling storms

reversed the thermal convection process into a prolonged surface cooling, reducing its global average from ~0.35 Km/s at storm onset to below 0 Km/s at the storm's peak (L_s ~210°). This surface cooling existed for nearly 95 and 82 sols when GDS-25 and GDS-34 events occur.

The suppression in heating rates through GDS events breaks down the daytime convection activity, eliminating deep thermal plumes and intense convective vortices. Accordingly, we find that the velocity scale of turbulent convection was globally lowered, for instance the convective velocity decreases by ~2.5 m/s during GDS-25 and GDS-34, from ~3 m/s at the onset of the storm along the equator (i.e., down to the typical values encountered on Earth's daytime CBL). The global weakening in convective activity was further amplified by enhanced dust transport during the dust storm season (after L_s ~180°), inducing higher wind shear on average by almost 50%. The equatorial friction velocity grows from ~0.75 m/s (prior to storm onset) up to up to ~1.1-1.2 m/s within the dust storm season for each simulated Martian year. As a combination of both impacts, the CBL depth experienced a drop down to as shallow as ~0.5 km, from as high as 9 km at the onsets of GDS-25 and GDS-34. Both storms led to the conversion of deep convective boundary layers into extremely shallow daytime boundary layers, even during the daytime at all local times. As a result, the planet was exposed to a long-term "global-darkness" state, in which its most extreme period (i.e., the number of sols with a CBL depth below 1 km) lasted for nearly 67 and 57 sols during GDS-25 and GDS-34 respectively. On the contrary, the less intense GDS in MY28 differed from its counterparts in MY25 and MY34. It could not negate surface kinematic heat flux globally, even at the storm's peak. Thus, the GDS-28 couldn't feature extremely shallow daytime boundary layers over the whole planet, as long-lasting as in GDS-25 and GDS-34 events.

Besides the seasonal and inter-annual variability, we observed significant impacts on the CBL dynamics governed by regional features. For the Martian CBL, the positive feedback of higher terrain elevation has been well documented, from the MEX radio occultation measurements. Consistent with this effect, our GCM simulations point out the existence of other factors that affect the convective boundary layer, such as the GDS-induced dust abundance and inverse contribution of thermal inertia. Regarding the latter effect, our GCM results showed that the lower thermal inertia enhances the turbulent convection, thus leading to deep CBL formation (such as in Amazonis Planitia,

Arabia Terra, Alba Patera and Elysium Mons), while relatively shallow CBLs are found over the tropics, i.e., ~5 km, in the Elysium Planitia, Xanthe Terra and Valles Marineris regions.

In terms of PBL formation over the polar caps, we observed the formation of a very stable boundary layer (vSBL) surrounding both polar caps up to a few tens of meters in depth. Such a regime, as observed in terrestrial polar regions (Grachev et al., 2005), is related to very weak turbulence and strong stratification, as a consequence of the perennial water and CO_2 polar caps which causes surface temperatures to remain very low. Finally, regarding dust feedback on polar caps, we find that the regional dust storm in MY 34 (RDS-34) exhibits a gradual impact over the southern polar cap, where the depth of the CBL is reduced down to 0.5 km, in comparison with the quiescent MY 33.

As a future work, thanks to the ongoing operations of InSight lander as well as MSL and Mars 2020 rover, we will expand the current investigation through detailed comparisons of inter-annual and seasonal variabilities between GCM and in-situ meteorological observations. In the present study, regarding the potential implications of global/regional dust storms, we examine the impacts of these extreme dust events on convective boundary layer dynamics. As a follow-up study, we will focus on the influences of global/regional dust storms on the near-surface turbulent energy, and thus the turbulent exchange of volatiles and tracers between the surface and atmosphere.

Chapter 5

Towards next-generation PBL models: Bridging meso-microscale limits with a new 3D scale-adaptive gray-zone turbulence model[1]

5.1 Introduction

Atmospheric turbulence is one of the key physical phenomena within the planetary boundary layer (PBL), influencing the exchanges of momentum, heat and moisture (Ito et al., 2015). Considering the spatial grid spacings of general circulation models (GCM) (Mechoso and Arakawa, 2015) or mesoscale models (Skamarock, 2004), typically ranging from $\mathcal{O}(100\ km)$ to $\sim \mathcal{O}(1\ km)$, turbulent transport of momentum, heat and moisture can not be explicitly resolved. Therefore, it needs to be parameterized given the fact that these grid sizes (Δ^{meso}) are often much larger than the size of the energy-containing turbulence eddies, $\mathscr{L}$, in the convective boundary layer (CBL) (Shin and Hong, 2013), which is comparable to the CBL depth $\sim \mathcal{O}(1\ km)$ (Beare, 2014). Considering that $\Delta^{meso} \gg \mathscr{L}$, all the turbulence is subgrid and modeled by the so-called one-dimensional (1D) planetary boundary layer (PBL) schemes (Cohen et al., 2015), which only treat the vertical mixing under the assumption of horizontal homogeneity (Honnert et al., 2011). At higher spatial grid spacings, typically sub-kilometer (Zhang et al., 2018; Efstathiou and Plant, 2019; Doubrawa and Muñoz-Esparza, 2020), horizontal components of

[1]This chapter is written based on the published article: Senel, C. B., Temel, O., Muñoz-Esparza, D., Parente, A., & van Beeck, J. (2020). Gray zone partitioning functions and parameterization of turbulence fluxes in the convective atmospheric boundary layer. Journal of Geophysical Research: Atmospheres, 125(22), e2020JD033581. Here, Cem Berk Senel led the research conceptualization, model development and validation, formal analysis, simulations and visualization of results, and the writing of the manuscript.

turbulent fluxes become important, while reaching to the microscale range (Wyngaard, 2004), and one-dimensional treatment of turbulence becomes problematic (Zhang et al., 2018). Using a sufficiently fine grid spacing (Δ^{micro}), spanning from $\mathcal{O}(100\ m)$ down to a few meters (Muñoz-Esparza et al., 2014b), the energy-containing large eddies can be explicitly resolved (large-eddy simulation) and the contribution of small subgrid scale eddies can be parameterized using subgrid scale (SGS) models. Despite that operational weather forecasting can be performed without explicitly resolving the large-scale structures (Janić, 2001), the effect of explicitly unresolved structures can be important for various applications. For instance, the realistic representation of planetary boundary layer processes that are three-dimensional by nature such as mountain-waves (Muñoz-Esparza et al., 2016), terrestrial (Huang et al., 2018) and Martian dust devils (Nishizawa et al., 2016), and flow over complex terrain (Goger et al., 2018) can only be performed by large-eddy simulations. It must be noted that such a necessity for three-dimensional explicit resolution of turbulence may not only arise as a result of topographical complexity but can be a result of land-sea interactions, leading to complex PBL features like low-level jets that can occur both over land (Djurić and Damiani Jr, 1980) and sea (Kalverla et al., 2019).

Application of LES techniques for operational weather forecasting is still beyond the modern computational resources. However, thanks to the advance in computing capabilities, numerical weather prediction (NWP) models can be used at sub-kilometer grid spacings, which corresponds to the transition zone between the operating scales of LES and one-dimensional PBL schemes, the so-called "terra incognita" or turbulence gray-zone (Wyngaard, 2004). The traditional turbulence parameterizations, devoted to either mesoscale or microscale limits, are no longer valid along the terra incognita, since they are originally designed for their own grid scale limits (Zhang et al., 2018; Chow et al., 2019; Doubrawa and Muñoz-Esparza, 2020). As noted before, the lack of three-dimensional representation of turbulent flux can lead to erroneous predictions in the planetary boundary-layer in addition to this methodological deficiency of one-dimensional schemes. Therefore, as an alternative to computationally-expensive LES techniques, three-dimensional parameterization of turbulent fluxes must be developed for next-generation NWPs, which can operate on sub-mesoscale ranges. Moreover, such schemes, which can bridge the microscale and mesoscale, can serve as a potential reliable

tool for further studies in multiscale nested boundary-layer simulations.

In recent years, there have been growing attempts to understand and characterize the structure of turbulence in the gray-zone. Honnert et al. (2011) designed a methodology to determine the subgrid scale partitioning functions (also known as partial similarity functions) within the gray-zone. This novel approach is based upon the idea that high-resolution LES data can be continuously upscaled from microscale to mesoscale grid spacings employing an explicit spatial filter. Then, they described a set of partitioning functions for the free CBL regime where there is no geostrophic wind. The proposed partitioning functions of Honnert et al. (2011) represent the ratio of subgrid scale to total (subgrid + resolved scales) turbulent fluxes. This was indeed a significant step for uncovering the black-box of terra-incognita, which contributes to the quantification of mesoscale-microscale transition. As the turbulent exchange of momentum, heat, moisture and aerosols between the surface and atmosphere exhibits a partially subgrid and partially resolved structure in gray-zone grid spacings, the knowledge of its partiality becomes highly essential for mesoscale-microscale bridging. In this manner, the given partitioning functions in Honnert et al. (2011) initiated to treat one of the key challenges, i.e. the distribution of partiality by the scales, encountered in gray-zone modeling. Later, Shin and Hong (2013) expanded this methodology imposing 4 different convective forcings to investigate the turbulence gray-zone from free to forced CBL regimes. Then, considering the CBL regime as Honnert et al. (2011), they parameterized the partitioning functions of the local/non-local vertical eddy heat fluxes and turbulence kinetic energy for two CBL regions: the mixed layer and boundary layer top. Thanks to this analysis, Shin and Hong (2015) improved the YSU PBL scheme (Hong et al., 2006) to make it suitable for gray-zone grid spacings. Ito et al. (2015) extended the applicability range of a PBL scheme (Mellor-Yamada level-3) (Nakanishi and Niino, 2006) toward the gray-zone grid spacings. They also quantified the grid spacing range of gray-zone as the $0.2z_i < \widehat{\Delta} < 1.5z_i$ where $\widehat{\Delta}$ is the gray-zone grid spacing and z_i is the PBL height. Boutle et al. (2014) found out a new weighting function between meso- and microscales for the turbulence kinetic energy (TKE), obtained from the partitioning results of Honnert et al. (2011). They applied this weighting function to blend the YSU PBL scheme with the Smagorinsky SGS model (Smagorinsky, 1963), to be able to simulate the stratocumulus clouds at gray-zone grid spacings. Efstathiou et al.

(2016) followed this approach, but applying to the CBL in terms of different convective forcings. Efstathiou and Plant (2019) further modified this model in blending the YSU PBL scheme with the dynamic Smagorinsky SGS model (Bou-Zeid et al., 2005). They found that the use of dynamic Smagorinsky model outperforms that of standard Smagorinsky model (Smagorinsky, 1963) for the blending in gray-zone grid spacings. Kurowski and Teixeira (2018) performed gray-zone simulations for the free CBL. Their idea was to extend the existing SGS model of Deardorff (1980) from microscale to mesoscale limit by means of a blended mixing length scale. As a further improvement, Zhang et al. (2018) found out a blended mixing length scale for the forced CBL in order to develop a 3D TKE closure for gray-zone grid spacings. To blend the local and non-local eddy heat fluxes in gray-zone, they utilized the existing partitioning functions of Shin and Hong (2013). They tested their model in a real-case application in Weather, Research and Forecasting (WRF) model (Skamarock et al., 2008c), however, their model was found to underestimate the near-surface potential temperature observations at gray-zone grid spacings.

Deriving partitioning functions of turbulence fluxes in gray-zone is of particular significance to represent the scale dependency of subgrid scale transport. This is because such functions can aid in blending local/non-local heat fluxes (Shin and Hong, 2015; Zhang et al., 2018), mixing or dissipation length scales (Boutle et al., 2014; Efstathiou and Beare, 2015; Zhang et al., 2018) or eddy diffusivity coefficients (Efstathiou et al., 2016; Efstathiou and Plant, 2019) between meso- and microscales, required for the development of gray-zone parameterizations. However, these attempts have been limited to solely address the scale dependency of TKE and vertical heat flux since the earliest study of Honnert et al. (2011) and later in Shin and Hong (2013, 2015), Boutle et al. (2014), Kurowski and Teixeira (2018). Recently, Honnert (2019) conducted a comprehensive analysis on the scale-dependency of all the terms of eddy momentum fluxes (6 terms), by partitioning SGS behavior in gray-zone grid spacings. However, this investigation deals only with the neutral ABL.

Within this context, the objective of the present study is to develop a parameterization that describes the subgrid scale representation of gray-zone turbulence over a wide stability range of the convective ABLs. Beyond the state-of-the-art, we quantify and parameterize all the SGS terms of eddy momentum fluxes (τ_{ij}, 6 terms), eddy heat fluxes (q_j, 3 terms) and turbulence kinetic energy (k), in gray-zone grid spacings. This is accomplished by

coarse-graining the high-resolution large-eddy simulations from microscale ($\Delta = 50\ m$) to mesoscale ($\Delta = 3\ km$) grid spacings. Our LES setup follows that of Shin and Hong (2013), extended over a wide range of convective instabilities ($1.8 \leq -z_i/L_o \leq 604.8$). We derive 10 partitioning functions for each of the following 3 CBL regions: lower mixed layer ($0.10 < z/z_i < 0.50$), upper mixed layer ($0.50 < z/z_i < 0.85$) and boundary layer top ($0.85 < z/z_i < 1.10$). It is worth noting that the mixed layer herein refers to the most dynamic part of convective boundary layer where a vigorous turbulence governs the mixing of atmospheric mass, momentum and energy (Stull, 2012). We distinguish this layer into lower and upper parts, to take better into account the surface-induced and free-atmospheric effects separately. Moreover, the boundary layer top (also known as the entrainment zone) denotes the part of convective boundary layer that restricts the growth of mixed layer with a strong temperature inversion (Brooks and Fowler, 2012), rising toward the free-atmosphere (Honnert et al., 2011). Finally, unlike the existing partitioning functions, where the turbulence kinetic energy and vertical heat flux depend only on the gray-zone grid spacing and the height of convective boundary layer, our proposed model takes also into account the convective instability as well as the CBL height.

5.2 Theory & Modeling

5.2.1 Details of the high-resolution LES setup

High-resolution large-eddy simulations are performed employing the LES version of the Weather Research and Forecasting (WRF) model, namely WRF-LES (Skamarock et al., 2008c). In WRF-LES, time integration is made by using third-order Runge-Kutta method. Horizontal and vertical spatial discretization are based on fifth- and third-order finite difference approximations, respectively. Forcing conditions are imposed following Shin and Hong (2013). They define 4 different CBL cases in terms of the surface kinematic heat flux, Q_s and the geostrophic wind, U_g, which correspond to CBL1, CBL5, CBL7 and CBL8 cases in Table 5.1. The convective instability of these cases span over a wide range from buoyancy-driven to shear-dominant dry CBLs, as listed in Table 5.1 in terms of the Obukhov length, L_o, relative to the boundary layer height, z_i, often used to quantify convective instability in the ABL, $\zeta_i = -z_i/L_o$, spanning convective roll, transition and pure cellular

Case	L_o	Q_s	U_g	z_i	$\zeta_i = -z_i/L_o$	L_o/z_i	u_*	w_*	u_*/w_*
	$[m]$	$[Km/s]$	$[m/s]$	$[m]$	$[-]$	$[-]$	$[m/s]$	$[m/s]$	$[-]$
CBL1	-2.2	0.20	0	1317.2	604.8	-0.002	0.178	2.036	0.087
CBL2	-3.7	0.40	5	1896.1	513.1	-0.002	0.273	2.965	0.092
CBL3	-14.5	0.20	5	1287.6	88.6	-0.011	0.334	2.021	0.165
CBL4	-30.4	0.10	5	1098.4	36.1	-0.028	0.340	1.526	0.223
CBL5	-67.4	0.20	10	1288.8	19.1	-0.052	0.557	2.021	0.276
CBL6	-131.2	0.10	10	1099.6	8.4	-0.120	0.554	1.526	0.363
CBL7	-245.0	0.05	10	1006.2	4.1	-0.244	0.542	1.178	0.460
CBL8	-554.0	0.05	15	1007.1	1.8	-0.550	0.711	1.178	0.604

Table 5.1: Forcing parameters for the selected large-eddy simulation cases. Here, L_o is the Obukhov length, Q_s is the surface kinematic heat flux and U_g is the geostrophic wind speed. Time and horizontally averaged CBL characteristics are calculated for $t = 6 - 7\ h$ in terms of the friction velocity, u_*, Deardorff's convective velocity, w_*, planetary boundary layer height, z_i, and convective instability scale, $\zeta_i = -z_i/L_o$.

convection regimes: $1.8 \leq \zeta_i \leq 604.8$ (Lemone, 1973; Grossman, 1982; Weckwerth et al., 1999; Salesky et al., 2017).Besides these, 4 additional cases (CBL2, CBL3, CBL4, CBL6) are simulated to better refine the distribution of convective instabilities.

Periodic boundary conditions are applied in the horizontal directions, and the terrain is considered to be flat. The horizontal domain extends over $L_x = L_y = 12\ km$ where the grid spacing is $\Delta = 50\ m$ with 240 equally spaced grid cells. The vertical extent of the computational domain is $L_z = 2.4\ km$, discretized with a uniform grid spacing of $\Delta_z = 30\ m$. An absorbing Rayleigh-damping layer is added to damp vertical velocity perturbations within the uppermost 400 m off the domain top (Klemp et al., 2008). To account for the influence of subgrid scales, Kosović (1997) Nonlinear Backscatter and Anisotropy (NBA) SGS model is used. We set the roughness length to $z_0 = 0.1\ m$ and Coriolis parameter to $f = 1 \times 10^{-4}\ s^{-1}$. The integration time of simulations is $t = 6$ hours with a time step $\Delta t = 0.5\ s$. Then, time-averaging is applied to the turbulence statistics during $t = 6 - 7\ h$.

5.2.2 Coarse-graining the LES to gray-zone scales

In the present study, large-eddy simulations of 8 CBL cases are upscaled utilizing a similar methodology to that proposed by Honnert et al. (2011), which is often referred to as the coarse-graining method (Zhang et al., 2018). According to this approach, horizontal means are successively employed to the high-resolution LES data in order to convey the model behavior toward coarser grid spacings. As such, this approach has been widely used in gray-zone studies (Honnert et al., 2011; Shin and Hong, 2013; Zhou et al., 2014; Shin and Hong, 2015; Ito et al., 2015; Zhang et al., 2018). These studies employ successive horizontal means thanks to the explicit filtering of high-resolution LES data by the use of the top-hat filter. This filter applies a rectangular function in physical space (a cardinal sine function in wavenumber space), in turn causing spurious eddy structures while removing higher wavenumbers (i.e. small eddies) than the cut-off filter. Although it is advantageous in its easiness of implementation, it is however disadvantageous in representing non-local wavenumbers within the filtered field, which may cause unrealistic eddy structures (Honnert, 2019). It is worth noting that the influence of different filters on the gray-zone turbulence have been discussed in detail recently by Honnert (2019). However, such brief comparison of filters was limited to visual inspection of one instantaneous snapshot and did not quantify differences in energy or spectral distribution. Considering the drawbacks of the top-hat filter as mentioned earlier, here we consider the Butterworth filter (Butterworth et al., 1930) for the coarse-graining method following the recent applications of Muñoz-Esparza et al. (2020) and Doubrawa and Muñoz-Esparza (2020). The Butterworth filter has a wavenumber response G as follows:

$$G(\kappa) = \frac{1}{\sqrt{1 + \left(\frac{\kappa}{\kappa_c}\right)^{2n}}}, \tag{5.1}$$

where κ is the wavenumber, n is the order of filter, κ_c is the cut-off filter in wavenumber space. This filter has the advantage of minimizing spurious energy content at high wavenumbers unlike the top-hat filter. Moreover, it brings the advantage of a clear scale-specific filtering to distinguish the resolved and subgrid scales. By using the Butterworth filter, we apply successive filtering operations to our high-resolution LES data (hereafter referred to as reference-LES) in Fourier space, varying the filter width. In other words, the

Filter	$\widehat{\Delta}$ $[m]$	$\epsilon_{E_{uu}}[\%]$	$\epsilon_{E_{vv}}[\%]$	$\epsilon_{E_{ww}}[\%]$	$\epsilon_{E_{\theta\theta}}[\%]$
2^{nd}-order Butterworth	250	**+8.3**	+50.4	+48.8	**−17.3**
3^{rd}-order Butterworth	250	−18.8	**+1.1**	**−7.9**	−40.8
4^{th}-order Butterworth	250	−34.1	−24.5	−33.1	−52.7
top-hat	250	+467.3	+1067	+1881	+591.8

Table 5.2: Mean Percentage Error (ϵ) for the energy spectra of $E_{uu}, E_{vv}, E_{ww}, E_{\theta\theta}$ along with the κ_r. Errors are calculated when $1.0 \leq \kappa_r \leq 3.5$, with respect to the reference-LES ($\Delta_{LES} = 50\ m$).

reference-LES data is upscaled from $\Delta_{LES} = 50\ m$ to mesoscale grid spacings of $\widehat{\Delta} = 3\ km$, so as to obtain the filtered turbulence characteristics through the gray-zone scales.

5.2.3 Determination of the order of the Butterworth filter

The order of Butterworth filter, n, is of high significance, as it characterizes the wave number response of the filter. Lower orders, i.e. near $n = 1$, produce a smoother transition from lower to high wavenumbers, which leads to a loss of scale selectivity. In contrast, higher orders, especially around $n = 16$, result in a more sharp cut-off, which is closer to the sharp spectral filter. Doubrawa and Muñoz-Esparza (2020) defined $n = 12$ in their real-case simulations at gray-zone grid spacings. However, in the present study, we determine the order of Butterworth filter as the order that better approximates to the behavior of the reference-LES at high wavenumbers (i.e. to mimic WRF's spectral characteristics). To do this, time and spanwise averaged energy spectra, E_{ii}, of u, v, w, θ are computed for the reference and filtered LES, then plotted in terms of the normalized streamwise wavenumber, $\kappa_r = \kappa_1/\kappa_f$. Regarding the normalization, a reference wavenumber, κ_f, is defined as $\kappa_f = 2\pi/\Delta_f$, where $\Delta_f = 7\Delta$ corresponding to the effective grid spacing of the WRF model as determined by Skamarock (2004). In this manner, the filtered LES is computed by applying two different explicit filters (top-hat and n^{th}-order Butterworth) to the reference-LES fields having $\Delta_{LES} = 50\ m$ grid spacing.

To illustrate the filtering process, we choose an arbitrary filter width, f_w, to be $f_w = \widehat{\Delta}/\Delta_{LES} = 5$, leading to a grid spacing of $\widehat{\Delta} = 250\ m$ that falls inside the gray-zone. As our aim is to mimic the spectral distribution of WRF model at

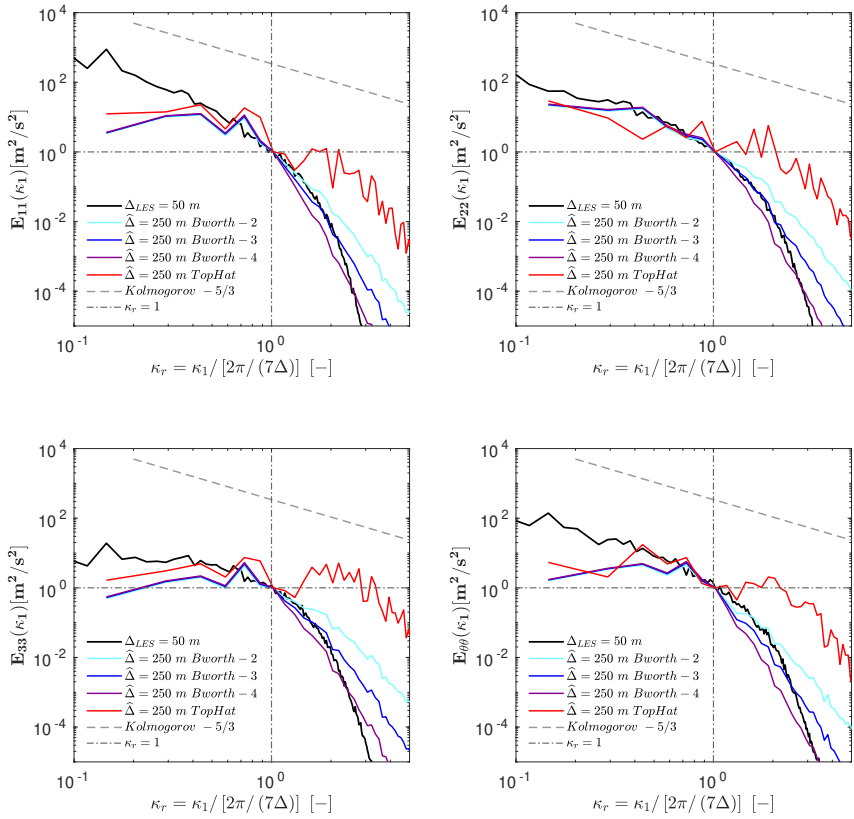

Figure 5.1: Time- and spanwise averaged $E_{ii}(\kappa_1)$ where $i = u, v, w, \theta$ along with the streamwise wavenumber, i.e. κ_1, normalized by the reference wavenumber, i.e. $\kappa_f = 2\pi/(7\Delta)$. The energy spectra is averaged in time between $t = 6 - 7h$ and computed at $z/z_i \approx 0.04$. Black solid line shows the reference-LES with $\Delta_{LES} = 50\ m$ grid spacing, while the colored solid lines refer to the filtered LES. Cyan, blue and purple solid lines are the filtered LES, inferred from the Butterworth filter at the gray-zone grid spacing of $\widehat{\Delta} = 250\ m$ (i.e. $\widehat{\Delta}_f = 1750\ m$) where $n = 2, 3, 4$ respectively. Red solid line presents the filtered LES by the top-hat filter at $\widehat{\Delta} = 250\ m$. Herein, gray dashed line displays the theoretical Kolmogorov −5/3 slope.

high wavenumbers, the filter grid spacing is determined as $\widehat{\Delta}_f = 7\widehat{\Delta} = 1750\ m$. The resulting spectra for the best 3 orders of Butterworth filter as $n = 2, 3, 4$ at $\widehat{\Delta}_f = 7\widehat{\Delta} = 1750\ m$ are presented in Fig. 5.1, in comparison with the reference-LES ($\Delta_{LES} = 50\ m$), all corresponding to $z/z_i \approx 0.04$. Here the selected case is CBL5. It is worth noting that each energy spectra is normalized by the energy spectra of the reference-LES at $\kappa_r = 1$. Thanks to this normalization, the energy spectra of both reference and filtered LES becomes $E_{ii} = 1$ at

$\kappa_r = 1$. The best proximity of n can be quantified by the trapezoidal integral, computing the area below the energy spectra from $\kappa_r = 1$ to $\kappa_{r,max} = 3.5$. Accordingly, the best value for the Butterworth filter, i.e. hereafter referred to as $\widetilde{n}$, can be easily deduced from Fig. 5.1 where the filtered LES approximates better to the reference-LES at high wavenumbers ($\kappa_r > 1$). Therefore, the best Butterworth order is $\widetilde{n} = 3$ for v and w, while the order of $\widetilde{n} = 2$ for u and the order of $\widetilde{n} = 4$ for θ fields in case of CBL5.

The integration results are listed in Table 5.2, calculating the mean percentage error, ϵ [%], of the filtered LES compared to the reference-LES. Results confirm that the $\widetilde{n} = 3$ is best for v and w to minimize the error, while $\widetilde{n} = 2$ for u and $\widetilde{n} = 4$ for θ. Table 5.2 also presents the mean percentage errors of the top-hat filter. This filter is simply applied as a box averaging, following the procedure employed by Honnert et al. (2011) and Shin and Hong (2013). Errors listed in Table 5.2 reveal that the top-hat filter is quite far from the energy spectra of reference-LES even at the gray-zone grid spacing of $\widehat{\Delta} = 250\ m$, leading to a systematic excess of energy at high wave numbers in Fig. 5.1, as further shown in the resulting filtered LES fields in Fig. 5.2. Therefore, one can state that, as anticipated, the use of the top-hat filter can cause unrealistic energy levels while applying the explicit filtering in gray-zone grid spacings, considerably affecting the resulting partitioning functions as will be shown later. To find out the best order of Butterworth filter for each variable and CBL case used, the same procedure is employed in calculating the trapezoidal integral of the energy spectra from $\kappa_r = 1$ to $\kappa_{r,max} = 3.5$ for 4 given variables (u, v, w, θ) and 8 simulated CBLs. Results are listed in Table 5.3 in terms of $\widetilde{n}$, leading to the lowest mean percentage errors. Thanks to this analysis, each variable and CBL case is filtered by its own particular order of the Butterworth filter through the gray-zone.

5.2.4 Functional form for the gray-zone partitioning functions

In order to parameterize the gray-zone partitioning functions of subgrid scale (SGS) turbulence quantities, the sigmoidal Gompertz function is utilized in the present study. This function was designed by Gompertz (1825) and has since then been used in numerous applications, as one of the most common functional form to reproduce the growth behaviour. Its evaluation extends from modeling the biological growth of plants (Tei et al., 1996), bacterial

Case	$\widetilde{n}_u$ [−]	$\widetilde{n}_v$ [−]	$\widetilde{n}_w$ [−]	$\widetilde{n}_\theta$ [−]
CBL1	2	2	2	2
CBL2	3	2	3	2
CBL3	4	2	4	4
CBL4	2	4	3	2
CBL5	2	3	3	2
CBL6	4	2	4	4
CBL7	2	3	3	3
CBL8	4	4	4	3

Table 5.3: Best order for the Butterworth filter, i.e. $\widetilde{n}_{u,v,w,\theta}$, giving the lowest mean percentage error for the energy spectra of $E_{uu}, E_{vv}, E_{ww}, E_{\theta\theta}$, with respect to the reference-LES.

cells (Zwietering et al., 1990; Liu et al., 2017) or tumours (Laird, 1964; d'Onofrio et al., 2011), through the analysis of disease spreads (e.g. COVID-19 pandemic (Torrealba-Rodriguez et al., 2020; Yue et al., 2020)). Likewise the given growth events, the gray-zone partitioning functions exhibit an abrupt expansion from $\sim$ 0 (microscale limit) to $\sim$ 1 (mesoscale limit), having a dichotomous plateau like behavior. Considering this similarity as well as the wide applicability, we select the sigmoidal Gompertz function as a reference functional form. It is defined in an expo-exponential basis as follows

$$\mathscr{H}(\mathrm{x}) = \alpha + (\beta - \alpha)\, e^{-e^{\gamma - \tau \mathrm{x}}}, \tag{5.2}$$

where the model constants in Eq. 5.2 are as follows: α is the upper asymptote, β is the lower asymptote, γ is the growth rate and τ refers to the inflection time at the maximum growth rate. It is worth noting that this function is a special member of Richards family together with 4 free parameters (Tjørve and Tjørve, 2017), i.e.

$$\mathscr{H}(\mathrm{x}) = \alpha + (\beta - \alpha)\, [1 + \upsilon e^{\gamma - \tau \mathrm{x}}]^{1/\upsilon}, \tag{5.3}$$

where $\lim_{\upsilon \to 0}(1 + \upsilon) \approx e^{\upsilon}$, the Richards function turns out to sigmoidal Gompertz function in Eq. 5.2.

So far, there have been limited attempts addressing the development of gray-zone partitioning functions in convective boundary layers. Specifically, the existing partitioning functions (Honnert et al., 2011; Boutle et al., 2014; Shin and Hong, 2013) are defined for the free CBL regime where there is no

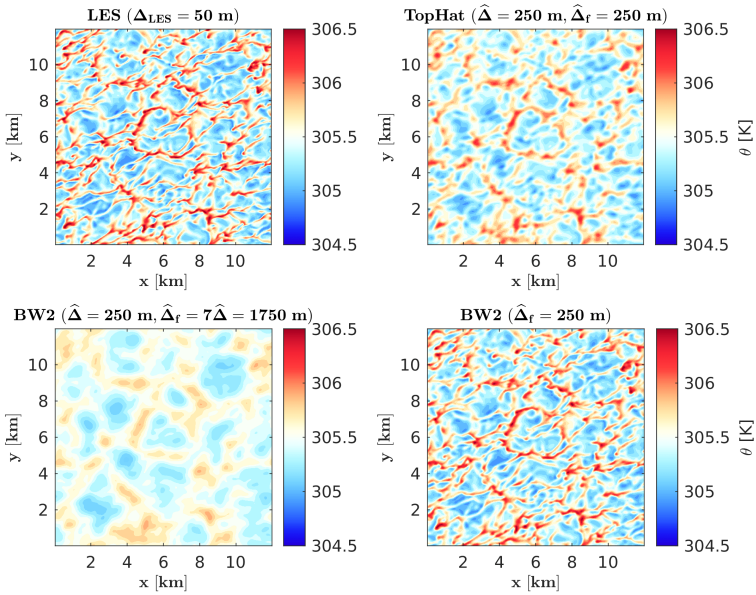

Figure 5.2: Instantaneous horizontal cross-sections of the potential temperature, θ, for the CBL5 case. Presented contour plots are calculated at $z/z_i \approx 0.04$ when t=6h. Top-left panel displays the reference-LES field having $\Delta^{LES} = 50\ m$ grid spacing. Top-right and bottom-right panels show the filtered LES fields at the gray-zone grid spacing of $\widehat{\Delta} = 250\ m$ by means of the top-hat and 2nd-order Butterworth (BW2) filters, respectively. Besides the bottom-left panel demonstrates the effective grid spacing of $\widehat{\Delta} = 250\ m$, resulting in $\widehat{\Delta}_f = 7\widehat{\Delta} = 1750\ m$ in order to mimic the model response of the WRF. The color bar ranges between 304.5 K (blue) and 306.5 K (red).

turbulence shear production. Moreover, these functions are proposed only for the turbulence kinetic energy (k) and vertical eddy heat flux ($w'\theta'$) (Honnert et al., 2011; Shin and Hong, 2013; Zhang et al., 2018) with respect to the gray-zone grid spacing, $\widehat{\Delta}$, and the PBL height, z_i.

$$\mathcal{P}_{\Delta}^{sgs} = f\left(\widehat{\Delta}/z_i\right), \tag{5.4}$$

where $\mathcal{P}_{\Delta}^{sgs} = \Phi^{sgs}/\Phi^{tot}$ denotes the SGS partitioning function in gray-zone grid spacings, representing the SGS contribution, Φ^{sgs}, to the total (resolved+SGS) eddy fluxes, Φ^{tot}.

As discussed in Sec. 5.1, our main goal is to develop a full 3D representation of partitioning functions in the turbulence gray-zone. This requires a parameterization for all the components of SGS eddy momentum fluxes: $\tau_{ij} =$

$u'u', v'v', w'w', u'v', u'w', v'w'$ and SGS eddy heat fluxes: $q_j = u'\theta', v'\theta', w'\theta'$. Our model aims to extend previous efforts and propose gray-zone partitioning functions over a comprehensive range of convective instabilities ranging from purely buoyant to strongly sheared CBL. To do this, the dependency of Eq. 5.4 is expanded including the effect of convective instability in terms of $\mathfrak{X}_i$ as follows

$$\mathcal{P}_{\Delta}^{sgs} = f\left(\widehat{\Delta}/z_i, \mathfrak{X}_i\right), \tag{5.5}$$

where $\mathfrak{X}_i = 1/\zeta_i = -L_o/z_i$ is the inverse of convective instability scale, ζ_i. As mentioned earlier, our model is built based on the sigmoidal Gompertz function. Recalling the Eq. 5.2 and replacing x with $\widehat{\Delta}/z_i$ reads

$$\mathcal{P}_{\Delta}^{sgs}\left(\widehat{\Delta}/z_i\right) = \alpha + (\beta - \alpha)\, e^{-e^{\gamma - \tau\left(\widehat{\Delta}/z_i\right)}}, \tag{5.6}$$

The effect of convective instability is considered in the proposed functional form, linking $\mathfrak{X}_i$ with τ and γ parameters. To illustrate, the τ translates the partitioning function horizontally, while the γ parameter shifting the function vertically. Here, τ and γ are defined as follows:

$$\begin{aligned} \tau &= C_1 + C_2 e^{\mathfrak{X}_i^{C_3}}, \\ \gamma &= G_1 + G_2 \tanh\left(G_3 \mathfrak{X}_i\right), \end{aligned} \tag{5.7}$$

leading to 6 additional unknowns more, $C_1, C_2, C_3, G_1, G_2, G_3$, in addition to α and β. By substituting Eq. 5.7 into Eq. 5.6 gives the final functional form of gray-zone partitioning functions as follows:

$$\mathcal{P}_{\Delta}^{sgs}\left(\widehat{\Delta}/z_i, \mathfrak{X}_i\right) = \alpha + (\beta - \alpha)\, e^{-e^{\left(G_1 + G_2 \tanh\left(G_3 \mathfrak{X}_i\right)\right) - \left(C_1 + C_2 e^{\mathfrak{X}_i^{C_3}}\right)\left(\widehat{\Delta}/z_i\right)}}, \tag{5.8}$$

It is worth noting that the Eq. 5.8 is both scale and stability dependent in an expo-exponential form. This definition results in 8 model parameters $(\alpha, \beta, C_1, C_2, C_3, G_1, G_2, G_3)$ for each turbulence fluxes at each particular CBL regions.

To define all the unknowns appearing in Eq. 5.8, we first obtain the gray-zone partitioning functions from our time- as well as horizontally-averaged reference-LES data (see Sec. 5.2.1). This high-resolution data is explicitly coarse-grained from 50 m grid spacing to 3 km by means of the Butterworth

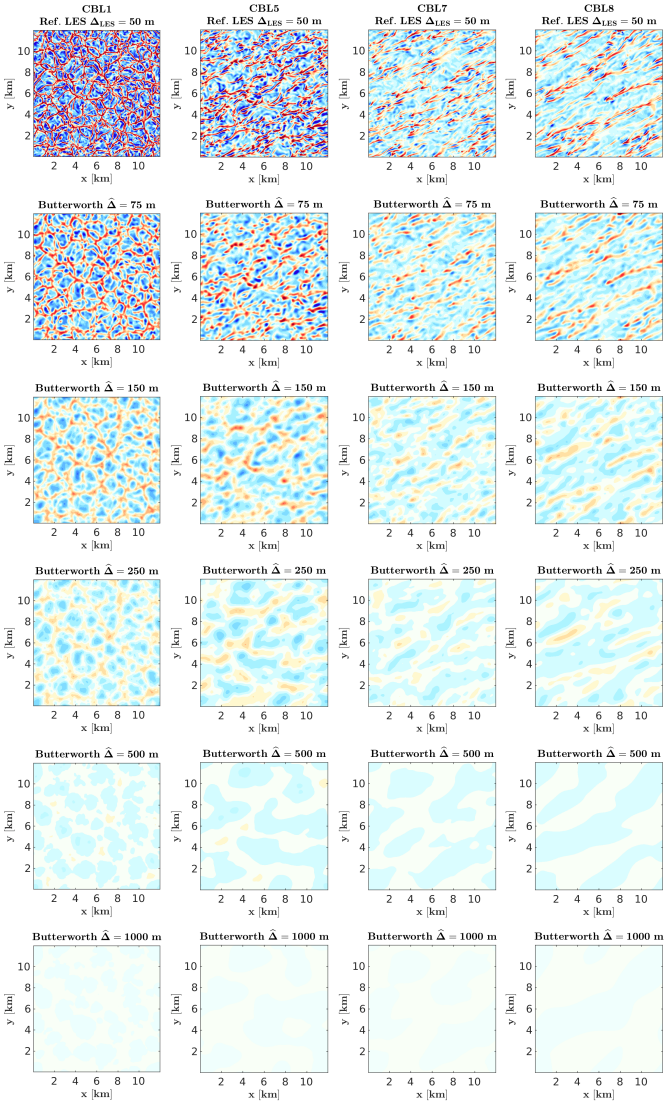

Figure 5.3: Instantaneous horizontal cross-sections of the vertical wind speed, w, at t=6h. From left to right panels, different convective instabilities are demonstrated respectively: purely buoyant (CBL1, 1st column), forced buoyant (CBL5, 2nd column), weakly sheared (CBL7, 3rd column) and strongly sheared (CBL8, 4th column) cases. Top panels display the coherent structures inferred from the reference-LES ($\Delta^{LES} = 50\ m$), while the below panels show the coarse-grained results at the gray-zone grid spacings of $\widehat{\Delta} = 75\ m, 150\ m, 250\ m, 500\ m, 1000\ m$ respectively. The color bar ranges between $-0.8\ m/s$ (blue) and $0.8\ m/s$ (red).

filter (see Sec. 5.2.2). The best order of Butterworth filter is determined from the spectral analysis in Sec. 5.2.3. Accordingly, these steps lead to provide gray-zone partitioning functions of turbulence fluxes Sec. 5.2.4. Then, the remaining unknown model parameters are determined by a nonlinear regression analysis via least squares method (Moré, 1978) (see Sec. 5.2.5).

5.2.5 Development of scale-aware three-dimensional gray-zone (Senel-Temel 3DPBL) turbulence model

The effect of coarse-graining is demonstrated in Fig 5.3 as horizontal cross-sections for the vertical velocity within the surface-layer $z/z_i \approx 0.04$ for $t = 6h$. Distinct types of coherent structures exist due to the difference in buoyancy and shear forcing mechanisms. Coherent structures form as convective cells for the buoyancy-driven CBL1, resulting from strong localized rising thermals surrounded by cold downdrafts (Schmidt and Schumann, 1989). Such that the size of these convective cells is comparable to the size of CBL, which is on order of $\mathcal{O}(1\ km)$. On the other hand, these cellular structures progressively turn into elongated convective rolls, due to the presence of the wind shear (CBL7 and CBL8). As shown in Fig 5.1, due to the increase in wind shear from CBL5 (forced buoyant condition) throughout CBL8 (strongly sheared condition), convective rolls become more elongated in the flow direction. This substantial alteration in coherent structures is of particular interest in the present study, since we aim to represent the stability dependency of gray-zone partitioning functions over a wide range of convective instabilities. To quantify how much convective the simulated case is, the Obukhov length is computed in Table 5.1, as ranging from $\zeta_i = 604.8$ to $\zeta_i = 1.8$ between the pure-buoyant (CBL1) and shear-dominant (CBL8) cases. Since the high L_o leads to augment the shear force with respect to the buoyant force, accordingly the ratio of friction velocity to the Deardorff's velocity scale (Deardorff, 1970), i.e. u_*/w_*, rises from 0.087 to 0.604 between the CBL1 and CBL8 (Table 5.1). This variation in u_*/w_* is consistent with the results of Shin and Hong (2013).

As described in Section 2.2, the reference-LES data is successively coarse-grained by means of the Butterworth filter. The filtered results are demonstrated in Fig. 5.3, where the gray-zone grid spacings are $\widehat{\Delta} = 75, 150, 250\ m$, then further increased to coarser grid spacings up to $\widehat{\Delta} = 500, 1000\ m$ in Fig 5.3. Filtering the reference-LES data to the gray-zone grid

spacing of $\widehat{\Delta} = 75\ m$ does not show a significant influence in the resolved turbulence. This is because such a grid spacing ($\widehat{\Delta} = 75\ m$) keeps mainly the resolved modes as is the case with the reference-LES ($\Delta_{LES} = 50\ m$). This similarity in coherent structures between the $\Delta_{LES} = 50\ m$ and $\widehat{\Delta} = 75\ m$ is consistent with the gray-zone range observed by Shin and Hong (2013) as beginning nearly $\widehat{\Delta} > 0.05 - 0.10 z_i$ for the CBL. In accordance with this description, the onset of gray-zone for the given CBLs in Fig 5.3 commences around $\widehat{\Delta} = 75\ m$. However, further increase in the gray-zone grid spacing, for instance towards the grid spacings of $\widehat{\Delta} = 250, 500\ m$, makes the turbulence more smoothed out. This behavior becomes more apparent in Fig 5.3, especially for the gray-zone grid spacing of $\widehat{\Delta} = 1\ km$, at which the grid spacing approaches to the mesoscale limit of CBL (i.e. $> 2z_i$ (Honnert et al., 2011; Shin and Hong, 2013)). As such a gray-zone grid spacing of $1\ km$ can be considered as the onset of mesoscale grid spacings in numerical weather prediction models, where the turbulence tends to vanish as shown in Fig 5.3. This interpretation also confirms that the turbulence in gray-zone stands for a transition state between mostly resolved LES (as will be shown later) and fully subgrid mesoscale grid spacings.

Considering that the production of turbulent fluxes (momentum, heat, moisture and aerosols) in the gray-zone is partially resolved and subgrid (Honnert et al., 2011), the distribution of its partiality needs to be quantified to represent the subgrid scale transport in the gray-zone. As mentioned earlier, this can be handled by retrieving the ratio of subgrid to total (resolved+subgrid) fluxes in terms of partitioning functions, i.e. $\mathscr{P}_{\Delta}^{sgs} = \Phi^{sgs}/\Phi^{tot}$.

In the present study, we determine the partitioning functions of resolved and SGS eddy fluxes of turbulence kinetic energy, k, momentum (τ_{ij}, 6 terms) and heat (q_j, 3 terms). The obtained results are presented in Fig. 5.4 for the partitioning of turbulence kinetic energy at 3 different CBL regions: lower mixed layer ($0.10 \leq z/z_i \leq 0.50$), upper mixed layer ($0.50 \leq z/z_i \leq 0.85$) and boundary layer top top ($0.85 \leq z/z_i \leq 1.10$). Here, the time and horizontally averaged partitioning functions are given for both resolved and SGS components of turbulence kinetic energy along with the gray-zone grid spacing normalized by the PBL height, $\widehat{\Delta}/z_i$. The markers in Fig. 5.4 refer to the resolved component, $\mathscr{P}_{\Delta}^{res}$, and subgrid component, $\mathscr{P}_{\Delta}^{sgs}$, partitioning functions at each altitude falling inside the given CBL region.

To determine the scale-dependency of these functions, the coarse-graining

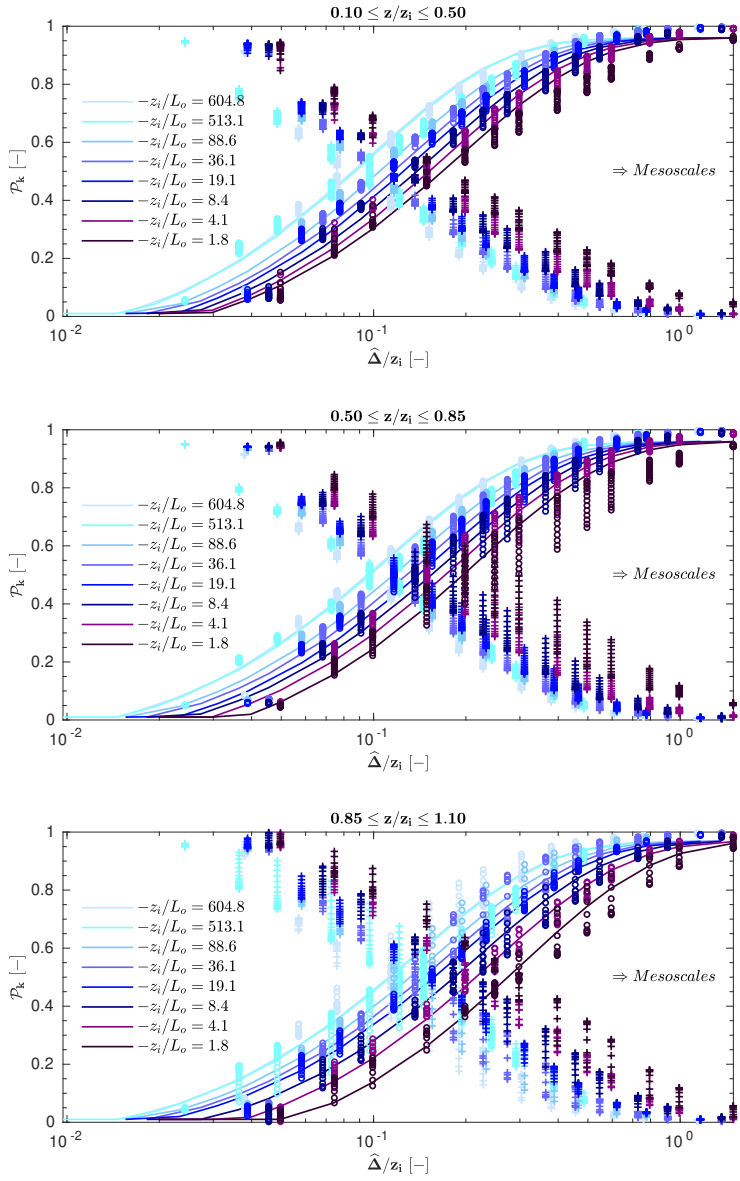

Figure 5.4: Gray-zone partitioning functions of resolved and SGS turbulence kinetic energy $\mathcal{P}_k$. Results are horizontally averaged in x, y, then averaged in time between $t = 6 - 7h$, for different levels of the convective instability scale, i.e. $\zeta_i = -z_i/L_o$. Plus and circular markers refer to the resolved and SGS TKE partitioning respectively, at each altitude within the given CBL region. Solid lines represent the proposed model in terms of the sigmoidal Gompertz functions.

method of Honnert et al. (2011) is utilized as follows:

$$\mathcal{P}_{\Delta}^{sgs}\left(\widehat{\Delta}\right) = \mathcal{P}_{LES}^{tot} - \mathcal{P}_{\Delta}^{res}\left(\widehat{\Delta}\right) = \left(\mathcal{P}_{LES}^{res} + \mathcal{P}_{LES}^{sgs}\right) - \mathcal{P}_{\Delta}^{res}\left(\widehat{\Delta}\right) = 1 - \mathcal{P}_{\Delta}^{res}\left(\widehat{\Delta}\right), \quad (5.9)$$

In Eq. 5.9, the first two terms on the right-hand side, $\mathcal{P}_{LES}^{res}$ and $\mathcal{P}_{LES}^{sgs}$, are the resolved and SGS partitioning functions, which are known from the reference-LES at $\Delta = 50\ m$. The sum of them are equal to 1. The second term, $\mathcal{P}_{\Delta}^{res}(\widehat{\Delta})$, denotes the resolved partitioning functions, determined by the Butterworth filter at a given gray-zone grid spacing, $\widehat{\Delta}$.

The distribution of partitioning functions in Fig. 5.4 reveals that the partitioning functions are dependent not only on the gray-zone grid spacing and PBL height, but also on the convective instability. Here, the latter ranges from $\zeta_i = 604.8$ (pure buoyancy, CBL1) to $\zeta_i = 1.8$ (strongly sheared, CBL8). Results reveal that the partitioning functions tend to shift upward as the convective instability increases. In other words, buoyancy- and shear-driven convective PBLs stand for the up and down (or left and right) limits of TKE partitioning functions, respectively. This behavior is valid for all the vertical CBL regions, however, the span of vertical shift increases from lower mixed layer to the upper layer. To illustrate this aspect, if the SGS partitioning ratio of TKE is considered at $\widehat{\Delta}/z_i = 0.2$, the vertical shift between up and down limits (CBL1 and CBL8) are 0.282, 0.312 and 0.385 for the lower mixed layer, upper mixed layer and boundary layer top, respectively. The stability-dependency of turbulence kinetic energy in gray-zone appears to become more significant in upper regions of the CBL, in particular within the entrainment-zone, $0.85 \leq z/z_i \leq 1.10$.

Moreover, the up and down limits of SGS TKE partitioning between the most buoyant (CBL1) and sheared (CBL8) conditions at $\widehat{\Delta}/z_i = 0.2$ are $\mathcal{P}_k^+ = 0.822$ and $\mathcal{P}_k^- = 0.540$ for the lower mixed layer, $\mathcal{P}_k^+ = 0.784$ and $\mathcal{P}_k^- = 0.472$ for the upper mixed layer, $\mathcal{P}_k^+ = 0.763$ and $\mathcal{P}_k^- = 0.378$ for the boundary layer top. Accordingly, the vertical shift in $\mathcal{P}_k$ between the most buoyant and sheared CBL corresponds to a percentile difference of 20.7%, 24.8%, 33.8% for these 3 CBL regions, respectively. This substantial shift between the most buoyant and sheared CBLs in subgrid scale TKE partitioning proves the strong influence of atmospheric stability on gray-zone partitioning functions, which has not been taken into account by any of the existing models so far.

The current gray-zone parameterizations (Honnert et al., 2011; Shin and

Hong, 2013; Boutle et al., 2014) only consider the free CBL regime. For instance, Shin and Hong (2013) derived an expression for $\mathcal{P}_k^{sgs}$ in two CBL regions: $0.10 \leq z/z_i \leq 0.80$ and $0.85 \leq z/z_i \leq 1.10$. This parameterization is built for the free convection regime where the surface heating, $Q_s = 0.20\ Km/s$, and geostrophic wind, $U_g = 0\ m/s$. Recently, Zhang et al. (2018) obtained the subgrid scale TKE partitioning the in gray-zone for the sheared CBL, $Q_s = 0.20\ Km/s$, and geostrophic wind, $U_g = 10\ m/s$, using coarse-graining method by the top-hat filter similar to Shin and Hong (2013). They found that their formulation for the sheared CBL is identical to the one proposed by Honnert et al. (2011) for the free CBL. However, our study reveals a considerable difference for $\mathcal{P}_k^{sgs}$ in gray-zone between free- and sheared CBLs as aforementioned. We attribute this effect to the spurious energy content introduced by the top-hat filter, together with the interplay among high wavenumber energy dissipation by the implicit filtering of the advection term and the advecting velocity.

In order to parameterize the gray-zone partitioning functions of SGS turbulence kinetic energy, $\mathcal{P}_k^{sgs}$, we derive a generic expression in terms of gray-zone grid spacing, PBL height and Obukhov length, i.e., $\mathcal{P}_\Delta^{sgs}\left(\widehat{\Delta}/z_i, \mathfrak{X}_i = L_o/z_i\right)$ for each of the three altitude ranges. As described in Sec. 5.2.2, we utilize the sigmoidal Gompertz functional form having 4 free-parameters: α, β, τ and γ (Eqs. 5.6-5.7). After applying a non-linear regression analysis to the mean of SGS turbulence kinetic energy partitioning at each vertical region in Fig. 5.4, all the model parameters are determined. Note that the regression analysis herein is based on the nonlinear least squares method (Moré, 1978). This regression analysis is successively applied with 5 outer iterations, where the first iteration returns the initial estimation without any lower or upper bounds for the α, β, τ, γ. Then, the second and third iterations compute the α and the β as the mean of performed CBL cases. The fourth iteration predicts the τ from the Eq. 5.6 and afterwards corrects in the last iteration where the γ is determined in terms of the functional form given in Eq. 5.7. Finally, the final form of the proposed $\mathcal{P}_k^{sgs}$ is given as follows:

$$\begin{aligned}\mathcal{P}_k^{sgs}\left(\widehat{\Delta}/z_i, \mathfrak{X}_i\right) &= \frac{\langle k\rangle_\Delta^{sgs}}{\langle k\rangle^{tot}}\left(\widehat{\Delta}/z_i, \mathfrak{X}_i\right) \\ &= \alpha + (\beta - \alpha)\, e^{-e^{(G_1+G_2\tanh(G_3\mathfrak{X}_i))-\left(C_1+C_2 e^{\mathfrak{X}_i^{C_3}}\right)\left(\widehat{\Delta}/z_i\right)}},\end{aligned} \tag{5.10}$$

where the model parameters are as follows:

$$
\begin{array}{l}
\qquad\qquad\qquad\qquad\qquad\qquad \alpha, \beta, C_1, C_2, C_3, G_1, G_2, G_3 \\
= \begin{cases}
\begin{array}{lllllllll} 0.96 & -50 & -20.00 & +9.13 & -0.03 & -3.81 & -0.06 & +0.18 \\ :0.10 \le z/z_i \le 0.50 \end{array} \\
\begin{array}{lllllllll} 0.96 & -50 & -19.99 & +8.91 & -0.03 & -3.84 & -0.26 & -0.26 \\ :0.50 \le z/z_i \le 0.85 \end{array} \\
\begin{array}{lllllllll} 0.97 & -50 & +20.00 & -6.37 & +0.06 & -3.86 & -0.09 & -1.96 \\ :0.85 \le z/z_i \le 1.10 \end{array}
\end{cases}
\end{array}
\tag{5.11}
$$

The proposed model in Eq. 5.10-5.11 represents the gray-zone partitioning functions of SGS turbulence kinetic energy, $\mathscr{P}_k^{sgs}$. In Fig. 5.5, we compare our model with respect to the existing models of Honnert et al. (2011) and Shin and Hong (2013). Considering that all these models are specifically developed for the free CBL regime, we display only our results for the CBL1 case. Note that CBL1 is identical to the CBL case simulated by Shin and Hong (2013).

Moreover, as the proposed model makes use of the Butterworth filter, the same procedure is repeated applying the top-hat filter for the sake of completeness and comparability to existing parameterizations. Results in Fig. 5.5 show that our proposed partitioning of k^{sgs} by the top-hat filter matches well with the model of Shin and Hong (2013). As our LES setup is based on the setup of Shin and Hong (2013) with the same convective forcing (Q_s = 0.20 Km/s and U_g = 0 m/s), this further verifies the validity of our LES and the partitioning functions across the gray-zone. While partitioning the CBL1 by the top-hat filter is in agreement with Shin and Hong (2013) and Honnert et al. (2011), however, all these partitionings considerably underestimate the proposed model derived employing the Butterworth filter, as well as Kurowski and Teixeira (2018). The most likely reason for this difference is the systematic energy overprediction of the top-hat filter as can be seen from the energy spectra presented in Fig. 5.1. The amount of that overprediction can also be noticed in Table 5.2 where the top-hat filter leads to considerably large errors at high wavenumbers with respect to the reference-LES. It is worth noting that the results of Kurowski and Teixeira (2018) underestimate all the presented TKE partitionings. This can be caused by the fact that their simulated surface heating values are pretty weak (Q_s = 0.03 – 0.06 Km/s). Another reason might be the fact that their TKE partitioning is obtained from

the LES model simulating at various grid spacings in gray-zone, inherently affected by parameterization issues. The use of an LES model with the existing SGS parameterizations is open to question in turbulence gray-zone (or terra incognita), as they are originally designed for their own limit (Wyngaard, 2004).

As mentioned earlier, the previous studies are limited to the SGS turbulence kinetic energy, k, and vertical eddy heat flux, $w'\theta'$. However, in order to make a full 3D representation of turbulence gray-zone, all the terms of SGS eddy momentum and heat fluxes are needed to be partitioned. This corresponds to 6 terms for SGS eddy momentum fluxes: $\tau_{ij} = u'u', v'v', w'w', u'v', u'w', v'w'$ and 3 terms for eddy heat fluxes: $q_j = u'\theta', v'\theta', w'\theta'$. Following the same methodology applied for the turbulence kinetic energy, partitioning of eddy momentum and heat fluxes are obtained by coarse-graining the high-resolution reference-LES data from microscale ($\Delta_{LES} = 50\ m$) toward mesoscale ($\widehat{\Delta} = 3\ km$) grid spacings. Likewise $\mathcal{P}_k$, the partitioning is employed for all the fluxes at 3 CBL regions, from lower and upper mixed layer to boundary layer top.

In Fig. 5.6, partitioning results of resolved and SGS fluxes are demonstrated for $u'u'$, $v'v'$, $w'w'$ $u'v'$, $u'w'$ and $w'\theta'$. Here, the CBL regime corresponds to the buoyant and sheared convection, where the surface forcings are $Q_s = 0.20\ Km/s$ and $U_g = 10\ m/s$ (CBL4). Results in Fig. 5.6 show that the partiality of gray-zone for the CBL is dependent on the vertical region, as observed for the partitioning of turbulence kinetic energy in Fig. 5.4. This is the reason why we consider each vertical CBL region separately.

In Fig. 5.6, the SGS partitioning of $u'u'$ and $v'v'$ indicates that the lower and upper mixed layers become more subgrid at a specific gray-zone grid spacing than the entrainment-zone, which is similar to the behavior of $k = 0.5(u'u' + v'v' + w'w')$ in Fig. 5.4. However, this is not the case for the partitioning of $w'w'$. Such that the latter flux tends to reach the fully-subgrid mesoscale limit earlier in the entrainment-zone. The reason for that can be explained from the time and horizontally averaged vertical profiles of total eddy momentum fluxes plotted in Fig. 5.6e. As the total flux of $w'w'$ is lower than that of $u'u'$ and $v'v'$ in entrainment zone, i.e. $0.85 \leq z/z_i \leq 1.10$, the significance of subgrid scales becomes dominant with respect to the total flux.

Moreover, Fig. 5.6 displays the gray-zone representation of $u'v'$ and $u'w'$. Note that, hereafter an arbitrary component of a momentum/heat flux, $\Phi'_i\Phi'_j$,

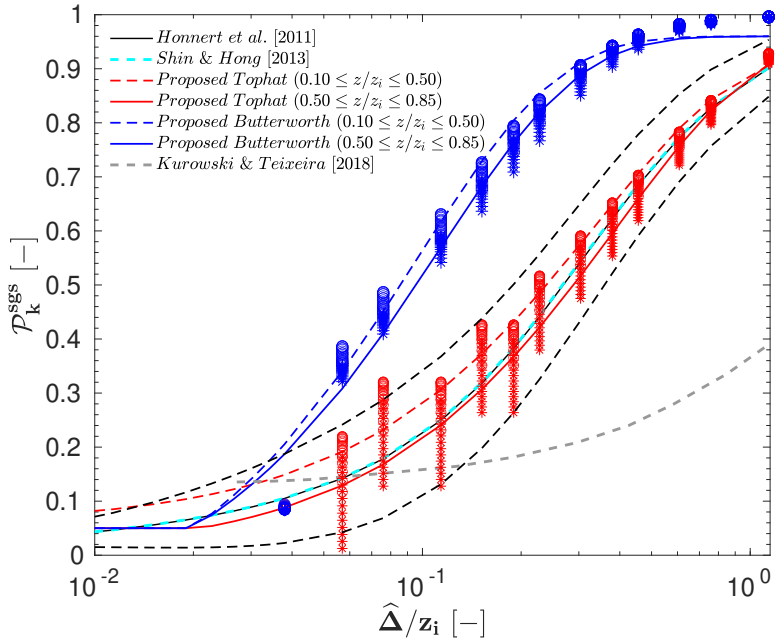

Figure 5.5: Gray-zone partitioning functions of the SGS turbulence kinetic energy, i.e. $\mathcal{P}_k^{sgs}$, along with the normalized gray-zone grid spacing, i.e. Δ/z_i. Markers display the SGS TKE partitioning at each altitude within the given CBL region. Circular and asterisk markers denote the partitioning ratios within the lower and upper mixed layers respectively. Blue dashed and solid lines refer to the proposed model derived via the Butterworth filter. Red dashed and solid lines are the mean of partitioning at each altitude display by the red circular and asterisk markers, respectively. Black solid line refers to the model of Honnert et al. (2011) proposed for $0.05 \leq z/z_i \leq 0.85$, where the black dashed lines denote the first as well as last vigintiles of the corresponding model. Solid line colored by cyan is the model of Shin and Hong (2013) described for $0.10 \leq z/z_i \leq 0.80$.

is referred to as a flux co-variance when $i \neq j$ and a flux variance when $i = j$. As Honnert (2019) pointed out for the neutral PBL, these fluxes lead to a larger dispersion at a given gray-zone grid spacing than the flux variances. This is due to the fact that the total (resolved+SGS) magnitude of flux variances reaches to $2\ m^2/s^2$, which dominates over that of flux co-variances. As the latter is on the order of $\mathcal{O}(-0.1\ m^2/s^2)$, this makes the flux co-variances more sensitive to the changes in subgrid scales with a wide dispersion in gray-zone. Furthermore, the flux co-variances, in particular $u'v'$, delay the subgrid scale transition through the more coarser grid spacings in gray-zone compared to the flux variances. For instance, the SGS partitioning of horizontal flux co-variance,

$\mathcal{P}_{u'v'}$ is lower than 0.1 at nearly $\widehat{\Delta}/z_i < 0.10$, whereas this value extends to $\widehat{\Delta}/z_i = 0.04$ for the flux variances. This means that the onset of gray-zone, which is nearly $\widehat{\Delta}/z_i \geq 0.04$ for flux variances, shifts to the larger grid spacings for flux co-variances. This can be approximated as $\widehat{\Delta}/z_i \geq 0.10$ for $u'v'$. In other words, an arbitrary grid spacing between $0.04 \leq \widehat{\Delta}/z_i \leq 0.10$ can fall in the gray-zone for the flux variances, while it can represent the microscale limit for the horizontal flux co-variance. This concludes that the lower (microscale) and upper (mesoscale) limits of gray-zone transition depend on the eddy flux under consideration, thus highlighting the reason why the partitioning functions are parameterized in terms of $\widehat{\Delta}/z_i$, as we do in Eq. 5.10. Besides the partitioning of eddy momentum fluxes, Fig. 5.6 presents the resolved and SGS partitioning of vertical eddy heat flux, $w'\theta'$, resembling to the behavior of the flux variances. Relatively high dispersion arises because of the altitude between the upper mixed layer and entrainment-zone, i.e. $0.8 \leq \widehat{\Delta} \leq 0.9$. Here is the region where the vertical eddy flux tends to vanish as can be seen in Fig. 5.6h.

Finally, to build a full 3D representation of turbulence gray-zone, we propose gray-zone partitioning functions of eddy momentum and heat fluxes employing the same methodology applied for the turbulence kinetic energy. The proposed model is derived in a stability-dependent formulation over a wide range of convective instabilities (listed in Table 5.4). The model parameters are determined in terms of the sigmoidal Gompertz function in Table 5.4 for 9 eddy fluxes within 3 different CBL regions, from the lower altitudes of the CBL toward the free-atmosphere. It is worth mentioning that this parameterization can be utilized in numerical weather prediction models to bridge meso- and microscales in a scale-aware form. This can be handled by

$$\begin{aligned} \tau_{ij}^{\Delta} &= \mathcal{P}_{\Delta}^{sgs}\left(\tau_{ij}^{meso}, \tau_{ij}^{micro}\right), \\ q_{j}^{\Delta} &= \mathcal{P}_{\Delta}^{sgs}\left(q_{j}^{meso}, q_{j}^{micro}\right), \end{aligned} \tag{5.12}$$

where $i, j = u, v, w$ and τ_{ij}^{Δ} and q_j^{Δ} are the SGS eddy momentum and heat fluxes in the gray-zone. The superscripts of meso and micro refer to the eddy fluxes at meso- and microscales respectively. Here, $\mathcal{P}_{\Delta}^{sgs}$ stands for the gray-zone partitioning functions as described earlier, which relates the subgrid scale transition between meso- and microscales given in Table 5.4.

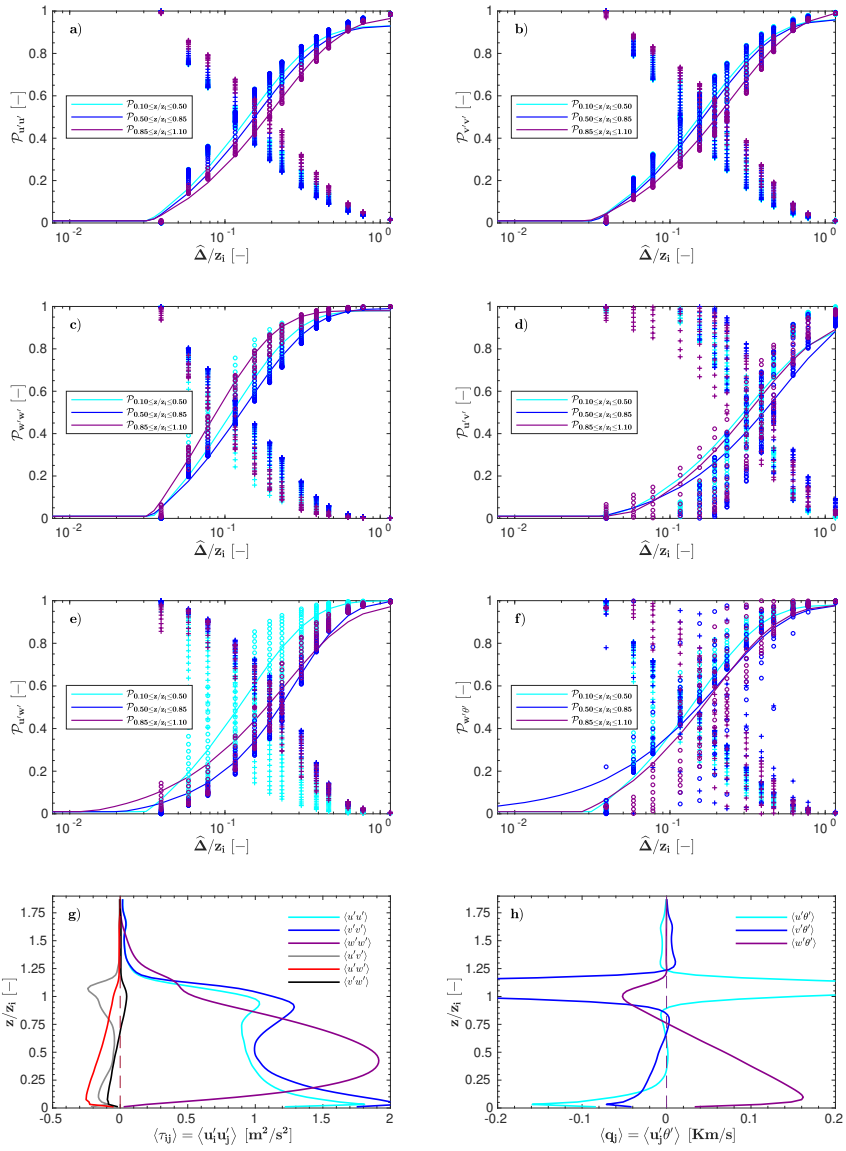

Figure 5.6: Time- and horizontally averaged gray-zone partitioning functions of momentum/heat eddy fluxes along with the normalized gray-zone grid spacing. Partitioning results are obtained for the CBL4 case ($Q_s = 0.20\ Km/s, U_g = 10\ m/s$) at 3 different CBL regions: $0.10 \leq z/z_i \leq 0.50$, $0.50 \leq z/z_i \leq 0.85$ and $0.85 \leq z/z_i \leq 1.10$. Plus and circular markers refer to the resolved and SGS partitioning respectively, at each altitude within the given CBL region. Solid lines represent the proposed model in terms of the sigmoidal Gompertz functions. Bottom panels show the time- and horizontally averaged vertical profiles of the total eddy momentum (left) and eddy heat (right) fluxes.

$0.10 < z/z_i < 0.50$	α	β	C_1	C_2	C_3	G_1	G_2	G_3
$\mathcal{P}^{sgs}_{u'u'}$	0.93	−50.00	−20.0000	8.9179	−0.0349	−3.7417	0.0775	−10.0000
$\mathcal{P}^{sgs}_{v'v'}$	0.96	−50.00	−20.0000	8.7476	−0.0285	−3.7830	−0.0291	−0.9933
$\mathcal{P}^{sgs}_{w'w'}$	0.98	−50.00	−18.9835	10.0337	−0.0121	−3.6625	−0.0822	−7.5387
$\mathcal{P}^{sgs}_{u'v'}$	0.91	−49.04	6.8392	−3.5020	0.9197	−3.8304	9.9949	−0.0807
$\mathcal{P}^{sgs}_{u'w'}$	1.00	−50.00	−3.6493	3.9982	−0.0084	−3.7916	−0.2418	−7.5474
$\mathcal{P}^{sgs}_{v'w'}$	0.89	−50.00	4.9713	1.5867	−0.0096	−3.9405	−0.4615	−5.8224
$\mathcal{P}^{sgs}_{u'\theta'}$	0.88	−50.00	−15.8755	14.6417	0.3737	−5.1804	−1.8002	−6.1799
$\mathcal{P}^{sgs}_{v'\theta'}$	0.96	−50.00	4.5636	−0.0026	−0.2930	−4.4727	−0.8613	−10.0000
$\mathcal{P}^{sgs}_{w'\theta'}$	0.98	−50.00	−19.9997	8.8767	−0.0333	−3.6974	0.0920	−10.0000
$0.50 < z/z_i < 0.85$	α	β	C_1	C_2	C_3	G_1	G_2	G_3
$\mathcal{P}^{sgs}_{u'u'}$	0.93	−50.00	−20.0000	8.6764	−0.0345	−3.7695	0.0561	−10.0000
$\mathcal{P}^{sgs}_{v'v'}$	0.96	−50.00	−20.0000	8.5267	−0.0319	−3.7712	0.0378	−10.0000
$\mathcal{P}^{sgs}_{w'w'}$	0.99	−50.00	−14.2520	7.7940	−0.0079	−3.7223	−0.0964	−5.3663
$\mathcal{P}^{sgs}_{u'v'}$	1.00	−19.48	14.5469	−12.6360	4.2728	−3.0076	−0.1510	−9.9882
$\mathcal{P}^{sgs}_{u'w'}$	1.00	−0.26	5.4726	−0.0001	−0.3710	0.3594	−0.3983	−10.0000
$\mathcal{P}^{sgs}_{v'w'}$	1.00	−50.00	20.0000	−6.2414	0.0411	−3.8196	−0.3433	−3.5935
$\mathcal{P}^{sgs}_{u'\theta'}$	1.00	−6.32	5.0714	−2.4067	0.4717	−2.1353	8.9804	−0.0869
$\mathcal{P}^{sgs}_{v'\theta'}$	1.00	−50.00	2.2490	−0.0107	−0.2324	−5.0903	−1.1623	−10.0000
$\mathcal{P}^{sgs}_{w'\theta'}$	0.98	−50.00	14.4327	−5.0352	0.1435	−3.9273	0.1099	−2.7564
$0.85 < z/z_i < 1.10$	α	β	C_1	C_2	C_3	G_1	G_2	G_3
$\mathcal{P}^{sgs}_{u'u'}$	0.97	−50.00	10.1655	−3.2523	0.2187	−3.7998	1.1203	−0.1604
$\mathcal{P}^{sgs}_{v'v'}$	1.00	−50.00	11.3025	−3.4596	0.1006	−3.8088	0.0168	−2.6832
$\mathcal{P}^{sgs}_{w'w'}$	0.98	−50.00	−19.9901	11.4900	−0.0168	−3.5375	−0.3530	−0.3448
$\mathcal{P}^{sgs}_{u'v'}$	0.93	−15.51	6.1345	−1.7257	0.1538	−2.6593	0.1107	−10.0000
$\mathcal{P}^{sgs}_{u'w'}$	0.98	−47.55	20.0000	−5.3487	−0.0285	−3.9396	−0.1911	−10.0000
$\mathcal{P}^{sgs}_{v'w'}$	0.95	−50.00	20.0000	−5.8812	0.0139	−4.0721	0.1538	−10.0000
$\mathcal{P}^{sgs}_{u'\theta'}$	0.94	−50.00	4.4690	−0.0011	−0.3179	−4.2404	−0.3875	−10.0000
$\mathcal{P}^{sgs}_{v'\theta'}$	0.90	−50.00	4.6073	0.5221	0.0110	−4.3302	−0.6129	−10.0000
$\mathcal{P}^{sgs}_{w'\theta'}$	0.98	−50.00	−13.4874	7.1407	0.0113	−3.9679	−0.3315	−10.0000

Table 5.4: Model parameters of the proposed partitioning functions, $\mathcal{P}^{sgs}$, in the turbulence gray-zone for 3 different CBL regions: $0.10 \leq z/z_i \leq 0.50$, $0.50 \leq z/z_i \leq 0.85$ and $0.85 \leq z/z_i \leq 1.10$.

5.3 Discussion & Conclusions

In the current study, we derive a full three-dimensional representation of gray-zone turbulence fluxes in the convective planetary boundary layer. Large-eddy simulations (reference-LES) are performed with the WRF-LES model for a variety of convective instabilities ranging from free to forced CBLs. The resulting reference-LES fields are coarse-grained by an explicit filter, from microscale grid spacings ($\Delta = 50\ m$) to typical mesoscale grid spacings ($\Delta = 3\ km$). The coarse graining method of Honnert et al. (2011) is also employed for reference, as it has been exercised by all of the previous studies on this topic. This approach makes use of the top-hat filter to the LES data, then conveying its model behavior toward relatively coarser grid spacings. However, results of our spectral analysis demonstrate that the use of top-hat filter for coarse-graining leads to unrealistic excessive energy levels, which prevent an accurate reproduction of the model's behavior at high wavenumbers.

The given overprediction is quantified by the integration of the energy spectra at high wavenumbers for each physical variable under consideration u, v, w, θ. To minimize the presence of high errors, we utilize a more scale-selective filter, namely the Butterworth filter. This filter provides a more controlled energy transition from lower to higher wavenumbers with a clear scale-specific filtering, which is recently applied in real-case gray-zone simulations by Muñoz-Esparza et al. (2020) at the upper troposphere and lower stratosphere and Doubrawa and Muñoz-Esparza (2020) in the atmospheric boundary layer. To obtain the best order of Butterworth filter, i.e. $\widetilde{n}$, trapezoidal integral of energy spectra are computed at high wavenumbers for each CBL case. Then $\widetilde{n}$ is determined as the order giving the lowest error with respect to the high-resolution reference-LES. In other words, the Butterworth order is considered as the order that best approximates to the model behavior of LES at high wavenumbers, retrieved from our spectral analysis. Therefore, our approach provides a promising way to evaluate the performance of a variety of spatial filters for the gray-zone LES upscaling.

Thanks to this analysis, each physical variable, i.e. u, v, w, θ, is filtered by its own specific order in the gray-zone. Then, the gray-zone partitionings of turbulence fluxes are computed for 8 CBL cases at 3 different CBL regions, i.e. lower and upper mixed layers as well as the boundary layer top where the entrainment-zone takes place. While earlier studies have solely addressed SGS

turbulence kinetic energy, k, and vertical eddy heat flux, $w'\theta'$, we present a full 3D representation of turbulence gray-zone in convective planetary boundary layer, including 10 SGS diagnostics: eddy momentum fluxes (τ_{ij}, 6 terms) and eddy heat fluxes (q_j, 3 terms), in addition to turbulence kinetic energy (k). To parameterize these partitioning functions we build a new functional form in terms of the sigmoidal Gompertz function with 4 free parameters. This form is expressed as a function of the gray-zone grid spacing, PBL height and the Obukhov length. The latter is included in our model to incorporate the stability-dependency into gray-zone partitioning functions, beyond the existing models where only the scale-dependency is considered.

Finally, we retrieve the full form of gray-zone partitioning functions in a scale-aware and stability-dependent form, which is valid over a wide range of convective instabilities from free to forced CBL regimes. These partitioning functions enable a more realistic way for flux-blending across the gray-zone. Thanks to this, more advanced PBL schemes could be built bridging meso- and microscales in a scale-aware form, which we are currently exploring and that will be reported in the future. In a subsequent study, we also aim to investigate the effect of topography in terms of partitioning functions. In our previous study, we made use of LES database to obtain a mixing length scale definition to compute the dissipation rate of TKE for non-neutral PBL over flat-terrain. We will extend this approach for heterogeneous terrain. Such improvements will lead to a three-dimensional turbulence closure for the numerical weather prediction models by extending the validity of our recent one-equation turbulence closure (Senel et al., 2019) or building more advanced two-equation PBL-specific closures as preliminarily suggested by Temel et al. (2018a).

Chapter 6

General conclusions

6.1 Summary and main results

The present thesis proposed a variety of novel turbulence models in a multi-scale framework, to advance the current knowledge on the nature of planetary boundary layer (PBL) turbulence appeared in the atmospheres of Earth and Mars.

The **first** model is a novel 1D PBL turbulence model based on a new theoretical mixing length scale formulation. This formulation was derived as a function of the atmospheric stability by means of our high-resolution large-eddy simulations (LES). The results of LES were verified with the wind speed measurements from the meteorological mast at the Test Centre for Large Wind Turbines at Høvsøre, Denmark. We developed a theoretical formulation for determining the mixing length scale, therewith combined with the updated closure coefficients derived under realizability constraints by Temel et al. (2018b). Our new planetary boundary layer scheme was then implemented into the Weather Research and Forecasting model to perform mesoscale simulations for the Høvsøre test site as an idealized case. Moreover, to further validate our new model, a real-data case was performed at the eXperimental Planetary boundary layer Instrumentation Assessment (XPIA) campaign. Results of the idealized case revealed that our new model well predicts the vertical distribution of potential temperature and wind speed, decreasing mean absolute errors for most of the stability levels despite a slight overestimation for near-neutral stable and very stable conditions. While for the real-data case, a significant improvement has been achieved by our new

model for both turbulence kinetic energy and dissipation rate in comparison to mast measurements for a 2-day period during the XPIA campaign.

The **second** model is the first attempt to establish a Mars-specific PBL turbulence model. Like the Earth counterpart, we came up with a new theoretical mixing length scale formulation. Hence, we carried out large-eddy simulations for the daytime Martian planetary boundary layer, varying from weak to strong levels of convective instability. Using the Mars implementation of planetWRF, the MarsWRF model, we determined the turbulence kinetic energy and dissipation rate to formulate the mixing length scale variation. We verified the performance of our model against an existing model currently in use by the MarsWRF model, the MRF scheme. Our model was tested in global and mesoscale simulations, comparing the depth of convective boundary layer (CBL) and near-surface meteorology conditions at the InSight landing site. Compared to the MRF scheme, our new model led to improve CBL depth predictions, which matched better with the radio occultation observations of the Mars Express (MEX) spacecraft. Furthermore, the estimation of near-surface winds at the InSight landing site was slightly improved by our new model.

In addition, one of the key components of the Martian atmosphere is its active dust cycle. The **third** model in this thesis is a new semi-interactive dust transport scheme within the MarsWRF framework, where the dust is lifted, advected by model winds, mixed, and allowed to sediment, which is then scaled to match two-dimensional maps of the observed daily column-integrated dust opacity. This allowed the vertical dust distribution and associated dust radiative heating to be controlled by model processes, while the horizontal dust distribution was constrained to follow spacecraft observations. We reported the effect of the dust cycle on Martian boundary layer meteorology, probing the inter-annual, seasonal, and regional variabilities by means of a decade-long GCM simulation from Mars Year 24–34. Enhanced dust transport lowered the global net surface heating rates, decreasing the turbulent mixing in CBL to virtually zero (within the dust storm season) and, enhanced the wind shear on average by almost 50%. As a superposition of both effects, during global dust storms (GDS) in Mars Year (MY) 25 and 34, we found that long-lasting extremely shallow daytime boundary layers can globally form as shallow as 0.5 km (but not for the less intense GDS in MY 28), unlike the 9 km deep and highly turbulent CBL formation at GDS onset and decay. Our GCM results

showed that the CBL suppression lasted as long as approximately 67 and 57 sols during GDS events in MY 25 and 34.

The **fourth** is a state-of-the-art gray-zone turbulence model developed for the so-called Terra-Incognita range of scales. We, for the first time, fully represented three-dimensional turbulence fluxes in the Terra Incognita, where the traditional turbulence models fail as they were originally designed for their own grid scale limits (Wyngaard, 2004; Shin and Hong, 2013; Zhang et al., 2018; Chow et al., 2019; Doubrawa and Muñoz-Esparza, 2020). To this end, we derived partitioning functions, representing the partitioning between subgrid and total turbulence fluxes. We made use of high-resolution large-eddy simulations (LES), which were performed with the Weather Research and Forecasting (WRF) model for various levels of convective instability, ranging from pure buoyant to strongly sheared convection. Then, the resulting reference-LES fields were successively coarse-grained from its original microscale grid spacing ($\Delta = 50\ m$) up to typical mesoscale grid spacings ($\Delta = 3\ km$). This process was applied by virtue of an advanced filter, i.e. the Butterworth filter (Butterworth et al., 1930). It enabled a clear scale-specific filtering that led to a more controlled energy transition from lower to higher wavenumbers, unlike the drawbacks of current filters in use. Eventually, we parameterized the subgrid scale (SGS) partitioning functions of ten SGS turbulence quantities: momentum fluxes (τ_{ij}, six terms), heat fluxes (q_j, three terms) and turbulence kinetic energy (k). Turbulence partitioning relations were parameterized in a scale-aware, stability- and height-dependent form, using the sigmoidal Gompertz function (Gompertz, 1825). Therefore, our new gray-zone turbulence model offers an advanced framework that bridges the mesoscale and microscale limits, and that is suitable for the development of next generation three-dimensional and multiscale turbulence parameterization methods, or planetary boundary layer schemes.

6.2 Areas for future research and improvements

Considering our results of idealized mesoscale simulations at the Høvsøre test site, new 1D PBL model for Earth brought the advance over existing models, i.e., MYNN and BouLac. Our model provided better distributions for wind speed and potential temperature over a wide range of atmospheric instability. While for the real-case test, one-way nested mesoscale simulations at the XPIA

campaign, near Rocky Mountains in Colorado, our new model exhibited improved skill in predicting turbulence kinetic energy and its dissipation rate, outperforming the existing models. Even though all the performed PBL models were able to reproduce the general behavior of the temperature measurements, some large biases have been observed for the wind speed. Yet, MYNN and BouLac schemes predicted them better than our model.

One reason may be the use of an existing formulation for the upper PBL, i.e., MYJ scheme, because our mixing length scale does not consider the interaction between the upper PBL and the free atmosphere. Another reason might be stemmed from the physical parameterizations used in our WRF simulations, such as the microphysics, cumulus convection, surface layer and land-surface coupling schemes. All these possibilities will be examined in detail as a future study. Besides, the new PBL model is based on the use of constant closure coefficients to determine eddy diffusivities of momentum and heat. As a follow-up study, those coefficients will be further calibrated in long-term WRF mesoscale simulations compared with comprehensive meteorological observations, such as the BLLAST field campaign: Boundary-Layer Late Afternoon and Sunset Turbulence, which was performed from 14 June to 8 July, 2011 in southern France.

Moreover, the applicability of our new 1D PBL model is not limited with the present Earth mesoscale assessments, which can be utilized in a broader sense. For instance, we recently implemented it to an in-house paleoclimate global circulation model (Senel et al., 2021a), based on the planetWRF model (Richardson et al., 2007). The goal is to examine the extreme climatic perturbations in the aftermath of Chicxulub impact that led to a massive catastrophe 66 million years ago (Senel et al., 2022). A 10-15 km sized asteroid hit the Earth on the Yucatán Peninsula in Mexico, triggering the Cretaceous-Paleogene (K-Pg) mass extinction, wiping out 75% of life including the non-avian dinosaurs. Here, we focus to examine the relative and combined roles of climate-active fine-grained ejecta over 20 years ensuing the Chicxulub impact, both for single and combined release of sulfur, soot and silicate dust. Moreover, we explore the severity of global cooling and darkness, therewith the post-impact photosynthetic activity on the Earth's flora and fauna. Our findings illuminate primary and secondary drivers of the impact winter and the consequent mass extinction at the K-Pg boundary. In the future, we will assess the new 1D PBL model also to investigate the dynamics of other mass

extinction events in the Earth's history, such as the Permian Mass Extinction in the Paleozoic Era 250 million years ago.

Regarding the Mars-based applications, we will extend our research on the Martian dust-turbulence interaction. Thanks to the continued operations of NASA's InSight lander, MSL Curiosity and Mars 2020 Perseverance rovers, we will carry out additional analysis between GCM and in-situ observations, addressing the changes in inter-annual and seasonal time scales. Concerning potential implications of global/regional dust storms, we examine the impacts of major dust events on convective boundary layer dynamics. As a future study, we will also look at the influences of global/regional dust storms on the near-surface turbulent kinetic energy, and hence the turbulent exchange of volatiles and tracers between the surface and atmosphere.

Finally, we built the full form of gray-zone partitioning functions in a scale-aware and stability-dependent form that is valid in a wide range of convective instabilities. These partitioning functions provide a more realistic way for flux-blending across the gray-zone. Thanks to this, more advanced PBL schemes can be designed bridging meso- and microscales in a scale-aware form, which we will investigate in the future. In a subsequent study, similar approach will be carried out to develop a Martian turbulence gray-zone model, for the first time, which will provide a scale-aware framework for the development of advanced Martian planetary boundary layer schemes.

Appendices

Appendix A

The momentum equation is given as follows:

$$\frac{\partial \widetilde{u}_i}{\partial t} + \frac{\partial}{\partial x_j}\left(\widetilde{u}_j \widetilde{u}_i\right) = -\frac{1}{\rho_0}\frac{\partial \widetilde{p}}{\partial x_i} + \frac{g}{\theta_0}\widetilde{\theta}\delta_{i3} - 2\epsilon_{ijk}\Omega_j \widetilde{u}_k - \frac{\partial \tau_{ij}^D}{\partial x_j} \tag{A.1}$$

Note that the molecular viscosity is neglected in Eq. A.1. After multiplying by $\widetilde{u}_i$,

$$\underbrace{\widetilde{u}_i \frac{\partial \widetilde{u}_i}{\partial t}}_{I} + \underbrace{\widetilde{u}_i \frac{\partial}{\partial x_j}\left(\widetilde{u}_j \widetilde{u}_i\right)}_{II} = \underbrace{-\widetilde{u}_i \frac{1}{\rho_0}\frac{\partial \widetilde{p}}{\partial x_i}}_{III} + \underbrace{\widetilde{u}_i \frac{g}{\theta_0}\widetilde{\theta}\delta_{i3}}_{IV} - \underbrace{\widetilde{u}_i \frac{\partial \tau_{ij}^D}{\partial x_j}}_{V} \tag{A.2}$$

Following some modifications to each terms, the resolved kinetic energy equation,

$$\frac{\partial \widetilde{K}}{\partial t} + \frac{\partial}{\partial x_j}\left(\widetilde{K}\widetilde{u}_j\right) = -\frac{1}{\rho_0}\frac{\partial}{\partial x_j}\left(\widetilde{p}\widetilde{u}_j\right) + \frac{g}{\theta_0}\delta_{i3}\left(\widetilde{u}_i\widetilde{\theta}\right) - \frac{\partial}{\partial x_j}\left(\tau_{ij}^D \widetilde{u}_i\right) + \tau_{ij}^D \frac{\partial \widetilde{u}_i}{\partial x_j} \tag{A.3}$$

where $\widetilde{K} = \frac{1}{2}\widetilde{u}_i\widetilde{u}_i$ denotes the resolved kinetic energy. Note that, hereby the total kinetic energy is $K = \widetilde{K} + K^{sgs}$ where K_{sgs} denotes the SGS kinetic energy. Applying the horizontal averaging gives,

$$\frac{\mathrm{d}\left\langle \widetilde{K}\right\rangle}{\mathrm{d}t} = -\frac{\mathrm{d}}{\mathrm{d}z}\left\langle \widetilde{K}\widetilde{w}\right\rangle - \frac{1}{\rho_0}\frac{\mathrm{d}}{\mathrm{d}z}\left\langle \widetilde{w}\widetilde{p}\right\rangle + \frac{g}{\theta_0}\left\langle \widetilde{w}\widetilde{\theta}\right\rangle - \frac{\mathrm{d}}{\mathrm{d}z}\left\langle \tau_{i3}^D \widetilde{u}_i\right\rangle + \left\langle \tau_{ij}^D \frac{\partial \widetilde{u}_i}{\partial x_j}\right\rangle \tag{A.4}$$

where $\left\langle \widetilde{K}\right\rangle$ denotes averaged resolved kinetic energy that can be decomposed into the mean field resolved kinetic energy, $\left\langle \overline{\widetilde{K}}\right\rangle$, and the resolved turbulence kinetic energy, $\widetilde{k}'$, i.e.

$$\underbrace{\frac{1}{2}\langle \widetilde{u}_i \widetilde{u}_i \rangle}_{\langle \widetilde{K} \rangle} = \underbrace{\frac{1}{2}\langle \widetilde{u}_i \rangle \langle \widetilde{u}_i \rangle}_{\left\langle \overline{\widetilde{K}} \right\rangle} + \underbrace{\frac{1}{2}\widetilde{u}_i' \widetilde{u}_i'}_{\widetilde{k}'} \tag{A.5}$$

After applying horizontal-averaging to the Eq. A.1, i.e.

$$\cancelto{0}{\left\langle \frac{\partial \widetilde{u}_i}{\partial t} \right\rangle} + \frac{\mathrm{d}}{\mathrm{d}z}\langle \widetilde{w}\widetilde{u}_i \rangle = -\frac{1}{\rho_0}\frac{\mathrm{d}\left\langle \widetilde{p} \right\rangle}{\mathrm{d}x_i} + \frac{g}{\theta_0}\delta_{i3}\left\langle \widetilde{\theta} \right\rangle - \left\langle 2\epsilon_{ijk}\Omega_j \widetilde{u}_k \right\rangle - \left\langle \frac{\mathrm{d}\tau_{i3}^D}{\mathrm{d}z} \right\rangle \tag{A.6}$$

where the brackets, i.e. $\langle \cdot \rangle$, denote the horizontal-averaging operator. The second term is moved to the right-hand side and expanded in two terms (I and II). After multiplying by $\langle \widetilde{u}_i \rangle$, i.e.

$$\begin{aligned} 0 = &\underbrace{-\langle \widetilde{u}_i \rangle \frac{\mathrm{d}}{\mathrm{d}z}\langle \widetilde{w} \rangle \langle \widetilde{u}_i \rangle}_{I} \underbrace{-\langle \widetilde{u}_i \rangle \frac{\mathrm{d}}{\mathrm{d}z}\left\langle \widetilde{w}'\widetilde{u}_i' \right\rangle}_{II} \\ &\underbrace{-\langle \widetilde{u}_i \rangle \frac{1}{\rho_0}\frac{\mathrm{d}\left\langle \widetilde{p} \right\rangle}{\mathrm{d}x_i}}_{III} + \underbrace{\langle \widetilde{u}_i \rangle \frac{g}{\theta_0}\delta_{i3}\left\langle \widetilde{\theta} \right\rangle}_{IV} \underbrace{-\langle \widetilde{u}_i \rangle \left\langle \frac{\mathrm{d}\tau_{i3}^D}{\mathrm{d}z} \right\rangle}_{V} \end{aligned} \tag{A.7}$$

Now, we will make further arrangements starting with the first term,

$$\underbrace{\langle \widetilde{u}_i \rangle \frac{\mathrm{d}}{\mathrm{d}z}\langle \widetilde{w} \rangle \langle \widetilde{u}_i \rangle}_{I} = \langle \widetilde{u}_i \rangle \langle \widetilde{u}_i \rangle \cancelto{0}{\frac{\mathrm{d}\langle \widetilde{w} \rangle}{\mathrm{d}z}} + \langle \widetilde{w} \rangle \frac{\mathrm{d}}{\mathrm{d}z}\underbrace{\left(\frac{1}{2}\langle \widetilde{u}_i \rangle \langle \widetilde{u}_i \rangle\right)}_{\left\langle \overline{\widetilde{K}} \right\rangle} = \langle \widetilde{w} \rangle \frac{\mathrm{d}}{\mathrm{d}z}\left\langle \overline{\widetilde{K}} \right\rangle \tag{A.8}$$

If we continue with the III, IV and V terms respectively,

$$\underbrace{\langle \widetilde{u}_i \rangle \frac{1}{\rho_0}\frac{\mathrm{d}\left\langle \widetilde{p} \right\rangle}{\mathrm{d}x_i}}_{III} = \frac{1}{\rho_0}\frac{\mathrm{d}}{\mathrm{d}z}\langle \widetilde{w} \rangle \left\langle \widetilde{p} \right\rangle \tag{A.9}$$

$$\underbrace{\langle \widetilde{u}_i \rangle \frac{g}{\theta_0}\delta_{i3}\left\langle \widetilde{\theta} \right\rangle}_{IV} = \frac{g}{\theta_0}\langle \widetilde{w} \rangle \left\langle \widetilde{\theta} \right\rangle \tag{A.10}$$

$$\underbrace{\langle \widetilde{u}_i \rangle \left\langle \frac{\mathrm{d}\tau_{i3}^{D}}{\mathrm{d}z} \right\rangle}_{V} = \frac{\mathrm{d}}{\mathrm{d}z} \left\langle \tau_{i3}^{D} \right\rangle \langle \widetilde{u}_i \rangle - \left\langle \tau_{ij}^{D} \right\rangle \left\langle \frac{\partial \widetilde{u}_i}{\partial x_j} \right\rangle \tag{A.11}$$

Substituting all the derived components into Eq.A.7 gives the mean field resolved kinetic energy equation, $\left\langle \overline{\widetilde{K}} \right\rangle$,

$$\begin{aligned} 0 = &- \langle \widetilde{w} \rangle \frac{\mathrm{d}}{\mathrm{d}z} \left\langle \overline{\widetilde{K}} \right\rangle - \langle \widetilde{u}_i \rangle \frac{\mathrm{d}}{\mathrm{d}z} \left\langle \widetilde{w}' \widetilde{u}_i' \right\rangle - \frac{1}{\rho_0} \frac{\mathrm{d}}{\mathrm{d}z} \langle \widetilde{w} \rangle \langle \widetilde{p} \rangle \\ &+ \frac{g}{\theta_0} \langle \widetilde{w} \rangle \left\langle \widetilde{\theta} \right\rangle - \frac{\mathrm{d}}{\mathrm{d}z} \left\langle \tau_{i3}^{D} \right\rangle \langle \widetilde{u}_i \rangle + \left\langle \tau_{ij}^{D} \right\rangle \left\langle \frac{\partial \widetilde{u}_i}{\partial x_j} \right\rangle \end{aligned} \tag{A.12}$$

Eventually, horizontally-averaged resolved TKE equation forms by subtracting $\left\langle \overline{\widetilde{K}} \right\rangle$ (Eq.A.12) from $\left\langle \widetilde{K} \right\rangle$ (Eq.A.4), i.e.,

$$\begin{aligned} 0 = &- \langle \widetilde{w} \rangle \frac{\mathrm{d} \left\langle \widetilde{k} \right\rangle}{\mathrm{d}z} + \langle \widetilde{u}_i \rangle \frac{\mathrm{d}}{\mathrm{d}z} \left\langle \widetilde{w}' \widetilde{u}_i' \right\rangle - \frac{1}{\rho_0} \frac{\mathrm{d}}{\mathrm{d}z} \langle p' w' \rangle \\ &- \frac{\mathrm{d}}{\mathrm{d}z} \left\langle \tau_{i3}^{D'} \widetilde{u}_i' \right\rangle + \frac{g}{\theta_0} \langle w' \theta' \rangle + \left\langle \tau_{ij}^{D'} S_{ij}' \right\rangle \end{aligned} \tag{A.13}$$

Arranging second term of right-hand side by additional horizontal-averaging and simple algebra, i.e.

$$\begin{aligned} \langle \widetilde{u}_i \rangle \frac{\mathrm{d}}{\mathrm{d}z} \left\langle \widetilde{w}' \widetilde{u}_i' \right\rangle &= \left\langle \left(\widetilde{u}_i - \widetilde{u}_i' \right) \frac{\mathrm{d}}{\mathrm{d}z} \left\langle \widetilde{w}' \widetilde{u}_i' \right\rangle \right\rangle \\ &= \left\langle \widetilde{u}_i \frac{\mathrm{d}}{\mathrm{d}z} \left\langle \widetilde{w}' \widetilde{u}_i' \right\rangle \right\rangle - \left\langle \widetilde{u}_i' \frac{\mathrm{d}}{\mathrm{d}z} \left\langle \widetilde{w}' \widetilde{u}_i' \right\rangle \right\rangle \\ &= - \left\langle \widetilde{u}_i' \widetilde{w}' \right\rangle \frac{\mathrm{d} \langle \widetilde{u}_i \rangle}{\mathrm{d}z} - \frac{\mathrm{d}}{\mathrm{d}z} \left\langle \underbrace{\left(\frac{1}{2} \left\langle \widetilde{u}_i' \right\rangle \left\langle \widetilde{u}_i' \right\rangle \right)}_{\widetilde{k}} \widetilde{w}' \right\rangle \end{aligned} \tag{A.14}$$

Substituting Eq.A.14 into Eq.A.13 gives the final form of the resolved turbulence kinetic energy budget equation, i.e.

$$0 = \underbrace{-\langle\widetilde{w}\rangle \frac{\mathrm{d}\left\langle\widetilde{k}\right\rangle}{\mathrm{d}z}}_{\mathcal{A}} \underbrace{-\frac{\mathrm{d}}{\mathrm{d}z}\left\langle\widetilde{kw'}\right\rangle}_{T^T} \underbrace{-\frac{1}{\rho_0}\frac{\mathrm{d}}{\mathrm{d}z}\left\langle\widetilde{p'w'}\right\rangle}_{T^P} \underbrace{-\frac{\mathrm{d}}{\mathrm{d}z}\left\langle\tau_{i3}^{D'}\widetilde{u_i'}\right\rangle}_{T^{sgs}}$$
$$\underbrace{-\left\langle\widetilde{u'w'}\right\rangle\frac{\mathrm{d}\langle\widetilde{u}\rangle}{\mathrm{d}z} - \left\langle\widetilde{v'w'}\right\rangle\frac{\mathrm{d}\langle\widetilde{v}\rangle}{\mathrm{d}z}}_{P^S} + \underbrace{\frac{g}{\theta_0}\left\langle\widetilde{w'\theta'}\right\rangle}_{P^B} + \underbrace{\left\langle\tau_{ij}^{D'}S_{ij}'\right\rangle}_{\epsilon}$$

where $\mathcal{A}$ denotes the advection, T^T, T^P, T^{sgs} denote the turbulence, pressure and SGS transport, respectively. P^S and P^B are the shear and buoyancy productions and ϵ stands for the dissipation.

Appendix B1: Sensitivity of the SGS model coefficients

We investigate the sensitivity of LES predictions to SGS model's set of coefficients. We perform LES calculations both using the present set of coefficients (see Section 2) and the updated ones (Muñoz-Esparza et al., 2014a). The results, shown in Fig. B1, correspond to LESq30 configuration.

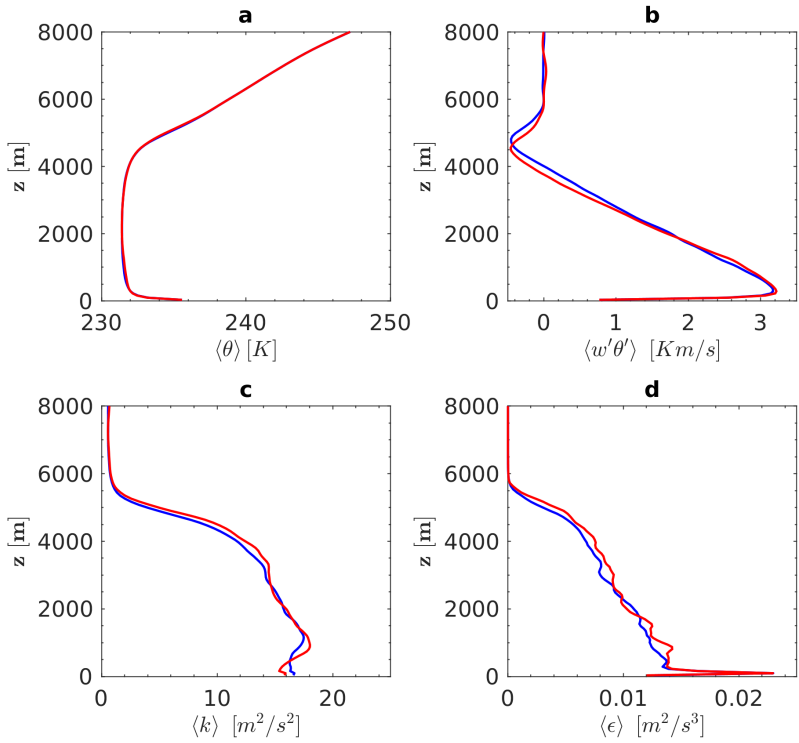

Figure B1: Sensitivity of LES computations to model coefficients: Vertical profiles of potential temperature (a), turbulent heat flux (b), turbulence kinetic energy (c), dissipation rate of turbulence kinetic energy (d) - blue: the present set of coefficients, red: the updated coefficients of (Muñoz-Esparza et al., 2014a).

Appendix B2: Sensitivity of the mixing length scale on the GCM

The sensitivity of the mixing length scale on the GCM results is investigated in Fig. B2 at location 27.5° N, 107° W at L_s = 44.5° when the local time is 17.0h. The existing mixing length scale is scaled by 80% and 120% in this manner. The vertical profiles of the potential temperature reveals that a scaling by ±20% leads to a variation in θ smaller than ± 1K.

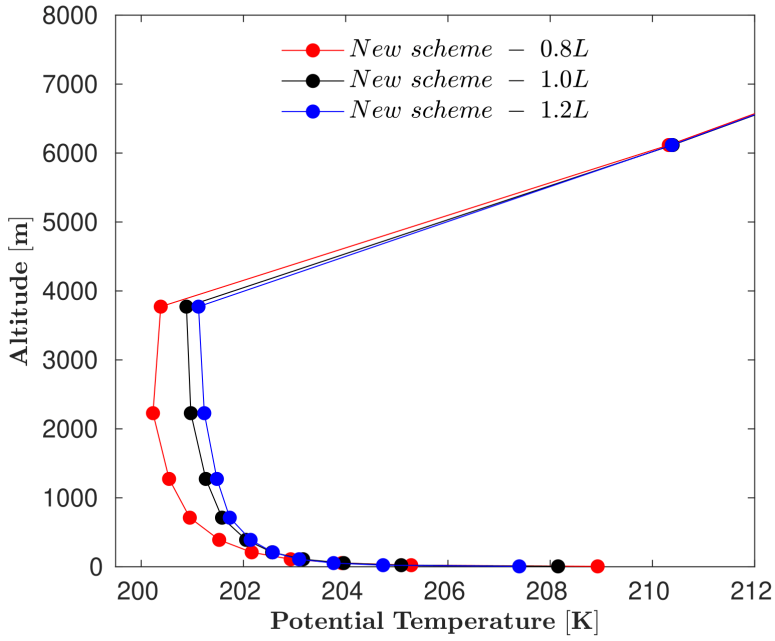

Figure B2: Regarding the mixing length scale sensitivity on potential temperature profiles, vertical profiles of potential temperature are plotted at 27.5° N, 107° W for L_s = 44.5°. The local time is 17.0h. 1.0L denotes the present value of length scale (black solid line). 0.8L and 1.2L are the scaled length scales with 80% (red solid line) and 120% (blue solid line) of the baseline length scale.

Appendix C: GCM vs. MEX radio occultations in terms of CBL depth

CBL predictions retrieved from the GCM are compared with the MEX radio occultation (RO) measurements by Hinson et al. (2008, 2019), during the northern spring in MY 27 (RO profiles 1-36), northern late winter in MY 27 (RO profiles 37-42) and northern early spring in MY 28 (RO profiles 43-118). Here, the L_s is the areocentric longitude, ϕ is the northern latitude, λ is the Eastern longitude, z_s is the local terrain elevations based on MOLA (Christensen et al., 2001) and in the GCM, z_i is the depth of CBL, l_t is the local true solar time. Note that MAE_{z_i} refers to the mean absolute error between the GCM and RO measurements.

RO	L_s [°]	ϕ [°N]	λ [°E]	$z_{s,MOLA}$ [km]	$z_{s,GCM}$ [km]	$z_{i,RO}$ [km]	$z_{i,GCM}$ [km]	MAE_{z_i} [km]	t_l [h]
1	34.7	53.6	206.3	-3.6	-3.7	2.60	2.39	0.21	17.1
2	35.1	52.5	271.7	-1.7	-1.9	5.40	2.78	2.62	17.1
3	39.6	39.5	336.7	-4.5	-4.4	4.40	4.58	0.18	17.1
4	40.5	37.3	9.4	-2.5	-2.5	5.70	5.30	0.40	17.1
5	44.5	27.5	107.0	-4.3	-4.3	4.60	5.15	0.55	17.1
6	45.9	24.4	106.9	-3.9	-3.8	5.50	6.02	0.52	17.1
7	47.1	21.8	205.0	-3.9	-3.8	5.20	7.56	2.36	17.2
8	47.8	20.6	74.0	0.2	0.2	9.40	8.06	1.34	17.2
9	48.4	19.3	303.0	-0.9	-0.9	7.70	7.66	0.04	17.2
10	48.8	18.6	8.4	-1.6	-1.7	8.40	6.45	1.95	17.2
11	49.0	18.0	172.0	-2.2	-2.9	6.90	6.99	0.09	17.2
12	49.1	17.8	73.8	-0.5	0.0	9.20	7.12	2.08	17.2
13	49.2	17.5	335.6	-2.9	-2.9	6.20	5.23	0.97	17.2
14	49.4	17.4	237.5	0.9	1.1	7.90	4.87	3.03	17.2
15	51.2	13.7	204.6	-3.6	-3.6	4.30	5.97	1.67	17.2
16	51.5	13.3	8.2	-1.5	-1.4	7.00	5.57	1.43	17.2
17	51.6	13.3	270.0	1.9	0.8	8.70	6.68	2.02	17.2
18	52.1	12.3	237.2	2.5	2.4	8.00	5.09	2.91	17.2
19	53.2	10.3	73.5	1.0	0.9	11.50	7.95	3.55	17.1
20	53.3	10.0	335.3	-3.1	-2.3	6.30	4.62	1.68	17.1
21	53.7	9.5	40.7	0.6	0.7	7.60	6.93	0.67	17.1
22	53.8	9.2	302.5	-0.6	-0.1	8.80	5.69	3.11	17.1
23	54.1	8.8	106.1	-0.7	-0.9	8.90	5.68	3.22	17.1
24	54.3	8.4	269.8	1.8	2.7	9.40	7.92	1.48	17.1
25	57.4	3.3	335.0	-2.8	-2.3	6.00	4.03	1.97	17.1
26	58.5	1.5	171.3	-3.0	-3.0	5.40	4.61	0.79	17.1
27	58.6	1.5	73.1	1.5	1.5	9.50	7.13	2.37	17.1
28	60.8	-1.9	105.7	0.3	-0.3	3.60	3.82	0.22	17.1
29	61.3	-2.5	73.0	1.9	1.7	8.30	5.90	2.40	17.1
30	62.2	-3.9	105.6	0.1	0.3	5.10	4.60	0.50	17.1
31	63.9	-6.4	171.0	-2.9	-2.2	3.90	4.40	0.50	17.1
32	64.8	-7.6	203.8	-1.1	-0.9	5.50	2.93	2.57	17.1
33	65.2	-8.3	171.0	-2.8	-1.9	4.90	3.96	0.94	17.1
34	66.5	-9.7	269.2	4.3	4.1	9.00	3.67	5.33	17.0
35	67.9	-12.1	170.7	-1.8	-1.8	3.00	3.80	0.80	17.0
36	69.2	-13.5	268.9	5.4	5.5	6.50	5.25	1.25	17.0
37	357.1	54.2	221.7	-3.0	-2.9	2.10	2.30	0.20	14.0
38	357.4	53.9	25.7	-3.9	-4.0	1.70	2.45	0.75	14.1
39	358.0	53.4	353.7	-4.8	-4.8	1.70	1.47	0.23	14.1
40	358.7	52.6	223.6	-2.8	-2.9	2.20	2.72	0.52	14.2
41	359.1	52.2	289.5	-3.5	-2.6	2.10	2.35	0.25	14.2
42	359.9	51.3	61.5	-3.6	-3.5	1.50	2.76	1.26	14.3
43	0.1	51.1	323.5	-4.7	-4.6	2.70	1.79	0.91	14.3
44	0.9	50.3	95.3	-4.6	-4.7	3.10	2.61	0.49	14.3
45	1.3	49.8	161.3	-3.8	-3.7	3.40	2.69	0.71	14.4
46	1.5	49.6	63.3	-3.5	-3.4	1.80	3.14	1.34	14.4
47	1.7	49.4	227.2	-2.4	-2.2	2.70	3.90	1.20	14.4
48	1.9	49.2	129.2	-4.7	-4.7	2.20	2.87	0.67	14.4
49	2.1	48.9	293.1	-1.5	-1.6	2.90	2.46	0.44	14.4
50	3.1	47.9	327.0	-4.5	-4.6	3.00	2.31	0.69	14.5
51	3.3	47.7	228.9	-2.0	-2.3	2.80	4.94	2.14	14.5
52	3.4	47.5	130.8	-4.7	-4.5	2.50	2.73	0.23	14.5
53	4.2	46.7	262.6	-0.3	-0.3	3.40	5.07	1.67	14.6
54	4.8	46.1	230.5	-1.7	-1.3	3.90	6.05	2.15	14.6
55	4.9	45.9	132.4	-4.7	-4.6	2.40	3.71	1.31	14.6
56	5.2	45.6	296.3	-1.1	-1.5	4.40	2.57	1.83	14.6
57	5.6	45.1	2.2	-4.2	-4.3	2.90	3.64	0.74	14.7
58	6.3	44.4	232.0	-1.1	-0.7	5.70	7.10	1.40	14.7
59	6.7	43.9	297.8	-1.5	-1.1	3.30	6.02	2.72	14.7

Table C1: Comparison between GCM vs. MEX RO measurements for profiles 1-59.

RO	L_s [°]	ϕ [°N]	λ [°E]	$z_{s,MOLA}$ [km]	$z_{s,GCM}$ [km]	$z_{i,RO}$ [km]	$z_{i,GCM}$ [km]	MAE_{z_i} [km]	t_l [h]
60	6.8	43.7	199.8	−4.0	−4.0	3.10	3.88	0.78	14.7
61	7.8	42.7	233.5	−0.3	−0.8	4.50	7.20	2.70	14.8
62	8.2	42.2	299.3	−1.2	−1.1	4.50	5.80	1.30	14.8
63	8.3	42.0	201.3	−3.9	−3.9	3.30	5.56	2.26	14.8
64	8.5	41.9	103.2	−5.0	−4.9	3.00	2.85	0.15	14.8
65	8.6	41.8	5.2	−3.8	−3.1	2.90	4.66	1.76	14.9
66	8.8	41.7	267.1	0.5	0.3	4.70	6.65	1.95	14.9
67	8.9	41.4	169.1	−3.8	−3.5	2.90	6.00	3.10	14.9
68	9.0	41.3	71.0	−3.1	−3.0	3.00	3.25	0.25	14.9
69	9.6	40.7	38.8	−1.6	−1.8	5.00	6.18	1.18	14.9
70	9.7	40.5	300.6	−1.2	−1.6	3.70	6.40	2.70	14.9
71	9.8	40.3	202.7	−3.9	−3.9	2.60	5.22	2.62	14.9
72	10.0	40.2	104.5	−5.0	−4.9	3.70	3.68	0.02	14.9
73	10.4	39.7	170.4	−3.9	−3.9	2.90	5.06	2.16	15.0
74	10.7	39.4	334.2	−4.5	−4.4	3.70	4.40	0.70	15.0
75	10.9	39.1	138.1	−4.3	−4.3	3.40	5.27	1.87	15.0
76	11.1	39.0	40.0	−0.9	−1.2	4.90	6.99	2.09	15.0
77	11.2	38.8	301.9	−1.7	−1.5	5.50	7.90	2.40	15.0
78	11.9	38.0	171.6	−3.9	−3.9	3.90	5.67	1.77	15.0
79	12.1	37.7	335.5	−4.4	−4.5	4.60	3.97	0.63	15.0
80	12.4	37.4	139.3	−4.2	−4.2	3.70	5.96	2.26	15.1
81	13.5	36.2	74.7	−2.6	−2.0	3.70	6.52	2.82	15.1
82	13.6	36.0	336.6	−4.3	−4.3	5.40	5.77	0.37	15.1
83	14.0	35.6	42.3	0.0	−0.3	6.20	7.36	1.16	15.1
84	15.0	34.5	75.8	−2.6	−2.6	3.50	7.24	3.74	15.2
85	15.5	33.9	43.4	−0.2	−0.5	5.90	7.55	1.65	15.2
86	16.2	33.2	272.9	0.7	0.8	7.80	7.47	0.33	15.2
87	16.4	32.8	76.8	−2.4	−2.5	3.50	4.93	1.43	15.3
88	16.6	32.6	338.7	−4.0	−4.1	4.90	4.83	0.07	15.3
89	17.0	32.2	44.4	−0.9	−0.7	6.30	9.18	2.88	15.3
90	17.1	32.0	306.2	−3.1	−3.2	3.80	5.21	1.41	15.3
91	17.9	31.1	77.7	−1.6	−2.3	4.10	6.74	2.64	15.3
92	18.1	30.9	241.5	2.0	2.3	6.70	7.66	0.96	15.3
93	21.4	26.9	309.0	−3.7	−3.1	5.70	5.41	0.29	15.5
94	21.6	26.8	210.9	−3.4	−2.9	4.90	7.17	2.27	15.5
95	23.0	25.1	211.8	−3.0	−2.9	5.70	7.98	2.28	15.5
96	23.9	24.2	245.0	2.4	2.9	7.40	8.24	0.84	15.6
97	24.5	23.5	212.7	−3.1	−2.7	5.80	8.06	2.26	15.6
98	25.1	22.7	82.1	−2.2	−2.3	4.50	6.26	1.76	15.6
99	25.2	22.6	344.0	−1.9	−2.6	8.30	6.14	2.16	15.6
100	26.3	21.4	279.1	−0.1	0.0	5.60	6.53	0.93	15.6
101	26.5	21.0	83.0	−2.9	−2.5	4.30	5.17	0.87	15.6
102	26.8	20.9	246.8	2.5	2.6	8.60	7.67	0.93	15.7
103	28.6	18.4	313.3	−3.5	−3.3	5.20	7.14	1.94	15.7
104	29.2	17.6	182.8	−3.3	−3.3	7.20	7.09	0.11	15.7
105	29.4	17.4	84.7	−3.7	−3.8	4.00	3.01	0.99	15.7
106	29.5	17.4	346.6	−1.7	−2.3	6.60	4.75	1.85	15.7
107	30.1	16.6	216.1	−2.2	−2.0	5.50	6.32	0.82	15.8
108	30.3	16.3	117.9	−3.2	−3.3	5.50	6.95	1.45	15.7
109	32.1	14.1	184.4	−3.2	−3.1	7.30	7.42	0.12	15.8
110	32.2	13.9	86.3	−3.8	−3.8	4.10	4.02	0.08	15.8
111	34.1	11.6	54.7	1.4	1.4	9.70	6.51	3.19	15.8
112	38.4	4.8	318.7	−1.3	−1.1	6.00	5.64	0.36	15.9
113	38.8	4.3	24.4	0.2	0.1	5.80	5.59	0.21	15.9
114	38.9	4.1	286.2	1.4	1.9	4.10	6.25	2.15	15.9
115	39.0	3.5	188.1	−3.2	−3.0	5.10	5.40	0.30	15.9
116	40.4	0.9	188.7	−2.9	−2.8	4.80	5.67	0.87	15.9
117	40.6	0.9	90.6	−0.4	−0.2	3.00	4.73	1.73	15.9
118	42.3	−3.6	156.5	−2.3	−2.4	5.10	5.02	0.08	15.9

Table C2: Comparison between GCM vs. MEX RO measurements for profiles 60–118.

References

Alinot, C. and Masson, C. (2005). k-ϵ model for the atmospheric boundary layer under various thermal stratifications. *Journal of Solar Energy Engineering*, 127(4):438–443.

Angevine, W. M., Jiang, H., and Mauritsen, T. (2010). Performance of an eddy diffusivity–mass flux scheme for shallow cumulus boundary layers. *Monthly Weather Review*, 138(7):2895–2912.

Aoki, S., Vandaele, A., Daerden, F., Villanueva, G., Liuzzi, G., Thomas, I., Erwin, J., Trompet, L., Robert, S., Neary, L., et al. (2019). Water vapor vertical profiles on Mars in dust storms observed by TGO/NOMAD. *Journal of Geophysical Research: Planets*, 124(12):3482–3497.

Arakawa, A. and Lamb, V. R. (1977). Computational design of the basic dynamical processes of the UCLA general circulation model. *General circulation models of the atmosphere*, 17:173–265.

Ayotte, K. W., Sullivan, P. P., Andren, A., Doney, S. C., Holtslag, A. A., Large, W. G., McWilliams, J. C., Moeng, C.-H., Otte, M. J., Tribbia, J. J., et al. (1996). An evaluation of neutral and convective planetary boundary-layer parameterizations relative to large eddy simulations. *Boundary-Layer Meteorology*, 79(1-2):131–175.

Balme, M. and Greeley, R. (2006). Dust devils on earth and mars. *Reviews of Geophysics*, 44(3).

Balogh, M., Parente, A., and Benocci, C. (2012). Rans simulation of abl flow over complex terrains applying an enhanced k-ϵ model and wall function formulation: Implementation and comparison for fluent and openfoam. *Journal of wind engineering and industrial aerodynamics*, 104:360–368.

Banfield, D., Spiga, A., Newman, C., Forget, F., Lemmon, M., Lorenz, R., Murdoch, N., Viudez-Moreiras, D., Pla-Garcia, J., Garcia, R. F., et al. (2020). The atmosphere of mars as observed by insight. *Nature Geoscience*,

pages 1–9.

Banta, R. M. (2008). Stable-boundary-layer regimes from the perspective of the low-level jet. *Acta Geophysica*, 56(1):58–87.

Basu, S. and He, P. (2014). Quantifying the dependence of temperature and refractive index structure parameters on atmospheric stability using direct and large-eddy simulations. In *Propagation Through and Characterization of Distributed Volume Turbulence*, pages PM2E–3. Optical Society of America.

Basu, S., Holtslag, A. A., Van De Wiel, B. J., Moene, A. F., and Steeneveld, G. J. (2008). An inconvenient "truth" about using sensible heat flux as a surface boundary condition in models under stably stratified regimes. *Acta Geophysica*, 56(1):88–99.

Basu, S. and Porté-Agel, F. (2006). Large-eddy simulation of stably stratified atmospheric boundary layer turbulence: a scale-dependent dynamic modeling approach. *Journal of the Atmospheric Sciences*, 63(8):2074–2091.

Basu, S., Wilson, J., Richardson, M., and Ingersoll, A. (2006). Simulation of spontaneous and variable global dust storms with the GFDL Mars GCM. *Journal of Geophysical Research: Planets*, 111(E9).

Beare, R. J. (2014). A length scale defining partially-resolved boundary-layer turbulence simulations. *Boundary-layer meteorology*, 151(1):39–55.

Beljaars, A. C. (1995). The parametrization of surface fluxes in large-scale models under free convection. *Quarterly Journal of the Royal Meteorological Society*, 121(522):255–270.

Bertrand, T., Wilson, R., Kahre, M., Urata, R., and Kling, A. (2020). Simulation of the 2018 global dust storm on Mars using the NASA Ames Mars GCM: A multitracer approach. *Journal of Geophysical Research: Planets*, 125(7):e2019JE006122.

Blackadar, A. K. (1962a). The vertical distribution of wind and turbulent exchange in a neutral atmosphere. *Journal of Geophysical Research*, 67.8:3095–3102.

Blackadar, A. K. (1962b). The vertical distribution of wind and turbulent exchange in a neutral atmosphere. *Journal of Geophysical Research*, 67(8):3095–3102.

Bou-Zeid, E., Meneveau, C., and Parlange, M. (2005). A scale-dependent lagrangian dynamic model for large eddy simulation of complex turbulent flows. *Physics of fluids*, 17(2):025105.

Bougeault, P. and Lacarrere, P. (1989a). Parameterization of orography-

induced turbulence in a mesobeta–scale model. *Monthly Weather Review*, 117(8):1872–1890.

Bougeault, P. and Lacarrere, P. (1989b). Parameterization of orography–induced turbulence in a mesobeta—scale model. *Mon. Wea. Rev.*, 117:1872–1890.

Boutle, I., Eyre, J., and Lock, A. (2014). Seamless stratocumulus simulation across the turbulent gray zone. *Monthly Weather Review*, 142(4):1655–1668.

Braun, S. A. and Tao, W.-K. (2000). Sensitivity of high-resolution simulations of hurricane bob (1991) to planetary boundary layer parameterizations. *Monthly Weather Review*, 128(12):3941–3961.

Bretherton, C. S. and Park, S. (2009). A new moist turbulence parameterization in the community atmosphere model. *Journal of Climate*, 22(12):3422–3448.

Brooks, I. M. and Fowler, A. M. (2012). An evaluation of boundary-layer depth, inversion and entrainment parameters by large-eddy simulation. *Boundary-layer meteorology*, 142(2):245–263.

Businger, J. A., Wyngaard, J. C., Izumi, Y., and Bradley, E. F. (1971). Flux-profile relationships in the atmospheric surface layer. *Journal of the atmospheric Sciences*, 28(2):181–189.

Busse, J. and Knupp, K. (2012). Observed characteristics of the afternoon–evening boundary layer transition based on sodar and surface data. *Journal of applied meteorology and climatology*, 51(3):571–582.

Butterworth, S. et al. (1930). On the theory of filter amplifiers. *Wireless Engineer*, 7(6):536–541.

Cancelli, D. M., Chamecki, M., and Dias, N. L. (2014). A large-eddy simulation study of scalar dissimilarity in the convective atmospheric boundary layer. *Journal of the Atmospheric Sciences*, 71(1):3–15.

Canut, G., Couvreux, F., Lothon, M., Pino, D., and Saïd, F. (2012). Observations and large-eddy simulations of entrainment in the sheared sahelian boundary layer. *Boundary-layer meteorology*, 142(1):79–101.

Catalano, F. and Moeng, C. H. (2010). Large-eddy simulation of the daytime boundary layer in an idealized valley using the weather research and forecasting numerical model. *Boundary-layer meteorology*, 137(1):49–75.

Changela, H. G., Chatzitheodoridis, E., Antunes, A., Beaty, D., Bouw, K., Bridges, J. C., Capova, K. A., Cockell, C. S., Conley, C. A., Dadachova, E., et al. (2021). Mars: new insights and unresolved questions. *International*

Journal of Astrobiology, 20(6):394–426.

Chow, F. K., Schär, C., Ban, N., Lundquist, K. A., Schlemmer, L., and Shi, X. (2019). Crossing multiple gray zones in the transition from mesoscale to microscale simulation over complex terrain. *Atmosphere*, 10(5):274.

Chow, F. K., Weigel, A. P., Street, R. L., Rotach, M. W., and Xue, M. (2006). High-resolution large-eddy simulations of flow in a steep alpine valley. part i: Methodology, verification, and sensitivity experiments. *Journal of Applied Meteorology and Climatology*, 45(1):63–86.

Christensen, P. R., Bandfield, J. L., Hamilton, V. E., Ruff, S. W., Kieffer, H. H., Titus, T. N., Malin, M. C., Morris, R. V., Lane, M. D., Clark, R., et al. (2001). Mars Global Surveyor Thermal Emission Spectrometer experiment: Investigation description and surface science results. *Journal of Geophysical Research: Planets*, 106(E10):23823–23871.

Christensen, P. R., Jakosky, B. M., Kieffer, H. H., Malin, M. C., McSween, H. Y., Nealson, K., Mehall, G. L., Silverman, S. H., Ferry, S., Caplinger, M., et al. (2004). The thermal emission imaging system (themis) for the mars 2001 odyssey mission. *Space Science Reviews*, 110(1-2):85–130.

Churchfield, M. J., Lee, S., Michalakes, J., and Moriarty, P. J. (2012). A numerical study of the effects of atmospheric and wake turbulence on wind turbine dynamics. *Journal of turbulence*, (13):N14.

Churchfield, M. J., Vijayakumar, G., Brasseur, J. G., and Moriarty, P. J. (2010). Wind energy-related atmospheric boundary layer large-eddy simulation using openfoam: Preprint. Technical report, National Renewable Energy Laboratory (NREL), Golden, CO.

Cohen, A. E., Cavallo, S. M., Coniglio, M. C., and Brooks, H. E. (2015). A review of planetary boundary layer parameterization schemes and their sensitivity in simulating southeastern us cold season severe weather environments. *Weather and forecasting*, 30(3):591–612.

Colaïtis, A., Spiga, A., Hourdin, F., Rio, C., Forget, F., and Millour, E. (2013). A thermal plume model for the Martian convective boundary layer. *Journal of Geophysical Research: Planets*, 118(7):1468–1487.

Colaprete, A., Haberle, R. M., and Toon, O. B. (2003). Formation of convective carbon dioxide clouds near the south pole of Mars. *Journal of Geophysical Research: Planets*, 108(E7).

Conrath, B. J. (1975). Thermal structure of the Martian atmosphere during the dissipation of the dust storm of 1971. *Icarus*, 24(1):36–46.

Davidson, L. (2011). Fluid mechanics, turbulent flow and turbulence modeling. *Div. of Fluid Dynamics, Dep. of Applied Mechanics, Chalmers University of Technology, Göteborg, Sweden*.

Davy, R., Davis, J. A., Taylor, P. A., Lange, C. F., Weng, W., Whiteway, J., and Gunnlaugson, H. P. (2010). Initial analysis of air temperature and related data from the Phoenix MET station and their use in estimating turbulent heat fluxes. *Journal of Geophysical Research: Planets*, 115(E3).

De Villiers, E. (2007). *The potential of large eddy simulation for the modelling of wall bounded flows*. PhD thesis, University of London Doctoral Thesis, London, UK.

Deardorff, J. W. (1970). Convective velocity and temperature scales for the unstable planetary boundary layer and for Rayleigh convection. *Journal of the Atmospheric Sciences*, 27(8):1211–1213.

Deardorff, J. W. (1972). Numerical investigation of neutral and unstable planetary boundary layers. *Journal of the Atmospheric Sciences*, 29(1):91–115.

Deardorff, J. W. (1980). Stratocumulus-capped mixed layers derived from a three-dimensional model. *Boundary-Layer Meteorology*, 18(4):495–527.

Degrazia, G. A., Moraes, O. L., and Oliveira, A. P. (1996). An analytical method to evaluate mixing length scales for the planetary boundary layer. *Journal of Applied Meteorology*, 35(6):974–977.

Degrazia, G. A., Rizza, U., Puhales, F. S., Goulart, A. G., Carvalho, J., Welter, G. S., and Marques Filho, E. P. (2009). A variable mesh spacing for large-eddy simulation models in the convective boundary layer. *Boundary-layer meteorology*, 131(2):277–292.

Degrazia, G. A., Rizza, U., Stefanello, M., Maldaner, S., Roberti, D. R., Martins, L. G. N., Anabor, V., Puhales, F. S., Dal Piva, E., Acevedo, O. C., et al. (2018). An overview of the micrometeorological field campaign at santa maria, southern brazil: the pampa-2016 experiment. *Meteorological Applications*, 25(3):435–444.

Djurić, D. and Damiani Jr, M. S. (1980). On the formation of the low-level jet over texas. *Monthly Weather Review*, 108(11):1854–1865.

Dohm, J. M., Barlow, N. G., Anderson, R. C., Williams, J.-P., Miyamoto, H., Ferris, J. C., Strom, R. G., Taylor, G. J., Fairén, A. G., Baker, V. R., et al. (2007). Possible ancient giant basin and related water enrichment in the Arabia Terra province, Mars. *Icarus*, 190(1):74–92.

Doubrawa, P. and Muñoz-Esparza, D. (2020). Simulating real atmospheric

boundary layers at gray-zone resolutions: How do currently available turbulence parameterizations perform? *Atmosphere*, 11(4):345.

Dyer, A. J. and Hicks, B. B. (1970). Flux-gradient relationships in the constant flux layer. *Quarterly Journal of the Royal Meteorological Society*, 96(410):715–721.

d'Onofrio, A., Fasano, A., and Monechi, B. (2011). A generalization of gompertz law compatible with the gyllenberg–webb theory for tumour growth. *Mathematical Biosciences*, 230(1):45–54.

Efstathiou, G., Beare, R., Osborne, S., and Lock, A. (2016). Grey zone simulations of the morning convective boundary layer development. *Journal of Geophysical Research: Atmospheres*, 121(9):4769–4782.

Efstathiou, G. and Beare, R. J. (2015). Quantifying and improving sub-grid diffusion in the boundary-layer grey zone. *Quarterly Journal of the Royal Meteorological Society*, 141(693):3006–3017.

Efstathiou, G. A. and Plant, R. S. (2019). A dynamic extension of the pragmatic blending scheme for scale-dependent sub-grid mixing. *Quarterly Journal of the Royal Meteorological Society*, 145(719):884–892.

Fedorova, A. A., Montmessin, F., Korablev, O., Luginin, M., Trokhimovskiy, A., Belyaev, D. A., Ignatiev, N. I., Lefèvre, F., Alday, J., Irwin, P. G., et al. (2020). Stormy water on Mars: The distribution and saturation of atmospheric water during the dusty season. *Science*, 367(6475):297–300.

Fenton, L. K. and Lorenz, R. (2015). Dust devil height and spacing with relation to the martian planetary boundary layer thickness. *Icarus*, 260:246–262.

Flaounas, E., Bastin, S., and Janicot, S. (2011). Regional climate modelling of the 2006 west african monsoon: sensitivity to convection and planetary boundary layer parameterisation using wrf. *Climate Dynamics*, 36(5-6):1083–1105.

Fonseca, R. M., Zorzano-Mier, M.-P., and Martín-Torres, J. (2018). Planetary boundary layer and circulation dynamics at Gale crater, Mars. *Icarus*, 302:537–559.

Forget, F., Hourdin, F., Fournier, R., Hourdin, C., Talagrand, O., Collins, M., Lewis, S. R., Read, P. L., and Huot, J.-P. (1999). Improved general circulation models of the Martian atmosphere from the surface to above 80 km. *Journal of Geophysical Research: Planets*, 104(E10):24155–24175.

Forget, F. and Montabone, L. (2017). Atmospheric dust on Mars: A review.

47th International Conference on Environmental Systems.

Fueten, F., Stesky, R. M., and MacKinnon, P. (2005). Structural attitudes of large scale layering in Valles Marineris, Mars, calculated from Mars Orbiter Laser Altimeter data and Mars Orbiter Camera imagery. *Icarus*, 175(1):68–77.

Garvin, J. B., Frawley, J. J., and Abshire, J. B. (1999). Vertical roughness of mars from the mars orbiter laser altimeter. *Geophysical research letters*, 26(3):381–384.

Germano, M., Piomelli, U., Moin, P., and Cabot, W. H. (1991). A dynamic subgrid-scale eddy viscosity model. *Physics of Fluids A: Fluid Dynamics*, 3(7):1760–1765.

Gheynani, B. T. and Taylor, P. A. (2010). Large-eddy simulations of vertical vortex formation in the terrestrial and Martian convective boundary layers. *Boundary-Layer Meteorology*, 137(2):223–235.

Gilliam, R. C. and Pleim, J. E. (2010). Performance assessment of new land surface and planetary boundary layer physics in the WRF-ARW. *Journal of Applied Meteorology and Climatology*, 49(4):760–774.

Goger, B., Rotach, M. W., Gohm, A., Fuhrer, O., Stiperski, I., and Holtslag, A. A. (2018). The impact of three-dimensional effects on the simulation of turbulence kinetic energy in a major alpine valley. *Boundary-layer meteorology*, 168(1):1–27.

Golombek, M., Kipp, D., Warner, N., Daubar, I. J., Fergason, R., Kirk, R. L., Beyer, R., Huertas, A., Piqueux, S., Putzig, N., et al. (2017). Selection of the insight landing site. *Space Science Reviews*, 211(1):5–95.

Gompertz, B. (1825). Xxiv. on the nature of the function expressive of the law of human mortality, and on a new mode of determining the value of life contingencies. in a letter to francis baily, esq. frs &c. *Philosophical transactions of the Royal Society of London*, (115):513–583.

Grachev, A. A., Fairall, C. W., Persson, P. O. G., Andreas, E. L., and Guest, P. S. (2005). Stable boundary-layer scaling regimes: the SHEBA data. *Boundary-Layer Meteorology*, 116(2):201–235.

Greybush, S. J., Wilson, R. J., Hoffman, R. N., Hoffman, M. J., Miyoshi, T., Ide, K., McConnochie, T., and Kalnay, E. (2012). Ensemble Kalman filter data assimilation of Thermal Emission Spectrometer temperature retrievals into a Mars GCM. *Journal of Geophysical Research: Planets*, 117(E11).

Grossman, R. L. (1982). An analysis of vertical velocity spectra obtained in the bomex fair-weather, trade-wind boundary layer. *Boundary-Layer*

Meteorology, 23(3):323–357.

Gryning, S. E., Batchvarova, E., Brummer, B., Jorgensen, H., and Larsen, S. (2007). On the extension of the wind profile over homogeneous terrain beyond the surface boundary layer. *Boundary-Layer Meteorology*, 124(2):251–268.

Guo, X., Lawson, W. G., Richardson, M. I., and Toigo, A. (2009). Fitting the Viking lander surface pressure cycle with a Mars general circulation model. *Journal of Geophysical Research: Planets*, 114(E7).

Guzewich, S. D., Lemmon, M., Smith, C., Martínez, G., de Vicente-Retortillo, Á., Newman, C., Baker, M., Campbell, C., Cooper, B., Gómez-Elvira, J., et al. (2019). Mars Science Laboratory observations of the 2018/Mars year 34 global dust storm. *Geophysical Research Letters*, 46(1):71–79.

Guzewich, S. D., Newman, C., Smith, M., Moores, J., Smith, C., Moore, C., Richardson, M., Kass, D., Kleinböhl, A., Mischna, M., et al. (2017). The vertical dust profile over Gale crater, Mars. *Journal of Geophysical Research: Planets*, 122(12):2779–2792.

Guzewich, S. D., Talaat, E. R., Toigo, A. D., Waugh, D. W., and McConnochie, T. H. (2013a). High-altitude dust layers on Mars: Observations with the Thermal Emission Spectrometer. *Journal of Geophysical Research: Planets*, 118(6):1177–1194.

Guzewich, S. D., Toigo, A. D., Richardson, M. I., Newman, C. E., Talaat, E. R., Waugh, D. W., and McConnochie, T. H. (2013b). The impact of a realistic vertical dust distribution on the simulation of the Martian general circulation. *Journal of Geophysical Research: Planets*, 118(5):980–993.

Haberle, R. (2015). Solar system/sun, atmospheres, evolution of atmospheres| planetary atmospheres: Mars. encyclopedia of atmospheric sciences.

Haberle, R. M., Leovy, C. B., and Pollack, J. B. (1982). Some effects of global dust storms on the atmospheric circulation of Mars. *Icarus*, 50(2-3):322–367.

Haberle, R. M., Pollack, J. B., Barnes, J. R., Zurek, R. W., Leovy, C. B., Murphy, J. R., Lee, H., and Schaeffer, J. (1993). Mars atmospheric dynamics as simulated by the NASA Ames General Circulation Model: 1. the zonal-mean circulation. *Journal of Geophysical Research: Planets*, 98(E2):3093–3123.

Hamilton, V. E., Vasavada, A. R., Sebastián, E., de la Torre Juarez, M., Ramos, M., Armiens, C., Arvidson, R. E., Carrasco, I., Christensen, P. R., De Pablo, M. A., et al. (2014). Observations and preliminary science results from the first 100 sols of MSL Rover Environmental Monitoring Station ground

temperature sensor measurements at Gale crater. *Journal of Geophysical Research: Planets*, 119(4):745–770.

Han, Y., Stoellinger, M., and Naughton, J. (2016). Large eddy simulation for atmospheric boundary layer flow over flat and complex terrains. In *Journal of Physics: Conference Series*, volume 753, page 032044. IOP Publishing.

He, P. and Basu, S. (2016). Extending a surface-layer cn2 model for strongly stratified conditions utilizing a numerically generated turbulence dataset. *Optics express*, 24(9):9574–9582.

Heavens, N., Richardson, M., Kleinböhl, A., Kass, D., McCleese, D., Abdou, W., Benson, J., Schofield, J., Shirley, J., and Wolkenberg, P. (2011a). Vertical distribution of dust in the Martian atmosphere during northern spring and summer: High-altitude tropical dust maximum at northern summer solstice. *Journal of Geophysical Research: Planets*, 116(E1).

Heavens, N., Richardson, M., Kleinböhl, A., Kass, D., McCleese, D., Abdou, W., Benson, J., Schofield, J., Shirley, J., and Wolkenberg, P. (2011b). The vertical distribution of dust in the Martian atmosphere during northern spring and summer: Observations by the Mars Climate Sounder and analysis of zonal average vertical dust profiles. *Journal of Geophysical Research: Planets*, 116(E4).

Heffter, J. L. (1980). Air Resources Laboratories atmospheric transport and dispersion model (ARL-ATAD). Technical report, National Oceanic and Atmospheric Administration, Silver Spring, MD (USA).

Hinson, D., Pätzold, M., Tellmann, S., Häusler, B., and Tyler, G. (2008). The depth of the convective boundary layer on Mars. *Icarus*, 198(1):57–66.

Hinson, D., Tyler, D., Lewis, S., Pätzold, M., Tellmann, S., Häusler, B., and Tyler, G. (2019). The Martian daytime convective boundary layer: Results from radio occultation measurements and a mesoscale model. *Icarus*, 326:105–122.

Holtslag, B. (2006). Preface: GEWEX atmospheric boundary-layer study (GABLS) on stable boundary layers. *Boundary-Layer Meteorology*, 118(2):243–246.

Hong, S.-Y., Noh, Y., and Dudhia, J. (2006). A new vertical diffusion package with an explicit treatment of entrainment processes. *Monthly weather review*, 134(9):2318–2341.

Hong, S.-Y. and Pan, H.-L. (1996). Nonlocal boundary layer vertical diffusion in a medium-range forecast model. *Monthly Weather Review*, 124(10):2322–

2339.

Honnert, R. (2019). Grey-zone turbulence in the neutral atmospheric boundary layer. *Boundary-layer meteorology*, 170(2):191–204.

Honnert, R., Masson, V., and Couvreux, F. (2011). A diagnostic for evaluating the representation of turbulence in atmospheric models at the kilometric scale. *Journal of the Atmospheric Sciences*, 68(12):3112–3131.

Horová, I., Kolacek, J., and Zelinka, J. (2012). *Kernel Smoothing in MATLAB: theory and practice of kernel smoothing*. World scientific.

Hu, X.-M., Nielsen-Gammon, J. W., and Zhang, F. (2010). Evaluation of three planetary boundary layer schemes in the wrf model. *Journal of Applied Meteorology and Climatology*, 49(9):1831–1844.

Huang, J. and Bou-Zeid, E. (2013). Turbulence and vertical fluxes in the stable atmospheric boundary layer. part i: A large-eddy simulation study. *Journal of the Atmospheric Sciences*, 70(6):1513–1527.

Huang, Q., Marsham, J. H., Tian, W., Parker, D. J., and Garcia-Carreras, L. (2018). Large-eddy simulation of dust-uplift by a haboob density current. *Atmospheric Environment*, 179:31–39.

Iacono, M. J., Delamere, J. S., Mlawer, E. J., Shephard, M. W., Clough, S. A., and Collins, W. D. (2008). Radiative forcing by long-lived greenhouse gases: Calculations with the aer radiative transfer models. *Journal of Geophysical Research: Atmospheres*, 113(D13).

Issa, R. I. (1986). Solution of the implicitly discretised fluid flow equations by operator-splitting. *Journal of computational physics*, 62(1):40–65.

Ito, J., Niino, H., Nakanishi, M., and Moeng, C. H. (2015). An extension of the mellor–yamada model to the terra incognita zone for dry convective mixed layers in the free convection regime. *Boundary-layer meteorology*, 157(1):23–43.

Janić, Z. I. (2001). Nonsingular implementation of the mellor-yamada level 2.5 scheme in the ncep meso model.

Janjić, Z. I. (1994). The step-mountain eta coordinate model: Further developments of the convection, viscous sublayer, and turbulence closure schemes. *Monthly Weather Review*, 122(5):927–945.

Janjić, Z. I. (2001). Nonsingular implementation of the Mellor-Yamada level 2.5 scheme in the ncep meso model. *NCEP office note*, 437:61.

Jankov, I., Gallus Jr, W. A., Segal, M., Shaw, B., and Koch, S. E. (2005). The impact of different wrf model physical parameterizations and their

interactions on warm season mcs rainfall. *Weather and forecasting*, 20(6):1048–1060.

Jiménez, M. and Cuxart, J. (2005). Large-eddy simulations of the stable boundary layer using the standard kolmogorov theory: Range of applicability. *Boundary-Layer Meteorology*, 115(2):241–261.

Jiménez, P. A. and Dudhia, J. (2012). Improving the representation of resolved and unresolved topographic effects on surface wind in the WRF model. *Journal of Applied Meteorology and Climatology*, 51(2):300–316.

Jiménez, P. A., Dudhia, J., González-Rouco, J. F., Navarro, J., Montávez, J. P., and García-Bustamante, E. (2012). A revised scheme for the WRF surface layer formulation. *Monthly Weather Review*, 140(3):898–918.

Joshi, M., Haberle, R. M., Barnes, J. R., Murphy, J., and Schaeffer, J. (1997). Low-level jets in the nasa ames Mars general circulation model. *Journal of Geophysical Research: Planets*, 102(E3):6511–6523.

Kahre, M., Hollingsworth, J., Haberle, R., and Montmessin, F. (2011). Coupling Mars' dust and water cycles: Effects on dust lifting vigor, spatial extent and seasonality. *Mars Atmosphere: Modelling and Observation. Laboratoire de Meteorologie Dynamique (LMD)*, pages 143–146.

Kahre, M., Hollingsworth, J., Haberle, R., and Wilson, R. (2015). Coupling the Mars dust and water cycles: the importance of radiative-dynamic feedbacks during northern hemisphere summer. *Icarus*, 260:477–480.

Kahre, M., Wilson, R., Haberle, R., and Hollingsworth, J. (2009). An inverse approach to modeling the dust cycle with two Mars general circulation models. *Mars Dust Cycle Workshop Ames Research Center*, pages 125–129.

Kaimal, J., Wyngaard, J., Haugen, D., Coté, O., Izumi, Y., Caughey, S., and Readings, C. (1976). Turbulence structure in the convective boundary layer. *Journal of the Atmospheric Sciences*, 33(11):2152–2169.

Kalverla, P. C., Duncan Jr, J. B., Steeneveld, G.-J., and Holtslag, A. A. (2019). Low-level jets over the north sea based on era5 and observations: together they do better. *Wind Energy Science*, 4(2):193–209.

Kass, D., Schofield, J., Kleinböhl, A., McCleese, D., Heavens, N., Shirley, J., and Steele, L. (2020). Mars Climate Sounder observation of Mars' 2018 global dust storm. 47(23):e2019GL083931.

Khani, S. and Porté-Agel, F. (2017). A modulated-gradient parametrization for the large-eddy simulation of the atmospheric boundary layer using the weather research and forecasting model. *Boundary-Layer Meteorology*,

165(3):385–404.

Kleinböhl, A., Schofield, J. T., Kass, D. M., Abdou, W. A., Backus, C. R., Sen, B., Shirley, J. H., Lawson, W. G., Richardson, M. I., Taylor, F. W., et al. (2009). Mars Climate Sounder limb profile retrieval of atmospheric temperature, pressure, and dust and water ice opacity. *Journal of Geophysical Research: Planets*, 114(E10).

Kleinböhl, A., Spiga, A., Kass, D. M., Shirley, J. H., Millour, E., Montabone, L., and Forget, F. (2020). Diurnal variations of dust during the 2018 global dust storm observed by the Mars Climate Sounder. *Journal of Geophysical Research: Planets*, 125(1):e2019JE006115.

Klemp, J., Dudhia, J., and Hassiotis, A. (2008). An upper gravity-wave absorbing layer for NWP applications. *Monthly Weather Review*, 136(10):3987–4004.

Kolmogorov, A. N. (1941). The local structure of turbulence in incompressible viscous fluid for very large reynolds numbers. In *Dokl. Akad. Nauk SSSR*, volume 30, pages 299–303.

Kosović, B. (1997). Subgrid-scale modelling for the large-eddy simulation of high-reynolds-number boundary layers. *Journal of Fluid Mechanics*, 336:151–182.

Kosović, B. and Curry, J. A. (2000). A large eddy simulation study of a quasi-steady, stably stratified atmospheric boundary layer. *Journal of the atmospheric sciences*, 57(8):1052–1068.

Kosović, B., Jimenez, P., Haupt, S., Martilli, A., Olson, J., and Bao, J. (2017). Recent developments and assessment of a three-dimensional pbl parameterization for improved wind forecasting over complex terrain. In *AGU Fall Meeting Abstracts*.

Kurowski, M. J. and Teixeira, J. (2018). A scale-adaptive turbulent kinetic energy closure for the dry convective boundary layer. *Journal of the Atmospheric Sciences*, 75(2):675–690.

Laird, A. K. (1964). Dynamics of tumour growth. *British journal of cancer*, 18(3):490.

Lampert, A., Pätzold, F., Jiménez, M. A., Lobitz, L., Martin, S., Lohmann, G., Canut, G., Legain, D., Bange, J., Martínez-Villagrasa, D., et al. (2016). A study of local turbulence and anisotropy during the afternoon and evening transition with an unmanned aerial system and mesoscale simulation. *Atmospheric Chemistry and Physics*, 16(12):8009–8021.

Larsen, S. E., Jørgensen, H. E., Landberg, L., and Tillman, J. (2002). Aspects of the atmospheric surface layers on Mars and Earth. *Boundary-Layer Meteorology*, 105(3):451–470.

Lavely, A., Lorenz, R., and Schmitz, S. (2021). Large-eddy simulation of titan's near-surface atmosphere: Convective turbulence and flow over dunes with application to huygens and dragonfly. *Icarus*, 357:114229.

Lawrence, D. M., Oleson, K. W., Flanner, M. G., Thornton, P. E., Swenson, S. C., Lawrence, P. J., Zeng, X., Yang, Z.-L., Levis, S., Sakaguchi, K., et al. (2011). Parameterization improvements and functional and structural advances in version 4 of the community land model. *Journal of Advances in Modeling Earth Systems*, 3(1).

Lee, C., Lawson, W., Richardson, M., Anderson, J., Collins, N., Hoar, T., and Mischna, M. (2011). Demonstration of ensemble data assimilation for Mars using dart, MarsWRF, and radiance observations from MGS TES. *Journal of Geophysical Research: Planets*, 116(E11).

Lee, C., Richardson, M. I., Newman, C. E., and Mischna, M. A. (2018). The sensitivity of solsticial pauses to atmospheric ice and dust in the MarsWRF general circulation model. *Icarus*, 311:23–34.

Lemone, M. A. (1973). The structure and dynamics of horizontal roll vortices in the planetary boundary layer. *Journal of the Atmospheric Sciences*, 30(6):1077–1091.

Lewis, S. R., Collins, M., Read, P. L., Forget, F., Hourdin, F., Fournier, R., Hourdin, C., Talagrand, O., and Huot, J.-P. (1999). A climate database for Mars. *Journal of Geophysical Research: Planets*, 104(E10):24177–24194.

Liu, H., Chen, N., Feng, C., Tong, S., and Li, R. (2017). Impact of electro-stimulation on denitrifying bacterial growth and analysis of bacterial growth kinetics using a modified gompertz model in a bio-electrochemical denitrification reactor. *Bioresource technology*, 232:344–353.

Liu, J., Richardson, M. I., and Wilson, R. (2003). An assessment of the global, seasonal, and interannual spacecraft record of Martian climate in the thermal infrared. *Journal of Geophysical Research: Planets*, 108(E8).

Liuzzi, G., Villanueva, G. L., Crismani, M. M., Smith, M. D., Mumma, M. J., Daerden, F., Aoki, S., Vandaele, A. C., Clancy, R. T., Erwin, J., et al. (2020). Strong variability of Martian water ice clouds during dust storms revealed from ExoMars Trace Gas Orbiter/NOMAD. *Journal of Geophysical Research: Planets*, 125(4):e2019JE006250.

Lu, H. and Porté-Agel, F. (2015). On the impact of wind farms on a convective atmospheric boundary layer. *Boundary-Layer Meteorology*, 157(1):81–96.

Lundquist, J. K., Wilczak, J. M., Ashton, R., Bianco, L., Brewer, W. A., Choukulkar, A., Clifton, A., Debnath, M., Delgado, R., Friedrich, K., et al. (2017). Assessing state-of-the-art capabilities for probing the atmospheric boundary layer: the xpia field campaign. *Bulletin of the American Meteorological Society*, 98(2):289–314.

Madeleine, J.-B., Forget, F., Millour, E., Montabone, L., and Wolff, M. (2011). Revisiting the radiative impact of dust on Mars using the LMD global climate model. *Journal of Geophysical Research: Planets*, 116(E11).

Madeleine, J.-B., Forget, F., Millour, E., Navarro, T., and Spiga, A. (2012). The influence of radiatively active water ice clouds on the Martian climate. *Geophysical Research Letters*, 39(23).

Mahrt, L. (1998). Stratified atmospheric boundary layers and breakdown of models. *Theoretical and Computational Fluid Dynamics*, 11(3-4):263–279.

Mahrt, L. (2014). Stably stratified atmospheric boundary layers. *Annual Review of Fluid Mechanics*, 46:23–45.

Mahrt, L. and Vickers, D. (2006). Extremely weak mixing in stable conditions. *Boundary-layer meteorology*, 119(1):19–39.

Martin, L. J. and Zurek, R. W. (1993). An analysis of the history of dust activity on Mars. *Journal of Geophysical Research: Planets*, 98(E2):3221–3246.

Martínez, G., Valero, F., and Vázquez, L. (2009). Characterization of the Martian convective boundary layer. *Journal of the atmospheric sciences*, 66(7):2044–2058.

Martinez, G. M., Valero, F., Vazquez, L., and Elliott, H. M. (2013). The martian planetary boundary layer: Turbulent kinetic energy and fundamental similarity scales. *Solar System Research*, 47(6):446–453.

Mason, P. J. (1989). Large-eddy simulation of the convective atmospheric boundary layer. *Journal of the atmospheric sciences*, 46(11):1492–1516.

Mason, P. J. and Derbyshire, S. H. (1990). Large-eddy simulation of the stably-stratified atmospheric boundary layer. *Boundary-layer meteorology*, 53(1-2):117–162.

McCleese, D., Heavens, N., Schofield, J., Abdou, W., Bandfield, J., Calcutt, S., Irwin, P., Kass, D., Kleinböhl, A., Lewis, S., et al. (2010). Structure and dynamics of the Martian lower and middle atmosphere as observed by the Mars Climate Sounder: Seasonal variations in zonal mean temperature, dust,

and water ice aerosols. *Journal of Geophysical Research: Planets*, 115(E12).

McCleese, D., Schofield, J., Taylor, F., Calcutt, S., Foote, M., Kass, D., Leovy, C., Paige, D., Read, P., and Zurek, R. (2007). Mars Climate Sounder: An investigation of thermal and water vapor structure, dust and condensate distributions in the atmosphere, and energy balance of the polar regions. *Journal of Geophysical Research: Planets*, 112(E5).

Mechoso, C. and Arakawa, A. (2015). Numerical models| general circulation models.

Mellor, G. L. and Yamada, T. (1974). A hierarchy of turbulence closure models for planetary boundary layers. *Journal of the Atmospheric Sciences*, 31(7):1791–1806.

Meneveau, C., Lund, T. S., and Cabot, W. H. (1996). A lagrangian dynamic subgrid-scale model of turbulence. *Journal of fluid mechanics*, 319:353–385.

Michaels, T. I. and Rafkin, S. C. (2004). Large-eddy simulation of atmospheric convection on Mars. *Quarterly Journal of the Royal Meteorological Society*, 130(599):1251–1274.

Milkovich, S. M., Head, J. W., and Marchant, D. R. (2006). Debris-covered piedmont glaciers along the northwest flank of the Olympus Mons scarp: Evidence for low-latitude ice accumulation during the Late Amazonian of Mars. *Icarus*, 181(2):388–407.

Millour, E., Forget, F., Lopez-Valverde, M., Lefevre, F., Gonzalez-Galindo, F., Lewis, S., Chaufray, J.-Y., Montabone, L., Zakharov, V., Spiga, A., et al. (2018). Exploring the interannual variablitity of the Martian atmosphere with the Mars Climate Database v5. 3. In *42nd COSPAR Scientific Assembly*, volume 42.

Mirocha, J. D., Churchfield, M. J., Muñoz-Esparza, D., Rai, R. K., Feng, Y., Kosović, B., Haupt, S. E., Brown, B., Ennis, B. L., Draxl, C., et al. (2017). Large-eddy simulation sensitivities to variations of configuration and forcing parameters in canonical boundary-layer flows for wind energy applications. Technical report, National Renewable Energy Lab.(NREL), Golden, CO (United States).

Mirocha, J. D., Lundquist, J. K., and Kosović, B. (2010). Implementation of a nonlinear subfilter turbulence stress model for large-eddy simulation in the advanced research wrf model. *Monthly Weather Review*, 138(11):4212–4228.

Mischna, M. A., Lee, C., and Richardson, M. (2012). Development of a fast, accurate radiative transfer model for the Martian atmosphere, past and

present. *Journal of Geophysical Research: Planets*, 117(E10).

Moeng, C. H. (1984). A large-eddy-simulation model for the study of planetary boundary-layer turbulence. *Journal of the Atmospheric Sciences*, 41(13):2052–2062.

Moeng, C. H. and Sullivan, P. P. (1994). A comparison of shear-and buoyancy-driven planetary boundary layer flows. *Journal of the Atmospheric Sciences*, 51(7):999–1022.

Moeng, C. -H. (2016). Lecture notes on the planetary boundary layer. Technical Report NCAR/TN-525+IA, NCAR - National Center for Atmospheric Research.

Monin, A. S. and Obukhov, A. M. (1954). Basic laws of turbulent mixing in the atmosphere near the ground. *Trudy geofiz. inst. AN SSSR*, 24:163–187.

Montabone, L., Forget, F., Millour, E., Wilson, R., Lewis, S., Cantor, B., Kass, D., Kleinböhl, A., Lemmon, M., Smith, M., et al. (2015). Eight-year climatology of dust optical depth on mars. *Icarus*, 251:65–95.

Montabone, L., Spiga, A., Kass, D. M., Kleinböhl, A., Forget, F., and Millour, E. (2020). Martian year 34 column dust climatology from Mars Climate Sounder observations: Reconstructed maps and model simulations. *Journal of Geophysical Research: Planets*, page e2019JE006111.

Montmessin, F., Forget, F., Rannou, P., Cabane, M., and Haberle, R. (2004). Origin and role of water ice clouds in the Martian water cycle as inferred from a general circulation model. *Journal of Geophysical Research: Planets*, 109(E10).

Moores, J. E., Lemmon, M. T., Kahanpää, H., Rafkin, S. C., Francis, R., Pla-Garcia, J., Bean, K., Haberle, R., Newman, C., Mischna, M., et al. (2015). Observational evidence of a suppressed planetary boundary layer in northern Gale crater, Mars as seen by the Navcam instrument onboard the Mars Science Laboratory rover. *Icarus*, 249:129–142.

Moré, J. J. (1978). The levenberg-marquardt algorithm: implementation and theory. In *Numerical analysis*, pages 105–116. Springer.

Moreira, D. and Moret, M. (2018). A new direction in the atmospheric pollutant dispersion inside the planetary boundary layer. *Journal of Applied Meteorology and Climatology*, 57(1):185–192.

Morrison, H. and Gettelman, A. (2008). A new two-moment bulk stratiform cloud microphysics scheme in the Community Atmosphere Model, version 3 (CAM3). part i: Description and numerical tests. *Journal of Climate*,

21(15):3642–3659.

Muñoz-Esparza, D., Kosović, B., García-Sánchez, C., and van Beeck, J. (2014a). Nesting turbulence in an offshore convective boundary layer using large-eddy simulations. *Boundary-layer meteorology*, 151(3):453–478.

Muñoz-Esparza, D., Kosović, B., Mirocha, J., and van Beeck, J. (2014b). Bridging the transition from mesoscale to microscale turbulence in numerical weather prediction models. *Boundary-layer meteorology*, 153(3):409–440.

Muñoz-Esparza, D., Sauer, J., Linn, R., and Kosović, B. (2016). Limitations of one-dimensional mesoscale pbl parameterizations in reproducing mountain-wave flows. *Journal of the Atmospheric Sciences*, 73(7):2603–2614.

Muñoz-Esparza, D., Sharman, R. D., and Lundquist, J. K. (2018). Turbulence dissipation rate in the atmospheric boundary layer: Observations and wrf mesoscale modeling during the xpia field campaign. *Monthly Weather Review*, 146(1):351–371.

Muñoz-Esparza, D., Sharman, R. D., and Trier, S. B. (2020). On the consequences of pbl scheme diffusion on utls wave and turbulence representation in high-resolution nwp models. *Monthly Weather Review*, 148(10):4247–4265.

Nadeau, D. F., Pardyjak, E. R., Higgins, C. W., Fernando, H. J. S., and Parlange, M. B. (2011). A simple model for the afternoon and early evening decay of convective turbulence over different land surfaces. *Boundary-layer meteorology*, 141(2):301–324.

Nakanishi, M. (2001). Improvement of the mellor–yamada turbulence closure model based on large-eddy simulation data. *Boundary-layer meteorology*, 99(3):349–378.

Nakanishi, M. and Niino, H. (2006). An improved Mellor-Yamada level-3 model: Its numerical stability and application to a regional prediction of advection fog. *Boundary-Layer Meteorology*, 119(2):397–407.

Nakanishi, M. and Niino, H. (2009). Development of an improved turbulence closure model for the atmospheric boundary layer. *Journal of the Meteorological Society of Japan. Ser. II*, 87(5):895–912.

Navarro, T., Madeleine, J.-B., Forget, F., Spiga, A., Millour, E., Montmessin, F., and Määttänen, A. (2014). Global climate modeling of the Martian water cycle with improved microphysics and radiatively active water ice clouds. *Journal of Geophysical Research: Planets*, 119(7):1479–1495.

Neary, L., Daerden, F., Aoki, S., Whiteway, J., Clancy, R. T., Smith, M., Viscardy, S., Erwin, J., Thomas, I., Villanueva, G., et al. (2020). Explanation for the increase in high-altitude water on Mars observed by NOMAD during the 2018 global dust storm. *Geophysical Research Letters*, 47(7):e2019GL084354.

Newman, C. E., Gómez-Elvira, J., Marin, M., Navarro, S., Torres, J., Richardson, M. I., Battalio, J. M., Guzewich, S. D., Sullivan, R., de la Torre, M., et al. (2017). Winds measured by the rover environmental monitoring station (REMS) during the Mars Science Laboratory (MSL) rover's bagnold dunes campaign and comparison with numerical modeling using MarsWRF. *Icarus*, 291:203–231.

Newman, C. E., Kahanpää, H., Richardson, M., Martínez, G. M., Vicente-Retortillo, A., and Lemmon, M. (2019a). MarsWRF convective vortex and dust devil predictions for Gale crater over 3 Mars years and comparison with MSL-REMS observations. *Journal of Geophysical Research: Planets*, 124(12):3442–3468.

Newman, C. E., Lee, C., Mischna, M. A., Richardson, M. I., and Shirley, J. H. (2019b). An initial assessment of the impact of postulated orbit-spin coupling on Mars dust storm variability in fully interactive dust simulations. *Icarus*, 317:649–668.

Newman, C. E., Lewis, S. R., Read, P. L., and Forget, F. (2002). Modeling the Martian dust cycle, 1. Representations of dust transport processes. *Journal of Geophysical Research: Planets*, 107(E12):6–1.

Newman, C. E. and Richardson, M. I. (2015). The impact of surface dust source exhaustion on the Martian dust cycle, dust storms and interannual variability, as simulated by the MarsWRF general circulation model. *Icarus*, 257:47–87.

Nielsen-Gammon, J. W., Powell, C. L., Mahoney, M. J., Angevine, W. M., Senff, C., White, A., Berkowitz, C., Doran, C., and Knupp, K. (2008). Multisensor estimation of mixing heights over a coastal city. *Journal of Applied Meteorology and Climatology*, 47(1):27–43.

Nishizawa, S., Odaka, M., Takahashi, Y. O., Sugiyama, K.-i., Nakajima, K., Ishiwatari, M., Takehiro, S.-i., Yashiro, H., Sato, Y., Tomita, H., et al. (2016). Martian dust devil statistics from high-resolution large-eddy simulations. *Geophysical Research Letters*, 43(9):4180–4188.

Noh, Y., Cheon, W., Hong, S., and Raasch, S. (2003). Improvement of

the k-profile model for the planetary boundary layer based on large eddy simulation data. *Boundary-layer meteorology*, 107(2):401–427.

Ordonez-Etxeberria, I., Hueso, R., and Sánchez-Lavega, A. (2018). A systematic search of sudden pressure drops on Gale crater during two Martian years derived from MSL/REMS data. *Icarus*, 299:308–330.

Parente, A., Gorlé, C., Van Beeck, J., and Benocci, C. (2011). Improved k–ε model and wall function formulation for the rans simulation of abl flows. *Journal of wind engineering and industrial aerodynamics*, 99(4):267–278.

Paton, M., Harri, A.-M., and Savijärvi, H. (2018). Measurement of Martian boundary layer winds by the displacement of jettisoned lander hardware. *Icarus*, 309:345–362.

Pätzold, M., Häusler, B., Tyler, G., Andert, T., Asmar, S., Bird, M., Dehant, V., Hinson, D., Rosenblatt, P., Simpson, R., et al. (2016). Mars express 10 years at Mars: observations by the Mars Express Radio Science experiment (Mars). *Planetary and Space Science*, 127:44–90.

Pedersen, J. G., Kelly, M., Gryning, S. E., Floors, R., Batchvarova, E., and Peña, A. (2012). Comparison of large eddy simulations of a convective boundary layer with wind lidar measurements. *Advances in Science and Research*, 8(1):83–86.

Perrin, C., Rodriguez, S., Jacob, A., Lucas, A., Spiga, A., Murdoch, N., Lorenz, R., Daubar, I., Pan, L., Kawamura, T., et al. (2020). Monitoring of dust devil tracks around the InSight landing site, Mars, and comparison with in situ atmospheric data. *Geophysical Research Letters*, 47(10):e2020GL087234.

Petrosyan, A., Galperin, B., Larsen, S. E., Lewis, S., Määttänen, A., Read, P., Renno, N., Rogberg, L., Savijärvi, H., Siili, T., et al. (2011). The Martian atmospheric boundary layer. *Reviews of Geophysics*, 49(3).

Pino, D., Jonker, H. J., De Arellano, J. V.-G., and Dosio, A. (2006). Role of shear and the inversion strength during sunset turbulence over land: characteristic length scales. *Boundary-layer meteorology*, 121(3):537–556.

Pla-Garcia, J., Rafkin, S. C., Kahre, M., Gomez-Elvira, J., Hamilton, V. E., Navarro, S., Torres, J., Marín, M., and Vasavada, A. R. (2016). The meteorology of Gale crater as determined from Rover Environmental Monitoring Station Observations and numerical modeling. Part I: Comparison of model simulations with observations. *Icarus*, 280:103–113.

Pla-García, J., Rafkin, S. C., Martinez, G., Vicente-Retortillo, Á., Newman,

C., Savijärvi, H., De la Torre, M., Rodriguez-Manfredi, J., Gómez, F., Molina, A., et al. (2020). Meteorological predictions for mars 2020 perseverance rover landing site at jezero crater. *Space science reviews*, 216(8):1–21.

Pleim, J. E. (2007). A combined local and nonlocal closure model for the atmospheric boundary layer. part i: Model description and testing. *Journal of Applied Meteorology and Climatology*, 46(9):1383–1395.

Porté-Agel, F., Meneveau, C., and Parlange, M. B. (2000). A scale-dependent dynamic model for large-eddy simulation: application to a neutral atmospheric boundary layer. *Journal of Fluid Mechanics*, 415:261–284.

Putzig, N. E. and Mellon, M. T. (2007). Apparent thermal inertia and the surface heterogeneity of Mars. *Icarus*, 191(1):68–94.

Putzig, N. E., Mellon, M. T., Kretke, K. A., and Arvidson, R. E. (2005). Global thermal inertia and surface properties of Mars from the MGS mapping mission. *Icarus*, 173(2):325–341.

Ramachandran, S. and Wyngaard, J. C. (2011). Subfilter-scale modelling using transport equations: large-eddy simulation of the moderately convective atmospheric boundary layer. *Boundary-layer meteorology*, 139(1):1–35.

Randall, D. A. (2000). *General circulation model development: past, present, and future*. Elsevier.

Rennó, N. O., Abreu, V. J., Koch, J., Smith, P. H., Hartogensis, O. K., De Bruin, H. A., Burose, D., Delory, G. T., Farrell, W. M., Watts, C. J., et al. (2004). MATADOR 2002: A pilot field experiment on convective plumes and dust devils. *Journal of Geophysical Research: Planets*, 109(E7).

Richardson, M. I., Toigo, A. D., and Newman, C. E. (2007). PlanetWRF: A general purpose, local to global numerical model for planetary atmospheric and climate dynamics. *Journal of Geophysical Research: Planets*, 112(E9).

Rodi, W. (2017). *Turbulence models and their application in hydraulics*. Routledge.

Rotunno, R., Chen, Y., Wang, W., Davis, C., Dudhia, J., and Holland, G. (2009). Large-eddy simulation of an idealized tropical cyclone. *Bulletin of the American Meteorological Society*, 90(12):1783–1788.

Sagaut, P. (2006). *Large eddy simulation for incompressible flows: an introduction*. Springer Science & Business Media.

Salesky, S. T., Chamecki, M., and Bou-Zeid, E. (2017). On the nature of the transition between roll and cellular organization in the convective boundary layer. *Boundary-layer meteorology*, 163(1):41–68.

Sato, H., Kurita, K., and Baratoux, D. (2010). The formation of floor-fractured craters in Xanthe terra. *Icarus*, 207(1):248–264.

Schmidt, H. and Schumann, U. (1989). Coherent structure of the convective boundary layer derived from large-eddy simulations. *Journal of Fluid Mechanics*, 200:511–562.

Schumann, U. (1975). Subgrid scale model for finite difference simulations of turbulent flows in plane channels and annuli. *Journal of computational physics*, 18(4):376–404.

Senel, C., Temel, O., Kaskes, P., Vellekoop, J., Goderis, S., Van Hove, B., and Karatekin, O. (2021a). Relative roles of impact-generated aerosols on photosynthetic activity following the chicxulub asteroid impact. In *Geological Society of America Abstracts with Programs*, volume 53, pages 1–1. Geological Society of America.

Senel, C. B., Kaskes, P., Temel, O., Vellekoop, J., Goderis, S., DePalma, R., Prins, M., Claeys, P., and Karatekin, O. (2022). Another one bites the dust: Photosynthesis collapse after chicxulub impact. *Nature*, ready for submission.

Senel, C. B., Temel, O., and Karatekin, O. (2020a). Spectral dynamics and turbulence energy cascade in the martian planetary boundary layer. In *AGU Fall Meeting Abstracts*, volume 2020, pages P080–0001.

Senel, C. B., Temel, O., Lee, C., Newman, C. E., Mischna, M. A., Muñoz-Esparza, D., Sert, H., and Karatekin, Ö. (2021b). Interannual, seasonal and regional variations in the martian convective boundary layer derived from gcm simulations with a semi-interactive dust transport model. *Journal of Geophysical Research: Planets*, 126(10):e2021JE006965.

Senel, C. B., Temel, O., Muñoz-Esparza, D., Parente, A., and van Beeck, J. (2020b). Gray Zone partitioning functions and parameterization of turbulence fluxes in the convective atmospheric boundary layer. *Journal of Geophysical Research: Atmospheres*, 125(22):e2020JD033581.

Senel, C. B., Temel, O., Porchetta, S., Muñoz-Esparza, D., and van Beeck, J. (2019). A new planetary boundary layer scheme based on LES: Application to the XPIA campaign. *Journal of Advances in Modeling Earth Systems*, 11:2655–2679.

Shih, T.-H., Liou, W. W., Shabbir, A., Yang, Z., and Zhu, J. (1995a). A new k-ϵ eddy viscosity model for high reynolds number turbulent flows. *Computers & Fluids*, 24(3):227–238.

Shih, T.-H., Zhu, J., and Lumley, J. L. (1995b). A new reynolds stress algebraic

equation model. *Computer methods in applied mechanics and engineering*, 125(1-4):287–302.

Shin, H. H. and Hong, S.-Y. (2011). Intercomparison of planetary boundary-layer parametrizations in the wrf model for a single day from cases-99. *Boundary-Layer Meteorology*, 139(2):261–281.

Shin, H. H. and Hong, S.-Y. (2013). Analysis of resolved and parameterized vertical transports in convective boundary layers at gray-zone resolutions. *Journal of the atmospheric sciences*, 70(10):3248–3261.

Shin, H. H. and Hong, S.-Y. (2015). Representation of the subgrid-scale turbulent transport in convective boundary layers at gray-zone resolutions. *Monthly Weather Review*, 143(1):250–271.

Skamarock, W. C. (2004). Evaluating mesoscale nwp models using kinetic energy spectra. *Monthly weather review*, 132(12):3019–3032.

Skamarock, W. C. and Klemp, J. B. (2008). A time-split nonhydrostatic atmospheric model for weather research and forecasting applications. *Journal of computational physics*, 227(7):3465–3485.

Skamarock, W. C., Klemp, J. B., Dudhia, J., Barker, D. M., Duda, M. G., Huang, X. Y., Wang, W., and Powers, J. G. (2008a). A description of the advanced research wrf version 3. Technical report, NCAR - National Center for Atmospheric Research Technical Notes (NCAR/TN-475+STR).

Skamarock, W. C., Klemp, J. B., Dudhia, J., Gill, D. O., Barker, D. M., Duda, M. G., Huang, X.-Y., Wang, W., and Powers, J. G. (2008b). G.: A description of the Advanced Research WRF version 3. In *NCAR Tech. Note NCAR/TN-475+ STR*. Citeseer.

Skamarock, W. C., Klemp, J. B., Dudhia, J., Gill, D. O., Barker, D. M., Wang, W., and Powers, J. G. (2008c). A description of the advanced research wrf version 3. ncar technical note-475+ str.

Smagorinsky, J. (1963). General circulation experiments with the primitive equations: I. the basic experiment. *Monthly weather review*, 91(3):99–164.

Smith, D. E., Zuber, M. T., Frey, H. V., Garvin, J. B., Head, J. W., Muhleman, D. O., Pettengill, G. H., Phillips, R. J., Solomon, S. C., Zwally, H. J., et al. (2001). Mars Orbiter Laser Altimeter: Experiment summary after the first year of global mapping of Mars. *Journal of Geophysical Research: Planets*, 106(E10):23689–23722.

Smith, M. D., Wolff, M. J., Lemmon, M. T., Spanovich, N., Banfield, D., Budney, C. J., Clancy, R. T., Ghosh, A., Landis, G. A., Smith, P., et al.

(2004). First atmospheric science results from the Mars Exploration Rovers Mini-TES. *Science*, 306(5702):1750–1753.

Sorbjan, Z. (2007). Statistics of shallow convection on Mars based on large-eddy simulations. Part 2: Effects of wind shear. *Boundary-Layer Meteorology*, 123(1):143–157.

Spiga, A. (2019). The planetary boundary layer of Mars. In *Oxford Research Encyclopedia of Planetary Science*.

Spiga, A., Banfield, D., Teanby, N. A., Forget, F., Lucas, A., Kenda, B., Manfredi, J. A. R., Widmer-Schnidrig, R., Murdoch, N., Lemmon, M. T., et al. (2018). Atmospheric science with insight. *Space Science Reviews*, 214(7):109.

Spiga, A., Barth, E., Gu, Z., Hoffmann, F., Ito, J., Jemmett-Smith, B., Klose, M., Nishizawa, S., Raasch, S., Rafkin, S., et al. (2016). Large-eddy simulations of dust devils and convective vortices. *Space Science Reviews*, 203(1–4):245–275.

Spiga, A., Faure, J., Madeleine, J.-B., Määttänen, A., and Forget, F. (2013). Rocket dust storms and detached dust layers in the Martian atmosphere. *Journal of Geophysical Research: Planets*, 118(4):746–767.

Spiga, A. and Forget, F. (2009). A new model to simulate the martian mesoscale and microscale atmospheric circulation: Validation and first results. *Journal of Geophysical Research: Planets*, 114(E2).

Spiga, A., Forget, F., Lewis, S., and Hinson, D. (2010). Structure and dynamics of the convective boundary layer on Mars as inferred from large-eddy simulations and remote-sensing measurements. *Quarterly Journal of the Royal Meteorological Society: A journal of the atmospheric sciences, applied meteorology and physical oceanography*, 136(647):414–428.

Spiga, A. and Lewis, S. R. (2010). Martian mesoscale and microscale wind variability of relevance for dust lifting. *Mars*, 5:146–158.

Stanzel, C., Pätzold, M., Greeley, R., Hauber, E., and Neukum, G. (2006). Dust devils on Mars observed by the high resolution stereo camera. *Geophysical Research Letters*, 33(11).

Stevens, B., Moeng, C.-H., and Sullivan, P. P. (1999). Large-eddy simulations of radiatively driven convection: Sensitivities to the representation of small scales. *Journal of the Atmospheric Sciences*, 56(23):3963–3984.

Storm, B., Dudhia, J., Basu, S., Swift, A., and Giammanco, I. (2009). Evaluation of the weather research and forecasting model on forecasting

low-level jets: Implications for wind energy. *Wind Energy*, 12(1):81–90.

Stull, R. B. (1988). *An Introduction to Boundary Layer Meteorology*. Atmospheric and Oceanographic Sciences Library. Springer Netherlands.

Stull, R. B. (2012). *An introduction to boundary layer meteorology*, volume 13. Springer Science & Business Media.

Stull, R. B. (2016). *Practical Meteorology: an algebra based survey of atmospheric science*. BC Campus.

Sukoriansky, S., Galperin, B., and Perov, V. (2005). Application of a new spectral theory of stably stratified turbulence to the atmospheric boundary layer over sea ice. *Boundary-Layer Meteorology*, 117(2):231–257.

Sullivan, P. P. and Patton, E. G. (2011). The effect of mesh resolution on convective boundary layer statistics and structures generated by large-eddy simulation. *Journal of the Atmospheric Sciences*, 68(10):2395–2415.

Sun, J., Lenschow, D. H., Burns, S. P., Banta, R. M., Newsom, R. K., Coulter, R., Frasier, S., Ince, T., Nappo, C., Balsley, B. B., et al. (2004). Atmospheric disturbances that generate intermittent turbulence in nocturnal boundary layers. *Boundary-layer meteorology*, 110(2):255–279.

Sun, J., Mahrt, L., Banta, R. M., and Pichugina, Y. L. (2012). Turbulence regimes and turbulence intermittency in the stable boundary layer during CASES-99. *Journal of the Atmospheric Sciences*, 69(1):338–351.

Sutton, J. L., Leovy, C. B., and Tillman, J. E. (1978). Diurnal variations of the martian surface layer meteorological parameters during the first 45 sols at two viking lander sites. *Journal of the atmospheric sciences*, 35(12):2346–2355.

Tei, F., Aikman, D., and Scaife, A. (1996). Growth of lettuce, onion and red beet. 2. growth modelling. *Annals of Botany*, 78(5):645–652.

Temel, O. (2018). *Multiscale modelling of the atmospheric boundary layer: Mesoscale/microscale coupling*. PhD thesis, Université de Mons.

Temel, O., Bricteux, L., and van Beeck, J. (2018a). Coupled wrf-openfoam study of wind flow over complex terrain. *Journal of Wind Engineering and Industrial Aerodynamics*, 174:152–169.

Temel, O., Bricteux, L., and van Beeck, J. (2018b). Coupled wrf-openfoam study of wind flow over complex terrain. *Journal of Wind Engineering and Industrial Aerodynamics*, 174:152–169.

Temel, O., Karatekin, Ö., Gloesener, E., Mischna, M. A., and van Beeck, J. (2019). Atmospheric transport of subsurface, sporadic, time-varying methane releases on Mars. *Icarus*, 325:39–54.

Temel, O., Senel, C. B., Porchetta, S., Muñoz-Esparza, D., Mischna, M. A., Van Hoolst, T., van Beeck, J., and Karatekin, Ö. (2020). Large eddy simulations of the Martian convective boundary layer: Towards developing a new planetary boundary layer scheme. *Atmospheric Research*, 250:105381.

Therry, G. and Lacarrère, P. (1983). Improving the eddy kinetic energy model for planetary boundary layer description. *Boundary-Layer Meteorology*, 25(1):63–88.

Thomas, R. J., Potter-McIntyre, S. L., and Hynek, B. M. (2017). Large-scale fluid-deposited mineralization in Margaritifer Terra, Mars. *Geophysical Research Letters*, 44(13):6579–6588.

Thompson, G., Field, P. R., Rasmussen, R. M., and Hall, W. D. (2008). Explicit forecasts of winter precipitation using an improved bulk microphysics scheme. part ii: Implementation of a new snow parameterization. *Monthly Weather Review*, 136(12):5095–5115.

Tjernström, M., Žagar, M., Svensson, G., Cassano, J. J., Pfeifer, S., Rinke, A., Wyser, K., Dethloff, K., Jones, C., Semmler, T., et al. (2005). Modelling the arctic boundary layer: an evaluation of six arcmip regional-scale models using data from the sheba project. *Boundary-layer meteorology*, 117(2):337–381.

Tjørve, K. M. and Tjørve, E. (2017). The use of gompertz models in growth analyses, and new gompertz-model approach: An addition to the unified-richards family. *PloS one*, 12(6).

Toigo, A. D., Lee, C., Newman, C. E., and Richardson, M. I. (2012). The impact of resolution on the dynamics of the Martian global atmosphere: Varying resolution studies with the MarsWRF GCM. *Icarus*, 221(1):276–288.

Toigo, A. D., Richardson, M. I., Ewald, S. P., and Gierasch, P. J. (2003). Numerical simulation of martian dust devils. *Journal of Geophysical Research: Planets*, 108(E6).

Torrealba-Rodriguez, O., Conde-Gutiérrez, R., and Hernández-Javier, A. (2020). Modeling and prediction of covid-19 in mexico applying mathematical and computational models. *Chaos, Solitons & Fractals*, page 109946.

Tyler, D. and Barnes, J. (2013). Mesoscale modeling of the circulation in the Gale crater region: an investigation into the complex forcing of convective boundary layer depths. *IJMSE*, 8:58–77.

Tyler, D., Barnes, J. R., and Skyllingstad, E. D. (2008). Mesoscale and large-eddy simulation model studies of the Martian atmosphere in support of

phoenix. *Journal of Geophysical Research: Planets*, 113(E3).

Udina, M., Sun, J., Kosović, B., and Soler, M. R. (2016). Exploring vertical turbulence structure in neutrally and stably stratified flows using the weather research and forecasting–large-eddy simulation (wrf–les) model. *Boundary-layer meteorology*, 161(2):355–374.

Vasavada, A. R., Chen, A., Barnes, J. R., Burkhart, P. D., Cantor, B. A., Dwyer-Cianciolo, A. M., Fergason, R. L., Hinson, D. P., Justh, H. L., Kass, D. M., et al. (2012). Assessment of environments for mars science laboratory entry, descent, and surface operations. *Space Science Reviews*, 170(1):793–835.

Veismann, M., Dougherty, C., Rabinovitch, J., Quon, A., and Gharib, M. (2021). Low-density multi-fan wind tunnel design and testing for the ingenuity mars helicopter. *Experiments in Fluids*, 62(9):1–22.

Vicente-Retortillo, Á., Martínez, G. M., Rennó, N. O., Lemmon, M. T., and de la Torre-Juárez, M. (2017). Determination of dust aerosol particle size at Gale crater using REMS UVS and Mastcam measurements. *Geophysical Research Letters*, 44(8):3502–3508.

Wang, C., Forget, F., Bertrand, T., Spiga, A., Millour, E., and Navarro, T. (2018). Parameterization of rocket dust storms on Mars in the LMD Martian GCM: modeling details and validation. *Journal of Geophysical Research: Planets*, 123(4):982–1000.

Weckwerth, T. M., Horst, T. W., and Wilson, J. W. (1999). An observational study of the evolution of horizontal convective rolls. *Monthly weather review*, 127(9):2160–2179.

Whiteway, J., Komguem, L., Dickinson, C., Cook, C., Illnicki, M., Seabrook, J., Popovici, V., Duck, T., Davy, R., Taylor, P., et al. (2009). Mars water-ice clouds and precipitation. *Science*, 325(5936):68–70.

Wilson, J. R. and Hamilton, K. (1996). Comprehensive model simulation of thermal tides in the Martian atmosphere. *Journal of the Atmospheric Sciences*, 53(9):1290–1326.

Wolff, M. J. and Clancy, R. T. (2003). Constraints on the size of martian aerosols from thermal emission spectrometer observations. *Journal of Geophysical Research: Planets*, 108(E9).

Wolff, M. J., Smith, M. D., Clancy, R., Spanovich, N., Whitney, B., Lemmon, M. T., Bandfield, J., Banfield, D., Ghosh, A., Landis, G., et al. (2006). Constraints on dust aerosols from the Mars Exploration Rovers using MGS overflights and Mini-TES. *Journal of Geophysical Research: Planets*, 111(E12).

Wolkenberg, P., Giuranna, M., Grassi, D., Aronica, A., Aoki, S., Scaccabarozzi, D., and Saggin, B. (2018). Characterization of dust activity on Mars from my27 to my32 by PFS-MEX observations. *Icarus*, 310:32–47.

Wood, R. and Bretherton, C. S. (2004). Boundary layer depth, entrainment, and decoupling in the cloud-capped subtropical and tropical marine boundary layer. *Journal of Climate*, 17(18):3576–3588.

Wu, Z., Li, T., Zhang, X., Li, J., and Cui, J. (2020). Dust tides and rapid meridional motions in the Martian atmosphere during major dust storms. *Nature Communications*, 11(1):1–10.

Wyngaard, J. C. (2004). Toward numerical modeling in the "terra incognita". *Journal of the atmospheric sciences*, 61(14):1816–1826.

Ye, Z., Segal, M., and Pielke, R. (1990). A comparative study of daytime thermally induced upslope flow on mars and earth. *Journal of the atmospheric sciences*, 47(5):612–628.

Yue, L., Tu, T., and Geng, X. (2020). Prediction and severity ratings of covid-19 in the united states. *Disaster Medicine and Public Health Preparedness*, pages 1–22.

Zhang, D.-L. and Zheng, W.-Z. (2004). Diurnal cycles of surface winds and temperatures as simulated by five boundary layer parameterizations. *Journal of Applied Meteorology*, 43(1):157–169.

Zhang, X., Bao, J.-W., Chen, B., and Grell, E. D. (2018). A three-dimensional scale-adaptive turbulent kinetic energy scheme in the wrf-arw model. *Monthly Weather Review*, 146(7):2023–2045.

Zhou, B., Simon, J. S., and Chow, F. K. (2014). The convective boundary layer in the terra incognita. *Journal of the Atmospheric Sciences*, 71(7):2545–2563.

Zwietering, M., Jongenburger, I., Rombouts, F., and Van't Riet, K. (1990). Modeling of the bacterial growth curve. *Appl. Environ. Microbiol.*, 56(6):1875–1881.

List of publications

Published articles in peer-reviewed journals

1. **Senel, C. B.**, Temel, O., Porchetta, S., Muñoz-Esparza, D., & van Beeck, J. (2019). A new planetary boundary layer scheme based on LES: Application to the XPIA campaign. Journal of Advances in Modeling Earth Systems, 11(8), 2655-2679.

2. **Senel, C. B.**, Temel, O., Muñoz-Esparza, D., Parente, A., & van Beeck, J. (2020). Gray zone partitioning functions and parameterization of turbulence fluxes in the convective atmospheric boundary layer. Journal of Geophysical Research: Atmospheres, 125(22), e2020JD033581.

3. **Senel, C. B.**, Temel, O., Lee, C., Newman, C. E., Mischna, M. A., Muñoz-Esparza, D., ... & Karatekin, O. (2021). Interannual, Seasonal and Regional Variations in the Martian Convective Boundary Layer Derived From GCM Simulations With a Semi-Interactive Dust Transport Model. Journal of Geophysical Research: Planets, 126(10), e2021JE006965.

4. **Senel, C. B.**, van Beeck, J., & Altinkaynak, A. (2022). Solving PDEs with a Hybrid Radial Basis Function: Power-Generalized Multiquadric Kernel. Advances in Applied Mathematics and Mechanics, doi:10.4208/aamm.OA-2021-0215.

5. **Senel, C. B.**, Kaskes, P., Temel, O., Vellekoop, J., Goderis, S., Prins, M., Claeys, P., & Karatekin, O. (2023). Another one bites the dust: Chicxulub dust plume triggers photosynthetic collapse. Nature Geoscience (in review).

6. Temel, O., **Senel, C. B.**, Porchetta, S., Muñoz-Esparza, D., Mischna, M. A., Van Hoolst, T., ... & Karatekin, O. (2021). Large eddy simulations of the Martian convective boundary layer: towards developing a new planetary boundary layer scheme. Atmospheric Research, 250, 105381.

7. Temel, O., Karatekin, O., Mischna, M. A., **Senel, C. B.**, Martínez, G., Gloesener, E., & Van Hoolst, T. (2021). Strong Seasonal and Regional Variations in the Evaporation Rate of Liquid Water on Mars. Journal of Geophysical Research: Planets, 126(10), e2021JE006867.

8. Temel, O., **Senel, C. B.**, Spiga, A., Murdoch, N., Banfield, D., & Karatekin, O. (2022). Spectral analysis of the Martian atmospheric turbulence: InSight observations. Geophysical Research Letters, 49(15), e2022GL099388.

9. Lee, F., **Senel, C. B.**, Karatekin, O., Dehant, V., Zhu, P., Zhang, H., Shi, Y. (2023). Discrete element simulations of rotation and structure stability: Binary near-Earth asteroid (65803) Didymos, the target of the DART mission. Earth & Planetary Physics (in review).

Conference presentations in the international meetings

1. **Senel, C. B.**, Temel, O., Porchetta, S., Sert, H., Karatekin, O. & van Beeck, J. (2020). Investigation of inter-annual and seasonal variations of the Martian convective PBL by GCM simulations. In EGU General Assembly Conference Abstracts (p. 18376).

2. **Senel, C. B.**, Temel, O., & Karatekin, O. (2022). Probing Martian turbulence kinetic energy and dissipation rate during major dust storms. In EGU General Assembly Conference, Vienna, 23-27 May.

3. **Senel, C. B.**, Temel, O., & Karatekin, O. (2020). Spectral dynamics and turbulence energy cascade in the Martian planetary boundary layer. In AGU Fall Meeting Abstracts (Vol. 2020, pp. P080-0001).

4. **Senel, C. B.**, Temel, O., Porchetta, S., & van Beeck, J. (2019). A new length scale model for the planetary boundary layer based on LES. In EGU General Assembly Conference Abstracts (p. 13101).

5. **Senel, C. B.**, Temel O., & Karatekin O. (2021). Environmental consequences of asteroid impacts by GCM simulations. In 7th International Academy of Astronautics (IAA) Planetary Defense Conference, virtual meeting, oral, 26–30 April 2021.
6. **Senel, C. B.**, Temel, O., Kaskes, P., Vellekoop, J., Goderis, S., Van Hove, B., & Karatekin, O. (2021). Relative roles of impact-generated aerosols on photosynthetic activity following the Chicxulub asteroid impact. In Geological Society of America Abstracts with Programs (Vol. 53, No. 6, pp. 1–1). Geological Society of America.
7. **Senel, C. B.**, & Karatekin O. (2022). Hypervelocity impact simulations of DART on asteroid Dimorphos: Impact-generated porosity and gravity anomalies, Session SB9 – Latest Science Results in Planetary Defence, Europlanet Science Congress, Granada, Spain, 18–23 Sep 2022. Awarded the EPSC Outstanding Poster Contest (OPC).
8. **Senel, C. B.**, & Karatekin, O., Raducan, S. & Luther, R. (2023). Post-impact porosity and gravity anomalies following the hypervelocity DART impact on asteroid Dimorphos in Lunar and Planetary Science Conference, Houston, Texas, US.
9. **Senel, C. B.**, & Karatekin, O. (2023). What if Near-Earth asteroid 99942 Apophis collides with Earth: Hypothetical impact assessment in 8th International Academy of Astronautics (IAA) Planetary Defense Conference (Sub-theme: New results on the effects of ocean and land NEO impacts and related damage footprints), Vienna, Austria, accepted.
10. **Senel, C. B.**, Temel, O. & Karatekin, O (2023). Martian interactive dust and water cycle GCM simulations as compared with TGO/NOMAD and MCS observations in European Geoscience Union (EGU), Vienna, Austria.
11. Stickle, A. M., DeCoster, M. E., Graninger, D. M., Kumamoto, K. M., Owen, J. M., Fahenstock, E. G., ..., Karatekin, O., ..., **Senel, C. B.**, Schwartz, R., Tusberti, F., Wunnemann, K. & Zhang, Y. (2023). Constraining Dimorphos's material properties and estimates of crater size from the DART impact in Lunar and Planetary Science Conference, Houston, Texas, US, LPSC, accepted.
12. Henry, G., Karatekin, O. & **Senel, C. B.** (2023). Thermophysical modeling for binary asteroids and application to Didymos in Lunar and Planetary Science Conference, Houston, Texas, US, LPSC, accepted.
13. Ritter, B., Karatekin, O., Carrasco, J. A., Tasev, E., Alavés Mañogil, H., Noeker, M., Van Ransbeek, E., Noiset, G., & **Senel, C. B.** (2022).

Measuring gravity with the GRASS instrument on the Hera mission, Europlanet Science Congress 2022, Granada, Spain, 18–23 Sep 2022, EPSC2022-1115.

14. Temel, O., **Senel, C. B.**, & Karatekin, O. The nighttime boundary layer of Mars as predicted by large-eddy simulations in European Geoscience Union (EGU), Vienna, Austria (2023).
15. Sert, H., Temel, O., **Senel, C. B.**, & Karatekin, O. (2020). A global circulation model for the asteroid impact simulations. In EGU General Assembly Conference Abstracts (p. 10832).
16. L. Montabone, N. G. Heavens, A. Pankine, M. Wolff, A. Cardesin-Moinelo, B. Geiger, F. Forget, E. Millour, A. Spiga, S. D. Guzewich, O. Karatekin, B. Ritter, L. Ruiz Lozano, **Senel, C. B.**, O. Temel, R. J. Lillis, K. S. Olsen, P. L. Read, A. C. Vandaele, S. Aoki, F. Daerden, L. Neary, J. M. Battalio, T. Bertrand, C. Gebhardt, R. M. B. Young, M. Giuranna, F. Oliva, P. Wolkenberg, S. J. Greybush, J. Hernández-Bernal, A. Sánchez-Lavega, A. Kleinboehl, M. A. Mischna, L. K. Tamppari, S. R. Lewis, P. Machado, F. Montmessin, H. Nakagawa, K. Ogohara, S. Robert, D. Titov, M. Vincendon & H. Wang. (2022). The case and approach for continuous, simultaneous, global mars weather monitoring from orbit. In 7th Mars Atmosphere Modelling and Observations workshop (MAMO), Paris, June.
17. L. Montabone, N. G. Heavens, A. Cardesin-Moinelo, F. Forget, S. D. Guzewich, O. Karatekin, R. Lillis, K. Olsen, A. C. Vandaele, M. Wolff, S. Aoki, J. M. Battalio, T. Bertrand, F. Daerden, C. Gebhardt, B. Geiger, M. Giuranna, S. J. Greybush, J. Hernández-Bernal, A. Kleinboehl, S. R. Lewis, P. Machado, E. Millour, M. A. Mischna, F. Montmessin, H. Nakagawa, L. Neary, K. Ogohara, F. Oliva, A. Pankine, P. L. Read, B. Ritter, S. Robert, L. Ruiz Lozano, A. Sánchez-Lavega, **Senel, C. B.**, A. Spiga, L. K. Tamppari, O. Temel, D. Titov, M. Vincendon, H. Wang, P. Wolkenberg & R. M. B. Young. (2022). The case and approach for continuous, simultaneous, quasi-global weather monitoring on Mars. In 44th COSPAR Scientific Assembly, Athens, July. Space Studies of the Earth-Moon System, Planets, and Small Bodies of the Solar System (B) Forward Planning for the Exploration of Mars (B4.3).